

GEOLOGIC, GEOCHEMICAL, AND GEOPHYSICAL CHARACTERIZATION  
OF THE GOLD DEPOSITS OF THE HORSESHOE BEND MINING DISTRICT,  
IDAHO: BUILDING A FOUR DIMENSIONAL MODEL FOR ORE EXPLORATION

by

Joshua Ekhoff

A thesis

submitted in partial fulfillment

of the requirements for the degree of

Master of Science in Geoscience

Boise State University

August 2016

© 2016

Joshua Ekhoﬀ

ALL RIGHTS RESERVED

BOISE STATE UNIVERSITY GRADUATE COLLEGE

**DEFENSE COMMITTEE AND FINAL READING APPROVALS**

of the thesis submitted by

Joshua Ekhoﬀ

Thesis Title: Geologic, Geochemical and Geophysical Characterization of the Gold Deposits of the Horseshoe Bend Mining District, Idaho: Building a Four Dimensional Model for Ore Exploration

Date of Final Oral Examination: 06 April 2016

The following individuals read and discussed the thesis submitted by student Joshua Ekhoﬀ, and they evaluated his presentation and response to questions during the final oral examination. They found that the student passed the final oral examination.

Mark D. Schmitz, Ph.D. Chair, Supervisory Committee

Paul R. Donaldson, Ph.D. Member, Supervisory Committee

Clyde J. Northrup, Ph.D. Member, Supervisory Committee

The final reading approval of the thesis was granted by Mark D. Schmitz, Ph.D., Chair of the Supervisory Committee. The thesis was approved for the Graduate College by Jodi Chilson, M.F.A., Coordinator of Theses and Dissertations.

## DEDICATION

For Adelaide, Oliver, Rheanne, Mom, and Dad.

## ACKNOWLEDGEMENTS

First and foremost I would like to acknowledge and thank my family for supporting me and believing in me throughout the course of my education. To my wife Rheanne, this work is just as much yours as it is mine, thank you for everything you do for me and our little family, I love you so much. To my children, Oliver and Adelaide, thank you for being so very patient when daddy had long days and nights of work, I promise to play with you more from now on 'til forever, I love you guys, you are and always will be my motivation. I would not be writing this now if not for the everlasting support of my mother, Martha, who has taught me the meaning of perseverance no matter what. Mom, I thank you for loving me and always having the right words when things get rough. My mother and father in law, Mike and Debbie, thank you, for not only being supportive in every way of your son in law being a forever student but for always being so enthusiastic about my work. Julie, thank you for being my family science buddy and for setting a standard for me to try and attain. Allison and Brand, your help has been invaluable and your company always uplifting. Stephen, thank you for making me feel like a king, even when I am most definitely not. Genn and Jeff, thanks for having me and for always being there for a good time.

I absolutely owe a debt I can never repay to my father, Jerry, for inspiring me to get out and love life wherever it takes me. Dad, you started me on my journey to pursue geology and my greatest life lessons come from you, you are my inspiration and guiding

force. I love you more than I can say and I hope that I can be half the human being as you.

I must acknowledge and thank my advisor Dr. Mark Schmitz for the work he has done with and for me not only on this project but on the work and guidance he has provided me in life. Thank you Mark, without your mentoring I would still be lost in the literal and metaphorical woods. Thank you also to Dr. Karen Viskupic, Dr. Sam Matson, Dr. Jen Pierce, and Dr. Warren Barrash for giving me research opportunities and making me believe that graduate school was a realistic goal for me. Thank you also to Dr. Paul Donaldson for doing your darndest to help me understand geophysics and your kindness and patience along the way. Thank you too to Dr. CJ Northrup for being the voice of the “boots on the ground” geologist that I will forever have in my head. Thank you Dr. Jim Crowley, Debbie Pierce, Dr. Sam Evans, Dr. Marion Lytle, Dr. Lee Liberty, and Dr. John Bradford for doing the brutal work of teaching me to (and then letting me) use your valuable labs and equipment, your patience is saintly.

I could not have finished any of this without the tremendous amount of help given to me by my fellow students. In particular I would like to thank Amanda Laib for repeatedly risking life and limb for my data collection, I owe you more than just a few. Thank you to Robin Trayler for being my field assistant, emergency ride, technical support and, most importantly, my friend. Huge thanks as well to Hank Hetrick and Kyle Lindsay for doing all the heavy lifting on the geophysical processing. Speaking of heavy lifting, thanks especially to Connor McMahon and Nick Mordhorst for enduring a brutal field season with me, and to Alyssa Chase for enduring the next. The efforts of Claire,

Philly Amanda, Darin, Nick, Kimberley, Janna, Tom, Jesse, Vince, Katie, and Lucy are also tremendously appreciated. Thank you all, so, so, much.

This work would not have been possible if not for the generous and trusting support of Trans-Challis Exploration and Development, LLC. Don Miller and Scott Phillips, thank you for taking a chance on a perfect stranger and giving me the opportunity to work on a thesis that is so rewarding.

## ABSTRACT

The Eocene aged Trans-Challis Fault System of central Idaho provides the tectonic and magmatic framework for a series of Au-Ag and Cu-Mo ore deposits. From its northernmost extension near Butte, Montana to its southwestern terminus in the Boise Basin of south-central Idaho the Trans-Challis Fault System is associated with some of the richest precious metal deposits found in Idaho. However, the southernmost tip of the Trans-Challis Fault System, composed of the Horseshoe Bend and Pearl mining districts, remains understudied, receiving little economic or academic attention. As a result, how the Pearl to Horseshoe Bend mining districts fit within the established framework of the Trans-Challis Fault System and associated mineralization is poorly characterized. Significantly, no high-resolution mapping or modern geochemical and geophysical techniques have been applied to areas within these historically productive mining districts. This study employs detailed bedrock mapping, high-precision U/Pb geochronology, high-resolution soil geochemistry, ground-based magnetic anomaly mapping, and electrical resistivity and induced polarization geophysical imaging to characterize spatial patterns to create a model for structurally controlled mineralization within the Horseshoe Bend Mining District.

Integration of these datasets with knowledge gained from other studies along the Trans-Challis Fault System has led to the characterization of the structural framework hosting mineralization near Horseshoe Bend, Idaho. Geologic mapping reveals NE-SW and E-W trending dike swarms and associated en echelon mineralized vein systems

oriented sub-parallel to the NE trend of the Trans-Challis Fault System. U/Pb ages on zircon grains within the dikes date emplacement during the late Early Eocene to the Early Oligocene. Surficial geochemistry surveys reveal east-west oriented, en echelon, zones of anomalously high gold concentrations with subordinate north-south oriented arms. Magnetic anomaly mapping reveals lineaments of sharp magnetic gradients spatially correlated with mapped dike patterns, as well as zones of magnetic lows spatially correlated with surface geochemical gold concentration anomalies. Electrical resistivity and induced polarization subsurface imaging techniques outline a series of east-west oriented, northeast stepping, conductivity, chargeability, and metal factor highs that correlate with a similarly oriented magnetic anomaly over the survey area, and en echelon mineralized vein systems mapped in adjacent bedrock.

The Early Oligocene age of the andesite dike phase reported to follow mineralization either extends the duration, or changes the timing, of the mineralizing events associated with this section of the Trans-Challis Fault System. Mapping, geochemical and geophysical data strongly suggest the controlling factor in mineralization location and geometry is the underlying structural framework of the system. Based on these geometries and orientations, a dextral Riedel shear array oriented  $070^{\circ}$  is proposed to adequately model the structural architecture controlling mineralization within the Horseshoe Bend Mining District.

## TABLE OF CONTENTS

DEDICATION .....	iv
ACKNOWLEDGEMENTS .....	v
ABSTRACT .....	viii
LIST OF TABLES .....	xv
LIST OF FIGURES .....	xvii
SECTION 1: BACKGROUND AND MOTIVATION .....	1
Introduction.....	1
Location .....	2
Project Background.....	3
Deposit Type.....	4
Methodology.....	6
Economic Considerations .....	7
SECTION 2: GEOLOGIC SETTING .....	10
Introduction.....	10
Precambrian Tectonic Setting.....	11
Sevier and Laramide Orogenies.....	12
Idaho Batholith.....	13
Western Idaho Shear Zone.....	14
Trans-Challis Fault System.....	14
Challis Volcanic Field.....	16

Idaho-Montana Porphyry Belt .....	17
Basin and Range .....	17
Snake River Plain.....	18
Regional Geology .....	19
Local Geology.....	21
<b>SECTION 3: GEOLOGIC MAPPING .....</b>	<b>23</b>
Introduction.....	23
Geologic Mapping .....	24
Description of Lithologic Units .....	24
Alluvium (Holocene) .....	25
Sediments of the Payette Formation (Miocene).....	25
Lamprophyre (Miocene) .....	25
Diabase/basalt (Miocene).....	26
Andesite (Oligocene) .....	26
Dikes, Undivided (Eocene).....	27
Rhyolite (Eocene) .....	27
Pyroxene-hornblende Diorite Porphyry (Eocene) .....	28
Biotite-hornblende Dacite Porphyry Dikes (Eocene) .....	29
Diorite (Cretaceous).....	30
Biotite Granodiorite (Cretaceous).....	31
Structure .....	31
<b>SECTION 4: GEOCHRONOLOGY .....</b>	<b>35</b>
Introduction.....	35

Results.....	35
LA-ICPMS Methods.....	37
CA-IDTIMS Methods.....	40
<b>SECTION 5: SURFACE GEOCHEMISTRY SURVEY .....</b>	<b>41</b>
Introduction.....	41
Sampling and Analysis .....	41
Results.....	43
Soil Analysis Methods .....	46
<b>SECTION 6: MAGNETIC SURVEY .....</b>	<b>48</b>
Introduction.....	48
Data Collection and Analysis.....	49
Results.....	50
<b>SECTION 7: ELECTRICAL RESISITIVITY AND INDUCED POLARIZATION SURVEY.....</b>	<b>53</b>
Introduction.....	53
Data Collection and Analysis.....	56
Electrical Resistivity Survey.....	57
Induced Polarization Survey .....	59
Metal Factor .....	61
<b>SECTION 8: DISCUSSION .....</b>	<b>63</b>
Interpretations and Conclusions.....	63
Surface Gold Anomalies .....	63
Total Field Magnetic Anomaly Lows .....	65
Dikes and Magnetic Edge Detection.....	67

Coincidence of IP/ER and Magnetic Trends .....	70
Intersection of Fracture Planes.....	72
Proposed Structural Model .....	74
SECTION 9: RECOMMENDATIONS .....	82
Improve the Structural Dataset .....	82
Additional Surface Geochemical Sampling .....	83
Ground Truth Magnetic Data.....	84
Extend IP/ER Coverage Over Known Veins .....	84
Excavation/Trenching Across Vein Systems.....	86
Timing of Mineralization.....	87
Ore Characterization .....	89
Targets.....	89
SECTION 10: CONCLUSIONS.....	92
REFERENCES .....	94
TABLES .....	102
FIGURES .....	105
APPENDIX A.....	155
Mine Summaries .....	155
APPENDIX B .....	170
Drill Records.....	170
APPENDIX C .....	172
Geologic Maps .....	172

APPENDIX D.....	179
ALS Geochemistry Lab Methods .....	179
APPENDIX E .....	183
Magnetic Anomaly Matlab Code.....	183
APPENDIX F.....	203
Magnetic Anomaly Maps and Figures .....	203
APPENDIX G.....	209
Electrical Resistivity, Induced Polarization, and Metal Factor Matlab Code.....	209
APPENDIX H.....	247
Independent Analysis of Surface Geochemistry Results .....	247

## LIST OF TABLES

Table 4.1.	Dike U/Pb.....	102
Table 5.1.	ALS Global geochemical methods. ....	103
Table 9.1.	Proposed sampling areas, including acreage, and approximate number of samples required to sample at 25' (8m) density. ....	104
Table A.1.	Historical mining claims within Trans-Challis, LLC. Property. Compiled from the Idaho Geological Survey. ....	157
Table A.2.	Anticlinal Claim.....	159
Table A.3.	Apex claim.....	159
Table A.4.	Atlanta Claim.....	160
Table A.5.	Ballentyne claim.....	160
Table A.6.	Bobtail claim.....	161
Table A.7.	Catherine claim.....	161
Table A.8.	Clagett claim.....	161
Table A.9.	Hall claim.....	162
Table A.10.	Kentuck claim.....	162
Table A.11.	Lambertine claim.....	163
Table A.12.	Lost claim.....	163
Table A.13.	Lucky boy claim.....	164
Table A.14.	Mammoth claim.....	164
Table A.15.	Marine Claim.....	165
Table A.16.	Mint claim.....	165

Table A.17.	Nellie claim.....	165
Table A.18.	Osborne claim .....	166
Table A.19.	Payette claim.....	167
Table A.20.	Quaker claim.....	167
Table A.21.	Sunny Side claim .....	168
Table A.22.	Topeka claim.....	168
Table B.1.	Summary of the Sunshine Mining drilling program from the 1980 to 1982 exploration of the Pearl Mining District. Note that none of these holes are in the current property area.....	171

## LIST OF FIGURES

Figure 1.1.	Porphyry copper-molybdenum and molybdenum deposits of the Idaho-Montana Porphyry Belt. Dashed red line, Salmon River suture. From Taylor et al., 2007. ....	105
Figure 1.2.	Location and ownership map of Trans-Challis property. ....	106
Figure 1.3.	Map of Trans-Challis, LLC property 1 mile (1.5km) west of Horseshoe Bend, Idaho. Thick black lines are reference baselines. Baseline intersection is approximate centroid of property. ....	107
Figure 1.4.	Schematic representation of hydrothermal mineral deposits and relative position in volcanic systems. Not all systems are suggested to be present at once. Note the position of the low sulfidation system and its interaction with meteoric water. From Hedenquist et al., 2000. ....	108
Figure 2.1.	Tectonic and magmatic elements discussed in text. Abbreviations and symbols as follows: pink polygon, Idaho Batholith; orange polygon, Challis Volcanics; yellow circle, Yellowstone caldera; red polygon, Boise County; WSRP, western Snake River Plain; WISZ, Western Idaho Shear Zone; Kgd, Cretaceous granodiorite of the Idaho Batholith; Tcv, Eocene Challis Volcanics. Adapted from Ickert et al., 2007; Moye et al., 1988; Taylor et al., 2007. ....	109
Figure 2.2.	Regional and local geology of the Horseshoe Bend Mining District. The district is located at the SW extent of the Trans-Challis Fault Zone and Idaho Porphyry Belt, which are marked by the NE trending faults on both maps. The inset shows the extent of the Pearl to Horseshoe Bend Mining districts as well as those of the Boise Basin. Kgd – Cretaceous granodiorite, Tcv – Tertiary Challis volcanics, Tcb – Tertiary Columbia River Basalts. Modified from Anderson, 1947; Kiilsgaard and Bennett, 1986; Lewis et al., 2012. ....	110
Figure 2.3.	Simplified geologic map of study area. Abbreviations: Kgd – Cretaceous granodiorite; Kd – Cretaceous diorite; Tdip – Eocene diorite porphyry; Tdp – Eocene dacite porphyry; Trp – Eocene rhyolite; Tad – Oligocene Andesite; Tdd – Miocene basalt/diabase; Tpf – Miocene Payette Formation; Qal – Quaternary alluvium. ....	111

Figure 2.4.	Concentrated node of mineralization (indicated by red circle) at the intersection of two fracture planes.....	112
Figure 3.1.	Joint strike frequency diagram from Saylor (1967). All joint sets are measured in units comprising the Idaho Batholith. Note that orientations are dominantly northeast and northwest, except in section 6. The property is within section 6 and is the only section that contains the Cretaceous diorite unit. Joint orientations here are north-south or northeast. ....	113
Figure 3.2.	Stereonet showing the poles to planes of measured movement planes (slickensides). The majority of points indicate northeast to east-west trending fractures, a potentially significant set of points indicate a conjugate subset of north trending fractures. ....	114
Figure 3.3.	A: Stereonet showing poles to planes of dike strikes and dips measured as part of this study as small filled circles. A strong trend of northeast oriented dikes is apparent in the data. Mean vector orientations are the larger filled circles, error on the mean shown as large unfilled ellipses. Red: diorite porphyry dikes, blue: andesite dikes, green: diabase dikes, light blue: dacite dikes, orange: rhyolite dikes. B: Rose diagram showing the orientation measurements of dikes where a reliable dip measurement was unavailable. The large majority of dikes are oriented between 50 and 70 degrees Dikes are not divided by lithology in the rose diagram.....	115
Figure 3.4.	A: Stereonet showing the pole to planes of measured vein strike and dips. The underground data from Anderson (1934) includes workings across the breadth of the Pearl to horseshoe Bend districts and is plotted in red, surface data from this study is plotted in black. Circled in blue are poles that represent east-west vein orientations. B: Rose diagram showing the orientation of veins from this study where dip was unable to be determined.....	116
Figure 3.5.	Riedel shear array, shown with a right-lateral or dextral sense of shear and oriented to the overall trend of the Trans-Challis Fault Zone, ~N70E. The Riedel shear array is an empirically derived prediction of fracture orientations in a pure strike-slip environment. Thick black lines are the primary planes of movement in a strike-slip fault. Thinner, gray lines are predicted orientations of the fractures accommodating movement. Lines P and R <sub>1</sub> are primary fractures and have the same sense of shear as the strike-slip fault. Line R <sub>2</sub> is a secondary fracture plane, conjugate to P and with opposite sense of movement. Lines T and X are tertiary fracture planes. Greek letters $\alpha$ , $\beta$ , $\lambda$ , and $\Delta$ are angles with predictable magnitudes, which are given within the angle arc. The principal direction of stress is shown as $\sigma_1$ , the direction of least stress is shown by $\sigma_3$ . Cardinal directions are in pink.....	117

Figure 3.6.	Riedel shear array of fig. 3.5 with an added trans-tensional component. Ore bodies will dilate in the direction of least stress, $\sigma_3$ , shown north to south here, and elongate in the direction of maximum stress, $\sigma_1$ , shown here as east to west and roughly parallel with fracture set P. The R1 fracture set is oriented N51E, similar to the general trend of dikes, ore bodies are hypothesized to follow this same trend. Where the N02W oriented R2 fracture set intersects the ore bodies and the dikes that guide mineralization the ore fluids may penetrate and cross the dike as illustrated in the center of the figure. ....	118
Figure 4.1.	Summary of relative (from Anderson, 1947) and absolute timelines. All ages given in millions of years (Ma) and errors are reported to $2\sigma$ . Absolute ages for Cretaceous diorite, Kd, from Gaschnig (pers. comm. 2016) and for the Payette Formation, Tpf, from Feeney et al. (2016)....	119
Figure 5.1.	Histogram of surface gold concentrations. 467 samples are represented in the 0-10ppb bin. Samples with gold concentrations >100ppb are binned together. ....	120
Figure 5.2.	Surface geochemical survey results. Plotted are surface (soil and rock chip) gold concentrations in ppb. Concentration considered anomalous, i.e. $\geq 20$ ppb are highlighted in red. Inset: Detailed surface survey of August 2015 covering parts of the Apex and Mammoth claims. ....	121
Figure 5.3.	Surface geochemical gold concentration gradient map. There is a distinct east-west trend to anomalies that can't be explained by survey geometry alone. Between east-west trends are anomalous zones that "cross" from one east-west trend to another, where these intersect major east-west trends the areal extent of anomalous zones increases. Values are plotted on log scale with values greater than 100 ppb capped at 100 ppb, and values less than 1 ppb shifted to 1 ppb. This was done to facilitate visualization between extreme ranges of gold concentrations (.001 to 2190 ppb). Samples greater than 20ppb in gold are marked with red crosses. The results of the detailed Mammoth survey are plotted as small red crosses for samples greater than 20 ppb gold, but are not included in the gradient map.....	122
Figure 5.4.	Au concentration (y-axis) vs. elemental concentration (x-axis) with the $R^2$ value of dotted linear trend line given. The high $R^2$ values of arsenic (0.9588) and bismuth (0.5069) are likely indicative that locally gold is hosted in arsenopyrite with Bi substituting into the arsenopyrite lattice in place of arsenic. Lesser correlations with Ag ( $R^2 = 0.2795$ ) and Cu ( $R^2 = 0.2383$ ) are likely due to the presence of pyrrargyrite and owoyheite, and chalcopyrite and tennantite, respectively, as ore minerals. ....	123

Figure 6.1.	Magnetic anomaly map reduced to pole data. Scale bar is nanoTesla (nT) deviation from mean. ....	124
Figure 6.2.	Magnetic anomaly Y (north-south) gradient data. Scale bar is nanoTeslas per meter (nT/m) deviation from mean. ....	125
Figure 7.1.	Ranges of electrical resistivity (ohm-m) and electrical conductivity (mS/m) for common earth materials. From Palacky, 1988. ....	126
Figure 7.2.	Location of IP/ER survey of July and August 2014. Numbers in red polygon are lines 1, 10, 20, and 27. Green dots indicate line segment endpoints. ....	127
Figure 7.3.	Schematic diagram of a dipole-dipole array. In step 1 current is injected at potential electrode pair 1 and apparent resistivity or chargeability is measured at electrode pairs from 3 onward, different levels of current flow path intersection, given by dashed lines give different levels of investigation, indicated by black dots. In step 2 current is inject at electrode pair 2, denoted in red, and measurements are made at electrode pairs 4 and onward, denoted by red dots. Repeating this process across the whole array gives the apparent resistivity or chargeability at a number of different points, from which inversion software can model resistivity and chargeability sections. ....	128
Figure 7.4.	Results of Electrical Resistivity survey. Lines point north. A roughly NE-SW trend of ER highs is apparent in the series of cross-sections. ...	129
Figure 7.5.	Results of Induced Polarization survey. Lines point north. A roughly NE-SW trend of IP highs is apparent in the series of cross-sections. ....	130
Figure 7.6.	Time integrated measure of IP. On the left is a theoretical decay curve with voltage potential indicated by the hashed area. Because equipment cannot measure the continuous decay of voltage the curve is sampled at multiple points during discharge to reconstruct the decay curve, as shown on the right. Modified from Parasnis (1975). ....	131
Figure 7.7.	Results of Metal Factor interpretation method. Lines point north. A roughly NE-SW trend of metal factor highs is apparent in the series of cross-sections. ....	132
Figure 7.8.	Results of Metal Factor interpretation method located in approximate position on map. Thick red lines are interpreted trends of metal factor highs. Inset: Original figure before map overlay. ....	133
Figure 8.1.	Surface geochemical gold concentration gradient map. There is a distinct east-west trend to anomalies that can't be explained by survey geometry	

alone. Between east-west trends are anomalous zones that “cross” from one east-west trend to another, where these intersect major east-west trends the areal extent of anomalous zones increases. Three, the Osborn, Kentuck-Mammoth, and Payette, east-west anomalous trends are circled in red, and one, the Quaker-Payette, north-south anomaly is circled in yellow. Values are plotted on log scale with values greater than 100 ppb capped at 100 ppb, and values less than 1 ppb shifted to 1 ppb. This was done to facilitate visualization between extreme ranges of gold concentrations (.001 to 2190 ppb). Samples greater than 20ppb in gold are marked with red crosses. The results of the detailed Mammoth survey are plotted as small red crosses for samples greater than 20 ppb gold, but are not included in the gradient map..... 134

Figure 8.2. Surface geochemical soil gold anomaly gradient map (B) and total field magnetic anomaly RTP map (B). The gold anomaly highs (reds on A) align relatively well with magnetic anomaly lows (blues on B). Hydrothermal destruction of primary magnetite and hydrothermal deposition of gold are hypothesized to be the drivers behind the resemblance..... 135

Figure 8.3. Total magnetic field anomaly reduced to pole gradient map of the Mammoth and Apex claims with surface gold concentrations  $\geq 20$ ppb plotted as red crosses. Blue line traces the trend of a magnetic low that crosses the Mammoth and Apex claims. Red line is projected strike of the exposed Mammoth vein. Note the correlation between magnetic low trend and strike of Mammoth vein with associated surface samples. Inset: location of Mammoth and Apex claims on the property. .... 136

Figure 8.4. The Quaker anomaly with RTP magnetic map inset. Red crosses are surface geochemical survey gold concentrations  $\geq 20$ ppb, colored polygons are mapped dikes. In general high gold concentrations overlap with magnetic lows. .... 137

Figure 8.5. The Mammoth and Apex claim areas showing results of the summer 2015 (small red crosses) and 2014 (large red crosses) surface geochemical sampling programs along with mapped dikes and edge detection magnetic results. Magnetic lineaments successfully outline the excavated Mammoth vein along its physical and geochemical trace westward up the Mammoth gully. Red crosses are surface geochemical gold concentrations  $\geq 20$ ppb, colored polygons are mapped dikes, crossed red picks symbols are old prospect pits, pick and shovel symbol is location of Mammoth mine excavation, hatched areas are mine or excavation dumps/waste piles. Inset: Whole property magnetic edge detection map with area of large map in the boxed region..... 138

- Figure 8.6. Close-up of area around Catherine claim showing dikes, summer 2014 surface geochemical survey gold concentrations, and edge detection magnetic anomaly results. Note correlation in center of image showing alignment of the three different exploration methods. Red crosses are surface geochemical gold concentrations  $\geq 20$ ppb, colored polygons are mapped dikes, crossed red picks symbols are old prospect pits, pick and shovel symbol is location of Mammoth mine excavation, hatched areas are mine or excavation dumps/waste piles. Inset: Whole property magnetic edge detection map with area of large map in the boxed region..... 139
- Figure 8.7. A: East-west trending Payette surface gold concentration anomaly shown with mapped dikes and magnetic edge detection results. Location of anomaly shown in boxed area of B. In the eastern half of the figure the three datasets align well and indicate a good target using the guidelines of figures 27 and 28. In the western half of the figure, near the crest of the ridge, the magnetic and geologic signatures fade out while the gold anomaly signature remains. The dichotomy of the eastern and western halves of the trend may warrant further exploratory work. Red crosses: surface gold  $\geq 20$ ppb. Black crosses: surface gold  $< 20$ ppb. Colored polygons: mapped dikes. Gradient map: magnetic edge detection results. .... 140
- Figure 8.8. Edge detection and metal factor comparison. Shown is the area of the IP/ER survey with only the magnetic edge detection results (left) and with metal factor overlaid (right). The red lines on the metal factor overlay indicates the general trends of anomaly highs. This appears to correlate well with the magnetic gradient trend across the area. .... 141
- Figure 8.9. A: Stereonet showing the pole to planes of measured vein strike and dips. The underground data from Anderson (1934) includes workings across the breadth of the Pearl to horseshoe Bend districts and is plotted in red, surface data from this study is plotted in black. Circled in blue are poles that represent east-west vein orientations. B: Rose diagram showing the orientation of veins from this study where dip was unable to be determined..... 142
- Figure 8.10. A mineralization node created by the intersection of east-west fracture planes (blue arrows) and north-south fracture planes (red arrows). Picture is looking at the north wall of the recent Mammoth mine excavation.... 143
- Figure 8.11. Mammoth mine. The light blue line indicates the trace of the Mammoth vein, strike and dip symbols represent orientation of fractures in the area. The Mammoth vein and fracture trends show the east-west trend of vein systems with NNW fracture intersections. Large red crosses: Orientation surface geochemical survey,  $\geq 20$  ppb. Small red crosses: Mammoth gully

surface geochemical survey,  $\geq 20$  ppb. Colored polygons: mapped dikes. Colored gradient map: north-south edge detection. Hashed areas: Mine dumps/excavation waste. Black/white squares with an A: Abandoned mine portals..... 144

- Figure 8.12. The figure shows a right-lateral Riedel shear array with geometry as given by Logan et al. (1979) and its' relationship to surface gold anomalies. A: Surface gold concentration gradient map with three east-west anomalies outlined by red ellipses and one north-south anomaly outlined by a blue ellipse. B: Riedel shear geometry rotated to the overall trend of the Trans-Challis Fault Zone, N70E, cardinal directions shown in pink. C: Image B overlain onto A and centered on the Quaker anomaly with surface gradient map removed, the locations of the ellipses and Osborn mine (blue star), Quaker anomaly (green star), and Mammoth mine (pick and shovel symbol) are unchanged. The Osborn, Kentuck, Quaker, Mammoth, and Payette labels represent named mining claims in the vicinity. Smaller, solid red ellipses are hypothetical fractures developed in shear array. Principal planes of movement (fractures) are indicated by the thick black lines oriented N70E, secondary movement planes are indicated by thinner black lines labeled P and R<sub>1</sub>, tertiary movement planes are shown by thin grey lines labeled R<sub>2</sub> and X, sense of movement is indicated by the black arrows. Note that the sense of movement on R<sub>2</sub> is antithetical to the rest of the array. .... 145
- Figure 8.13. Au concentration (y-axis) plotted according to UTM easting. The series of plots encompass the north to south width of the Kentuck-Quaker-Mammoth trend of gold anomalies. The bottom graph plots all samples from previous eight graphs without regard to northing. .... 147
- Figure 8.14. Incremental spatial autocorrelation analysis of all surface geochemistry samples weighted by gold concentration value, processing done in ArcGIS. The peak z-score of 9.98 occurs as 258m..... 148
- Figure 8.15. Periodogram of the UTM 4860815 N sampling line. The lowest frequency peak occurs at 0.0039 which corresponds to an anomaly spacing of 256m. .... 149
- Figure 9.1. Proposed sampling areas for future high density surface geochemical surveys. .... 150
- Figure 9.2. Area of proposed Osborne IP/ER survey. Five 1200' (360m) north-south lines that cross the Osborne draw, each separated by ~400' (120m) are proposed. Green lines are of previously completed IP/ER survey. Black lines are proposed new lines. .... 151

Figure 9.3.	Area of proposed Mammoth IP/ER survey. Three 600' (180m) north-south lines across the Mammoth gully, each separated by ~200' (60m), are proposed. Black lines are proposed new lines. ....	152
Figure 9.4.	Osborne Jeep trail and vein system. Improving the jeep trail that ascends the Osborne draw would serve the dual purposes of improving access and exposing sections of the Osborne vein. Note northeast trend to en echelon vein sets (red lines). ....	153
Figure 9.5.	Areas of proposed Mammoth excavations shown in cross-hatched polygons. Orange lines are preexisting roads or cuts. Red crosses are surface geochemical results of 20ppb or greater. ....	154
Figure C.1.	Topographic and claim map produced by Dunn Land Survey for this project with geologic map of Alvarez and Ojala (1981) overlain. ....	173
Figure C.2.	Geologic map of the Pearl to Horseshoe Bend mining districts from Lindgren (1898). ....	175
Figure C.3.	Map showing location of the Pearl to Horseshoe Bend mining districts from Anderson (1934). ....	176
Figure C.4.	Geologic map of the Pearl to Horseshoe Bend mining districts from Anderson (1934). ....	177
Figure C.5.	Geologic map of the property and surrounding area from Alvarez and Ojala (1981) ....	178
Figure E.1.	Combined magnetic anomaly grids. ....	194
Figure E.2.	Combined and interpolated magnetic anomaly grids. ....	195
Figure E.3.	Reduced to Pole (RTP) magnetic anomaly grid. Scale is nT. ....	199
Figure E.4.	Original data magnetic anomaly grid. Scale is nT. ....	200
Figure E.5.	X-derivative (E-W gradient) magnetic anomaly grid. Scale is nT/m. ....	201
Figure E.5.	Y-derivative (N-S gradient) magnetic anomaly grid. Scale is nT/m. ....	202
Figure F.1.	Combined magnetic anomaly map. Black lines show the trace of individual collection lines. Scale bar in nT. ....	204
Figure F.2.	Interpolated total field magnetic anomaly map as produced in Matlab. Final map produced in ArcGIS. Scale bar in nT. ....	205

Figure F.3.	Interpolated reduced to pole magnetic anomaly map as produced in Matlab. Final map produced in ArcGIS. Scale bar in nT. ....	206
Figure F.4.	Interpolated x-derivative (east-west magnetic gradient) magnetic anomaly map as produced in Matlab. Final map produced in ArcGIS. Scale bar in nT. ....	207
Figure F.5.	Interpolated y-derivative (north-south magnetic gradient) magnetic anomaly map as produced in Matlab. Final map produced in ArcGIS. Scale bar in nT. ....	208
Figure H.1.	Surface geochemistry gold concentration map produced by independent consulting geologist Tom Gesick, 2016.....	250

## SECTION 1: BACKGROUND AND MOTIVATION

### **Introduction**

The Trans Challis Fault System (TCFS) and the Idaho - Montana Porphyry Belt (IMPB) are closely associated with a necklace of mines and ore bodies that stretches from southwestern Idaho northeast into Montana (Figure 1.1) (Kiilsgaard et al., 1986). The productive mining districts of the Boise Basin (southwestern end of TCFS, CUMO deposit in Figure 1.1) to “the richest hill on earth” in Butte, Montana (northeast) bookend this trend and, along with numerous districts in between, have received extensive economic and academic attention. The Pearl to Horseshoe Bend mining districts were recognized and exploited early on in the development of mining along the TCFS and IMPB (Lindgren, 1898; Ballard, 1924; Anderson, 1934). However, because they lie just west of the Boise Basin boom, scant work has been done to characterize and place them within the overall context of central Idaho mining and geology. The goal of this thesis is to apply a variety of modern geological and geophysical tools to characterize a portion of the Horseshoe Bend mining district within the context of the greater TCFS trends and provide an exploration model for the study area.

The thesis is centered on a mixed brown- and greenfield site hereafter referred to as “the property”. The property is at the northeastern end of the Pearl to Horseshoe Bend mining districts (Figure 1.2), an area which has received little attention. This provides a unique opportunity to conduct exploration and reconnaissance level geoscientific work in an area with relatively well constrained boundary conditions and a proven track record of

ore production but with no modern and little historic geologic work. The need to characterize the property before economic exploitation is clear; detailed, high resolution geologic mapping coupled with modern geochemistry, geochronology, and geophysical techniques completed as part of this research will accomplish this as well as help to constrain how the Pearl to Horseshoe Bend districts fit within the framework of the TCFS and IMPB and begin to answer questions on the timing and tempo of igneous and mineral activity associated with the TCFS and IMPB.

### **Location**

The Pearl District is located in Gem and Boise counties of west-central Idaho, 32km north of the city of Boise, 14km miles east of the town of Emmett. The district stretches 14km from the old mining town of Pearl northeast to Horseshoe Bend at the eastern boundary of the district; at about 3.2km wide the district spreads over 47 km<sup>2</sup>.

The property is located ~20 miles north of Boise and immediately west of Horseshoe Bend. The property is in the Horseshoe Bend Mining District, the northeasternmost of a string of mining districts now commonly referred to as the Pearl Mining District. The Pearl to Horseshoe Bend mining districts occupy one of the westernmost bastions of the Idaho Batholith north of the Snake River Plain. To the east the granites of the Idaho Batholith rise abruptly out of the low lying lake sediments and flood basalts that surround and encroach upon the island of granodiorite and diorite that hosts the dikes swarms and mineralization of the Pearl to Horseshoe Bend mining districts. The property is located in the northeastern portion of the Horseshoe Bend District, covering 9 km<sup>2</sup> immediately west of Horseshoe Bend and extending to the southwest for ~3.5 km along a NE-SW trending ridge ending 2 km due east of Rock Creek.

The property can be accessed from Idaho State Highway 55 near Horseshoe Bend via the Old Emmett Road. The Old Emmett Road is a well maintained dirt road that leads to a county solid waste transfer station adjacent to the property. To access, follow State Highway 55 30km north from its intersection with State Highway 44 in Boise. At the intersection with Old Emmett Rd, turn west on the Old Emmett Road, paralleling the Payette River, for 3.5km to the entrance to the property marked by a green gate on the south side of the road.

### **Project Background**

Past work (e.g. Anderson, 1934) has linked the Pearl to Horseshoe Bend mining districts to the better known mining districts of the Boise Basin, 22km to the west-northwest. Previous research in this area has focused on the Boise Basin (e.g. Lindgren, 1898; Ballard, 1924; Ross, 1933; Anderson, 1947; LaFranchi et al., 1985; Kiilsgaard et al., 1986; McCarthy and Kiilsgaard, 2001; Leppert and Gillerman, 2004) with less attention given to the Pearl and Horseshoe Bend districts. What is now commonly referred to as the Pearl District is made up of the Horseshoe Bend, Willow Creek, Rock Creek, Crown Point, Westview, and Pearl mining districts. The history reported here is for the whole Pearl District and mine summaries (Appendix I) are limited to those within the current property bounds.

Lindgren (1898) produced the first geologic report on the Boise Basin and Pearl districts for the USGS as part of a wider series on the mining districts of Idaho. Anderson (1934) focused solely on the Pearl to Horseshoe Bend districts and provided the first detailed map. Saylor (1967) studied the petrology of the districts of the Boise Basin and Pearl and the sparsely mapped area between them.

Placer work in the district began in the 1860s as an extension of the Boise Basin mining boom (Lindgren, 1898). The first lode was worked in 1870 at the Red Warrior mine. The majority of activity in the district was between 1894 and 1908 with the last mines associated with the initial boom shutting down in the early 1920s (Anderson, 1934). District-wide there were hundreds of workings and dozens of mines; most mining activity was concentrated along the southwest portion of the district near the town of Pearl. Early mining was done on free-milling ore in the oxidized zone, with a few mines (e.g. the Lincoln and Checkmate mines) near Pearl, producing from the reduced zone. Gem State Consolidated worked in the district in the late 1950s and early 1960s. Sunshine Mining Company and Moneca Mining Company explored, but did not develop any properties in, the district in the early 1980s (Alvarez and Ojala, 1981).

### **Deposit Type**

The current work focuses on property scale spatial trends, detailed characterization or analysis of ore material has not been undertaken; consequently, the following discussion of deposit type and mineralization characteristics has been adapted from previous work in the Pearl to Horseshoe Bend mining districts (Ballard, 1924; Anderson, 1934; Anderson, 1947).

The Horseshoe Bend mining district mineralization occurs as intermediate depth, low to intermediate sulfidation, hydrothermal epigenetic veins and fissures of sulfides concentrated along en echelon ellipses where tensional stress has created space for deposition (Figure 1.4). The mineralization is very similar to that reported in the Boise Basin gold districts of Quartzburg and Grimes Pass (Anderson, 1934; Anderson, 1947).

Mineral assemblages are consistent with hydrothermal alteration at intermediate depths and temperatures in a low to intermediate sulfidation systems (Ridley, 2013).

Mineralization is mostly confined to epigenetic veins and fissures of sulfides concentrated along zones of gouge in hanging walls or footwalls; replacement in the country rock is minor. The mineralization in the area generally strikes east-west (Anderson, 1934). Field evidence suggests that mineralizing fluids followed permeability pathways sub-parallel to parallel with east-west trending dikes. In most cases fluids appear to contact the dike and spread laterally along its length, only penetrating where fractures cut the dike. Nodes of mineralization concentrate where east-northeast to east-west trending dikes or fractures intersect the northwest trending fractures. Alvarez and Ojala (1981) reported bleaching, sericitization, and pyritization along wallrock to be a good guide to ore. Mineralization is confined along shattered zones or in bands near fissures. (Anderson, 1934)

The mineralized zones host mainly galena, sphalerite, arsenopyrite, and pyrite, with smaller amounts of chalcopyrite, tetrahedrite, various sulfides, and gold. Most historical workings were in the oxidized upper portion of lodes. In addition to gold, argentite, silver, ruby silver (pyrargyrite), and horn silver (chlorargyrite) have been reported in the oxidized zone. Gangue consists of fractured and altered country rock, quartz, dolomite and calcite. Lodes pinch in and out and vary from a few inches to 30 feet wide, typically about 3-4 feet wide. Mineralization is concentrated in areas where syn-depositional structures created space for mineral deposition. Most deposit workings have been near the intersection of shear planes and dikes. Lodes on the property strike generally east-west and dip north. (Anderson, 1934)

## Methodology

Previous mapping in the Pearl to Horseshoe Bend districts has been confined to 1:24,000 scale or greater maps; I mapped the property at a 1:4,000 scale. There is currently no publicly available surface geochemistry data available for the greater Pearl districts; a new, ~650 sample, surface geochemistry orientation survey and a 93 sample, 8m center detailed surface geochemistry survey have been conducted across the property to characterize spatial trends in gold anomalies. Timing of mineralization within the Pearl and Boise Basin mining districts has been constrained by relative dating methods (Anderson, 1934; Anderson, 1947), but the complex patterns and assemblage of dikes within the Pearl districts have had no absolute geochronologic dating done on them; cooling ages for zircons contained within five dikes of four different lithologies are reported here to test the relative dating and constrain timing of mineralization. Regional aero-magnetic anomaly maps are available that cover the Pearl districts and property area, but they are not appropriate for assessing detail at a scale useful for comparison with 1:4000 geologic mapping; a new, high-resolution magnetic anomaly dataset has been acquired to explore unexposed or subsurface lithologic trends. Drill records for the area are sparse or proprietary, thus detailed subsurface data is limited to past workers descriptions of underground mine workings; a non-invasive electrical resistivity and induced polarization geophysical survey was conducted over a portion of the property to assess continuity of features exposed on the surface with those hidden in the subsurface.

Mineralization along, and dikes associated with, the IMPB are reported to be controlled by structural features manifested as the Trans-Challis Fault System. Due in part to poor exposure and in part to its' intraplutonic setting the structural makeup within

the property and the district as a whole is poorly constrained; this thesis integrates new, detailed (1:4,000 or finer) geologic mapping, with the new geochronological, surface geochemical, magnetic anomaly, and electrical resistivity/induced polarization geophysical data to build a predictive structural model for exploration of mineral resources within the property and to explore genetic links to regional geology.

### **Economic Considerations**

The towns of Horseshoe Bend (population 666, located 2.25km to the east) and Emmett (population 6,510, 22.5km to the west) are the nearest population centers. Boise, Idaho's largest city and the state capital, is located 32km to the south. The property is supplied with 3 phase 440 power and has access to water via water rights secured along the Payette River. A river-cut terrace adjacent to the Old Emmett Road hosts the county waste transfer station. The terrace is sufficiently large to be suitable for base operations and has area suitable to host base operations for mining. The Idaho Northern and Pacific Railroad links Horseshoe Bend with Cascade and Emmett and is adjacent to Old Emmett Road along the property, though it is not currently active. The property is accessible all year but winter muds can make motorized travel difficult.

The climate of the area is typical of the high desert of southwest Idaho, sparsely vegetated with woody vegetation confined to areas with springs or ephemeral streams. Average rainfall is 48cm per year and, average snowfall is 142 cm per year, with an average of 108 days of precipitation per year. The average high is 31° C (88° F) in July with an average low of -6° C (22° F) in January. The main fork of the Payette River flows throughout the year and demarcates (west end) and bisects (east end) the northern margins of the districts. Average discharge of the Payette River at U.S.G.S. monitoring

station 13247500 approximately 9.7 km upstream of the property is 3190 cfs. Roughly 5km upstream of the property is a diversion dam.

The lowest elevation of the site is 792m near the river, maximum elevation is 1280m at the crest of the ridge that runs through the property. The ridge is moderately rugged with steeper slopes on northern aspects. The region is semi-arid and dominated by low lying brushes and grasses. Dense vegetation and cottonwoods grow in draws with an adequate spring fed water supply.

The most productive mines in the current project area are the Osborne, the Nellie, and the Kentuck. Low production mines or those with scant past records in the current area are the: Anticlinal, Apex, Atlanta, Ballentyne, Bobtail, Catherine, Claggett, Hall, Lambertine, Lost, Lucky Boy, Mammoth, Marine, Mint, Sunny Side, and Topeka claims. Claims within the current property boundaries but without historical mention are the Catherine, Payette, Quaker, and Wonder Lode. The OG01-16 group of claims cover the area worked as the Osborne mine, the OG17-24 claims lie between the river and the Kentuck lode and encompass what was possibly the Nellie or Hall workings.

The Sunshine mining company reported production of 10,000 - 20,000 ounces of gold, in addition to “considerable silver, and a little lead and zinc”. “Extensive” workings, defined as shafts hundreds of feet deep or lateral workings of greater than 1,000 feet, were reported for the Lincoln, Checkmate, Black Pearl, Leviathan, Friday, Dewey, Osborne, Nellie, Kentuck, El Paso, and I.X.L. lodes (Alvarez, and Ojala, 1981). The deepest shafts were at the Checkmate (585 feet) and the Lincoln (540 feet) mines. The Nellie, Kentuck, El Paso, and I.X.L. mines had crosscuts that reached depths

exceeding the Checkmate and Lincoln shafts. At 1,000 feet below the surface these crosscuts are the deepest workings in the district (Anderson, 1934).

## SECTION 2: GEOLOGIC SETTING

### **Introduction**

The swath of land encompassed within the Trans-Challis Fault System (TCFS) spans a diverse region of geologic settings. To the east it cuts the fold and thrust belt of the Sevier orogeny, as it crosses central Idaho the TCFS is interwoven with Eocene Challis Volcanics before it transects the width of the Cretaceous Idaho Batholith. On its western edge the TCFS terminates at a juncture of the Idaho Batholith, Western Idaho Shear Zone, Columbia River Basalts, Basin and Range, and the Snake River Plain. The underlying architecture of the TCFS is controlled by a Paleoproterozoic suture or shear zone between two Archean continental blocks. From its eastern extent in Montana to its termination in southwest Idaho the TCFS spans ~340 km in space and 1.8 billion years of western North American history; these relationships in space and time are shown in (Figure 2.1) and are discussed in detail in this chapter.

This chapter will give an overview of the tectonic and magmatic elements that comprise the geologic settings that make extraction of ore along the TCFS and IMPB viable today. In addition to a discussion on the local and regional geology surrounding the property, this chapter will treat the tectonomagmatic elements from oldest to youngest, including: the Precambrian tectonic setting, the Sevier and Laramide orogenies, the Idaho Batholith, the Western Idaho Shear Zone, the Trans-Challis Fault System, the Challis Volcanics, the Idaho-Montana Porphyry Belt, the Basin and Range, and the Western Snake River Plain.

### **Precambrian Tectonic Setting**

The history of the Trans-Challis Fault System begins with the near simultaneous amalgamation of the Archean Wyoming Province to the Hearne and/or the Medicine Hat block(s) at ca. 1.8 Ga and their accretion to the Laurentian margin (O'Neill and Lopez, 1985; Mueller and Frost, 2006). The Wyoming Province is an Archean craton composed of at least three Archean sub-provinces that have all been acting as a unified cratonic block since very early in Earth's history, indicated by an enriched  $^{207}\text{Pb}/^{204}\text{Pb}$  isotopic signature that is unique in North America to the Wyoming Province and is uniform across all three sub-provinces (Mogk et al., 1992). The Hearne block is a sub-domain of the Churchill province in central Canada composed of tholeiite dominated greenstone belts and associated plutons and sediments (Maclachlan et al, 2005). The Great Falls Tectonic Zone in Montana and southwestern Saskatchewan and its extension through Idaho as the Trans-Challis Fault System is the ancient collisional margin between the Wyoming Province and the Hearne block of the Churchill province (O'Neill and Lopez, 1985). The Great Falls Tectonic Zone has alternatively been interpreted as a reactivated intracontinental shear zone (Boerner et al., 1997). In either case the argument for Eocene extensional activity focusing along a northeast trending lineament from Idaho to Montana is rooted in the idea that the features follow zones of weakness in ancient basement rocks that underlie and control the structure of Phanerozoic rocks. The northeast-southwest trending zone of crustal weakness created by this juxtaposition has been recurrently activated throughout the intervening 1.8 billion years, most pertinently manifested as the Trans-Challis Fault System to Great Falls Tectonic Zone trend of fault systems. (Mueller and Frost, 2006).

## Sevier and Laramide Orogenies

By the mid-Early Triassic the Wyoming and Hearne cratonic blocks composed the western margin of Laurentia which was, at the time, the west coast of the supercontinent of Pangea. As Pangea began to break up, and the Atlantic Ocean began to open, the ring of continents that were encircled by the Panthalassa Ocean began to encroach upon its margins, eventually leading to what is now the Pacific Ocean and the circum-Pacific orogenic belts. It was then that North America began its westward march, overriding the Kula and Farallon (later Juan de Fuca) plates. Concurrently, the North American Cordillera, with ancestral roots in the break-up of the earlier supercontinent of Rodinia, began to take shape with the initiations of the Sevier and later the Laramide orogenies. The oceanic plates being subducted beneath western North America carried on them island arcs that, either, had been formed elsewhere and carried along to the subduction zone, or, were created as a result of the subduction. The arc material that was not subducted accreted to the margin of the continent, eventually growing the continent to its present extent. The boundary between old, cratonic continent and new, accreted continent is based on a change in the  $^{87}\text{Sr}/^{86}\text{Sr}$  isotopic ratio from radiogenic, continental signatures,  $^{87}\text{Sr}/^{86}\text{Sr}$  0.706, to less radiogenic, oceanic signatures,  $^{87}\text{Sr}/^{86}\text{Sr}$  0.704.

(Dickinson, 2004)

The Sevier orogeny was the western manifestation of the Cordilleran uplift from ~150 Ma to ~50 Ma, and is noted for stacked thrust sheets of Paleozoic and Mesozoic sedimentary rocks that fractured along preexisting bedding planes, often called “thin-skinned” thrusting. By contrast the Laramide orogeny was along the eastern edge of the Sevier orogeny, affected the western edge of the stable craton, and initiated later, at about

70 Ma, with a similar timing of termination. The markedly different crustal packages that the Sevier and Laramide orogenies affected led to two distinct styles of deformation along the orogenic front. While the Sevier orogeny stacked relatively young sedimentary beds, the Laramide reactivated ancient fault systems within stable cratonic blocks to produce uplifted cores of basement rock and thick, mountain building, blocks with stratigraphic sequences largely intact.

### **Idaho Batholith**

The late Cretaceous saw the continued accretion of arc terranes to the continental margin and the waning stages of the Sevier orogenesis. In addition to the volcanic sequences of Cretaceous age that are attributed to arc volcanism, such as the Elkhorn Mountains Volcanics (Tilling et al., 1968) or the Crowsnest Volcanics (Crook, 1962) volcanics, a series of plutons were emplaced along the western margin of the continent, in a long magmatic arc evidenced today by a belt of batholiths stretching the length of western North America. At the time most of Idaho lay within this Cordilleran magmatic arc that resulted from the active tectonic margin. A collection of plutons, of mostly similar age and composition, that dominate the geology of central Idaho are known as the Idaho Batholith. The southern portion of the batholith is known as the Atlanta Lobe and is Late Cretaceous in age, 86 – 73 Ma. The northern portion, known as the Bitterroot Lobe, is younger, Late Cretaceous to Paleocene, and thought to represent a pulse of magmatism separate from that which emplaced the Atlanta lobe (Gaschnig et al., 2007). The Idaho Batholith is intruded entirely within a Precambrian crust of metasedimentary rocks and is composed of dominantly peraluminous granite (Gaschnig et al., 2011). The Idaho Batholith and the Precambrian units it intrudes are the hosts for the Eocene to

present features that give rise to the ore bodies that are exploited today along the Trans-Challis Fault System and Idaho Montana Porphyry Belt.

### **Western Idaho Shear Zone**

The Western Idaho Shear Zone (WISZ) is a zone of high strain that marks the boundary between the western edge of Laurentia to the east and accreted terranes to the west from Clearwater, Idaho south to the western Snake River plain. The continental to oceanic  $^{87}\text{Sr}/^{86}\text{Sr}$  isotopic gradient signature across the WISZ is steep and reflects the overprinting of earlier suture zones by the WISZ (Benford et al., 2010). The shear zone is taken to be the mid-crustal level of a Late Cretaceous intra-arc shear zone (McClelland et al., 2000). Giorgis et al. (2008) placed the timing of deformation along the shear zone between 105 and 90 Ma. based on fabric and U-Pb zircon dating. The WISZ forms the western boundary of the Idaho Batholith and has as its southern terminus the granodiorites of the Pearl districts, though there is evidence it may continue south of the western Snake River Plain (Benford et al., 2010). It is unknown if the presence of such a structure has influenced the patterns or style of mineralization in the area.

### **Trans-Challis Fault System**

The Trans-Challis Fault System (TCFS), is an ~270 km long northeast trending series of steeply dipping normal faults, grabens, and calderas (Lewis et al., 2012) that hosts extrusive volcanics as well as a series of plutons and associated swarms of mafic to felsic dikes (Gaschnig et al., 2007). The dikes and dike swarms within the TCFS generally strike northeast and are parallel or sub-parallel to the trend of the structures of the TCFS (Lewis et al., 2012). Kiilsgaard and Bennett (1986) consider the continuity of the faults, grabens, calderas, and associated dikes swarms to be strong evidence of

Eocene rifting and extension across central Idaho. Graben subsidence and normal faulting occurred pre-, syn-, and post-volcanic activity within the Challis Volcanic Field (Moye et al., 1988). It is therefore inferred that faulting associated with the TCFS predates, and is continuous through, hypabyssal dike emplacement and any associated ore bodies. The TCFS is closely associated with a series of precious metal deposits known as the Idaho Montana Porphyry Belt (Figure 2.2). The TCFS is proposed to be contiguous with the Great Falls Tectonic Zone (GFTZ) that extends from the Idaho-Montana border to Saskatchewan, Canada (O'Neill and Lopez, 1985). The TCFS and the GFTZ are thought to be the Phanerozoic manifestation of either a Proterozoic suture between the Archean Wyoming and Hearne cratons (O'Neill and Lopez, 1985) or as a reactivated Archean intracontinental shear zone (Boerner et al., 1997). In either case the argument for Eocene extensional activity focusing along a northeast trending lineament from Idaho to Montana is rooted in the idea that the features follow zones of weakness in ancient basement rocks that underlie and control the structure of Phanerozoic rocks.

Extension in the Eocene began when the rapid subduction of the Farallon plate off the west coast of North America began to slow and the subducting slab transitioned from a flat-slab subduction regime to one of slab rollback (Janecke, 1992; Stock and Molnar, 1988). In slab rollback the angle of subduction of the subducting plate steepens either due to decreased convergence velocity or a change in the angle of convergence. As the subducting plate begins to dive at a steeper angle a zone of extension is created in the area once underlain by the shallowly subducting plate (Snyder et al., 1976). The transition from compressional to extensional tectonics in a region results in the thinning of the crust, anatexis, and a higher heat flow. The higher heat flow allows more

widespread volcanic activity, which is closely associated with mineralization (Rowland and Simmons, 2012).

### **Challis Volcanic Field**

The 51 – 44 Ma Challis Volcanic field is the largest of a number of Eocene volcanic fields in the northern Cordillera termed the Challis-Kamloops Belt. The Challis-Kamloops Belt extends from at least central Wyoming to southern British Columbia and possibly into Alaska (Dostal et al, 2003) and includes the 53-45 Ma Sanpoil field in southern British Columbia, the 60-50 Ma Montana alkalic province, the 49-44 Ma Absaroka field, the 69-47 Black Hills field in eastern Wyoming, and the 44 Ma Rattlesnake Hills in central Wyoming (Moye et al., 1988; Sanford and Snee, 2005). Fields and provinces within the Challis-Kamloops Belt are calc-alkaline to alkaline and have been attributed to either, or both, subduction related (e.g. Dudás, 1991) and/or within-plate extension (e.g. Ewing, 1980). The interpretation of the tectonic setting for volcanism across the Challis-Kamloops Belt varies widely from location to location; proposed settings include volcanic arc (Ewing, 1980), rifted arc (Dostal et al., 2001), slab window (Brietsprecher et al, 2003), and continental extension (Morris et al., 2000). The Challis Volcanic Field is regarded as an “unambiguous”, syn-volcanic, intra-arc rift basin (Janecke et al., 1997), though some questions remain as to the role of subduction and slab windows (Schleiffarth and Larson, 2013). The Challis Volcanic Field is considered the surficial expression of the dike swarms that are included in the Challis Intrusive Province (Gaschnig et al., 2011) and as a result of the mechanisms which emplaced the Eocene Trans-Challis Fault System (Moye et al., 1988; Janecke et al., 1997), and closely linked to the Idaho-Montana Porphyry Belt string of deposits (Taylor et al., 2007).

### **Idaho-Montana Porphyry Belt**

The Idaho Montana Porphyry Belt (IMPB) is a string of molybdenum or copper-molybdenum deposits that spans from the Hawkeye deposit in north-central Montana to the CUMO deposit in the Boise Basin of south-central Idaho (Figure 1.1). Most, though not all, of the deposits are within the Trans-Challis Fault System to Great Falls Tectonic Zone band of northeast oriented normal faults. On its southwest end the IMPB terminates at its intersection with the Western Idaho Shear Zone (WISZ) or Salmon River Suture Zone, at the northeastern end it becomes buried by the sediments of the Western Canadian Sedimentary Basin. The Salmon River Suture Zone (SRSZ) is a zone of stacked and thrust sedimentary packages that comprised the basin separating arc terranes to the west and the North American craton to the east. The basin fill marine sediments were later amalgamated to the cratonic margin as the basin closed.  $^{40}\text{Ar}/^{39}\text{Ar}$  dating of 23 deposits and associated intrusives along this trend by Taylor et al. (2007) return ages of  $38.80 \pm 0.30$  (k-spar, CUMO deposit, Boise Basin) to  $85.10 \pm 0.30$  (sericite, White Cloud deposit, Beaverhead County, Mt.), errors are  $1\sigma$ . Geochemical and radiogenic isotopic data suggest that the deposits have more radiogenic and evolved characteristics the further inboard they are from the WISZ and SRSZ. Deposits do not seem to be geographically aligned along any age, composition, or emplacement depth trends; instead, they are controlled by the composition and structure of underlying basement rock (Taylor et al., 2007).

### **Basin and Range**

The Basin and Range province is a large extensional region centered on Nevada and includes parts of Idaho, Oregon, Utah, and California. The region is characterized by

roughly north-south trending mountain ranges that area a result of a series of similarly oriented horst and graben structures. Extension began ca. 20-25 Ma along the Northern Nevada Rift and continues to the present (Wells et al., 2000). Extension initiated with the cessation of compression associated with the Cordilleran orogeny as the over-thickened crust began to relax. North-south oriented Basin and Range faults are truncated by the track of the Miocene Yellowstone Hotspot (Pierce and Morgan, 1992) in southern Idaho but are evident again on the north side of the Snake River Plain. Basin and Range associated extension is responsible for much of the uplift and exhumation across southern Idaho.

### **Snake River Plain**

The Snake River Plain is composed of two segments, the eastern and western. The northeast trending eastern Snake River Plain (ESRP) is commonly associated with the passage of the Yellowstone Hotspot track and attributed to the voluminous volcanic and magmatic activity of the hotspot passing underneath and “burning” a path through the crust. The western Snake River Plain (WSRP) is a northwest oriented graben filled with intercalated lake sediments, volcanic tuffs, and basalt outpourings. Where the ESRP is thought to record the passage of the Yellowstone Hotspot, the WSRP is thought to be a result the impingement of the mantle plume responsible for the hotspot in the southwestern Idaho-southeastern Oregon-north-central Nevada region. (Pierce and Morgan, 1992) The western end of the Trans-Challis Fault System and associated mineralization abruptly terminate at the juncture of the WSRP, Basin and Range faulting, and the  $^{87}\text{Sr}/^{86}\text{Sr}$  0.706 line in southwestern Idaho.

## Regional Geology

The Pearl to Horseshoe Bend Mining districts lie along the western edge of the Cretaceous Idaho Batholith in primarily quartz diorite, granodiorite, and tonalite. The districts are included in a zone of trench parallel NW-SE oriented intra-arc extension associated with the subduction of the Farallon plate beneath North America in the Eocene (Anderson, 1934; Janecke, 1992), i.e. the NE-SW oriented Trans-Challis Fault System. The district is at, and within, the southwestern extent of the TCFS. Extension is often accompanied by strike-slip motion, leading to varying intervals of compression and tension that serve to fracture the rock and create space for mineralizing fluids to move through the rock.

The Pearl to Horseshoe Bend mining districts, as well as those in the nearby Boise Basin (e.g. Quartzburg and Grimes Pass), are most commonly classified as shallow to medium depth epithermal systems. Both shallow and medium depth epithermal genetic models are predicated on the presence of volcanic activity. The extension and resultant volcanic activity in the Eocene propagated along an underlying zone of weakness inherited from Precambrian tectonic activity (O'Neill and Lopez, 1985). In Idaho the subduction of the Farallon plate caused the Sevier Orogeny; the Idaho Batholith and the mountains of central Idaho present today are the physical manifestations of that episode of mountain building. The Sevier Orogeny began at ~170 Ma and continued until ~50 Ma when slab rollback and associated extensional activity began (Simonsen, 1997). During that time a series of island arcs and possibly continental materials were accreted to the edge of the continent (Hamilton, 1963; Lund, 1988). As the material was accreted, the heavy, cold, and wet slab was forced beneath the more buoyant continental material,

ultimately providing a source of fluids and volatiles to mobilize deep seated rock and precious metals.

To the south of the Pearl districts is the Western Snake River Plain (WSRP), a large tectonic graben with bimodal volcanics associated with the Miocene Yellowstone hotspot track (Armstrong et al., 1975; Pierce and Morgan, 1992). The graben is filled with Late Miocene lacustrine sediments of ancient Lake Idaho, of these the Payette Formation is in fault contact with the granodiorite of the Idaho Batholith along the southern and eastern edges of the district (Anderson, 1934). LA-ICPMS and CA-IDTIMS yield ages of  $\sim 9.9$  and  $9.0057 \pm 0.0082$  Ma for the lowest exposed sedimentary units associated with the Payette Formation near Emmett, Idaho (Feeney et al., 2016).

After initial exposure and erosion of the Cretaceous Idaho Batholith and the Eocene Idaho-Montana Porphyry Belt dikes, basalts associated with the Columbia River Basalts (CRBs) capped the erosional surface. Today the basalt cap is surficially extensive to the west and northwest of the district but only scattered remnants remain within the districts themselves (Lewis et al., 2012).

The Boise Ridge Fault lies eight miles to the east of Horseshoe Bend; it is a north-south trending Basin and Range normal fault that marks the western edge of the Quartzburg-Grimes Pass mining districts (Lewis et al., 2012). Basin and Range extensional tectonics began 25 to 20 million years ago (Wells et al., 2000), after the conclusion of the Challis episode and continues, in areas, to the present. Horseshoe Bend sits in a graben or half-graben created by down-dropping along the west side of the Boise Ridge Fault by 600-900m The western bound on the graben is the fault contact between

the Payette Formation and the granodiorite or diorite of the Idaho Batholith. The contact trends northeast across the southeastern corner of the property.

### **Local Geology**

The property is hosted within predominantly granodiorite of the Idaho Batholith. Locally a northeast-southwest elongate diorite stock was emplaced at 88 Ma (Gaschnig, pers. comm., 2015) and is considered coeval with the larger granodioritic body. However, in places, the two lithologies share a sheared contact surrounded by a zone of gneissic banding in the granodiorite and diorite.

The banding is compositional with bands of aligned micas, primarily biotite, separated by zones of feldspar. The gneissic banding is interpreted to be a magmatic foliation due to the absence of stretched or deformed quartz.

Anderson (1947), in a report on the Boise Basin, described the sequence of intrusions after pluton emplacement as the diorite stock, dacite porphyry, quartz monzonite porphyry, syenite porphyry, rhyolite porphyry, andesite, diabase, and lamprophyre from oldest to youngest. Ballard (1924) included a diorite porphyry phase on the list, but did not place it in sequence. Based on crosscutting relationships in the Boise Basin, Anderson (1947) placed gold and silver mineralization before the diabase phase and after the andesite phase. Recent geochronological work, from other workers and undertaken as part of this study, places the diorite stock in the Cretaceous at about 88 Ma (Gaschnig, personal communication, 2015), the dacite, rhyolite, and diorite porphyries at 48-47.5 Ma, and the andesite at 30.5 Ma (this study).

The attitudes of the dikes within the property are dominantly east-northeast but range from nearly due east-west to north-south (Figure 2.3; Plate 1). Where measurable,

the dip on the dikes is most commonly steep, 70 to 90 degrees, and varies between north- and south-dipping. The larger east-west trending diabase dikes have a shallower dip at around 40 degrees and variably dip to the north or south as well. The attitude and composition of these dikes indicate an origin likely separate from the bulk of the Eocene age dikes in the area; currently they are interpreted as feeder dikes for Columbia River Basalts. Using Anderson's relative chronology and the new age data on the andesite facies of diking constrains the diabase phase to no earlier than 31 Ma.

Fractures on the property generally strike east-northeast to east-west with a conjugate set that strikes to the northwest. Dips on both sets are generally steeply to the north, although some dip to the south. Mineralization is primarily confined to epigenetic veins and fissures of sulfides concentrated along hanging or footwalls; replacement in the country rock is minor (Anderson, 1934). The mineralization in the area generally strikes east-west or east-northeast. Field evidence suggests that mineralizing fluids followed permeability pathways sub-parallel to parallel with east-west trending dikes. In most cases the fluids contact the dike and spread laterally along its length, only penetrating where north-northwest trending fractures cut the dike. Nodes of mineralization (Figure 2.4) concentrate where the two fracture sets intersect. Alvarez and Ojala (1981) reported bleaching, sericitization, and pyritization along wallrock to be a good guide to ore.

## SECTION 3: GEOLOGIC MAPPING

### **Introduction**

Available previous exploration work covering the property has been confined to coarse geologic maps (e.g. Lindgren, 1898; Anderson, 1934; Saylor, 1967; Alvarez and Ojala, 1981). As of December 2015, no records of surface geochemical samples or geophysical work have been found for the area. Past drill records for the Pearl to Horseshoe Bend districts are limited to a small drilling program conducted by Sunshine Mining in 1982 (Appendix II, Table 1), near Pearl and outside of the current Trans-Challis property. The Osborne mine near the northern margin of the property was discussed in some detail by Anderson (1934). The exploration work carried out by Trans-Challis LLC, beginning in March of 2014 has included the establishment of a new, 10' contour, topographic base map via air flown ortho-photography, geologic mapping, surface geochemistry soil surveys, Induced Polarization (IP) and Electrical Resistivity (ER) geophysical surveys, magnetic anomaly geophysical surveys, geochronology on significant lithologies in the area, and excavation along the previously mined vein at the Mammoth Mine. Results of geologic, geophysical, and geochemical efforts have been obtained independently from each other and, as much as possible, the implications from one have not been used to influence those of another. The following sections detail, in order, the methods and results of the geologic mapping, initial geochronology, geochemical soil surveys, Induced Polarization (IP) and Electrical Resistivity (ER) geophysical surveys, and magnetic anomaly geophysical surveys.

## **Geologic Mapping**

The Trans-Challis property was first mapped by Lindgren (1898) as part of the initial efforts to characterize the geology of the Boise Basin, Lindgren recognized then the possible genetic connection between the Pearl to Horseshoe Bend districts and the mining districts of the Boise Basin. Anderson (1934) was the next to map the area as part of a focus on the links between the Boise Basin and Pearl to Horseshoe Bend districts, the whole swath of land from Pearl to Horseshoe Bend was covered in a brief summer mapping project as part of this endeavor. Saylor (1967) covered the area again as part of a masters in geology thesis seeking to understand the petrology of the mining districts and to fill in the unmapped gap between the Boise Basin and the Horseshoe Bend districts. Alvarez and Ojala (1981) produced a map of the area but it is based almost entirely on Anderson and Saylor's earlier work. All four maps are included in Appendix III: Geologic Maps. The author carried out a detailed mapping program in the summer and early fall of 2015 that focused solely on the Trans-Challis LLC. property. The product of the most recent mapping focuses on the presumably Eocene aged dikes and their relationships with the country rock, fracture patterns, and mineralization trends.

## **Description of Lithologic Units**

Unit descriptions are in chronologic order from youngest to oldest. Descriptions are based on field, hand sample, and thin section observations combined with geochronologic work conducted at Boise State University as part of this study and published ages from other workers. Unless noted, unit ages were obtained at Boise State University (BSU) using Laser Ablation Inductively Coupled Plasma Mass Spectrometry (LA-ICPMS) to measure uranium and lead (U/Pb) ratios in zircon mineral separates from

individual dike phases and Chemical Abrasion Isotope Dilution Mass Spectrometry (CA-IDTIMS). Ages are reported in millions of years (Ma.) with 2-sigma error ( $2\sigma$ ). LA-ICPMS also returns multi-element data which is not discussed here.

#### Alluvium (Holocene)

Sand, gravel, cobbles, and boulders eroded from granitic and dioritic valley walls and included dikes. Deposited where stream volume and/or gradient could not support the material as suspended or bed load; such as the meanders on which the mapped alluvium sits. Current terrace is a mix of alluvium from stream sediment transport and colluvium from the hills above.

#### Sediments of the Payette Formation (Miocene)

Well sorted silt, sand, and gravel, angular to moderately rounded, poorly to well indurated. Not studied as part of this project beyond cursory examination. Alternating beds of silicified arkosic sandstone and slope-forming shales. Locally, beds dip to the west or southwest and either on-lap or are in fault contact with the Idaho Batholith along the eastern margin of the property. Described by Lindgren (1898); no type locality given. More recent work has placed the formation at 9.00 Ma. (Freeney et al., 2016)

#### Lamprophyre (Miocene)

Medium grained, brown, mafic, feldspathic, micaceous, idiomorphic, and friable. Biotite and phlogopite comprise > 90% of the rock in hand sample, with scattered feldspars comprising the remaining 5%. All grains are less than 1mm in diameter, biotite is euhedral and feldspar equant.

The lamprophyre outcrops extremely poorly, the one mapped instance trends NNE at the bottom of a recently washed out gully. The dike is emplaced along

preexisting anastomosing and en-echelon shears in the granodiorite. No contacts with other dikes are observed in this locality, in the Boise Basin lamprophyres are observed cutting all other Eocene dike lithologies (Anderson, 1947).

#### Diabase/basalt (Miocene)

Dark gray to black, fine grained to aphanitic, tan to reddish brown on aphanitic, weathered or altered surfaces. The diabase is the only dike variety in the area that contains vesicles and can be amygdaloidal. Amygdules are 2-3mm wide, commonly calcite filled and occasionally quartz filled. The ground mass is dominantly plagioclase, pyroxene, and amphibole. Phenocrysts are of the same composition as the groundmass and typically 2-4mm long, however the rock is not obviously porphyritic.

The diabase dikes have two mapped occurrences in the area; in both instances they trend ENE and dip  $\sim 40^\circ$ . The northern of the two dikes dips to the north while the southern dike dips to the south. Both are 4-5m thick and exhibit vesicles or amygdules along their margins. Basalt dikes in the area are aphanitic and highly altered, much thinner, typically 50cm or less, trend NNE, and do not contain vesicles. Basalt dikes closely resemble the highly weathered andesite dikes.

#### Andesite (Oligocene)

Light to dark gray on fresh surfaces, weathered surfaces are typically light to medium gray or greenish gray. Most commonly the andesite is aphyric and badly weathered in outcrop and hand sample. Outcrops are generally friable and break with a splintery fracture. The dikes may contain phenocrysts of small, 1-2mm feldspars or rounded 2-4mm quartz grains. Where dark colored, the andesite closely resembles the diorite porphyry, especially when containing feldspar phenocrysts or in areas where there

is fresh exposure. Weathered outcrops can closely resemble the weathered basalt/diabase dikes or the weathered or hydrothermally altered diorite porphyry dikes.

Andesite dikes are typically narrow, 1-2 meters, and trend in a northeasterly direction, often parallel or subparallel with the trend of diorite porphyry dikes in close proximity and in-line with the trend of the Trans-Challis system as a whole. As the strike of the dikes appears unaffected by topography, dips are thought to be steep, i.e. greater than 70°.

Field identification was based on presence or absence of phenocrysts to help distinguish from the diorite porphyry, the presence or absence of vesicles to help distinguish from the basalt or diabase, and the friable or splintery nature of the outcrop. Field identification of aphanitic, dark colored rocks was often difficult. Additionally, the andesite dikes occasionally contain quartz phenocrysts that appear to have been entrained from the surrounding granodiorite during emplacement. Diabase/basalt dikes can appear similar in weathered outcrop but are typically thicker (4-5m), have a shallower dip (~40°), and tend to trend in a more E-W direction. Geochronologic work completed as part of this study returned an age of  $30.44 \pm 0.02$  Ma. Age was obtained using CA-IDTIMS on U/Pb in zircon at the IGL at Boise State University.

#### Dikes, Undivided (Eocene)

Dikes of uncertain composition, most are probably rhyolite or dacite porphyry. They are, in general, very fine grained, however, granophyric textures are also present.

#### Rhyolite (Eocene)

Light gray to pinkish brown on fresh surfaces, reddish brown to brown on weathered surfaces, aphanitic groundmass, phenocrysts are approximately 40% feldspar,

40% quartz, 10% biotite, and 10% hornblende. Phenocrysts of feldspar are up to 15mm long and 5mm wide, but most commonly <3mm. Feldspars are tabular to equant, and often embayed. Phenocrysts of quartz are 2 to 6 mm in diameter, occasionally up to 11mm. The quartz occurs as rounded grains with translucent rims and opaque, light tan interiors or as pseudomorphs of feldspar. Biotite crystals are 2-3mm in diameter, black, hexagonal or tabular, and often extensively altered to chlorite. Hornblende phenocrysts are 1-3 mm wide and up to 5mm long, black, and tabular to rounded in morphology.

The rhyolite dikes do not cut any other dike facies, although in the Boise Basin Anderson (1947) noted that they are crosscut by lamprophyre dikes in underground workings. The high quartz content of the rhyolite dikes promotes a more resistant nature, as a consequence outcrops of rhyolite are typically more ledge forming than any other dike series in the area and, when combined with their unique lithology, traceable over greater distances. Rhyolite dikes are up to 5m in width and trend northeast. As the strike of the dikes appears unaffected by topography, dips are thought to be steep, i.e. greater than 70°. The largest rhyolite dikes are extensively altered, suggesting emplacement before the last hydrothermal event. Geochronologic work completed as part of this study returned an age of  $47.50 \pm 0.09$  Ma. Age was obtained using CA-IDTIMS on U/Pb in zircon at the IGL at Boise State University.

#### Pyroxene-hornblende Diorite Porphyry (Eocene)

Medium to dark gray or black, tan to greenish weathering porphyry comprising 5 to 20% phenocrysts in a very fine grained to medium-grained ground mass. Phenocrysts are dominantly feldspars with up to 10 mm wide rounded and embayed potassium feldspars and smaller but typically more numerous plagioclase that can be up to 5mm

long and 2mm wide. Plagioclase is euhedral to subhedral and typically tabular. Pyroxene constitutes 5 to 10% of phenocrysts and is typically 0.5 to 1mm in width, amorphous in shape, and black in color. Hornblende phenocrysts are black to dark greenish gray, up to 5mm long and 2-3 mm wide, euhedral, approaching tabular, crystals and comprise 5 to 10% of the rock. The only phenocrysts that can be consistently identified in the field are the conspicuously lighter colored feldspars in a dark gray to black aphanitic groundmass. Pyrite is locally found as 2-3 mm inclusions in the porphyritic feldspars as well as smaller, 1-2mm grains in the aphanitic groundmass.

Diorite porphyry is the most common dike lithology in the area. Field classification was generally based on the presence of feldspar phenocrysts in an outcrop that could be traced for a few tens of meters and/or lithologically similar outcrops along the same trend in the vicinity. Mapping of some andesite or diabase dikes as diorite porphyry is possible because field identification of one dark gray to black, aphanitic lithology from another was often difficult. The dikes generally trend to the northeast, dip between 75-85°, dominantly to the south with a few to the north, and range in width from tens of centimeters to greater than 5 meters with 1-2 meter thick dikes being the mode. Geochronologic work completed as part of this study returned an ages of  $47.92 \pm 0.10$  to  $47.52 \pm 0.02$  Ma. Ages were obtained using CA-IDTIMS on U/Pb in zircon at the IGL at Boise State University.

#### Biotite-hornblende Dacite Porphyry Dikes (Eocene)

Distinctly porphyritic medium gray to light gray weathering porphyry, containing up to 80% phenocrysts in an aphanitic groundmass. Roughly 60% of the phenocrysts are prismatic, tubular plagioclase feldspar crystals up to 10 mm long and 5 mm wide. In hand

sample the feldspars often exhibit zoning from core to rim, with translucent white to pink cores and opaque white to tan rims. Euhedral hexagonal biotite crystals up to 3 mm in diameter make up ~20% of the phenocrysts; on weathered faces the biotite often leaves hexagonal voids. The remaining 20% of phenocrysts are a blue-green to black amphibole, likely hornblende. The hornblende can be up to 10 mm long and 2 mm wide. Rounded quartz phenocrysts are locally present. Quartz phenocrysts are confined to dike margins and can be contained in xenoliths of country entrained during emplacement. Quartz in diorite is therefore interpreted to be xenocrystic in nature.

Dacite dikes are typically 3-5 meters wide and trend E-W. Outcrops tend to be expressed as zones of dacite rubble. The dacite is crosscut by diorite porphyry and crosscuts the diorite stock to granodiorite contact, but is not observed crosscutting any other dike facies. The dikes are often altered or bleached where they contact other dike facies. As the strike of the dikes appears unaffected by topography, dips are thought to be steep, i.e. greater than 70°. Geochronologic work completed as part of this study returned an age of 48.03 ±0.05 Ma. Age was obtained using CA-IDTIMS on U/Pb in zircon at the IGL at Boise State University.

#### Diorite (Cretaceous)

Fine to coarse grained, equigranular, grades from mottled white and black to black granitoid. Mafic minerals are primarily hornblende with subordinate biotite; felsic minerals are dominantly plagioclase with subordinate potassium feldspar and quartz.

The diorite stock covers roughly the western half of the map area and, with reference to larger scale maps produced by the Idaho Geologic Survey, is overall elongate to the northeast. The contact with the granodiorite to the east is marked by a gneissose

fabric and trends northeast-southwest in a stair step fashion, with north-trending zones of shear. Work by Gaschnig (unpublished pers. comm., 2015) and not part of this study has returned an age of  $87.4 \pm 1.70$  Ma. for the diorite.

### Biotite Granodiorite (Cretaceous)

Medium to coarse grained, equigranular, light to medium gray granitoid. Grain size averages 1 to 3 mm, locally up to 4mm. Texture is granitic and isotropic, except at the contact with the diorite stock. Near its western margins the granodiorite takes on a distinct foliation of the biotite that approaches a gneissose compositional layering.

### **Structure**

Structural measurements are reported using the right hand rule: if the right hand is placed on the plane being measured the thumb points along strike and fingers point down dip. Results are presented as rose diagrams and stereonet.

A rose diagram shows the strike but not dip of a feature and is useful for presenting strikes where the dip was unable to be determined. The diagram is essentially a histogram placed onto a circle or compass; the 360 degrees of a circle are separated into equal subdivisions (bins), each measurement (n) is categorized and placed into a bin with the length (or height) of each bin corresponding to the number of measurements in each bin. Bin sizes used here are in ten degree increments, e.g.  $000^\circ$  to  $010^\circ$  and  $010^\circ$  to  $020^\circ$ , etc.

A stereonet projects the lower hemisphere of a sphere onto a plane as a specialized graph which looks similar to lines of latitude and longitude on a globe. Planes can be projected as great circle traces onto a stereonet which preserve the attitude (strike) and aspect (dip) of planes as measured on the ground. By imagining a pole stuck

orthogonally through the center of the plane, the strike and dip of a plane can be plotted as a single point on the stereonet. This point is referred to as the pole to the plane.

Stereonet has the advantage of quantitatively displaying large quantities of measurements to illustrate trends in data. Here they are used to show patterns in dike, vein, and slickenside orientations, and their sense of dip.

The bulk of the property area is composed of the granodiorite and diorite units. The granodiorite and diorite are both internally homogenous bodies with joint strikes dominantly to the north and northeast (Figure 3.1, section 6). Any large fractures that may be present in the granodiorite and diorite are difficult to distinguish because of the compositional homogeneity and the isotropic fabric of the units. The exception is an unmapped zone of magmatic foliation, likely Cretaceous in age, which upon examination in the field appears coeval with emplacement of the granodiorite and diorite. The zone, where exposed, forms a halo around the granodiorite to diorite contact and is speculatively interpreted to be a result of emplacement induced shearing between the two rock bodies. The foliation is present as preferential alignment of micaceous minerals along sub-horizontal planes. In places the quartz is undeformed, indicating that foliation is magmatic and formed during emplacement and not during a later ductile shearing event. However, in other locations quartz grains are more oblate, making a definite interpretation of this feature difficult. The observations and interpretations above are from field and hand sample observation only; no thin section or lab work was done to investigate these hypotheses.

Surfaces preserving signs of fault movement, or slickensides, are illustrated as the stereonet in Figure 3.2. The majority of slickensides are generally northeast trending with

northern aspect dips. Not as numerous are a set of slickensides that trend north-northwest and dip predominantly to the west. This is significant as it indicates a conjugate set of fractures that are not dilatant at the time of emplacement but may help control the geometry of the system and accommodate the north-south widening of east-west propagating fractures. This is illustrated with a hypothetical Riedel shear array constructed for the property (Figure 3.5).

Dikes on the property trend  $270^{\circ}$  to  $360^{\circ}$  and dip to the north, clustering around orientations of  $060^{\circ}$  to  $070^{\circ}$  and  $080^{\circ}$  to  $090^{\circ}$  (Figure 3.3). The rhyolite is the exception, it has the same trend but dips predominantly to the south, or  $000^{\circ}$  to  $090^{\circ}$  using the right hand rule. Notably absent from dike orientation patterns are any dikes that strike to the northwest. This contrasts with the slickenside orientations that show evidence for northwest trending fracturing.

Two datasets for mineralized veins are reported here: 1) data collected as part of the most recent mapping campaign over the property area and 2) strikes and dip data of veins as reported by Anderson (1934) from his observations of ore veins exposed in underground workings still accessible at the time of his report. Figure 3.4 shows the poles to the planes of veins as measured underground throughout the districts (red) by Anderson (1934) and at the surface within the property (black) as part of this study. Anderson's data show a strong east-west orientation of mined veins. The surface data from the current study shows greater scatter but still show a general east-west mineralization trend. It should be noted that veins measured at the surface may not be ore grade.

Figures 3.1 through 3.4 illustrate a dichotomy in structural patterns between the pattern displayed by joints and slickensides and the pattern displayed by dikes and veins. Joints and slickensides show dominantly northeast trending orientations with subordinate northwest trending orientations; dikes and veins display a more equitable distribution between those oriented northeast and those oriented east-west. The measured veins show a preponderance to an east-west orientation. From this set of relationships, I infer that the Eocene dikes, being younger and more competent, imposed a structural anisotropy into the homogenous and isotropic nature of the existing pluton. Within the previously uniform pluton, Eocene to Oligocene dikes were emplaced along the northeast and east-west oriented  $R_1$  and P fracture sets respectively. The emplacement of the dikes created local disruptions of the stress field and furthered a preferential north-south dilatancy to the east-west oriented P fracture set. Hydrothermal fluids took advantage of the localized anisotropic nature within the pluton and migrated along the P fracture sets.

Figures 3.2, 3.3, and 3.4 illustrate that, while the Trans-Challis Fault System and associated dike swarms as a whole are oriented ENE-WSW within the Pearl to Horseshoe Bend districts and across Idaho in general, locally the veins and lodes strike E-W. The mineralized veins and ore zones are likely arranged en echelon in a northeast-trending series of steps. This is illustrated in Figure 3.5 which takes the Riedel shear model and overlays hypothetical ore bodies on the  $R_1$  fracture plane. A necessary tenet of this model is that to create a system with an echelon E-W oriented fractures widening in the north-south direction there must have been a dextral sense of movement to the system. This can be used as a predictive tool for locating mineralized veins on the property beyond their known extents.

## SECTION 4: GEOCHRONOLOGY

### **Introduction**

Previous work (Ballard, 1924; Anderson, 1934; Anderson, 1947) on dikes in the Pearl and Boise Basin mining districts associated with the Trans-Challis Fault System has established a relative timing sequence of Eocene diking and mineralization. The goal of the geochronologic work presented as part of this thesis is to test the veracity of the established sequence and constrain the timing of mineralization. Establishing an absolute age sequence will allow the timing and tempo of magmatic intrusions to be compared to other locations across the TCFS and placed within the regional tectonomagmatic framework. Additionally, the combination of the relative sequence of events and absolute ages allows the timing(s) of the pulse(s) of mineralization to be constrained. Constraining mineralization timing will help provide a more focused exploration guide. The units selected for geochronologic work are the: granodiorite, diorite, diorite porphyry, dacite, rhyolite, andesite, and lamprophyre. Tandem high spatial resolution, LA-ICPMS and high precision, CA-IDTIMS U/Pb methods are utilized on magmatic zircon separated from pluton and dike lithologies. All work was completed at the Boise State University Isotope Geology Laboratory.

### **Results**

Initial LA-ICPMS geochronologic results return ages of: dacite porphyry  $48.65 \pm 0.78$  Ma., rhyolite porphyry  $47.83 \pm 0.56$  Ma., diorite porphyry  $\sim 47.37 \pm 0.68$  Ma., and andesite of  $\sim 31.15 \pm 0.83$  Ma., all errors are  $2\sigma$ . High-precision CA-IDTIMS has further

constrained these ages to: dacite porphyry,  $48.03 \pm 0.05$  Ma., rhyolite porphyry,  $47.50 \pm 0.09$  Ma., diorite porphyry  $47.92 \pm 0.10$  Ma. and  $47.52 \pm 0.02$ , and andesite to  $30.44 \pm 0.02$  Ma., all errors  $2\sigma$ . These ages constrain the timing of the bulk of intrusive activity, and any associated mineralization within the property to within a 0.5 Ma window in the early Eocene Lutetian stage, between 47.5 and 48 Ma. (Table 4.1). The early Oligocene age of 30.44 Ma. for the dated andesite dike is consistent with extrusive and intrusive activity of the Salmon Creek Volcanics in Owyhee County to the south (Ekren et al., 1981) and the Kamiah Volcanics in Idaho County to the north (Jones, 1982) and if the relative chronology established by Anderson (1934; 1947) is followed constrains mineralization to no earlier than the Late Oligocene. It should be noted that rock names assigned within this report are not necessarily the same as those of earlier works, further study is needed to reconcile any discrepancies or verify new distinctions.

Uranium-Lead (U-Pb) dating on zircon crystals contained within selected dikes was conducted during December of 2015 via Laser Ablation Inductively Coupled Plasma Mass Spectrometry (LA-ICPMS) at Boise State University's Isotope Geology Laboratory (IGL) by the author under the direction of Dr. Mark Schmitz. Dikes were selected for geochronologic work based on three criteria: (1) their presumptive order in Anderson's (1947) relative timeline, with initial emphasis placed on covering the spread of possible ages, (2) the likelihood that the sampled lithologies would contain zircon amenable to radiometric dating techniques, and (3) the mapped varieties exposed at the time of reconnaissance work in the summer of 2014. LA-ICPMS and CA-IDTIMS work has been conducted on five dikes of varying lithology: a dacite porphyry which is earliest in Anderson's sequence, a phenocryst poor variant of the diorite porphyry found

immediately adjacent to exposed mineralization at the Mammoth Mine, a phenocryst rich variant of the diorite porphyry more typical of the type identified extensively throughout the property, a rhyolite porphyry dike, and an andesite of uncertain composition that often resembles either the diorite porphyry or the diabase/basalt dikes in the area. The previously established relative timeline (Anderson, 1947) and the new absolute age chronology developed for this study are summarized in Figure 4.1.

The quartz monzonite and syenite in Anderson's sequence were not identifiable dikes in the area during the most recent mapping project and are therefore not included in the initial geochronologic work, the diabase was considered unlikely to contain sufficient zircon crystals to date and was consequently rejected for preliminary work, lamprophyre's are most amenable to rubidium-strontium dating techniques and not used in the U-Pb work, zircons recovered from the lamprophyre returned a Cretaceous age using LA-ICPMS and are interpreted to be xenocrysts from the surrounding granodiorite.

#### **LA-ICPMS Methods**

Zircon grains were separated from rocks using standard techniques and annealed at 900°C for 60 hours in a muffle furnace. Grains exhibiting the most angular morphologies and fewest inclusions under transmitted light microscopy were mounted in epoxy and polished until their centers were exposed. Cathodoluminescence (CL) images were obtained with a JEOL JSM-1300 scanning electron microscope and Gatan MiniCL. Zircon was analyzed by laser ablation inductively coupled plasma mass spectrometry (LA-ICPMS) using a ThermoElectron X-Series II quadrupole ICPMS and New Wave Research UP-213 Nd:YAG UV (213 nm) laser ablation system. In-house analytical protocols, standard materials, and data reduction software were used for acquisition and

calibration of U-Pb dates and a suite of high field strength elements (HFSE) and rare earth elements (REE). Zircon was ablated with a laser spot of 25  $\mu\text{m}$  wide using fluence and pulse rates of 5 J/cm<sup>2</sup> and 10 Hz, respectively, during a 45 second analysis (15 sec gas blank, 30 sec ablation) that excavated a pit  $\sim$ 25  $\mu\text{m}$  deep. Ablated material was carried by a 1.2 L/min He gas stream to the nebulizer flow of the plasma. Quadrupole dwell times were 5 ms for Si and Zr, 200 ms for <sup>49</sup>Ti and <sup>207</sup>Pb, 80 ms for <sup>206</sup>Pb, 40 ms for <sup>202</sup>Hg, <sup>204</sup>Pb, <sup>208</sup>Pb, <sup>232</sup>Th, and <sup>238</sup>U and 10 ms for all other HFSE and REE; the resulting integrated sweep duration is 950 ms. Background count rates for each analyte were obtained prior to each spot analysis and subtracted from the raw count rate for each analyte. For concentration calculations, background-subtracted count rates for each analyte were internally normalized to <sup>29</sup>Si and calibrated with respect to NIST SRM-610 and -612 glasses as the primary standards. Ablations pits that appear to have intersected glass or mineral inclusions were identified based on Ti and P signal excursions, and associated sweeps were discarded. U-Pb dates from these analyses are considered valid if the U-Pb ratios appear to have been unaffected by the inclusions. Signals at mass 204 were normally indistinguishable from zero following subtraction of mercury backgrounds measured during the gas blank (<1000 cps <sup>202</sup>Hg), and thus dates are reported without common Pb correction; rare analyses that appear contaminated by common Pb were rejected based upon mass 204 greater than baseline.

For U-Pb and <sup>207</sup>Pb/<sup>206</sup>Pb dates, instrumental fractionation of the background-subtracted ratios was corrected and dates were calibrated with respect to interspersed measurements of zircon standards and reference materials. The primary standard Plešovice zircon (Sláma et al., 2008) was used to monitor time-dependent instrumental

fractionation based on two analyses for every 12 analyses of unknown zircon. A polynomial fit to the standard analyses yields each sample-specific fractionation factor. A secondary correction to the isotopic ratios of 1.3-3.3% (dependent upon experiment) was made based upon the bias in recovered weighted mean dates from the secondary zircon reference materials Temora (418 Ma) and FC1 (1098 Ma), which were measured twice for every 20 analyses of unknown zircon. This secondary correction is believed to mitigate matrix-dependent variations due to contrasting compositions and ablation characteristics between the Plešovice zircon and other standards (and unknowns); because all primary and secondary standards are chemically abraded, bias between standards is not considered due to variable Pb-loss effects.

Radiogenic isotope ratio and age error propagation for all analyses includes uncertainty contributions from counting statistics and background subtraction. For spot analyses that are individually interpreted (e.g., detrital zircon analyses), the uncertainty from the standard calibration is propagated into the error on each date. This uncertainty is the local standard deviation of the polynomial fit to the regularly spaced primary standard measurements versus time for the time-dependent, relatively larger Pb/U fractionation factor, and the standard error of the mean of the consistently time-invariant and smaller  $^{207}\text{Pb}/^{206}\text{Pb}$  fractionation factor. Age interpretations are based on  $^{207}\text{Pb}/^{206}\text{Pb}$  dates for analyses with  $^{207}\text{Pb}/^{206}\text{Pb}$  dates >1000 Ma. Analyses with >20% positive discordance and >10% negative discordance are not considered. The  $^{206}\text{Pb}/^{238}\text{U}$  dates are used for analyses with  $^{207}\text{Pb}/^{206}\text{Pb}$  dates <1000 Ma. Errors on the  $^{207}\text{Pb}/^{206}\text{Pb}$  and  $^{206}\text{Pb}/^{238}\text{U}$  dates from individual analyses are given at  $2\sigma$ .

### CA-IDTIMS Methods

U-Pb geochronology methods for isotope dilution thermal ionization mass spectrometry follow those previously published by Davydov et al. (2010) and Schmitz and Davydov (2012). Zircon crystals were subjected to a modified version of the chemical abrasion method of Mattinson (2005), reflecting a preference to prepare and analyze carefully selected single crystal fragments. All analyses were undertaken on crystals previously mounted, polished and imaged by cathodoluminescence (CL), and selected on the basis of zoning patterns. U-Pb dates and uncertainties for each analysis were calculated using the algorithms of Schmitz and Schoene (2007) and the U decay constants of Jaffey et al. (1971). Uncertainties are based upon non-systematic analytical errors, including counting statistics, instrumental fractionation, tracer subtraction, and blank subtraction. These error estimates should be considered when comparing our  $^{206}\text{Pb}/^{238}\text{U}$  dates with those from other laboratories that used tracer solutions calibrated against the EARTHTIME gravimetric standards. When comparing our dates with those derived from other decay schemes (e.g.,  $^{40}\text{Ar}/^{39}\text{Ar}$ ,  $^{187}\text{Re}-^{187}\text{Os}$ ), the uncertainties in tracer calibration (0.05%; Condon et al., 2007) and U decay constants (0.108%; Jaffey et al., 1971) should be added to the internal error in quadrature. Quoted errors for calculated weighted means are thus of the form  $\pm X(Y)[Z]$ , where X is solely analytical uncertainty, Y is the combined analytical and tracer uncertainty, and Z is the combined analytical, tracer and  $^{238}\text{U}$  decay constant uncertainty.

## SECTION 5: SURFACE GEOCHEMISTRY SURVEY

### **Introduction**

The surface geochemical survey is a combination of soil and rock chip analyses designed primarily to assess surface gold concentration across the property, with ~10% of collected samples submitted for more extensive multi-element analyses. Gold is one of the most inert and immobile of elements. Therefore, if sampled at the correct depth, the surface concentrations of gold are representative of conditions in the bedrock immediately below or adjacent to the sample location (Boyle, 1979; Cook and Dunn, 2006). Presented in this chapter are the results of two surface geochemistry surveys; one is a 643 sample orientation survey conducted across the entire property, the other is a 93 sample, 25 foot center, survey conducted across the westward projection of the exposed vein at the Mammoth Mine.

### **Sampling and Analysis**

An initial, orientation surface geochemical sampling survey was conducted over the entire property from March to June 2014. The sampling grid consists of 29 east - west lines with 120m north-south line intervals, samples are spaced with 60m between centers along lines for a total of 643 samples. In August of 2015 a detailed sampling program was carried out along and above the gully extending west from the Mammoth claim. The Mammoth sampling grid consists of five lines running roughly NW-SE along ridgelets that extend from the top of the main NE-SW trending ridge with 8m between centers for a total of 93 samples. Of those 93 samples 10 samples thought to most closely match the

projection of the exposed Mammoth vein were selected for full elemental analysis. For both surveys, 0.5 to 1 kg samples were collected from the upper B soil horizon, typically at a depth of ~45 cm. In areas where the soil cover was too thin to collect from the upper B horizon, i.e. the upper B horizon did not exist, samples were collected from just above the regolith.

Samples in the initial orientation survey were processed according to ALS Minerals Ltd. recommended procedures at Boise State University. Samples collected for the detailed follow up survey in the summer of 2015 were collected and sieved for material >1cm in the field before shipment, without any preprocessing at Boise State University, to ALS labs in Reno. Both sets of samples were processed as soil plus rock chip samples by ALS labs. Samples processed at Boise State University were dried at room temperature on a wood pallet before being crushed and screened to -80 (180 µm) mesh. After screening 50 gram aliquots were shipped to ALS Labs in Reno, NV, fine material in excess of 50g and the coarse reject are stored at BSU. 643 soil samples were collected on the property and subsequently analyzed for gold concentration at ALS Labs. Gold concentration was determined using the Au-ICP21, Au-GRA21, Au-TL42, and Au-AA23 ALS Lab methods. 155 of the 643 samples were analyzed for 50 elements using the ME-MS41 ALS method. Elemental analysis included: Ag, Al, As, B, Ba, Be, Bi, Ca, Cd, Ce, Co, Cr, Cs, Cu, Fe, Ga, Ge, Hf, Hg, In, K, La, Li, Mg, Mn, Mo, Na, Nb, Ni, P, Pb, Rb, Re, S, Sb, Sc, Se, Sn, Sr, Ta, Te, Th, Ti, Tl, U, V, W, Y, Zn, Zr. See Appendix IV Soil Analysis Methods, for full descriptions of ALS Global procedures.

## Results

In the property scale orientation survey the largest anomaly is 2190 ppb and collected immediately west of the exposed Mammoth vein, 17 samples are over 100 ppb, 21 samples are between 50-100 ppb, 54 samples are between 20-50 ppb, 85 samples between are 10-20 ppb, 169 samples are between 5-10 ppb, 297 samples are less than 5 ppb. Sample gold concentration distribution is shown as a histogram in (Figure 5.1).

Surface geochemical soil and rock chip samples are intended for use as a first order guide to further sampling and exploration programs. By sampling from at least the B horizon, or below, the presence of gold, which is relatively immobile in the soil, should be a result of weathering of the bedrock and is unlikely to be a product of other transportation processes depositing eroded gold from farther afield. Boyle (1979) suggests that normal gold content in soils is typically less than 5 ppb (0.005 ppm) and that values greater than 10 ppb (0.01 ppm) should be considered anomalous and warrant further investigation. As part of the British Columbia Geologic Survey's efforts to provide published industry standards for mineral exploration Cook and Dunn (2006) report B horizon soil Au values at the 3Ts epithermal Au-Ag prospect in central B.C. of up to 223.1 ppb and typically in the range of 10-100 ppb. These results are from directly over known epithermal gold veins sourced from dike lithologies similar to those in the Pearl district. Other elemental indicators of gold are Ag, Hg, Sb, and As in addition to numerous others that are site or deposit specific (Boyle, 1979). Here we have used a value of  $\geq 20$  ppb as the benchmark for anomalously high soil gold content that warrants further investigation. Using this criteria an east-west trend to anomaly patterns becomes apparent in Figure 5.2, with a subordinate set of north-south trending anomalies.

As a visual exercise the surface gold concentration results can be plotted as a gradient map using the nearest neighbor interpolation method (Figure 5.3). This allows the visual integration of the whole range of gold concentration values beyond the greater than or less than 20ppb method presented above as well as beginning to define the shape and outline of potentially exploitable ore bodies. Two major features of the dataset are apparent in the surface gold concentration gradient map.

One, that there are at least three east-west trending zones of anomalous highs. The most northerly and shortest of these trends is centered near the Osborne mine in claim OG08. Based on the current geochemical data and the previous mining work done around the Osborne it becomes apparent that the Osborne vein system exists as northeast stepping en echelon east-west trending veins and fractures. To the south, the largest and most extensive of the anomalous zones extends east-west from the Mammoth claim across the property to the Kentuck claim, including a large anomalous zone near the Quaker claim. This system also steps to the northeast as it moves east. Historical data is not as good for this area but would indicate, along with excavation work at the Mammoth mine, that the vein systems are also east-west trending. These are also likely to exist as en echelon sets. At the southern tip of the Payette claim another string of anomalies trends east-west. The trend exists in an area with only scant prior work (very shallow prospect pits) done on it and in an area where the exposure is poor to non-existent and thus constitutes what would be a blind target. The anomalous trend is bracketed to the north and south by adjacent sampling lines that do not indicate extensive east-west mineralization, limiting the width of the zone to a maximum of 240m. The trend is a composite of two different sampling trips along the UTM 4860220N sampling line, that

the anomalies span the divide between two sampling trips indicates sampling contamination is likely not the source of the anomalous values.

The second major feature are north-south oriented anomalies that cross from one major east-west trend to another, much like the rungs of a ladder. Where these two anomalous trends intersect there tends to be an expansion of the areal extent of the two sets of anomaly trends. An especially apparent example of this is the “rung” between the large Quaker anomaly and the long, thin anomaly just south of the Payette claim. There is a fairly consistent 700-800m spacing between major east-west trends.

The pattern and geometry of the anomalous zones throughout the property area suggests an underlying fabric of fractures that exist as east-west dilatant features trending en echelon to the northeast with conjugate north-south oriented fractures serving to translate stress through the system and opening pathways for mineralizing fluids. This confirms structural data reported by Anderson (1934) for vein systems throughout the entirety of the Pearl to Horseshoe Bend mining districts that shows that veins strike predominantly east-west and dip steeply to the north.

155 samples were randomly chosen for full 50+ elemental analysis at ALS Global labs. These samples are not uniformly distributed over the study area and cannot be used to give a spatial outline to any elemental indicators for mineralization. They can, however, be used as a guide to what elements are, besides gold, the best predictors of gold and to help characterize mineralization style by assessing the ratios of other precious metals to gold.

Gold/silver ratios range from 1:17.9 for all samples, to 1:18.7 for samples >20ppb Au, to 1:19.2 for samples >50ppb gold. A decreasing Au/Ag ratio for increasingly gold

rich soil samples is common among relatively young ore deposits where silver associated with mineralization has had less time to mobilize away from its original location, this effect increases with age due to silver being less chemically stable than gold (Boyle, 1979). Anderson (1947) reports that ore gold is most commonly found in or associated with pyrite, arsenopyrite, sphalerite, and galena. While no significant correlation was found between gold concentration and lead or zinc concentration, arsenic ( $R^2 = 0.9588$ ) and bismuth ( $R^2 = 0.5069$ ) both have results that indicate they may be promising tracers of gold mineralization, the arsenic is likely due to gold being hosted in arsenopyrite and the bismuth is likely due to it sharing similar chemical characteristics as arsenic and possibly substituting into arsenopyrite. Additionally, Ag and Cu, returned  $R^2$  values greater than 0.2, and Mo an  $R^2$  of greater than 0.1. Figure 5.4 plots gold concentration against concentrations of the elements commonly associated with gold such as: Ag, As, Bi, Cu, Hg, Mo, Pb, Sb, Te, Tl, W, and Zn with associated  $R^2$  values. The copper correlation is likely due to gold ore in the district being subordinately linked with chalcopyrite and tennantite while the silver is likely indicative of the presence of pyrargyrite and owyheeite that Anderson (1934) reported to be present in some deposits in the Pearl to Horseshoe Bend districts.

### **Soil Analysis Methods**

For soil Au analyses all samples were first analyzed using the Au-TL42/43 or the Au-ICP21 methods from ALS Labs. Au-TL42/43 and Au-ICP21 methods returned 18 samples of the 643 that had concentrations greater than 100 ppb, of those 14 were reanalyzed using the Au-AA23/24 or the Au-GRA21 methods. Of the reanalyzed samples 11 still returned values greater than 100 ppb, 3 analyses returned concentrations

significantly less than 100 ppb, and one returned a significantly higher concentration. This may be attributable to micro-nuggets of gold that could localize high gold concentrations to one aliquot of a sample while leaving another aliquot barren. Au-ICP21 and Au-GRA21 methods were used when the ME-MS41 methods was used for the analysis of additional elements. Detailed analysis methods are provided by ALS Global and given in Appendix IV: Surface Geochemistry Methods. Table 5.1 outlines the lab methods soils samples collected during the above surveys.

## SECTION 6: MAGNETIC SURVEY

### **Introduction**

The purpose of a magnetic survey is to identify areas of anomalously weak or strong magnetic signatures and their spatial relationships to features highlighted by the other surveys or mapping. Magnetic anomaly mapping is especially sensitive to the presence of minerals with high magnetic susceptibilities, e.g. magnetite. For the purposes of this survey it is presumed that Eocene dikes will have a greater concentration and preservation of magnetically susceptible minerals than the surrounding host rock and that these minerals will be some of the most easily destroyed minerals during hydrothermal alteration. Consequently, highly altered zones should appear as magnetic lows. Therefore, magnetic anomalies may be used as proxies for covered or sub-surface dikes or as evidence of possible to mineralization.

Anomalies occur where there is a higher concentration and non-random orientation of magnetically susceptible minerals, and, because the Earth's magnetic field varies through time, it is unlikely that discrete bodies will have the same magnetic orientation as other bodies given a sufficient gap in time. Additionally, the depth to source of a magnetic anomaly will affect the intensity; that is small, shallow magnetic bodies can produce the same magnetic signal as large, deep magnetic bodies. After emplacement, fault movements, weathering, erosion, re-melting, or hot hydrothermal waters can erase or partially obscure the magnetic record of the host rock. Because the survey is designed to look at deviations from the norm, large bodies relative to the area of

the survey that have a relatively uniform magnetic signal do not influence the presence of anomalies, though they may alter the intensity. The property has large bodies of background plutonic rocks that carry a magnetic signature of their own, however, because they presumably encompass the whole area of the property they will not affect the location of anomalies. Where plutonic rocks are not present or are buried the sedimentary rock that is in their place will, likewise, not provide an anomalous signal because any magnetic minerals present in the sediments or sedimentary rock have either been destroyed or are randomly oriented and not able to provide a coherent signal.

The magnetic survey data is presented here in two different forms. One is the total field magnetic anomaly which plots deviations, in nanoTeslas (nT), from the mean magnetic field strength of the surveyed area. The other is an edge detection method that maps the rate of change of the magnetic field from one location to the next, with units of nanoTeslas per meter (nT/m), in either the north-south or the east-west directions.

### **Data Collection and Analysis**

The magnetic survey was conducted between October 2014 and March 2015. The local magnetic field for the Horseshoe Bend area is between 52,000 and 53,000 nT. The survey consists of 53 north-south lines with 60m between lines. Line locations and intervals were selected to correspond with sample spacing interval along the east-west surface geochemical survey lines. A Geometrics G-856AX Memory-Mag Proton Precession Magnetometer was used as a base station for diurnal variation correction. A Geometrics G-858 MagMapper cesium sensor magnetometer was used for continuous, 1-second interval, mobile data collection. Data processing was done with MagMapper software, and in-house Matlab code authored by Kyle Lindsay.

Initial processing was done in Magmapper 2000 using the built in remove drop-outs, range despiking, and destriping features. Matlab was used for additional despiking, reduction to pole, edge detection, and plotting. The Matlab code for the magnetic anomaly survey can be found in Appendix E.

The reduction to pole technique plots the despiked original data as if the reading were taken at the Magnetic North Pole, where the magnetic field is perpendicular to the surface of the Earth. The edge detection technique seeks to define the edge of detected anomalies by plotting the gradient, or steepness of slope, between points. Anomalies will have rapid associated gradient changes at their edges.

### **Results**

Edge detection results indicate a series of northeast trending anomalies in addition to east-west features that are slightly less distinct, both are likely associated with a host that has an anomalous magnetite content in comparison to the background plutonic rock. Total field magnetic anomaly results roughly define the area of and contacts between the diorite stock, the granodiorite, and the Payette Formation sands as well as establish the overall homogeneity of the plutonic bodies.

The reduced to pole (RTP) magnetic anomaly map (Figure 6.1) is the original data corrected to simulate acquisition at the North Pole, where the magnetic field inclination is 90°. This serves to most accurately center readings over their true place of origin. Uncorrected, or “original”, data plots with the same map pattern but slightly offset from true position. As such, treating the original and RTP data separately would be redundant, and accordingly the discussion herein is limited to RTP results. Likewise, both the north-south, or “y”, and east-west, or “x”, gradients are used to highlight the edges of features

based on the same data set. The y gradient looks at abruptness of change in the magnetic signal along a north-south line, and the x gradient looks at the abruptness of change in the magnetic signal in the east-west direction. It follows that the y gradient is therefore best at highlighting linear features that extend in the east-west direction and the complementary x gradient best highlights north-south features. Because the expected features in the area are thought to be roughly northeast, both data sets should highlight the features of interest well, but because the overall trend of the district is slightly south of northeast and data indicates veins strike generally east-west the y gradient data set will be discussed in the text. The uncorrected total field anomaly and x gradient maps can be found in Appendix F.

The RTP data highlights three major domains in the background lithology. In the southeast corner of the property a muted magnetic signal and the sudden loss of sharply defined features is likely indicative of the granodiorite being covered by the sands of the Payette Formation, the apparent coincidence of the transition on the RTP total field magnetic anomaly map with the contact between the granodiorite and Payette Formation on the geologic map provides a good indication that magnetic survey is doing a reasonable job of distinguishing diverse lithologies. Less clear is the transition from granodiorite to diorite. In general, areas mapped as granodiorite do record an elevated magnetic signature compared to areas mapped as diorite. However, due to the presence of a great many truly anomalous areas in the plutonic rocks and the uncertain location of the granodiorite-diorite contact over much of the property, the line between the two is less well defined than for the granodiorite-Payette Formation contact.

When looking at the RTP magnetic anomaly map the area of the river cut terrace is also distinct from the rest of the map. However, the river cut was much more aggressively processed to remove bad data readings than the rest of the property due to the high proportion of anthropogenic material in the area resulting in a smoother signal. What can be seen in the river cut is one or two generally northeast-southwest trending anomalies that coincide with much more sharply defined anomalies on either side of the alluvium. In fact, a number of northeast-southwest and east-west trending features can be seen across the whole of the map and are highlighted effectively on the Y-gradient magnetic anomaly map (see Appendix F). In addition to the NE trending linear features a pair of bullseye anomalies occur in the extreme northeastern portion of the property, apparent on both the RTP and the Y-gradient maps.

## SECTION 7: ELECTRICAL RESISTIVITY AND INDUCED POLARIZATION SURVEY

### **Introduction**

The IP, ER, and associated metal factor (MF) survey was conducted over a portion of the site to assess subsurface lithologic characteristics and structure. The goal of the survey is to identify dikes and possible zones of mineralization in the subsurface by exploiting differences in the conductivity and chargeability of the subsurface.

An electrical resistivity (or inversely, conductivity) anomaly is produced when a current that is passed through the substrate encounters an area of higher or lower resistance than the average, this is described empirically by Archie's Law. Archie's Laws are a set of empirically derived equations that relate the electrical resistivity of a rock to its fluid saturation. Since most rocks are good insulators most of the electrical current carried through a body of rock is done so by the fluids filling fracture and pore space within a rock. Different lithologies in various stages of weathering have characteristic porosities, conductivities (of the rock and interstitial fluid), and levels of fluid saturations, cementation and tortuosity. These variables are summarized in Archie's Law:

$$C_t = \frac{1}{a} C_w \phi^m S_w^n \quad (\text{eq. 1})$$

Where,  $\phi$  is porosity,  $C_t$ , is the electrical conductivity of a fluid saturated rock,  $C_w$  is the conductivity of the fluid,  $S_w$  is the saturation of the fluid,  $m$  is a cementation exponent of the rock,  $n$  is a saturation exponent, and  $a$  is the tortuosity of the permeable

pathways. The range of expected resistivities (or conductivities) is illustrated in Figure 7.1. This basic equation is then modified appropriately to describe crystalline, sedimentary, or shaley rocks, as well as having different forms to accommodate various saturations, permeabilities, or fluids.

Rocks and minerals have a wide range of resistivities that can be exploited to provide nonintrusive measurements of the subsurface. Generally speaking, sedimentary rocks or sediments (e.g. sandstone, limestone, or unconsolidated alluvium) have lower resistivity than competent crystalline rocks. This is because resistivity is highly dependent on the presence or absence of water, the more permeable and porous sedimentary units have more pathways for conductive water.

This contrast can be utilized to distinguish between crystalline basement rock and water saturated unconsolidated overburden. Contrasts or anomalies in resistance may be created in crystalline rock by virtue of faults or fractures providing permeable pathways for fluid penetration or by the juxtaposition of markedly different lithologies as a result of composition (e.g. granite in contact with basalt). Anomalies in crystalline rock may also be produced where there is a high concentration of minerals associated with ores, i.e. possess metallic properties, and that tend to be better conductors than their host rocks. For the purposes of this survey the areas of enhanced conductivity associated with mineralization are of the greatest interest.

Induced polarization (or chargeability) is a measure of the time it takes for a section of ground to dissipate the charge or polarization that is induced by the same electrical current applied during the resistivity phase of the survey. The current will induce ions of opposite polarization, positive or negative, to build up on either side of a

particle depending on the current flow path, when the current is turned off the ions won't immediately dissipate but instead will discharge over some course of time - the rate of this discharge can be measured. As with resistivity, different materials will accumulate and dissipate charge at different rates, the contrast between materials can be used to produce chargeability maps of the subsurface. In particular, minerals often associated with ore formation, such as pyrite, galena, or magnetite, conduct electrons like a metal (electronic conduction) and produce strong IP signatures. Clays may also exhibit strong IP signatures because the negatively charged ions accumulate on their plate-like grain boundaries, in turn this attracts positively charged ions to their surfaces. Because the surface to volume ratio of clay particles is so large this can lead to a substantial accumulation of positively charged ions that impede the movement of "free" positive ions. When a current is applied the accumulation of positive ions is disrupted, when the current is then switched off the positive ions will re-accumulate on the grains, the re-accumulation is manifested as a decaying IP signal.

As stated previously, one of the primary goals of the ER/IP survey is to identify zones of likely mineralization not apparent on the surface. As is often the case in geophysics, ER and IP provide non-unique results that can lead to different interpretations. For example, a resistivity low (conductivity high) may be the result of a water saturated medium or due to the presence of sulfides associated with mineralization. Likewise, a chargeability high may be the result of a thick layer of clay (membrane polarization) or the presence of pyrite, galena, or magnetite (electrode polarization). In both cases a signal attributable to sulfides or other minerals associated with mineralization may also be interpreted as something else. However, while the sulfide

signal is present in both methods, the materials responsible for the variably interpretable signal in ER are not the same as the cause for spurious IP signals. To identify zones of likely mineralization this phenomenon is exploited via a parameter known as the metal factor (MF). Because the IP effect is intrinsically linked to resistivity, the resistivity of the country rock hosting an IP anomaly can be corrected for by dividing the IP result by the apparent resistivity to highlight areas that are both conductive and chargeable, i.e. possess the properties of a metal.

This chapter will detail, in order, survey methods and implementation, resistivity methods and results, induced polarization methods and results, metal factor parameterization and results, and followed by a discussion on how the results for each method can be integrated into a broader understanding of the subsurface.

### **Data Collection and Analysis**

An induced potential (IP) and electrical resistivity (ER) survey was conducted across most of the river cut terrace on the west side of the property near the county waste transfer station in July and August of 2014 (Figure 7.2). The location was chosen because the alluvium cover on the terrace precluded any outcrop mapping of the geology and because preliminary geologic surveys indicate that structures exposed in the hills above the site should continue, unexposed, underneath the site. Additionally, the site was chosen for its ease of access and gentle topography that would help to facilitate the speed with which this initial orientation survey could be completed.

Fifty-four individual, 180m dipole-dipole lines with 60m overlaps were run on a north-south grid with 30m spacing between lines for a total of 27 lines. The survey covered a total area of  $\sim 0.2 \text{ km}^2$  (212,000  $\text{m}^2$ ). Electrode spacing was 5m on all lines. Data

was collected on a Syscal Pro 10-channel resistivity meter, with a 12-volt internal battery, set in standard mode 10 channel dipole-dipole array (Figure 7.2) and using electrodes 36-72 in sequence for ER and IP measurements. The resistivity, or rho ( $\rho$ ), and IP injection pulse duration was 1 second, with semi-logarithmic sampling of 3 to 20 partial chargeability slices. The constant injection value,  $V_{ab}$ , was set to 800V. Typical current was ~1.25 to 0.625 amps. Electrode spacing was 5m, with maximum collected individual line lengths of 180m (36 electrodes x 5m between electrodes = 180m). Lines longer than 180m are acquired by overlapping sequential lines by 60m and splicing results together in data processing. Stack minimum was set to 4 and maximum to 16. A depth level of 10 was used. A quality factor, Q, of 4 was set for termination of individual measurements. Data was processed using Prosys II, Res2Dinv, and Matlab software at Boise State University. The Matlab code can be found in the appendices and was authored by Hank Hetrick.

### Electrical Resistivity Survey

#### Results

Figure 7.4 shows the results of the electrical resistivity (ER) survey across all 27 lines collected in this study, with line 9 omitted due to bad data. There is a trend of resistivity highs (conductivity lows), shown as reds, that runs roughly northeast-southwest. Highly resistive areas are interpreted to be crystalline, silicic rock bodies that impede electrical conductivity. Areas of low resistance (blues) are interpreted to be either more porous and permeable materials that contain ion filled water in the pore spaces or metals/sulfides that make good conductors. The majority of blue to green areas are interpreted as water saturated alluvium, where there are anomalous zones of low

resistance surrounded by zones high resistance are areas of possible ore bodies. The general northeast-southwest trend is consistent with other data sets in this study and others that indicate northeast trending dikes and structures on the property.

### Methods

Electrical resistivity (ER) surveys use the conductive properties of the shallow subsurface to map in two dimensions, length and depth, the resistivity of the material through which the charge passes. The principle is governed by an application of Ohm's Law:

$$I = \frac{V}{R}, \text{ (eq.2)}$$

where I is the current in amperes, V is the voltage measured across the conductor in volts, and R is the resistance of the conductor in ohms. By knowing the voltage and current input, the resistance of the circuit can be solved for. Resistivity can be thought of as the inverse of conductivity. The survey creates a circuit through the ground with electrodes spaced along the circuit path and a resistivity meter (similar to an ohmmeter) at one end of the circuit to measure the charge received at each electrode station. A special version of Ohm's Law, known as Archie's Law:

$$I = \frac{R_t}{R_0}, \text{ (eq.3)}$$

where I is current in amperes,  $R_t$  is fluid saturated rock resistivity, and  $R_0$  is the resistivity of rock filled only with water, empirically relates the resistivity of earth materials to electrical circuits.

As the electrical current passes through the ground some materials underground will be more conductive (less resistive) than others; the difference between applied charge and measured charge at each electrode along the line can then be attributed to

differing subsurface electrical properties, and will result in different measured resistivities. By varying the pairs of electrodes used to collect these measurements, a two-dimensional depth slice can be constructed showing subsurface features. ER surveys are often used to determine the location of the water table by taking advantage of the large conductive difference between salty, ion-filled water and rocks that tend to act as insulators. Similarly, the typical resistance of bodies of rock is much lower in areas with high metal content.

### Induced Polarization Survey

#### Results

Figure 7.4 shows the results of the induced polarization (IP) survey conducted as part of this study. Shown are 26 of 27 lines collected (line 9 omitted due to bad data). Reds are areas of higher chargeability; blues are areas of low chargeability. Peaks in chargeability are interpreted to trace a roughly northeast-southwest overall trend across the survey area. Chargeability highs (reds) are interpreted to be zones where metals and/or sulfides are likely to be most probable with the caveat that clays/shales can also produce chargeability highs. The northeast-southwest trend of chargeability highs and interpreted possible sulfide zones is congruent with other datasets from this study and others indicating a northeast trend to lithology and structures in the area.

#### Methods

The induced polarization (IP) subsurface imaging technique utilizes the same equipment and same setup as the ER survey. In a combined ER/IP survey, an initial voltage is put through the circuit to measure resistance, this same voltage will “charge” materials in the subsurface to different degrees depending on the material’s capability to

store a charge, or “chargeability”. When the current is shut off these materials will dissipate the charge at different rates and be measurable as a decaying electrical charge after current shut-off (Figure 7.6). This relationship is expressed in the equation:

$$m = \frac{V_0 - V(t)}{V_0}, \text{ (eq.4)}$$

where  $m$  is the slope of the decay curve over a small timer interval,  $V_0$  is the voltage applied before the current was shut off, and  $V(t)$  is the residual voltage measured after a very short time from the cut-off of  $V_0$  and is a proxy for polarization at the instant the current is turned off. By sampling the residual voltage multiple times after current cut-off a decay curve for each pulse can be constructed and an IP effect measured.

Whereas an ER survey measures the resistivity of materials and treats the ground as a resistor in an electrical circuit, an IP survey measures the capacity or chargeability of materials and treats the ground like a capacitor in an electrical circuit. Not widely used outside of the sphere of ore exploration, IP surveys are especially sensitive to the presence of sulfides. Therefore, IP surveys are good guides to possible ore bodies in areas where mineralization is thought to occur in sulfidized zones, such as within the epithermal Au-Ag or porphyry Cu systems. The measurements for an IP survey are taken immediately after each pulse of current is shut off in an ER survey, and as such record the exact same sections of ground so that ER and IP surveys may be directly compared to assess differing properties of materials in the subsurface. Using a mathematical construct to relate ER and IP surveys to each other the combination of the two methods over the same space can be used to produce a metal factor for each data point. The metal factor is discussed in the following section.

### Metal Factor

The metal factor (MF), as devised by Marshall and Madden (1959), is used to correct for the resistivity of the country rock during an IP survey. The MF is obtained by dividing the IP readings by those of the ER survey for the same station, and since that number will be very small, multiplying by some large constant. In the survey discussed here the resulting equation is, with units of conductivity in inverse Ohmmeters:

$$MF = 2 \times 10^9 \frac{IP}{ER} \quad (\text{eq.5})$$

The metal factor serves to accentuate the difference between massive sulfides and areas with disseminated sulfides due to massive sulfides having much lower resistivity values than disseminated zones. Figure 7.6 shows the results of the metal factor interpretation method.

### Results

As best as possible interpretations of results were made without relying on previous geologic knowledge of the property area. Hank Hetrick, a geophysics PhD. candidate without a priori knowledge of the property, was relied on for selecting promising trends in the data as well as technical help with completing the data processing. In general, northeast to southwest trends can be identified in all three methods of the IP/ER survey.

The ER survey (Figure 7.5) shows the depth to the water table across the river-cut terrace that hosts the county waste transfer station as well as depth to bedrock in addition to areas of high resistivity. The areas of high resistivity that rise above the bedrock contact may be interpreted as dikes that have better resisted the erosive action that created the terrace than the surrounding bedrock and therefore as likely avenues for mineralizing

fluids to follow. The resistivity peaks that rise above the base bedrock have a northeast-southwest trend to them.

The IP survey (Figure 7.5) highlights the areas where sulfide levels are significantly above background concentrations. Sulfides in the property area are known to occur in certain dike lithologies, particularly the diorite porphyry, as well as in the ores that have been mined in the area. Sulfides are not likely to remain in place during, or be unaffected by, extensive erosional activity along river channels and should therefore be confined to areas where they were protected during the cutting of the terrace such as where they are surrounded by bedrock or dikes. Consequently, the IP signature looks similar to the ER results, with a surface layer that has, in general, lower chargeability than a lower, bedrock hosted layer. Where the IP anomalies rise above that interface they are likely to be the result of variations in topography after erosion due to more physically resistant features such as dikes. In places, sequentially smaller peaks above the bedrock-sediment interface may be interpreted as a dike plunging into the surrounding bedrock. Like the ER anomalies, these peaks also seem to have an overall northeast-southwest trend to them.

As stated in the previous section, the metal factor (Figure 7.7) highlights the areas where the sulfides are enriched in comparison to other, possibly sulfide bearing, rocks due to their concentration and subsequent greater conductivity (lesser resistivity). This visualization process should enhance the sulfidized zones even when the zones are contained within siliceous bedrock or dikes. The pattern of MF highs follows the familiar pattern of ER and IP anomalies and trends northeast-southwest (Figure 7.8).

## SECTION 8: DISCUSSION

### **Interpretations and Conclusions**

The goal for the current phase of property development is to identify, through the combination of exploration techniques and historic data, the first order controls on mineralization location within the property bounds. Discussed and shown below are predictions and inferences that can be made with the current data set and discussion on how to further investigate the ideas proposed.

The general method that will be followed is surface geochemistry results will be used as a guide for areas of known mineralization. From there, areas with a geologic or geophysical pattern that seems to coincide with surface geochemical anomalies will be identified and predictions with possible explanations given. Last, a proposed test on these predictions will be explained and, if data is already available to make the test, results will be presented, if no data is available suggestions or targets for data acquisition will be made. This exercise will be done by overlaying, in map view, the four major data sets available: surface geochemistry, geology, magnetic anomalies, and induced potential (IP) electrical resistivity (ER) results. Historical data will be used where appropriate.

### **Surface Gold Anomalies**

It has been established in Section 5: Geochemistry that surface gold concentration trends are reliable indicators of subsurface mineralization. I propose here that the location and geometry of these trends can be used to infer underlying structural and lithological controls on mineralization.

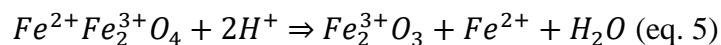
As discussed in section 5, Surface Geochemistry, the major trends in surface gold concentrations are east-west oriented with sub-ordinate north-south oriented crossing trends. Three anomalous east-west zones (Figure 8.1) have been noted: (1) a small, possibly en echelon, trend near the Osborn vein, (2) a wide, long, possibly en echelon trend spanning the property from the Mammoth to Kentuck claims, east to west, and (3) a long, thin southern trend just south of the Payette claim. Additionally, at least one north-south trend crossing the divide between the anomaly surrounding the Quaker claim (the “Quaker anomaly”) and the southern Payette trend of anomalies.

The Osborn and Kentuck – Mammoth anomalies step northward moving west to east, suggesting that they behave similarly to the mined vein systems in the Pearl to Horseshoe Bend districts as described by Anderson (1934). In that report Anderson, who had access to still open underground workings, described the ore bodies as being east-west elongate ellipses strung in an en echelon pattern along an east-northeast to west-southwest trend. The pattern of anomalies revealed in the current survey confirms that that holds true across the Trans-Challis property area. In a system of fractures with a right-lateral sense of shear this geometry would be expected. Boyle (1979) and Cook and Dunn (2006), suggest that surface geochemical gold anomalies are an accurate representation of the shape of mineralized zones in unexposed bedrock; therefore, the presence and patterns of surface gold anomalies will be used in the rest of this discussion as the baseline to compare the geological, magnetic, IP/ER, and historical datasets, to as well as the starting point for property scale structural interpretations. The probability that surface gold anomalies accurately represent actual mineralization is therefore considered high.

### **Total Field Magnetic Anomaly Lows.**

I propose that mineralization is more likely to occur in areas of total field Reduced to Pole (RTP) magnetic anomaly lows than in magnetic highs.

As discussed in the interpretation of magnetic survey results (Section 6, Results), magnetic anomalies are largely dependent on the presence or absence of the mineral magnetite. Magnetite ( $Fe_3O_4$ ) is a mineral common to igneous and metamorphic rocks, with greater abundance as the iron and magnesium content of the rock increases, i.e. as they become more mafic. Magnetite is an oxide that is especially susceptible to alteration or destruction (to hematite,  $Fe_2O_3$ ) in the presence of hot, acidic fluids; that is, fluids that are capable of holding gold and other ore constituents in solution need a low pH and high temperatures - the same conditions that alter/destroy magnetite (Mücke and Cabral, 2005). This relationship is expressed as:



Therefore, in regions where mineralization is known to be present, as in the case of the Pearl mining districts, areas of magnetic lows can reasonably be assumed to have a good probability of hydrothermal alteration with a good likelihood that some of this alteration occurred along with ore deposition.

This idea can be tested by comparing total field RTP anomaly results to surface geochemical gold anomaly results ( $Au \geq 20$  ppb). And indeed, when viewed side by side the surface geochemical gold anomaly contour map shows remarkable correlation with the RTP results (Figure 8.2). The densely sampled, previously mined, and recently excavated area around the Mammoth mine provides a good opportunity to test this idea with the data available currently. Figure 8.3 shows the area of the Mammoth claim with

the geologic, >20ppb gold concentration geochemical, and RTP magnetic datasets plotted. The high density surface geochemical sampling program sought to bracket the previously mined vein that was excavated in 2013. The old drifts and the new excavation reveal that the vein strikes 084° at the Mammoth mine and that if projected west traces up the gully that trends in an east-west orientation to the west of the Mammoth workings. A series of muted magnetic lows follow this same trend and would seem to corroborate the hypothesis. That these lows are not as striking as others in the surveyed area is not surprising because the Mammoth vein is most likely not one of the major vein systems on the property, as indicated by the limited work on the mine in the past, and a magnetic low signature is more likely to be swamped by nearby highs.

Areas with greater magnetic lows and spatially correlated geochemical anomalies may possibly contain more extensive mineralization than what is seen at the Mammoth. Figure 8.4 shows an area near the Quaker claim of magnetic lows that spatially overlaps 19 closely spaced surface geochemical gold concentration anomalies, hereafter referred to as the Quaker anomaly. The area pictured has a couple of prospect pits from earlier work and some small cart roads, presumably used to access those workings, but otherwise no significant work has been done on the surface of the Quaker anomaly. Likewise, the topography and soil mantle in the Quaker anomaly make exposure limited and determining geologic controls problematic. However, the combination of surface geochemistry and magnetic data make the Quaker anomaly worthy of further exploration for potentially untapped resources. It should be noted that at the base of the large flatiron which contains the Quaker anomaly there is a good sized dump with an associated portal

that may access the anomaly at depth. Lateral distance from the dump to anomaly is about 460m.

Other areas exhibit this same relationship and hold potential as well; they include: portions of the previously described Payette anomaly (section 8, Surface Gold Anomalies), a four sample string immediately east of the Catherine claim, and a series of gold highs and magnetic lows that follows the Osborne gully.

### **Dikes and Magnetic Edge Detection**

I propose that magnetic lineaments, especially those shown in Fig. 6.2, are due to the presence of dikes in the subsurface; that those dikes guide mineralization trends; and that, for the same reasons discussed in Section 8, Total Field Magnetic Anomaly Lows, the magnetic signature and dike pattern can be used to identify likely areas of mineralization.

As noted in the literature on the area (e.g. Anderson, 1934) (discussion in Section 2, Local Geology), mineralization in the Pearl districts is typically parallel to sub-parallel to Eocene dikes in the area. This observation is strongly supported by Anderson's examinations of the ore veins in the underground workings still accessible in 1934. The most recent geologic mapping and magnetic survey work has demonstrated a strong spatial correlation between mapped dikes and the linear magnetic trends in the edge detection magnetic anomaly maps.

It has been established (sections 5, Surface Geochemistry, Results; 8, Surface Gold Anomalies and; 8, Total Field Magnetic Anomaly Lows.) that surface gold anomaly (i.e. mineralization) trends follow magnetic lows, and therefore, have a magnetic signature. It has also been established (sections 6, Magnetic Survey, Results; and 8, Total

Field Magnetic Anomaly Lows.) that the mineral magnetite largely controls the magnetic field strength of a material. For reasons discussed below, Eocene and younger dikes on the property should produce a stark magnetic contrast with the Cretaceous plutonic rock they are hosted in. This contrast can be mapped as a magnetic gradient in nanoTeslas per meter, nT/m, which shows the change in field strength from one spot to the next. For a more detailed discussion see Section 7, Data Collection and Analysis.

Therefore, in theory, magnetic gradient lineaments should correlate with either mineralized trends or mapped dikes, and in some cases both. Furthermore, these lineaments can serve as guides to locating zones of possible mineralization when used in conjunction with surface geochemistry, unexposed dike segments, or both. Noting that, as discussed above, mineralization is often subparallel to dikes in the district, magnetic lineaments can serve as powerful exploration tools. Once potential mineralization guiding dikes are identified, their unexposed extents and locations may be predicted by following magnetic edge detection anomalies that are spatially correlated with dikes of interest. Areas where those dikes may be in close contact with mineralization are likely to be areas where the RTP magnetic map shows lows and/or the edge detection magnetic map loses fidelity. Figure 8.5 shows the densely sampled area around the Mammoth mine and how a well constrained combination of magnetic gradient, surface geochemical, and geological datasets may define exploration targets.

As discussed in the previous section, magnetic anomalies are due in large part to the presence or absence of magnetite, which is easily destroyed by ore bearing fluids. Additionally, the Eocene to Oligocene dikes especially the dacites, diorites, and andesites are more mafic than the country rock that they are hosted in and should contain more

magnetite. These two ideas, combined with the fact that, in general, the dikes are half the age of the rocks they are contained in and roughly the same age as the mineralizing event, indicate that linear trends in magnetic data are most likely to be the trace of dikes and not some other feature. The overlay of the surface geochemical, geologic, and magnetic edge detection data sets indicate that indeed this is a viable assumption.

Once again using the area around the Mammoth claim as a control, the magnetic edge detection data outlines the trace of the dike(s) that acted as guides during the mineralization event around the mine. The edge detection also may indicate that one, mostly unexposed, larger dike with splays coming off it runs across the claim and may be a first order guide to other mineralized zones.

Figure 8.6 shows an unworked area at the eastern edge of the Catherine claim and south of the Mammoth claim where a small east to west surface geochemical anomaly coincides with an east-west trending mapped dike and an east-west trending magnetic edge. The dike bends to the southwest where it enters the area of the Catherine claim where an old prospect pit indicates past exploration. The overlay of the geochemical, geologic, and magnetic datasets provide the opportunity to explore targets that were missed by past work in the area.

Figure 8.7 shows an area just south of the previously discussed Quaker anomaly and a 10 sample (out of 21) east-west trend of surface gold concentration anomalies. This area has only been lightly explored in the past with a few prospect pits but shows the same linear alignment of surface geochemical, geologic, and magnetic anomaly trends, at least along the western half of the line. Near the crest of the primary northeast trending ridge on the property the magnetic and geologic indicators die out but the gold anomaly

trend continues. Poor exposure along the ridge crest and the north aspect slopes may have led to a misinterpretation of the dike trends and the deep mantle of soil and data dropouts in the same area may have led to a muted magnetic signal. Further work along this trend would serve to improve these data sets as well test the proposed exploration guidelines.

### **Coincidence of IP/ER and Magnetic Trends**

I propose that the induced polarization and electrical resistivity surveys reveal a continuation of northeast stepping en echelon east-west mineralized zones that coincide with areas of magnetic lows.

Simply put, the IP/ER and magnetic geophysical surveys image two different phenomena that are hypothesized to follow the same set of structural controls and therefore the property wide magnetic dataset may be used to target areas for the more data dense, but more resource intensive, IP/ER surveys. The Induced Polarization (IP)/Electrical Resistivity (ER) surveys when used in conjunction with the Metal Factor (MF) represent the best way to ascertain the probability of mineralized zones at depth, short of drilling. As discussed in Section 7, Induced Potential and Electrical Resistivity Survey, the two parts of such a survey each explore a fundamental electrical property of a circuit created by placing electrodes into the ground and measuring the response. The electrical resistivity method samples the current received along pairs of electrodes and compares this to the known current put into the ground. With this method the Earth can be thought of as a resistor in an electrical circuit and the survey a measure of the resistance of the Earth to electrical conductivity. The induced polarization method measures the decay in charge through the same space after the ER current is switched off, with the idea that different materials will be polarized, or “charged”, differently with the

same current. With this method the Earth can be thought of as a capacitor that continues to dissipate a charge even after the input electrical current is turned off.

These two methods, ER and IP, are contingent upon two properties that serve to make metals physically unique, their high conductivity (low resistivity) and high chargeability (high polarization potential). While there are other physical parameters that may lead to low resistivity (e.g. salt water) or high chargeability (e.g. clays) no other materials possess the combination of high conductivity and high chargeability other than sulfides and certain non-ore minerals (e.g. graphite). Therefore, areas that return anomalous conductivity and chargeability signatures are the most likely to host metal or the sulfides that host metal. This is known as the “metal factor” (eq. 4), obtained by dividing the measured chargeability signal by the conductivity signal. The three methods discussed above used in conjunction can provide a robust model of the shallow subsurface and delineate likely ore bodies and their lithologic or structural controls.

Section 8, Dikes and Magnetic Edge Detection, outlines the idea that magnetic lineaments are primarily the result of dikes having a magnetic signal that is in sharp contrast to the bodies of rock they are hosted in; Section 8, Total Field Magnetic Anomaly Lows, discusses how the muting of a magnetic signal is indicative of hydrothermal alteration. Assuming that these are true, and that mineralization follows the same planes of weakness that the dikes exploited, it is reasonable to assume that IP and metal factor signatures highlighting lithologic differences and mineralization differences should follow the same basic trends as magnetic lineaments and that the magnetic signatures are likely to become muted in areas of metal factor highs. Figure 8.8 plots the results of the metal factor interpretation of the IP and ER results from the survey

conducted on the property on the same map as the magnetic edge detection results. The result is an apparent alignment of muted magnetic lineament lows with metal factor trends, as predicted.

Potential ore bodies may be investigated, without drilling, by identifying magnetic lineaments from the magnetic edge detection map that coincide with areas of magnetic lows (from the total field magnetic anomaly map) and gold highs (from the surface geochemistry map) and conducting detailed IP/ER surveys over them.

The IP/ER survey was conducted over the river cut terrace because the alluvium and the colluvium have completely buried rock outcrops in the survey area and any geochemical signal cannot be assured to be a result of underlying bedrock and not transported material. A magnetic data set could be collected over the IP/ER survey area because it is a measure of magnetic field strength that is integrated from depth, allowing for the effects of surface cover to be minimized. However, the current datasets do allow for a reasonable expectation that the IP/ER method can be carried out over select areas on the property and successfully identify mineralized zones. The first step on this path would be to conduct an orientation survey over a known vein system that has corroboratory information available, such as the Osborn or Mammoth systems, to ground truth what is suggested by the current terrace survey.

### **Intersection of Fracture Planes**

I propose that the intersection of east-northeast to west-southwest and north to north-northwest trending fractures creates the locus from which mineralization spreads along east-west trends.

The combination of two or more intersecting fractures is a classic exploratory target due to the geometry and brecciation associated with such features. Field evidence and the data sets collected here suggest that the Trans-Challis property is no different.

As discussed in Section 3, Structure, there are two major fractures sets within the property area. The first is an east-west or east-northeast to west-southwest trending set of fractures that host the majority of the vein sets on the property, these tend to dip steeply to the north (Figure 8.9). The second is a north to north-northwest set of fractures that do not appear to host vein sets. Where the NNW fractures intersect the east-west, vein hosting fractures, nodes of mineralization are often present (Figure 8.10). This phenomenon is seen at the outcrop to the property scales; such a range in scales suggests that this relationship is fundamental to the deposit characteristics.

Two criteria must be met to produce the pockets of highly mineralized rock at the intersections of east-west vein systems with the NNW trending fractures as observed. The first is that the two fractures sets must have been either preexisting or, forming at the same time as, the mineralizing event. The second is that the system must have been dilatant in the north-south direction to allow for the east-west propagation of mineral hosting trends, while the NNW set remained relatively closed. The NNW set of fractures contain many slipfaces but little gouge, indicating that they were more strike-slip than tensional in nature. The existence of mineralized nodes indicates that where the two fracture sets meet the combination of two different movement vectors created space, likely through brecciation, for ore forming fluids to concentrate. The Riedel shear pattern (Figure 3.6) closely replicates these conditions and offers a model for exploration going forward.

The combination of the geologic, geochemical, and geophysical data sets can be used to identify areas where such a nexus of fractures may exist that warrant further work. The detailed exploration work that has been done at the Mammoth mine provides a proof of concept working model with which to expand to other areas (Figure 8.11).

The combined geologic, geochemical, and geophysical datasets point to many possible areas throughout the property where this may occur. Some of these areas are highlighted in Section 9, Recommendations.

### **Proposed Structural Model**

Figure 8.11 shows a right-lateral Riedel shear array oriented to  $070^{\circ}$  and centered on the Quaker anomaly, geometry for a Riedel shear array as shown is given by Logan et al. (1979). The figure is a combination of Figures 3.6 and 8.1 and shows how the hypothetical shear array given in Section 3, Structure, overlays with gold anomalies defined in the surface geochemistry survey. The P, R<sub>1</sub>, and R<sub>2</sub> fracture planes correlate very well with the location, shape, and extent of mapped anomalies. Based off of the work described in this thesis the proposed Riedel shear model predicts the geometry of, and kinematic controls on, the mineralization in the property.

In the figure the smaller, solid red ellipses illustrate how a hypothetical series of fractures or mineralized zones may develop in the shear array. The fractures would dilate in the direction of least stress ( $\sigma_3$ ) and elongate in the direction of principal stress ( $\sigma_1$ ), indicated by red arrows on uppermost filled ellipse. The principal planes of movement (fractures) are dextral strike-slip features oriented N70E, parallel to the trend of the Trans-Challis Fault System (TCFS). Secondary movement planes are indicated by thinner

black lines labeled P and R<sub>1</sub>, it is on these planes that mineralization is most likely to occur.

For ore bearing fluids to be able to exploit the fractures created within rocks the fractures need to be brecciated, too little movement and the rock is not sufficiently fractured to allow movement of fluids, too much movement and the brecciated rock becomes a fine grained fault gouge impermeable to fluid flow. The principal movement planes and the R<sub>1</sub> and P fracture planes therefore define the geometry of the system. Fracturing and mineralization are bounded by the principal movement planes, giving the system (in this case the TCFS) a characteristic geometry and orientation (070°). Mineralization is most likely to occur within the bounds of the system, but cannot propagate along the larger strike-slip fractures that have impermeable, fine grained fault gouge. Therefore, ore bearing fluids exploit the less active secondary fracture planes, R<sub>1</sub> and P, which remain brecciated and are dilatant to accommodate lateral movement along the primary fracture planes. Any deviations from the overall trend of the TCFS, both locally and regionally, in the proposed strike-slip system could result in trans-tensional or trans-compressional zones. Tertiary movement planes are shown by the thin grey lines labeled R<sub>2</sub> and X with sense of movement indicated by the black arrows. Note that the sense of movement on R<sub>2</sub> is antithetical to the rest of the array.

The anomaly pattern (panel A) and structural data (given on stereonets in figures 3.2, 3.3, and 3.4) indicate a series of en echelon E-W trending ellipses along the R<sub>1</sub> fracture, with the orientation of the propagating tips controlled by the P fracture. When the shear array is oriented in the direction of the overall trend of the TCFS and empirically derived (e.g. Logan et al., 1979) internal fracture angles are applied, the R<sub>1</sub>

fracture is oriented  $051^\circ$ , the P fracture  $082^\circ$ , and the  $R_2$  fracture  $358^\circ$ . The alignments and orientations of the  $R_1$ , P, and  $R_2$ , fracture planes closely match the alignment and shape of mapped gold anomalies for the property area. For example, the  $R_1$  fracture explains the spacing and orientation of the three large anomalies indicated by the hollow red ellipses. The P fracture aligns very well with orientation of veins in the Pearl to Horseshoe Bend mining districts given by Anderson (1934), for example the vein exposed at the Mammoth mine strikes  $084^\circ$  and veins underground as reported by Anderson (1934) and plotted in Figure 3.4 are overwhelmingly east-west oriented. The  $R_2$  fracture plane aligns with the north-south trending Quaker to Payette anomaly indicated by the blue ellipse.

During the development of a Riedel fracture pattern the primary movement planes, here indicated by the N70E oriented thick black lines, are the last fracture planes to develop, it should also be noted that Figure 8.11 is an illustration of the Riedel shear array over the property area and the fracture pattern and fractures can exist at many scales and the fractures do not necessarily have to be where they are indicated. With that in mind, the location of the primary strike slip movement planes may interpreted in three ways: (1) they do not exist because they never developed, this is considered unlikely given the 20 million year period of similar dike orientations, (2) the property area only incorporates the interior of the array and the large strike-slip faults occur outside the study area, this seems most likely, but given the scalable geometry of the Riedel shear array there is probably some manifestation of a primary fracture plane in the study area, or (3) the primary strike-slip faults are actually dip-slip faults and are represented by the

river canyon in the northwest and the granodiorite to Payette Formation contact in the southeast.

Dike and magnetic edge detection lineament patterns also closely match the orientations of the R<sub>1</sub> and P fracture planes. The tertiary set of fractures are not proposed to have accommodated much movement and to not be dilatant; accordingly, we do not see dikes that are oriented along either the R<sub>2</sub> (358°) or X (303°) orientations. Only the more mobile, less viscous hydrothermal fluids were able to migrate along these paths, and even then to a much less extent than along the larger east-west and northeast oriented pathways. Crucially however, the tertiary pathways do allow for the transfer of fluids from one secondary fracture plane to another, providing the “rungs” to the proposed ladder like structure.

The migration of fluids along these tertiary fracture planes creates two important sets of conditions for further exploration: (1) The intersection of tertiary fracture sets with secondary fracture sets creates another possible setting for breccia pipes and highly concentrated mineralization (“nodes), and (2) a guide to undiscovered mineralized bodies, that is, where east-west mineralization trends pinch out exploration along these fracture planes may be warranted. In the case of condition (2) speculation may be taken one step farther. If the pinch out occurs on the east end of the vein system, the proposed Riedel shear model and observed en echelon pattern of vein development predicts that exploring to the north of the pinch out is more likely to produce a new system than exploring to the south. Likewise, if the pinch out is at the west end of the vein system, further exploration to the south may be more fruitful than to the north.

Furthermore, the apparent regular spacing of gold concentration anomalies shown on Plate 3, Gradient Map of Surface Geochemistry, suggests that the geometry of the proposed shear array may give rise to a predictable spacing between mineralized zones. Examination of the gold concentration anomaly map suggests a semi-regular east-west spacing of ~400m between the ~400m wide anomalous zones in the main en echelon northeast stepping Kentuck-Quaker-Mammoth anomaly pattern. Within this en echelon set, there is a ~200-250m north-south offset between each anomalous zone. There is an ~500m gap between the Kentuck-Quaker-Mammoth line of anomalies and the Payette anomaly to the south and a similar offset between the Kentuck-Quaker-Mammoth zone and the Osborn anomaly to the north.

Figure 8.12 shows the gold concentrations (y-axis) versus UTM easting (x-axis) for the eight surface geochemistry survey lines that encompass the Kentuck-Quaker-Mammoth anomalous zone. The aforementioned 400m wide anomalies separated by 400m clustering is apparent in the plot where the east-west sample lines are plotted together regardless of their UTM northing position. The plots for the individual east-west sample lines, denoted by the average northing of the sample locations, highlights a higher frequency anomaly spacing of ~200 to 250m. Figure 8.13 shows the results of an incremental spatial autocorrelation by distance analysis of the surface geochemistry dataset that was run in ArcGis. The analysis shows a peak at ~260m for gold concentration recurrence intervals. Figure 8.14 shows the result of one of a series of periodograms that were calculated along east-west trending lines along the Kentuck-Quaker-Mammoth line of anomalies. The most pronounced peak occurs at .0039, which corresponds to a peak in gold concentration values at recurrence intervals of 258m.

Multiple lines of investigation indicate that anomalies are likely to occur every ~250m and to coalesce into large anomalous zones approximately every 500m in east-west oriented trends. Similarly, an echelon offset in the north-south direction is about 200 to 250m within an east-west trend and ~500-600m north to south between east-west oriented trends of anomalies. However, it should be noted that the periodograms have their peaks at the lowest frequency interval, and due to the nature of the peak it is considered suspect. Likewise, the spatial analysis performed in ArcGIS considered all sample location simultaneously and did not discriminate between anomalous trends; therefore, the peak at ~260m may be the result of the sampling grid (60m sample centers, 120m between lines). All lines of inquiry indicate that there is a regular spacing to fracture patterns and gold mineralization which may follow. However, the sampling may need to be densified or extended over a larger area to bear this out in a more thorough manner.

#### Timing of Activity Along the Trans-Challis Fault System

The similarity in dike geometry and patterns between 47.5 Ma Eocene dikes and the 30.5 Ma Oligocene andesite dikes suggests that the regional stress fields that were responsible for the orientation of Eocene structures continued through to at least the Oligocene. Alternatively, the character of the TCFS near Horseshoe Bend may have evolved from primarily extension in the Eocene to primarily strike-slip in the Oligocene or later and from dominantly northeast oriented to east-west oriented fractures respectively. Additional geochronology of northeast and east-west oriented dikes may shed further light on the evolution of the system through time. The relative timing of mineralization provided by Anderson (1947) is therefore not constrained to the Eocene

but, instead, pulses of mineralization may have occurred throughout that ~18 million year interval and continued even later. The presence of Oligocene aged hydrothermally altered dikes gives credence to Anderson's (1934; 1947) tentative proposal that mineralization may have occurred as late as the Miocene. In fact, one would predict that the tectonic stressors that give rise to the regional stress regime should end with the onset of Basin and Range extension, which may only be beginning to have an effect locally around Horseshoe Bend. The north-south oriented Boise Ridge Fault has been interpreted to be an extensional Basin and Range feature, while at the same time subduction off the west coast due west of the field area continues to the present, this puts the southwestern end of the TCFS in a transitional area between primarily compressive tectonics to the north and primarily extensional tectonics to the south. Locally, the juxtaposition of these two regimes does not rule out the possibility that the stress framework responsible for the structural geometry has been active to the present.

Beginning with the deep seated and recurrently active suture of the Wyoming and Hearne cratons and continuing with Eocene magmatism and (possibly into the present) extension, the location and geometry of mineralized zones within the property area is most likely the result of mineralizing fluids repeatedly taking advantage of conduits and ground preparation conditions that are inherited from past events. Once the proper set of host conditions are created the deposition of mineralized bodies is just a matter of being in the right place at the right time, and the longer that those goldilocks conditions are maintained the greater the chance of mineralization within an area. The new geochronology and the proposed structural model indicate that the conditions that are ripe for mineralization were maintained over at least 17.5 Ma and possibly longer. This does

not serve to help put a precise time fingerprint on the deposit but is a positive indicator that the deposit has had ample time for multiple mineralizing events to occur in a properly prepared area.

## SECTION 9: RECOMMENDATIONS

In addition to a review of the literature for the area, the work done on the property to date is primarily a surface reconnaissance of the first order geologic controls on the system hosting mineralization. This includes geologic mapping, geochronology on dikes hypothesized to be contemporaneous with mineralization, magnetic anomaly mapping to indicate diking or mineralizing activity in an area, and an induced polarization (IP) and electrical resistivity (ER) survey to explore the subsurface expression of features observed on the surface. At the time of writing no known drilling program has been conducted at any location within the property boundaries. Therefore, the recommendations given below are for further surface work and non-intrusive sub-surface geophysical reconnaissance with speculation on possible drill targets.

### **Improve the Structural Dataset**

Geologic mapping and structure modeling may be improved by additional time spent collecting structure specific data to increase the number of data points in the structural dataset and explore the nature of the foliated zone and its impact on the system. This can be done in conjunction with other work on the property and need not be its own project. Outcrops freshly exposed by excavation or infrastructure work would be excellent targets for obtaining the best measurements. This work will test the veracity of the proposed structural model.

### **Additional Surface Geochemical Sampling**

The survey grid carried out across the whole area of the property was done with a relatively coarse resolution of 120m line spacings with 60m centers and has outlined five areas that warrant higher density sampling programs.

One of those areas, the Mammoth gully, has already been sampled at the 8m center resolution and has more precisely located the trace of a known vein system. The vein at the Mammoth has proven continuous over ~300m and is likely to continue beyond. A sampling program bracketing what has already been completed could extend the known length of this system and may map a connection to the more westward Quaker anomaly.

Other promising areas that warrant high density sampling are: the Osborn gully, the Quaker anomaly, the east-west trending linear Payette anomaly and its possible connection to the Quaker anomaly, and the Kentuck anomaly nearly adjacent to the Quaker anomaly's western side.

The Osborn is a promising target because of its well documented past history of production and the show on the surface because of past activity. The Kentuck and Quaker anomalies are promising both because of their size and of the possibility of being continuous with the Mammoth trend. The Payette anomaly and especially its connection to the Quaker anomaly is promising for what it may reveal about the pathways that mineralizing fluids may have followed. Initial recommendations would be to sample within the anomalies first to pinpoint their source before stepping out of the currently defined bounds to map their extent. The areas around the Mammoth and Osborn, because they have the most known resource potential, should be the highest priority. Figure 9.1

outlines the proposed sampling areas. Table 9.1 details acreage of proposed sample areas and approximate number of samples to be collected if proposed areas are sampled at 8m sample center intervals. Sample density does not have to be at 8m, for very large areas a coarser resolution may be sufficient to start.

### **Ground Truth Magnetic Data**

The geologic map and magnetic map are in overall agreement on the location of dikes and mineralized zones within the property, however, areas of disagreement between the two exist. Work should be conducted to reconcile the two datasets to generate the most accurate representation possible. This work would include sampling lithologies in areas of good overall correlation and in areas of possible alteration for magnetic susceptibility or polarity testing. Depending on the rigor desired this test this may be done in the field or in a lab. Normal or reverse magnetic polarization and general magnetic susceptibility may be obtained by handheld instruments in the field, if quantitative comparison of results with the existing magnetic dataset is desired more thorough lab work may be required. With a better model of individual dike lithology magnetic signatures, areas where geologic and magnetic fit are poor may be revisited to possibly reinterpret surface geology.

### **Extend IP/ER Coverage Over Known Veins**

Two induced polarization (IP) and electrical resistivity (ER) surveys bracketing the Osborn and Mammoth veins are recommended as the next steps for IP/ER work. These surveys will serve the dual purposes of providing detailed noninvasive subsurface knowledge of potentially exploitable ore bodies and establishing baseline characteristics

of ore body mineralization to guide interpretation of IP/ER results over areas of unknown potential.

It is recommended that the IP and ER survey be extended from the eastern margin of the IP/ER survey already completed and bracket the exposed trace of the Osborn vein. This will allow for a direct comparison of the IP/ER signal to areas of known mineralization which will, in turn, allow for more robust interpretation of IP/ER results elsewhere on the property. Five 360m lines spaced 100m apart bracketing the Osborne vein up the draw that exposes the majority of previous workings are recommended. This would provide a very good dataset to characterize the Osborne vein system as well as provide reference for other IP/ER surveys. Figure 9.2 shows the recommended Osborne survey area and possible line locations.

The recommended survey bracketing the Mammoth vein would provide the same benefits as the Osborne survey but without the advantage of being directly adjacent to the previous IP/ER survey. However, high density soil sampling across, and excavation of, the Mammoth vein have already been completed and, in conjunction with the existing magnetic and geologic data, account for the highest resolution dataset anywhere on the property. Four 360m lines spaced 100m apart bracketing the Mammoth vein are recommended. The suggested survey area and approximate line locations for the Mammoth area are shown in Figure 9.3.

The location of the IP and ER survey completed as part of the current work was chosen primarily because physical observations of the ore hosting bodies is impossible due to cover. Additionally, the relatively flat and easy to access river terrace was chosen to facilitate access, and introduce IP/ER survey techniques to the small team of students

who conducted the survey. The results of this survey need to be corroborated with results of surveys over areas of known mineralization and lithology.

### **Excavation/Trenching Across Vein Systems**

Before more extensive exploratory work is done on areas identified as potentially ore bearing but with no past record of production, e.g. the Quaker anomaly (see Section 5, Surface Gold Anomalies, for discussion) the two areas with known past production and surface showings should be analyzed for both current economic potential and to best characterize the system before stepping out into less proven exploratory targets.

In this vein, further excavation or trenching is recommended along the Mammoth and Osborn vein traces. Preliminary exposure of the Osborn vein may be accomplished by improving the old jeep trail that ascends the Osborn draw. To facilitate further work on the Osborn system this road will need to be improved regardless, the opportunity to sample and study the Osborn vein in the numerous places where it appears to be in contact with the road should not be wasted. The path of the existing jeep trail and approximate location of the Osborn vein are shown in Figure 9.4.

The high density surface geochemical survey along the trace of the Mammoth vein has successfully outlined the vein trace and highlighted zones of potential ore grade mineralization. The recommended next step is to expose the top few feet of these areas for detailed sampling and geologic study. Results of the surface geochemical surveys and suggested excavation areas are shown in Figure 9.5.

### **Timing of Mineralization**

Further geochronologic work is recommended to firmly establish the sequence and timing of events during the intrusive and mineralizing episodes of the property's evolution.

Geochronologic results from this study (see Section 4, Geochronology) indicate that mineralization within the Pearl to Horseshoe Bend mining districts may have occurred later than previously anticipated or have been the result of multiple, discrete events.

Previous work, notably by Anderson (1934; 1947), in the Boise Basin and Pearl to Horseshoe Bend mining districts indicated that mineralization occurred after the andesite and before the diabase phases of diking. Field relationships along the Trans-Challis Fault System indicate that the emplacement of dike facies associated with both occurred during the late Early to middle Eocene, 50 – 41 Ma. Because mineralized veins crosscut TCFS dikes Anderson (1947) proposed that mineralization was no older than the Eocene and possibly as young as the Miocene. A new age ( $30.44 \pm 0.02$  Ma) for the andesite phase does not rule out Eocene mineralization, but also does not require it. It is possible the mineralizing event(s) occurred much later or lasted much longer than previously thought.

Initial age results obtained from the dacite, diorite porphyry, and rhyolite dikes on the property are in agreement with the accepted timeline for Eocene TCFS/IMPB events and range from 48 to 47.5 Ma. The diorite porphyry occurred in at least two distinct pulses that bracket the dacite and rhyolite phases implying that the ubiquitous diorite porphyry mapped across the property was penecontemporaneous with at least those two

phases. The geochronology results have several explanations, each of which would impact the exploration model used to locate ore.

One, that mineralization occurred much later, ~ 15 Ma, than previously thought. Two, that there was more than one mineralizing event. Three, that there is more than one episode of andesitic dike emplacement. If mineralization occurred much later (explanation 1), the dike series associated with mineralization may need to be adjusted as well as the proposed tectonomagmatic driver. If number two is true, the implementation of multiple exploration models may be needed to account for different environments of mineralization. If three is true a careful parsing of dike lithologies will be required to distinguish Eocene andesite from Oligocene andesite. The repeated injection of mafic diorite dikes suggests that a fresh source of metals was available for at least ~2 Ma.

There is also the possibility that the initial identification of the ca. 31 Ma. dike lithology was incorrect and that the dated andesite is actually a basaltic andesite and may fall under the diabase umbrella that Anderson (1947) concluded occurred after the mineralizing event. If so, and if mineralization is bracketed by the andesite and diabase phases of diking then there may be a significant time window, ~15 Ma, for mineralization to occur.

Mineralization is most likely to occur during pulses of magmatism because the heat and fluids associated with magma bodies are the most likely to be metal rich in this area. A detailed geochemical study of vein, dike, and altered and unaltered country rock to further constrain the timing, tempo, and character of mineralization would begin to answer these questions. Initial geochemical studies could focus on establishing the isotopic character (e.g.  $\delta^{18}\text{O}$ ,  $\delta\text{D}$ , and  $^3\text{He}/^4\text{He}$ ) of fluid inclusions within the ore and

compare those to the isotopic fingerprint of each dike phase and look for characteristic patterns that may suggest one magma body over another. Additionally, Re/Os dates on arsenopyrite that hosts the gold mineralization would provide direct, though more imprecise than U/Pb on zircon, timing of mineralization. For example Morelli et al. (2007) apply these techniques to the Muruntau gold deposit in Uzbekistan.

### **Ore Characterization**

Extensive petrologic work has been done on the ores of the Pearl to Horseshoe Bend and Boise Basin Mining districts and the host rocks they are contained in (e.g. Anderson (1934), Anderson (1947), Ballard (1924), Saylor (1957)) and to a first order what has been learned before is applicable within the property boundaries as well. However, due to the unique nature of individual ore bodies, corroboratory work should be undertaken for the individual vein systems within the property. This will serve to confirm and reassess previous work as well as identify characteristics that may be unique to each system that would impact the potential exploration and exploitation methods for individual vein systems.

This work can be done as appropriate samples are collected during the course of other work in the area and need not be an individual project. As of this writing only cursory field examination of ore material exposed in dumps or as float has been completed.

### **Targets**

With the data currently available the highest priority targets for further work on the property should be the relatively well understood Osborn and Mammoth vein systems.

The ~40 acre Quaker anomaly appears to have the greatest potential among the “blind” targets and next to the Mammoth and Osborn areas the most promising area for work. The Kentuck and Payette anomalies have potential for future work and parts of their systems may be explored with work recommended for higher priority areas but the Kentuck and Payette should be considered subordinate to the Osborn, Mammoth, and Quaker areas.

Because veins are dominantly east-west striking and steeply oriented, drill holes that are low-angle and north-south would have the best chance of intersecting veins perpendicular to their orientation, with the exception of the north-south trending anomaly connecting the Payette and Quaker anomalies. The Osborne vein could best be intercepted by low-angle holes oriented to the south and drilled along where the Old Emmett Road meets the northern boundary of the property. This would have the advantage of increasing the depth of intersection with the vein system. Initial drilling at the Mammoth should be through the old dump and oriented to the north to both assess the previously mined material and to intercept the known vein at a relatively shallow depth before proceeding with longer drill holes to assess the depth of the vein. The deeper extents of the Mammoth vein may be best intersected by a series of holes drilled along the pediment surface marking the contact between the granodiorite and Payette Formation to the south of the Mammoth gully or from along the bottom of the next east-west oriented gully to the south of the Mammoth gully. A series of low-angle north oriented holes along the granodiorite-Payette Formation contact may also help to delineate the Payette claim anomaly in the southern portion of the property. The Quaker anomaly should be intersected by low-angle, south oriented holes drilled along the edge

of the river terrace outlined by the Qal and diorite contact and along the base of the flat irons where they meet the Old Emmett Road.

Where possible drilling should be done with core rigs to obtain samples of unaltered vein material as well as to be able to orient vein, dike, and fracture intersections and thus further constrain the structural model.

## SECTION 10: CONCLUSIONS

The work included here presents a conceptual model for structurally controlled mineralization in the property area and for dike swarm associated deposits along the Trans-Challis Fault System as a whole. It is proposed that mineralization is controlled by either pre- or syn-depositional fracture planes and that mineralization location can be inferred from: (1) gold anomaly signatures, (2) dike and vein trends/orientations, (3) magnetic anomaly trends, and (4) apparent resistivity, induced polarization, and metal factor signatures. Breccia pipes at the intersection of two fracture planes are classic exploratory targets. The model presented here lays out not only a geometry for these intersections but predictable, and testable, spatial patterns. The conceptual model is based on a 070° oriented dextral Riedel shear array, the 070° orientation was chosen because not only is it the overall alignment of the Trans-Challis Fault System but also because dikes within the property are oriented dominantly to the northeast.

The supporting pieces of evidence for items 1-4 are summarized below. (1) A first order assumption made within this context is that gold anomalies indicated by surface geochemical surveys are associated with, and indicative of, underlying structural and lithological controls on mineralization. Gold is a heavy and chemically stable element; therefore, when sampled at appropriate depths it is reasonable to assume that physical and chemical processes have not displaced gold too far from its source, this is validated within the literature. (2) High resolution geologic mapping completed herein confirms the general 070° trend of the dike swarm as well as internally oriented dike trends

consistent with the R<sub>1</sub> and P fracture subsets of the shear array. Mineralized vein orientations measured as part of this study and within the literature are dominated by near east-west orientations consistent with the orientation of the proposed P fracture plane. (3) The total field magnetic anomaly map accurately distinguishes lithologic units. Magnetic lineaments highlighted by the edge detection method further distinguish long, narrow lithologic units within homogenous country rock; both total field and edge detection anomalies are corroborated by close agreement with the geologic map. Hot, acidic hydrothermal fluids associated with mineralization have been proposed to destroy the magnetic signatures of host rocks; these areas are marked by either magnetic lows within homogenous host rock in total field magnetic anomaly maps and/or by the muting of continuous trends in the edge detection method. (4) Low apparent resistivity anomalies are well established in the literature as a signal of either water saturation or as a result of the presence of conductive sulfides. Likewise, high induced polarization anomalies are well established in the literature to be the result of ion-trapping clay layers or the presence of chargeable sulfides. The metal factor is a way to account for the presence of water saturation and clays as spurious signals in ore exploration and focus efforts on areas that are both conductive and chargeable. The general trend of metal factor highs aligns well with observed dike, gold anomaly, and magnetic trends.

The new geologic, geochronologic, geochemical, and geophysical datasets discussed within this text reinforce the geometry inherent in, and the implications of, the Riedel shear array model. A robust and testable mineral exploration guide is outlined by integrating these datasets and the predictable implications of the Riedel shear array conceptual model.

## REFERENCES

- Alvarez, T. J., Ojala, G.L., (1981) Pearl Project, Gem and Boise counties, Idaho. Project memorandum No. 2. 1980 exploration program. Sunshine Mining Company Exploration. Unpublished.
- Anderson, A. L. (1934). Geology of the Pearl-Horseshoe Bend gold belt, Idaho. Pamphlet - Idaho Bureau of Mines and Geology, 36.
- Anderson, A. L. (1936). Petrology of Pearl-Horseshoe Bend porphyry belt. *Pan-American Geologist*, 65(1), 78.
- Anderson, A. L. (1947). Geology and ore deposits of Boise Basin, Idaho. U.S. Geological Survey Bulletin, 119-319.
- Armstrong, R.L., Leeman, W. P., Malde, H.E. (1975). "K-Ar dating, Quaternary and Neogene volcanic rocks of the Snake River Plain, Idaho". *American journal of science* (1880) (0002-9599), 275 (3), p. 225
- Ballard, S. M., & In Piper, A. M. (1924). Geology and gold resources of Boise Basin, Boise County, Idaho. Idaho Bureau of Mines and Geology Bulletin (9), Bureau of Mines and Geology, University of Idaho.
- Benford, B., Crowley, J., Schmitz, M., Northrup, C. J., & Tikoff, B. (2010). Mesozoic magmatism and deformation in the northern Owyhee Mountains, Idaho; implications for along-zone variations for the western Idaho shear zone. *Lithosphere*, 2(2), 93-118. doi:<http://dx.doi.org/10.1130/L76.1>
- Boerner, D. E., Craven, J. A., Kurtz, R. D., Ross, G. M., & Jones, F. W. (1998). The Great Falls Tectonic Zone: Suture or intracontinental shear zone? 1. *Canadian Journal of Earth Sciences*, 35(2), 175-183

- Boyle, R. W. (1979). The geochemistry of gold and its deposits (together with a chapter on geochemical prospecting for the element). *Bulletin - Geological Survey of Canada*, (280), 584.
- Breitsprecher, K., Thorkelson, D. J., Groome, W. G., & Dostal, J. (2003). Geochemical confirmation of the Kula-Farallon slab window beneath the Pacific Northwest in Eocene time. *Geology (Boulder)*, 31(4), 351-354.
- Colgan, J. P., Dumitru, T. A., Reiners, P. W., Wooden, J. L., & Miller, E. L. (2006). Cenozoic tectonic evolution of the Basin and Range province in northwestern Nevada. *American Journal of Science*, 306(8), 616-654.
- Condon, D., Schoene, B., Bowring, S., Parrish, R., McLean, N., Noble, S., and Crowley, Q., 2007, EARTHTIME; isotopic tracers and optimized solutions for high-precision U-Pb ID-TIMS geochronology: *Eos, Transactions, American Geophysical Union*, v. 88, no. 52, Suppl., p. Abstract V41E-06.
- Cook, S. J., & Dunn, C. E. (2006). Preliminary results of the cordilleran geochemistry project; a comparative assessment of soil geochemical methods for detecting buried mineral deposits, 3Ts Au-Ag prospect (NTS 093F/03), central British Columbia. Paper - Ministry of Energy, Mines and Petroleum Resources, 237-257.
- Crook, K. A. W. (1962). Alkali-feldspars from the Crowsnest Volcanics, Alberta. *The Canadian Mineralogist*, 7, Part 2, 253-263.
- Davydov, V. I., Crowley, J. L., Schmitz, M. D., and Poletaev, V. I., 2010, High-precision U-Pb zircon age calibration of the global Carboniferous time scale and Milankovitch-band cyclicity in the Donets Basin, eastern Ukraine: *Geochemistry, Geophysics, Geosystems*, 10.1029/2009GC002736.
- Dickinson, W. R. (2004). Evolution of the North American cordillera. *Annual Review of Earth and Planetary Sciences*, 32, 13-45.
- Dostal, J., Church, B. N., Reynolds, P. H., & Hopkinson, L. (2001). Eocene volcanism in the Buck Creek Basin, central British Columbia (Canada); transition from arc to extensional volcanism. *Journal of Volcanology and Geothermal Research*, 107(1-3), 149-170. doi:[http://dx.doi.org/10.1016/S0377-0273\(00\)00261-4](http://dx.doi.org/10.1016/S0377-0273(00)00261-4)

- Dostal, J., Breitsprecher, K., Church, B. N., Thorkelson, D. J., & Hamilton, T. S. (2003). Eocene analcime-bearing volcanic rocks from the Challis-Kamloops belt of south central British Columbia; geochemistry and tectonic implications. *Abstracts with Programs - Geological Society of America*, 35(4), 7.
- Dudas, F. O. (1991). Geochemistry of igneous rocks from the Crazy Mountains, Montana, and tectonic models for the Montana Alkalic Province. *Journal of Geophysical Research*, 96, 13-13,277. doi:<http://dx.doi.org/10.1029/91JB00246>
- Ekren, E. B., McIntyre, D. H., Bennett, E. H., & Malde, H. E. (1981). Geologic map of Owyhee County, Idaho, west of longitude 116 degrees U. S. Geological Survey, Reston, VA.
- Ewing, T. E. (1980). Paleogene tectonic evolution of the Pacific Northwest. *Journal of Geology*, 88(6), 619-638.
- Feeney, D. Lewis, R., Isakson, V., & Schmitz, M. (2016) Refined stratigraphy of the Weiser embayment, west-central Idaho. Abstract. Geological Society of America, Rocky Mountain Section Annual Meeting. Session 13. Cenozoic Volcanism in the Inland Northwestern United States.
- Gaschnig, R. M., Vervoort, J. D., Lewis, R. S., King, E., & Valley, J. W. (2007). Multiple punctuated pulses of voluminous silicic magmatism in Idaho; in situ geochronology and isotope geochemistry of the Idaho Batholith. *Abstracts with Programs - Geological Society of America*, 39(6), 608.
- Gaschnig, R. M., Vervoort, J. D., Lewis, R. S., & Tikoff, B. (2011). Isotopic evolution of the Idaho Batholith and Challis Intrusive Province, northern US Cordillera. *Journal of Petrology*, 52(12), 2397-2429. doi:<http://dx.doi.org/10.1093/petrology/egr050>
- Giorgis, S., McClelland, W., Fayon, A., Singer, B., and Tikoff, B., 2008, Timing of deformation and exhumation in the western Idaho shear zone, McCall, Idaho: *Geological Society of America Bulletin*, v. 120, p. 1119–1133, doi: 10.1130/B26291.1.

- Hamilton, W.R., 1963, Metamorphism in the Riggins Region, Western Idaho: U.S. Geological Survey Professional Paper 436, 95 p.
- Jaffey, A.H., Flynn, K.F., Glendenin, L.E., Bentley, W.C., and Essling, A.M., 1971, Precision measurements of half-lives and specific activities of <sup>235</sup>U and <sup>238</sup>U: *Physical Review C*, 4:1889-1906.
- Janecke, S. U. (1992), Kinematics and timing of three superposed extensional systems, east central Idaho: Evidence for an Eocene tectonic transition, *Tectonics*, 11(6),1121–1138, doi:10.1029/92TC00334
- Janecke, S. U., Hammond, B. F., Snee, L. W., & Geissman, J. W. (1997). Rapid extension in an Eocene volcanic arc; structure and paleogeography of an intra-arc half graben in central Idaho. *Geological Society of America Bulletin*, 109(3), 253-267.
- Kiilsgaard, T. H., & Bennett, E. H. (1985). Mineral deposits in the southern part of the Atlanta lobe of the Idaho Batholith and their genetic relation to tertiary intrusive rocks and to faults. *U.S. Geological Survey Bulletin*, 153-165.
- Kiilsgaard, T. H., Fisher, F. S., & Bennett, E. H. (1986). The trans-Challis fault system and associated precious metal deposits, Idaho. *Economic Geology and the Bulletin of the Society of Economic Geologists*, 81(3), 721-724.
- LaFranchi, S. E., Baum, L. F., & Sprenke, K. F. (1985). Geological, geophysical, and geochemical techniques for locating buried placer deposits in the Boise Basin, Idaho. *Abstracts with Programs - Geological Society of America*, 17(4), 250.
- Leppert, D. E., & Gillerman, V. S. (2004). Structural preservation of gold deposits; northwest-trending faults in the Boise Basin. *Abstracts with Programs - Geological Society of America*, 36(4), 4.
- Leppert, D. E., & Gillerman, V. S. (2009). Site inspection report for abandoned and inactive mines on land administered by the U.S. Bureau of Land Management in the Boise Resource Area, Idaho; Ada County, and Osborne Mine, Gem County. Staff Report - Idaho Geological Survey, 184.

- Lewis, R.S., Link, P.K., Loudon, R.S., Long, S.P. (2012) Geologic Map of Idaho. Idaho Geological Survey. Geologic map 9.
- Lindgren, W. (1898). Part 3; the mining district of the Idaho Basin and the Boise Ridge, Idaho. United States Geological Survey Annual Report, 18, Part 3, 617-719.
- Logan, J. M., Friedman, M., Higgs, N., Dengo, C., Shimamoto, T. (1979). Experimental studies of simulated gouge and their application to studies of natural fault zones. Open-File Report - U.S. Geological Survey, 305-343.
- Lund, K., 1988, The Salmon River suture, western Idaho: An island arc-continent boundary, in Link, P.K., and Hackett, W.R., eds., Guidebook to the Geology of Central and Southern Idaho: Idaho Geological Survey Bulletin 27, p. 99–107.
- MacLachlan, K., Davis, W. J., & Relf, C. (2005). U/Pb geochronological constraints on Neoproterozoic tectonism: Multiple compressional events in the northwestern Hearne domain, western Churchill Province, Canada. *Canadian Journal of Earth Sciences*, 42(1), 85-109.
- Marshall, D. J., and T. R. Madden, 1959, Induced polarization: A study of its causes: *Geophysics*, 24, 790–816
- Mattinson, J.M., 2005, Zircon U-Pb chemical abrasion ("CA-TIMS") method: combined annealing and multi-step partial dissolution analysis for improved precision and accuracy of zircon ages: *Chemical Geology* 220:47-66.
- McCarthy, J. H., & Kiilsgaard, T. H. (2001). Soil gas studies along the Trans-Challis Fault System near Idaho City, Boise County, Idaho. *U.S. Geological Survey Bulletin*, 12.
- McClelland, W.C., Tikoff, B., and Manduca, C.A., 2000, Two phase evolution of accretionary margins: Examples from the North American Cordillera: *Tectonophysics*, v. 326, p. 37–55, doi: 10.1016/S0040-1951(00)00145-1.
- Mogk, D.W., Mueller, P.A., and Wooden, J.L. (1992) The significance of Archean terrane boundaries: evidence from the northern Wyoming Province. *Precambrian Research*, 55: 155-168.

- Morelli, R., Creaser, R. A., Seltnann, R., Stuart, F. M., Selby, D., & Graupner, T. (2007). Age and source constraints for the giant Muruntau gold deposit, Uzbekistan, from coupled re-os-he isotopes in arsenopyrite. *Geology (Boulder)*, 35(9), 795-798. doi:<http://dx.doi.org/10.1130/G23521A.1>
- Morris, G. A., Larson, P. B., & Hooper, P. R. (2000). "Subduction style" magmatism in a non-subduction setting; the Colville Igneous Complex, NE Washington state, USA. *Journal of Petrology*, 41(1), 43-67. doi:<http://dx.doi.org/10.1093/petrology/41.1.43>
- Moye, F. J., Hackett, W. R., Blakley, J. D., & Snider, L. G. (1988). In Link P. K., Hackett W. R. (Eds.), *Regional geologic setting and volcanic stratigraphy of the Challis Volcanic Field, central Idaho* Idaho Geol. Surv., Moscow, ID.
- Mücke, A. and Cabral, A.R. (2005) Redox and nonredox reactions of magnetite and hematite in rocks. *Chemie der Erde*, 65, (271-278).
- Mueller, P. A., & Frost, C. D. (2006). The Wyoming province: A distinctive Archean craton in Laurentian North America. *Canadian Journal of Earth Sciences*, 43(10), 1391-1397.
- O'Neill, J. M., & Lopez, D. A. (1985). Character and regional significance of Great Falls tectonic zone, east-central Idaho and west-central Montana. *AAPG Bulletin*, 69(3), 437-447.
- Pierce, K. I., Morgan, L. A., (1992). "The track of the Yellowstone hot spot; volcanism, faulting, and uplift". *Memoirs - Geological Society of America* (0072-1069), 179, p. 1.
- Ridley, J. (2013) *Ore Deposit Geology*. p. 164-183. Cambridge University Press.
- Ross, C. P. (1933). "The lode deposits in the Boise Basin, Idaho". *Economic geology and the bulletin of the Society of Economic Geologists* (0361-0128), 28 (4), p. 329.
- Rowland, J. V., & Simmons, S. F. (2012). Hydrologic, magmatic, and tectonic controls on hydrothermal flow, Taupo volcanic zone, New Zealand; implications for the formation of epithermal vein deposits. *Economic Geology and the Bulletin of the*

Society of Economic Geologists, 107(3), 427-457.

doi:<http://dx.doi.org/10.2113/econgeo.107.3.427>

- Sanford, R. F., & Snee, L. W. (2005). Geology and stratigraphy of the Challis Volcanic Group and related rocks, Little Wood River area, south-central Idaho, with a section on geochronology. *U.S. Geological Survey Bulletin*, 22.
- Saylor, T. E. (1967) The geology of the Pearl-Pioneerville area, Idaho. Published master's thesis. Western Reserve University. Cleveland, Ohio.
- Schleiffarth, W. K., & Larson, P. B. (2013). Petrogenesis of Challis Volcanic Group, east-central Idaho. *American Geophysical Union Fall Meeting, 2013*, Abstract V51C-2679.
- Schmitz, M.D., Davydov, V.I., 2012, Quantitative radiometric and biostratigraphic calibration of the global Pennsylvanian – Early Permian time scale: Geological Society of America Bulletin, 124:549-577.
- Schmitz, M.D., Schoene, B., 2007, Derivation of isotope ratios, errors and error correlations for U-Pb geochronology using  $^{205}\text{Pb}$ - $^{235}\text{U}$ -( $^{233}\text{U}$ )-spiked isotope dilution thermal ionization mass spectrometric data: Geochemistry, Geophysics, Geosystems doi:10.1029/2006GC00149.
- Simonsen, S.W. (1997)  $^{40}\text{Ar}/^{39}\text{Ar}$  ages of Eocene dikes and the age of extension in a Tertiary magmatic arc, Idaho and Montana. Published master's thesis. University of Montana. Missoula, Montana.
- Sláma, J., Košler, J, Condon, D.J., Crowley, J.L., Gerdes, A., Hanchar, J.M., Horstwood, M.S.A., Morris, G.A., Nasdala, L., Norberg, N., Schaltegger, U., Schoene, B. Tubrett, M.N, Whitehouse, M.J. 2008. Plešovice zircon — A new natural reference material for U–Pb and Hf isotopic microanalysis. *Chemical Geology*, 249: 1-35.
- Snyder, W. S., Dickinson, W. R., & Silberman, M. L. (1976). Tectonic implications of space-time patterns of Cenozoic magmatism in the western United States. *Earth and Planetary Science Letters*, 32(1), 91-106.

- Taylor, C. D., Winick, J. A., Unruh, D. M., & Kunk, M. J. (2007). Geochronology and geochemistry of the Idaho-Montana Porphyry Belt. *U.S. Geological Survey Circular*, 26-39.
- Tilling, R. I., Klepper, M. R., & Obradovich, J. D. (1968). K-Ar ages and time span of emplacement of the Boulder Batholith, Montana. *American Journal of Science*, 266(8), 671-689.
- Wells, M. L., Snee, L. W., & Blythe, A. E. (2000). Dating of major normal fault systems using thermochronology; an example from the Raft River detachment, Basin and Range, western United States. *Journal of Geophysical Research*, 105, 16-16-327. doi:<http://dx.doi.org/10.1029/2000JB900094>
- Sláma, J., Košler, J., Condon, D.J., Crowley, J.L., Gerdes, A., Hanchar, J.M., Horstwood, M.S.A., Morris, G.A., Nasdala, L., Norberg, N., Schaltegger, U., Schoene, B., Tubrett, M.N., Whitehouse, M.J. 2008. Plešovice zircon — A new natural reference material for U–Pb and Hf isotopic microanalysis. *Chemical Geology*, 249: 1-35.

## TABLES

**Table 4.1. Dike U/Pb**

<b>Lithology</b>	<b>ICPMS age (Ma.)</b>	<b>error (2<math>\sigma</math>) Ma.</b>
Andesite Dike	31.15	0.83
Diorite Porphyry Dike	47.37	0.68
Rhyolite Porphyry Dike	47.83	0.56
Dacite Porphyry Dike	48.65	0.78
Diorite Porphyry Dike	49.39	0.7

**Table 5.1. ALS Global geochemical methods.**

Short Description	Fire Assay Fusion, *AAS Finish	Determination of trace level gold by solvent extraction	Fire Assay Fusion ***ICP-AES Finish	Precious Metal Gravimetric Analysis	Ultra trace level methods using **ICP-MS and ICP-AES
Decomposition	Fire Assay Fusion	Aqua Regia	Fire Assay Fusion	Fire Assay Fusion	Aqua Regia
Analytical Method	AAS	ICP-MS or AAS	ICP-AES	Gravimetric	ICP-AES or ICP-MS
Element(s)	Gold	Gold	Gold	Gold	60 elements
Sample Weight (g)	30	25	30	30	N/A
Lower Limit (ppb)	5	1	1	5	.005-10
Upper Limit (ppb)	10,000	1,000	10,000	1,000,000	10-10,000
Default Overlimit Method	Au-GRA21	Au-OG43/44	Au-AA25	N/A	N/A

**Table 9.1. Proposed sampling areas, including acreage, and approximate number of samples required to sample at 25' (8m) density.**

<b>Anomaly</b>	<b>~sq. m</b>	<b>sq. feet</b>	<b>~acreage</b>	<b># of samples</b>
Mammoth*	26000	279861	6	93
Osborn	45000	484376	11	161
Quaker	165000	1776044	41	589
Payette	176000	1894446	43	629
Kentuck	130000	1399307	32	464
Mammoth East	83000	893404	21	296
Mammoth West	83000	893404	21	296
Total	708000	7620841	175	2529

*\*indicates sampling program already completed*

## FIGURES

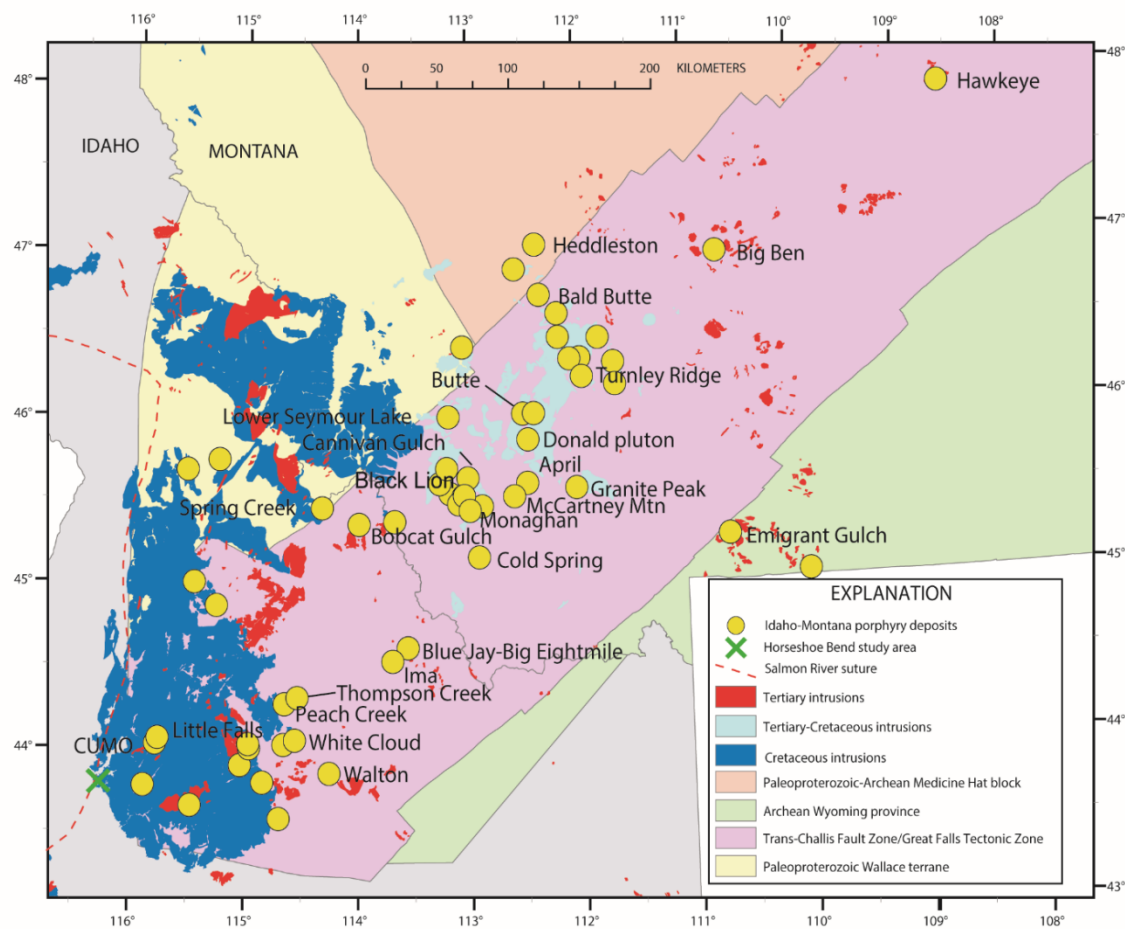


**Figure 1.1. Porphyry copper-molybdenum and molybdenum deposits of the Idaho-Montana Porphyry Belt. Dashed red line, Salmon River suture. From Taylor et al., 2007.**

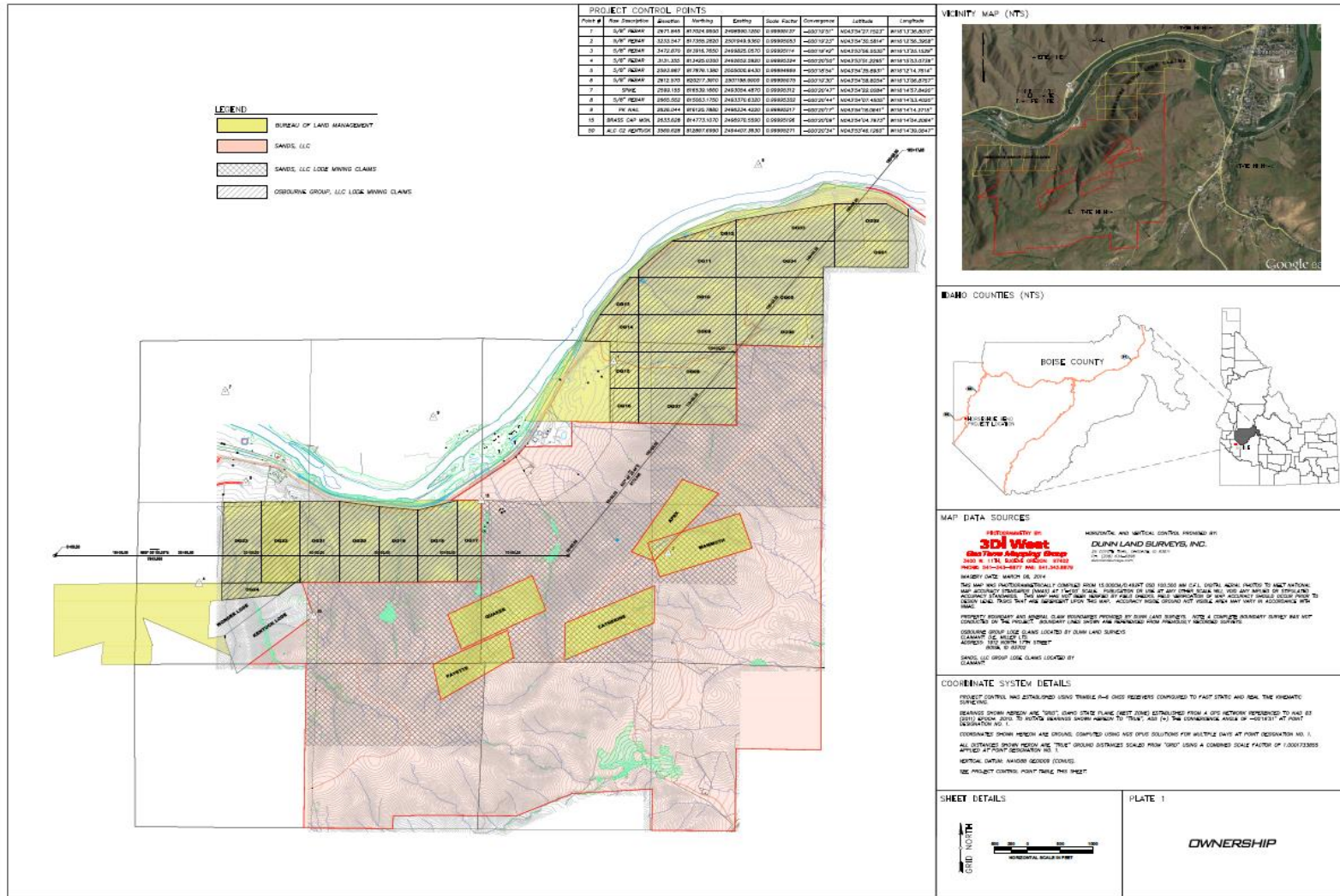
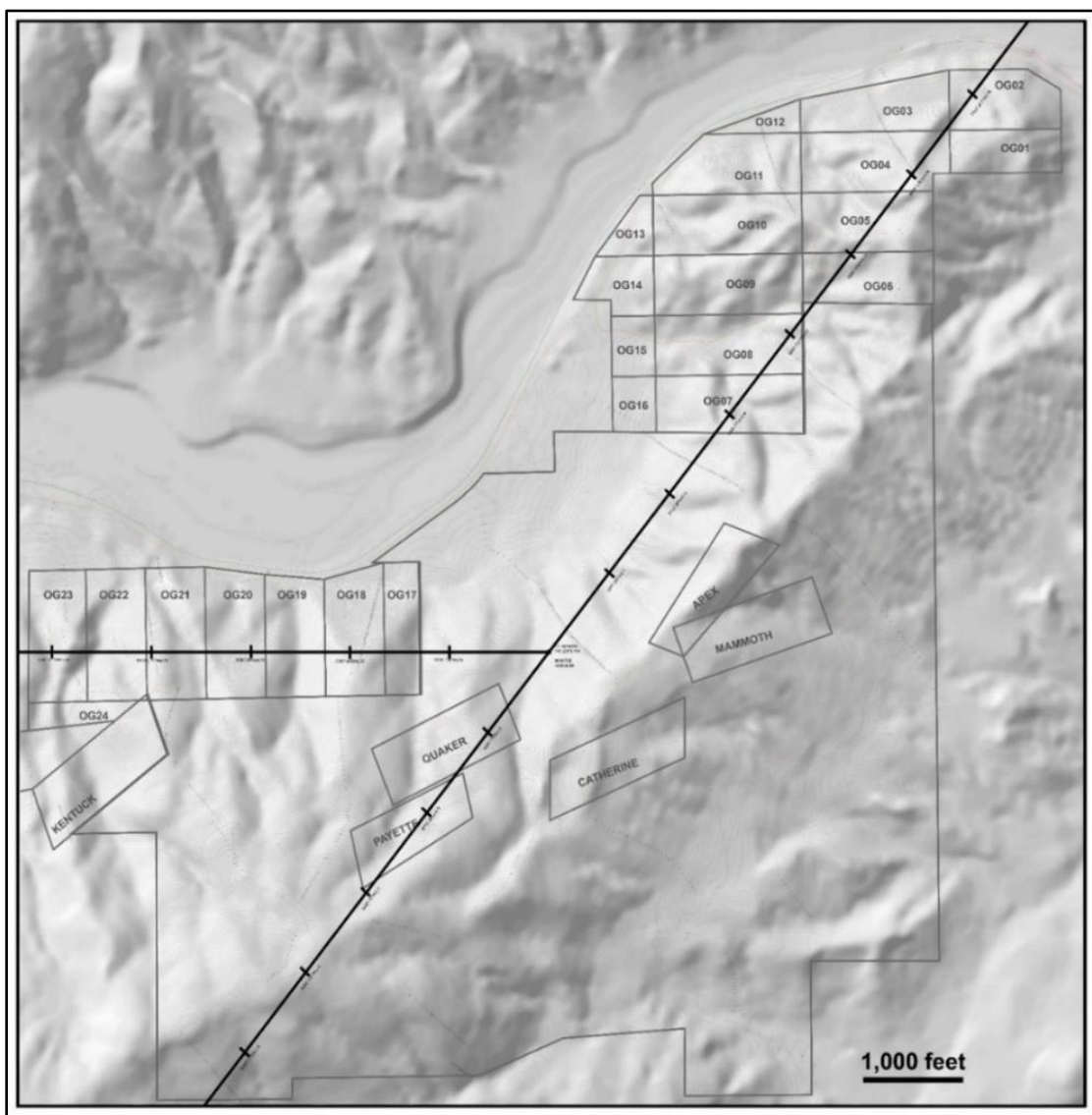
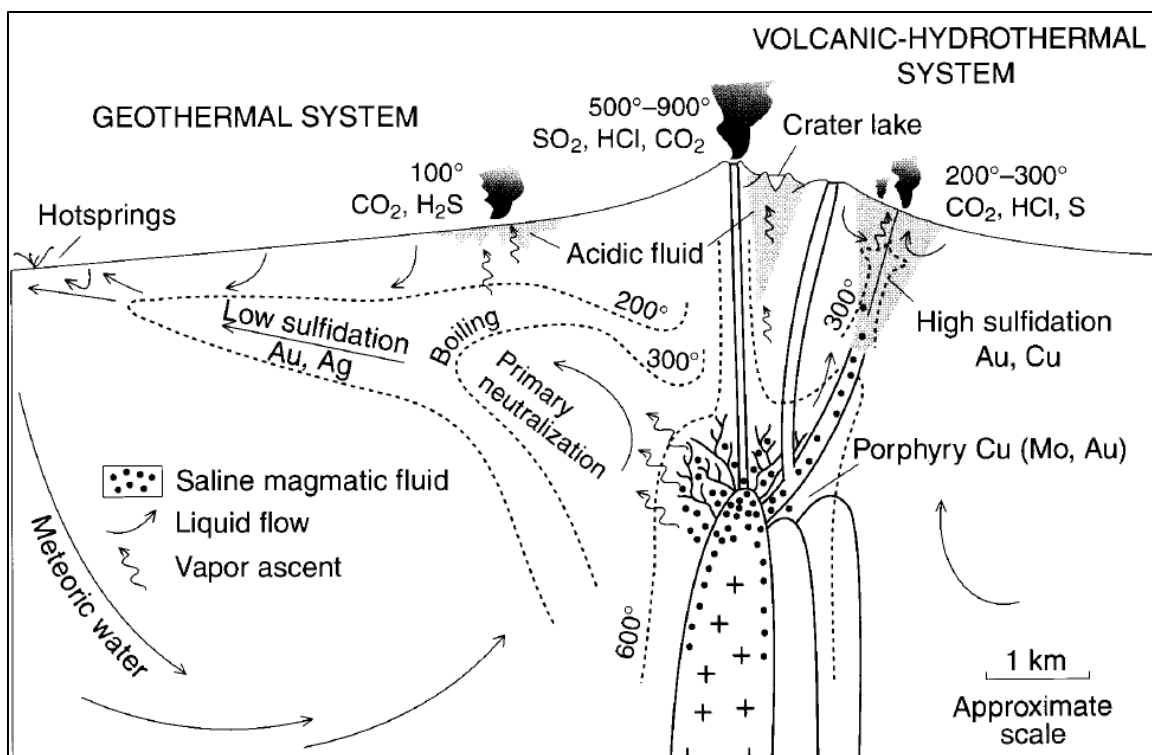


Figure 1.2. Location and ownership map of Trans-Challis property.



**Figure 1.3. Map of Trans-Challis, LLC property 1 mile (1.5km) west of Horseshoe Bend, Idaho. Thick black lines are reference baselines. Baseline intersection is approximate centroid of property.**



**Figure 1.4.** Schematic representation of hydrothermal mineral deposits and relative position in volcanic systems. Not all systems are suggested to be present at once. Note the position of the low sulfidation system and its interaction with meteoric water. From Hedenquist et al., 2000.

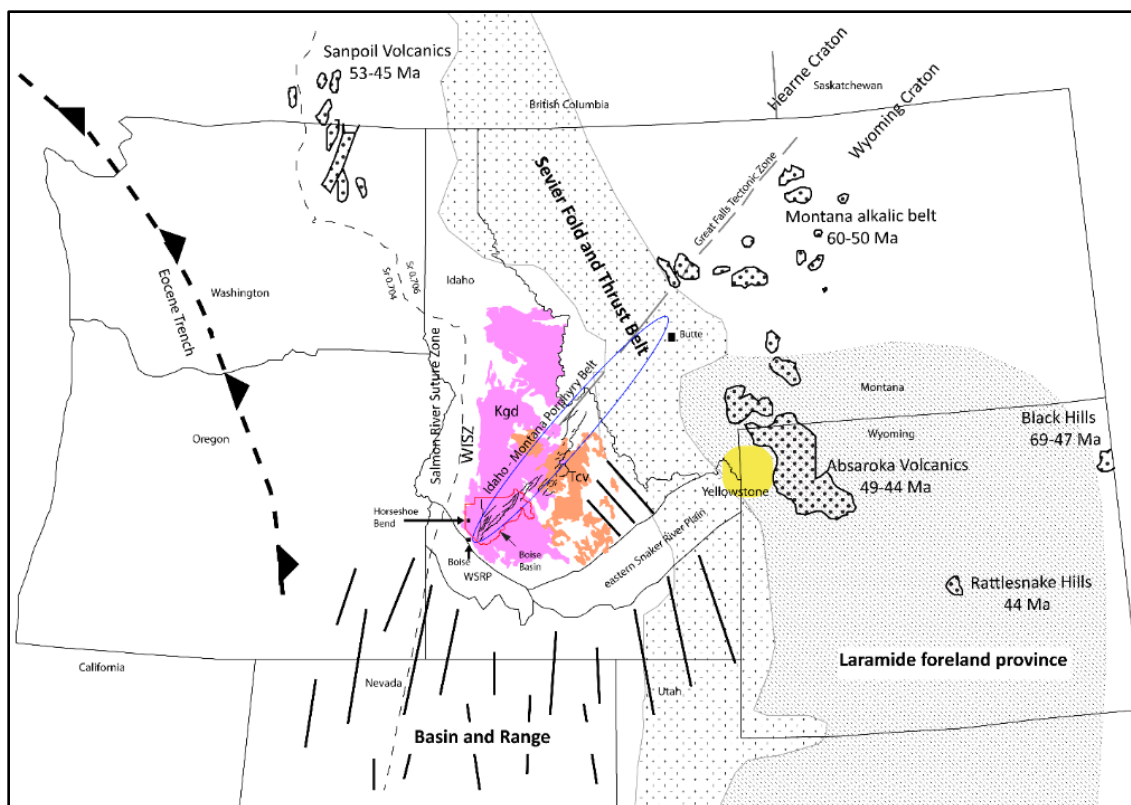


**Figure 2.1. Tectonic and magmatic elements discussed in text. Abbreviations and symbols as follows: pink polygon, Idaho Batholith; orange polygon, Challis Volcanics; yellow circle, Yellowstone caldera; red polygon, Boise County; WSRP, western Snake River Plain; WISZ, Western Idaho Shear Zone; Kgd, Cretaceous granodiorite of the Idaho Batholith; Tcv, Eocene Challis Volcanics. Adapted from Ickert et al., 2007; Moye et al., 1988; Taylor et al., 2007.**

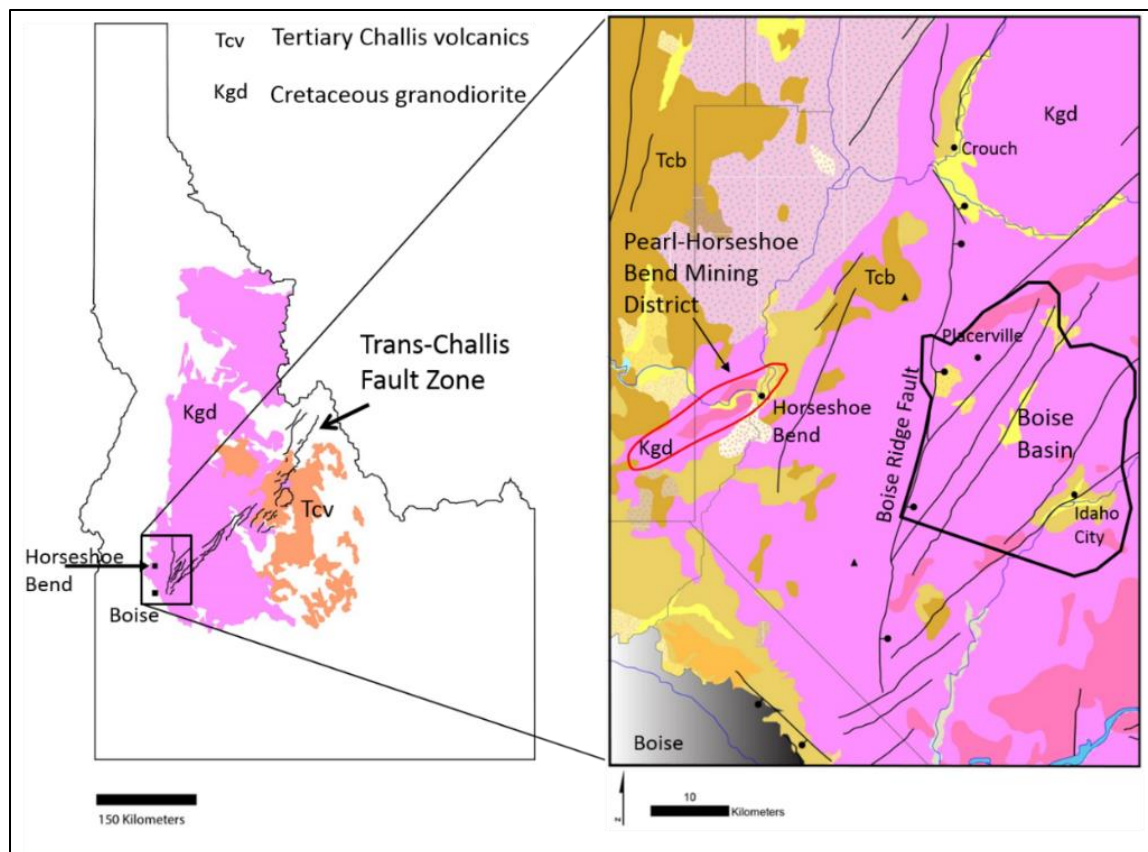


**Figure 2.2. Regional and local geology of the Horseshoe Bend Mining District. The district is located at the SW extent of the Trans-Challis Fault Zone and Idaho Porphyry Belt, which are marked by the NE trending faults on both maps. The inset shows the extent of the Pearl to Horseshoe Bend Mining districts as well as those of the Boise Basin. Kgd – Cretaceous granodiorite, Tcv – Tertiary Challis volcanics, Tcb – Tertiary Columbia River Basalts. Modified from Anderson, 1947; Kiilsgaard and Bennett, 1986; Lewis et al., 2012.**

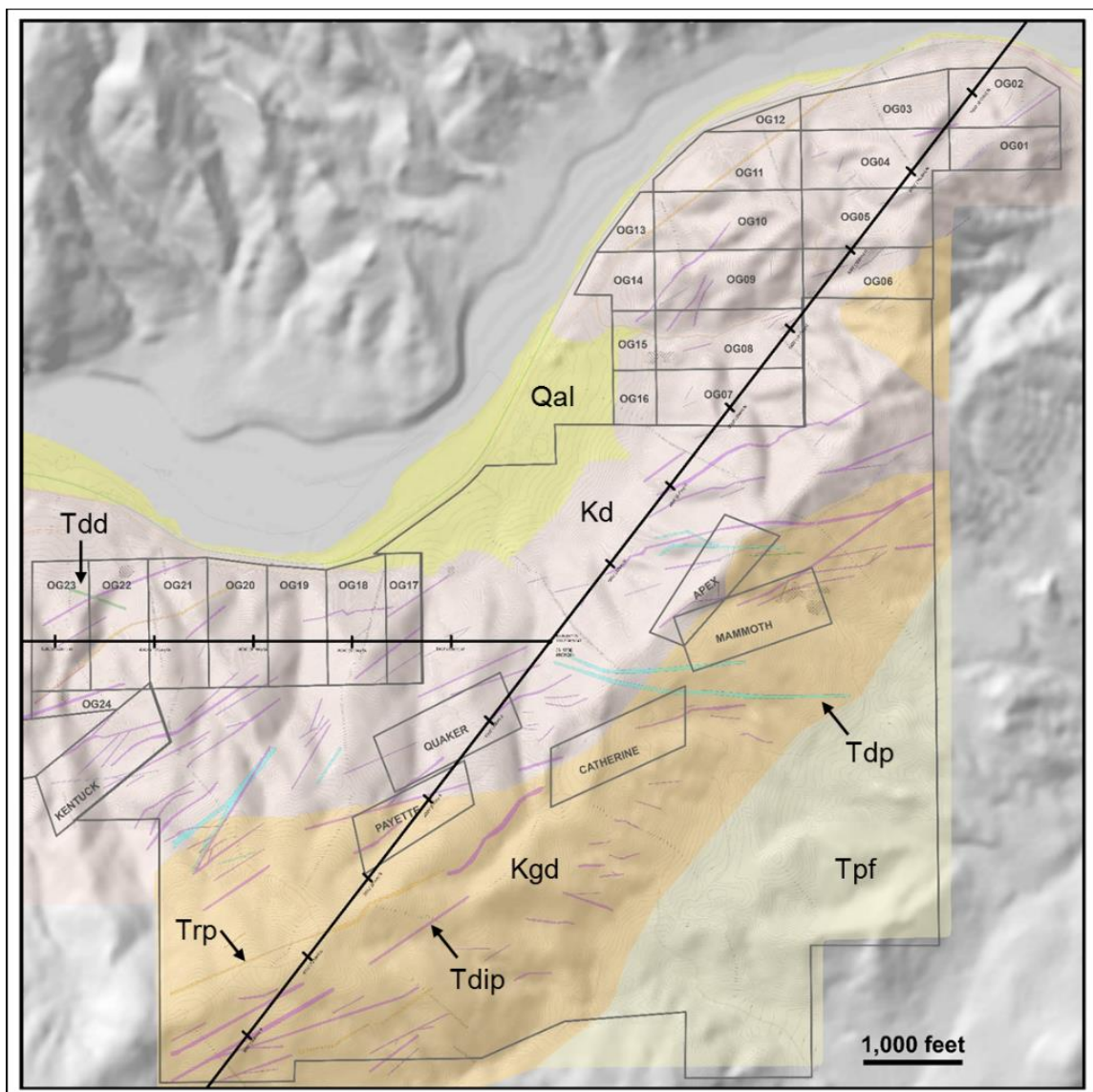


**Figure 2.3. Simplified geologic map of study area. Abbreviations: Kgd – Cretaceous granodiorite; Kd – Cretaceous diorite; Tdip – Eocene diorite porphyry; Tdp – Eocene dacite porphyry; Trp – Eocene rhyolite; Tad – Oligocene Andesite; Tdd – Miocene basalt/diabase; Tpf – Miocene Payette Formation; Qal – Quaternary alluvium.**



**Figure 2.4.** Concentrated node of mineralization (indicated by red circle) at the intersection of two fracture planes.

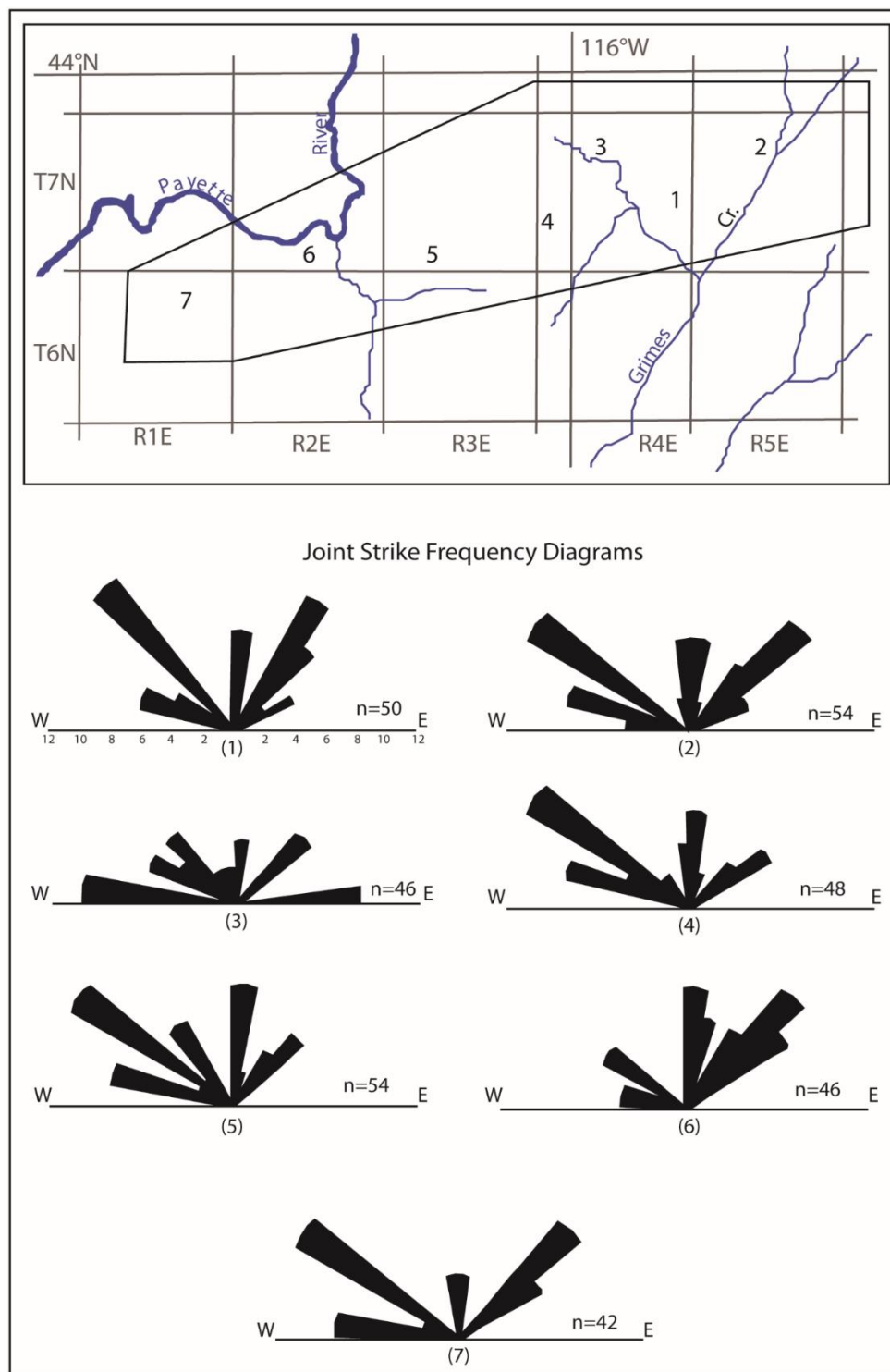


**Figure 3.1. Joint strike frequency diagram from Saylor (1967). All joint sets are measured in units comprising the Idaho Batholith. Note that orientations are dominantly northeast and northwest, except in section 6. The property is within section 6 and is the only section that contains the Cretaceous diorite unit. Joint orientations here are north-south or northeast.**

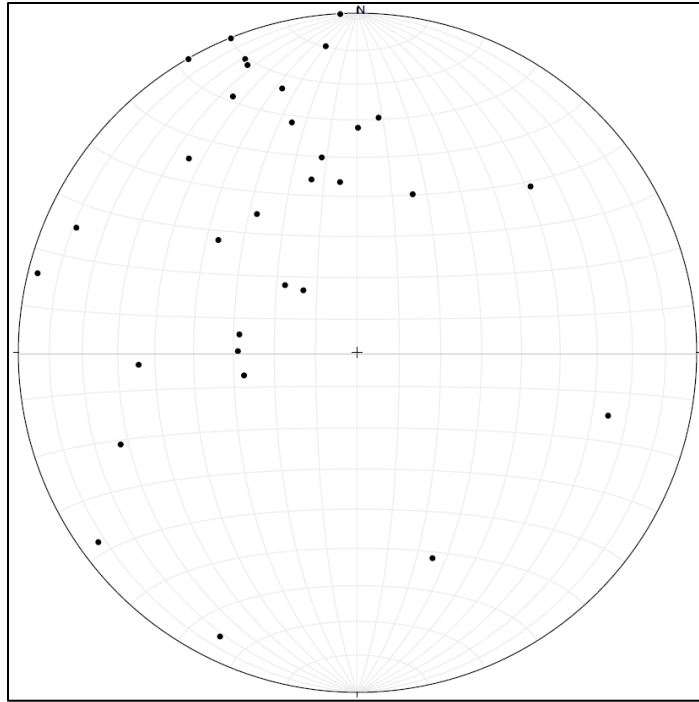


**Figure 3.2.** Stereonet showing the poles to planes of measured movement planes (slickensides). The majority of points indicate northeast to east-west trending fractures, a potentially significant set of points indicate a conjugate subset of north trending fractures.

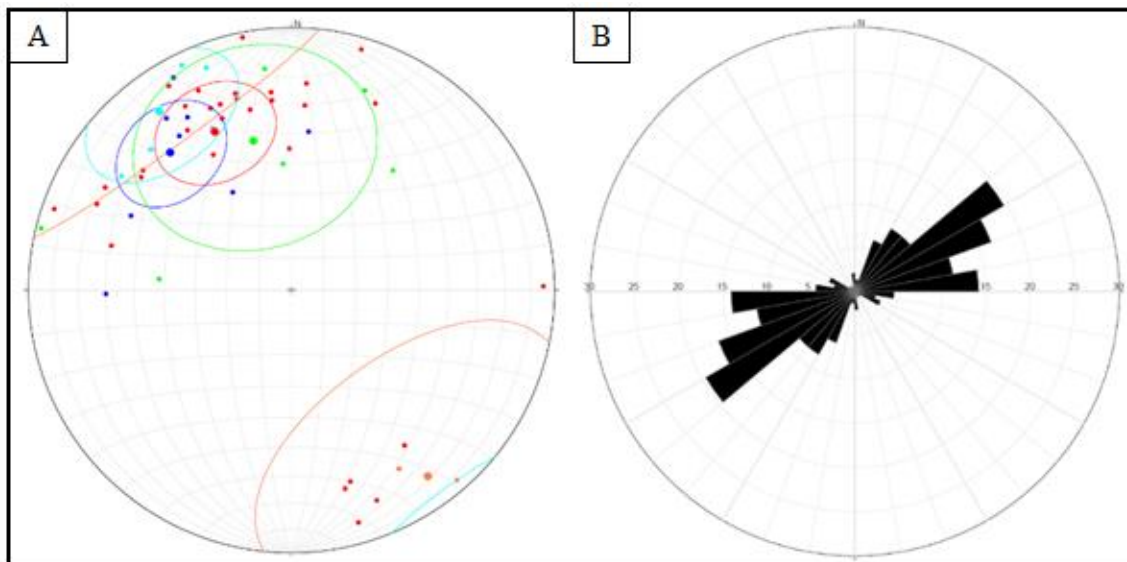


**Figure 3.3. A: Stereonet showing poles to planes of dike strikes and dips measured as part of this study as small filled circles. A strong trend of northeast oriented dikes is apparent in the data. Mean vector orientations are the larger filled circles, error on the mean shown as large unfilled ellipses. Red: diorite porphyry dikes, blue: andesite dikes, green: diabase dikes, light blue: dacite dikes, orange: rhyolite dikes. B: Rose diagram showing the orientation measurements of dikes where a reliable dip measurement was unavailable. The large majority of dikes are oriented between 50 and 70 degrees. Dikes are not divided by lithology in the rose diagram.**

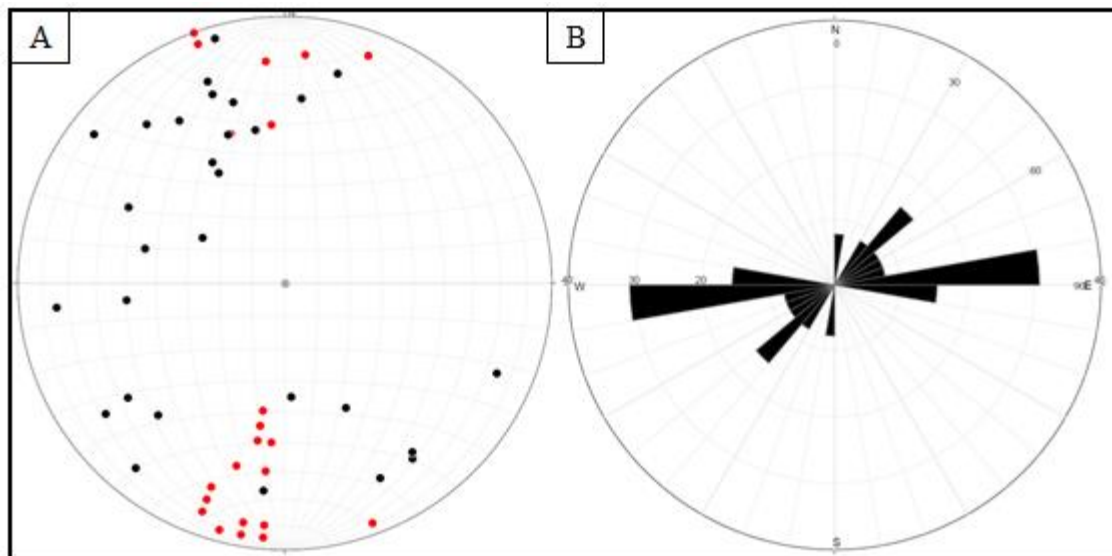


**Figure 3.4. A: Stereonet showing the pole to planes of measured vein strike and dips. The underground data from Anderson (1934) includes workings across the breadth of the Pearl to horseshoe Bend districts and is plotted in red, surface data from this study is plotted in black. Circled in blue are poles that represent east-west vein orientations. B: Rose diagram showing the orientation of veins from this study where dip was unable to be determined.**

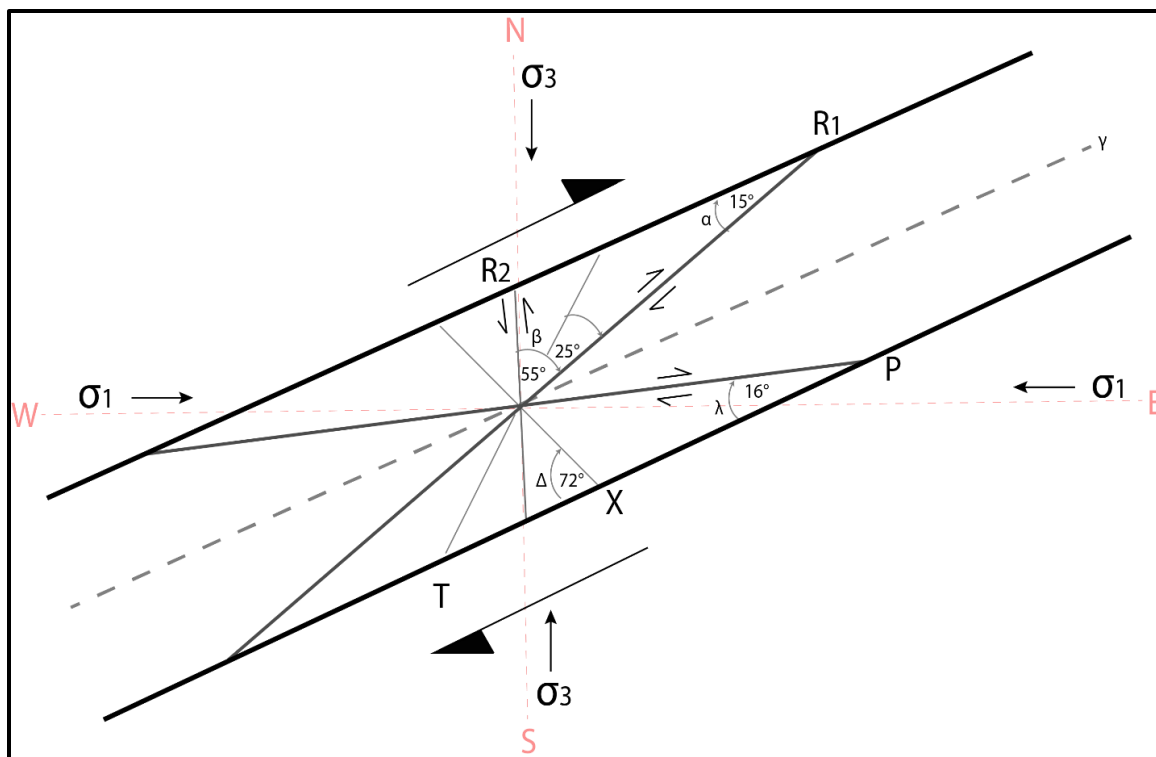


**Figure 3.5. Riedel shear array, shown with a right-lateral or dextral sense of shear and oriented to the overall trend of the Trans-Challis Fault Zone, ~N70E. The Riedel shear array is an empirically derived prediction of fracture orientations in a pure strike-slip environment. Thick black lines are the primary planes of movement in a strike-slip fault. Thinner, gray lines are predicted orientations of the fractures accommodating movement. Lines P and R<sub>1</sub> are primary fractures and have the same sense of shear as the strike-slip fault. Line R<sub>2</sub> is a secondary fracture plane, conjugate to P and with opposite sense of movement. Lines T and X are tertiary fracture planes. Greek letters  $\alpha$ ,  $\beta$ ,  $\lambda$ , and  $\Delta$  are angles with predictable magnitudes, which are given within the angle arc. The principal direction of stress is shown as  $\sigma_1$ , the direction of least stress is shown by  $\sigma_3$ . Cardinal directions are in pink.**

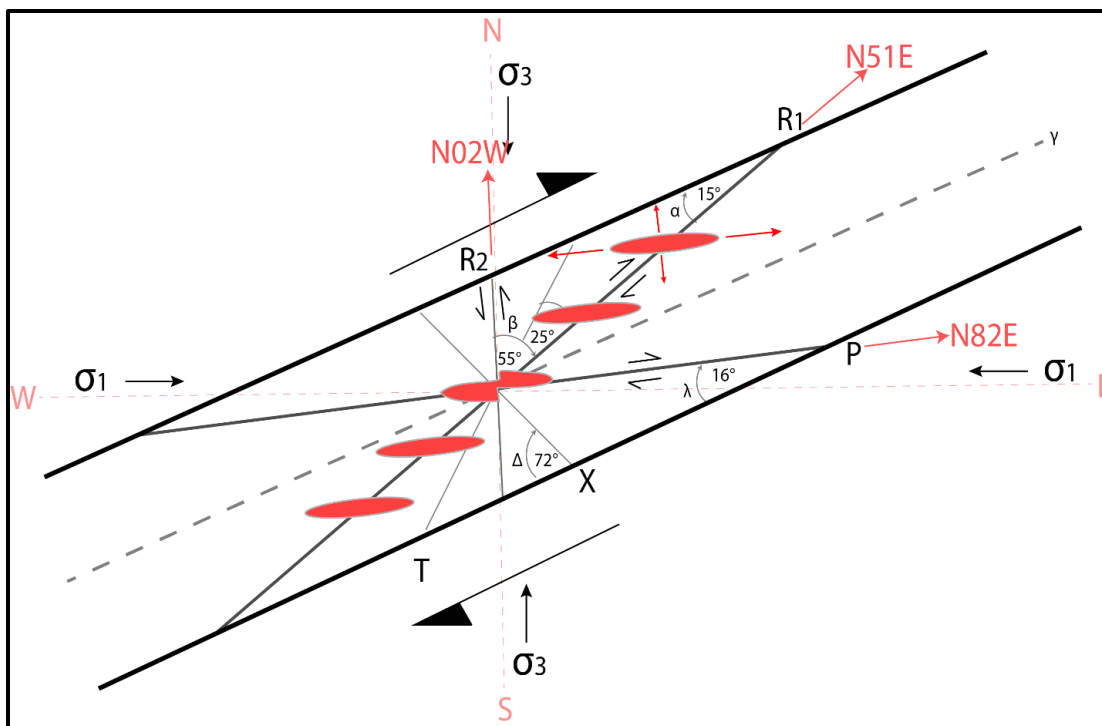


**Figure 3.6.** Riedel shear array of fig. 3.5 with an added trans-tensional component. Ore bodies will dilate in the direction of least stress,  $\sigma_3$ , shown north to south here, and elongate in the direction of maximum stress,  $\sigma_1$ , shown here as east to west and roughly parallel with fracture set P. The R1 fracture set is oriented N51E, similar to the general trend of dikes, ore bodies are hypothesized to follow this same trend. Where the N02W oriented R2 fracture set intersects the ore bodies and the dikes that guide mineralization the ore fluids may penetrate and cross the dike as illustrated in the center of the figure.

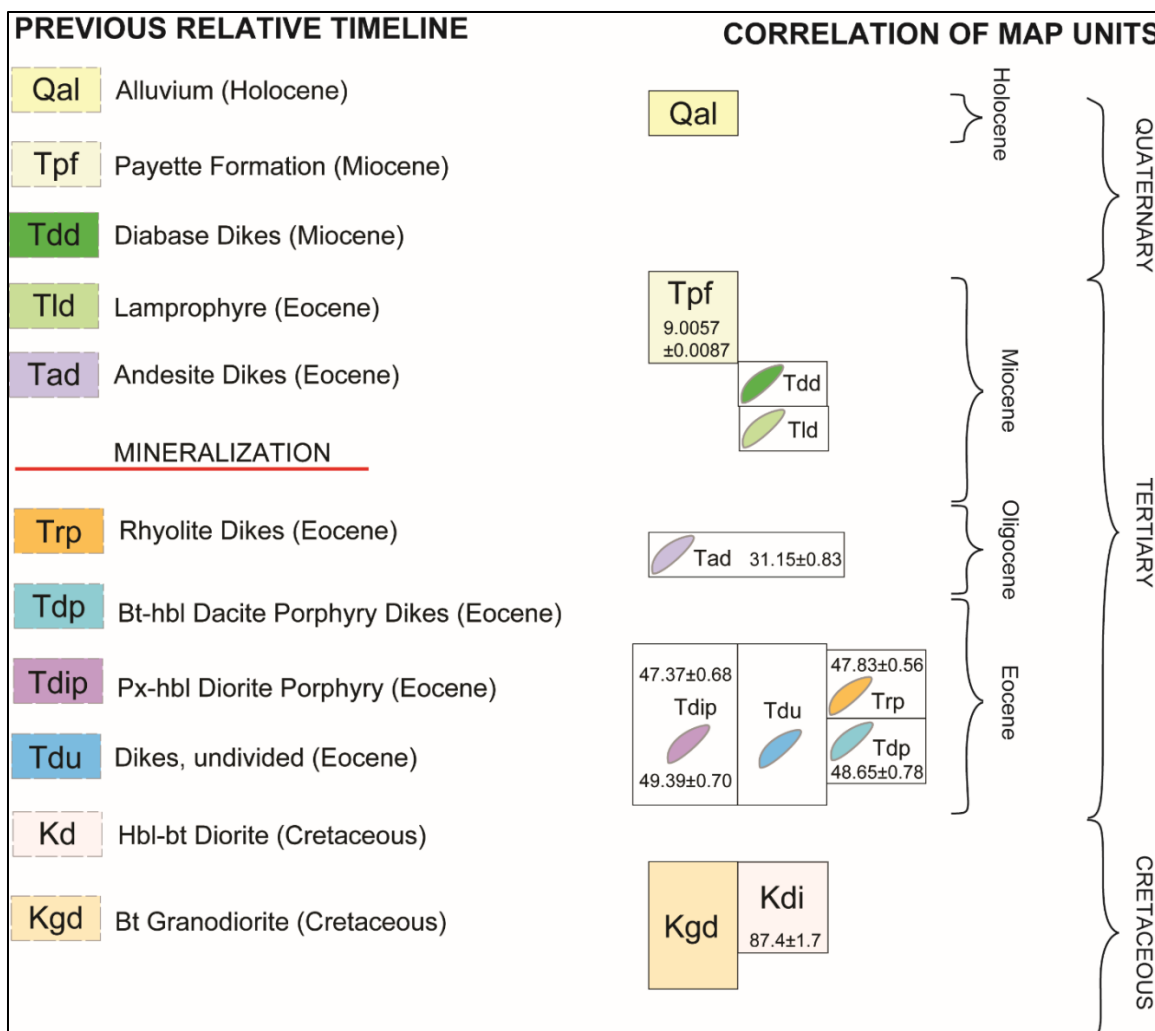


**Figure 4.1. Summary of relative (from Anderson, 1947) and absolute timelines. All ages given in millions of years (Ma) and errors are reported to  $2\sigma$ . Absolute ages for Cretaceous diorite, Kd, from Gaschnig (pers. comm. 2016) and for the Payette Formation, Tpf, from Feeney et al. (2016).**

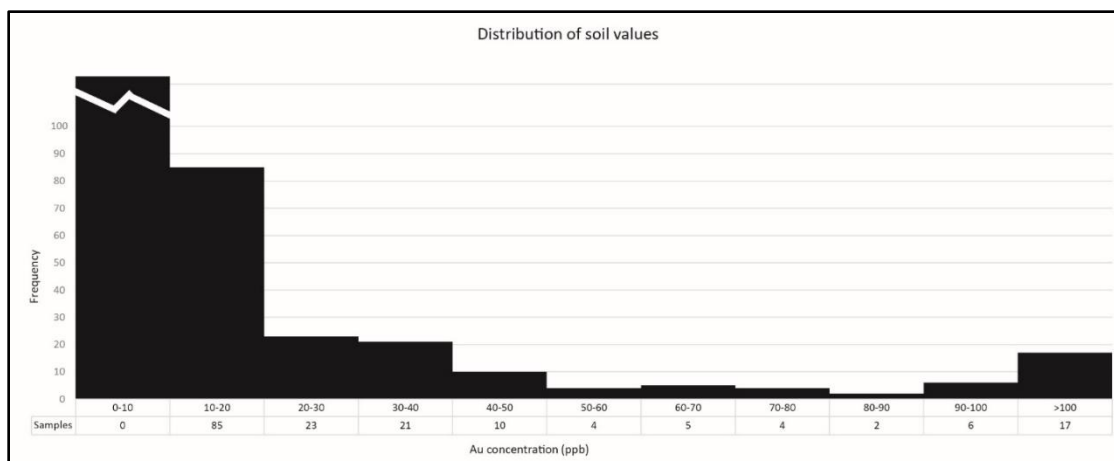


**Figure 5.1. Histogram of surface gold concentrations. 467 samples are represented in the 0-10ppb bin. Samples with gold concentrations >100ppb are binned together.**

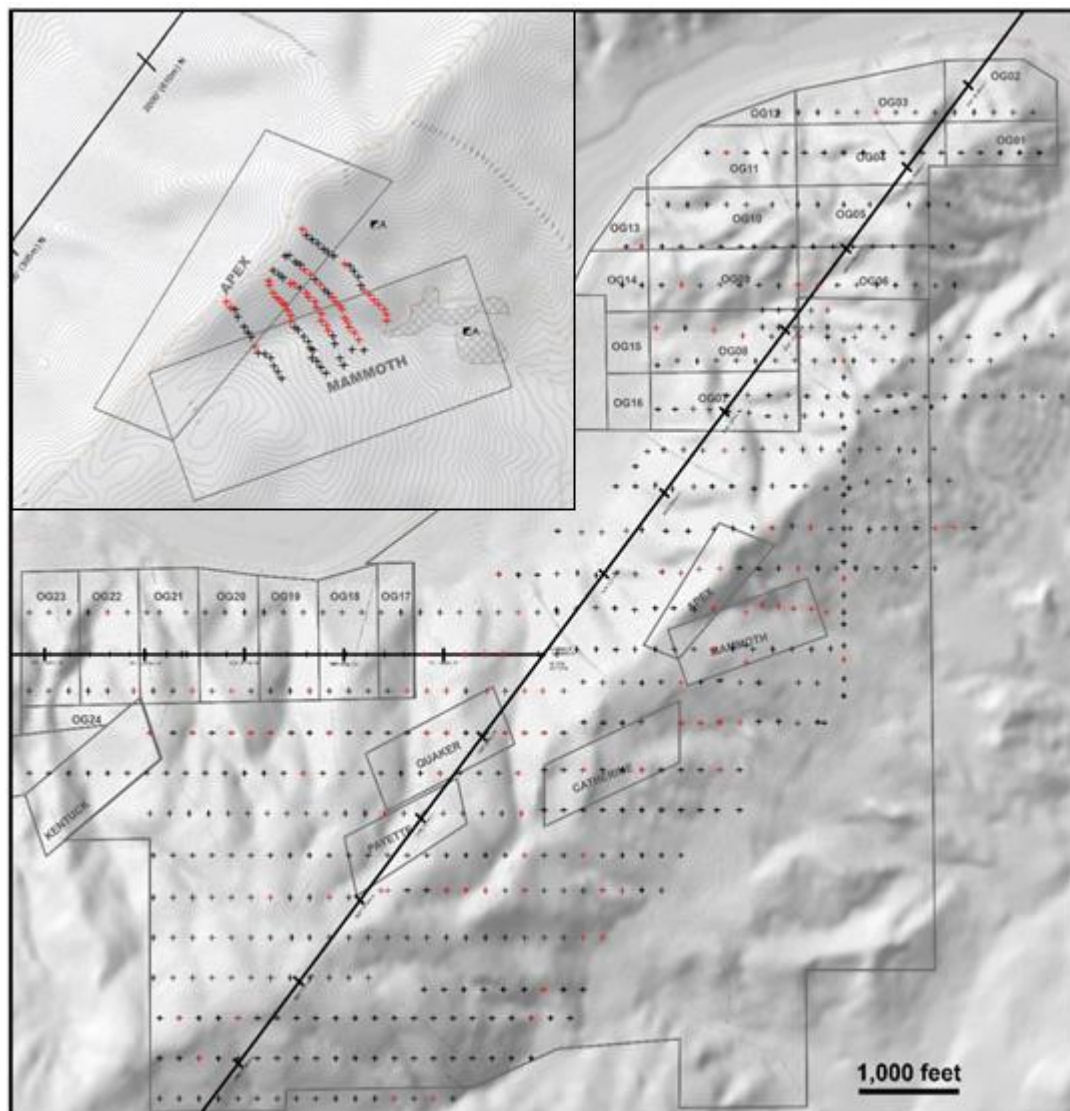


**Figure 5.2. Surface geochemical survey results. Plotted are surface (soil and rock chip) gold concentrations in ppb. Concentration considered anomalous, i.e.  $\geq 20$ ppb are highlighted in red. Inset: Detailed surface survey of August 2015 covering parts of the Apex and Mammoth claims.**

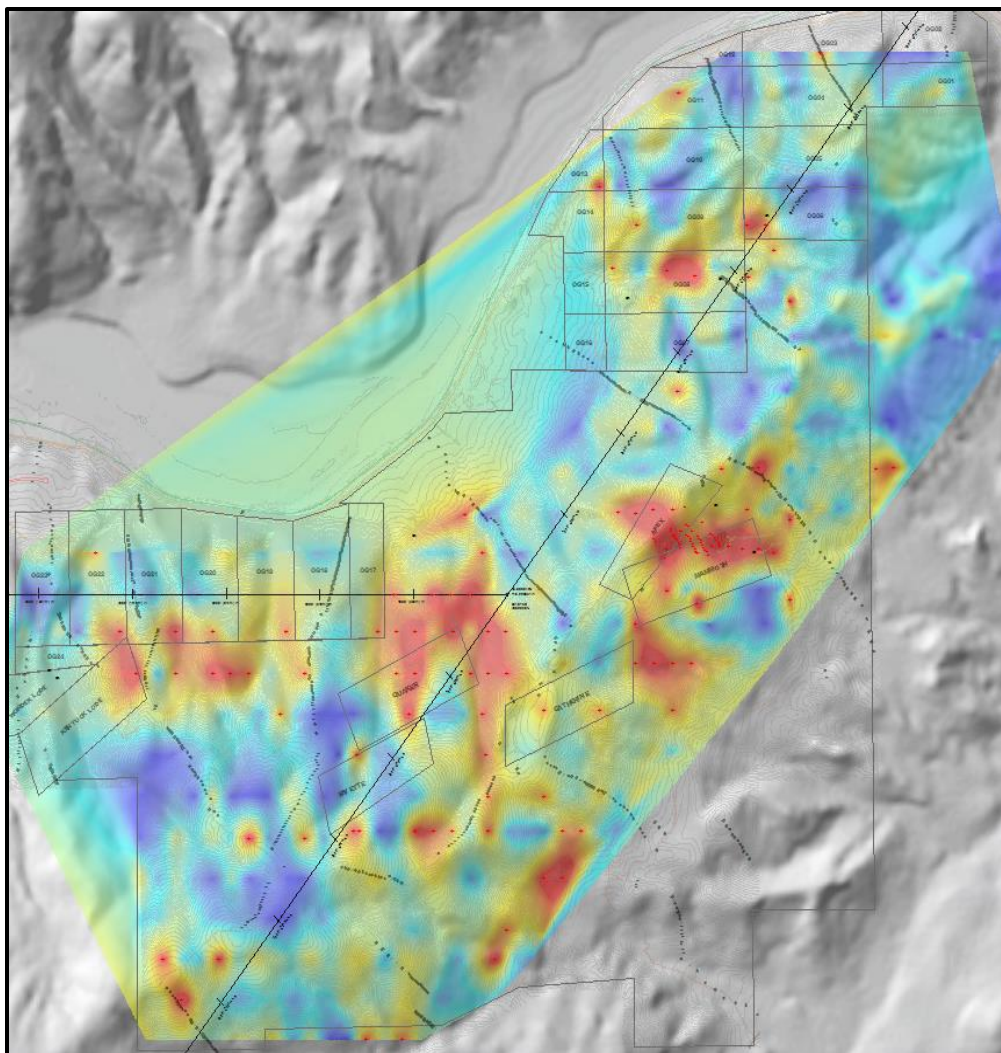


**Figure 5.3. Surface geochemical gold concentration gradient map. There is a distinct east-west trend to anomalies that can't be explained by survey geometry alone. Between east-west trends are anomalous zones that "cross" from one east-west trend to another, where these intersect major east-west trends the areal extent of anomalous zones increases. Values are plotted on log scale with values greater than 100 ppb capped at 100 ppb, and values less than 1 ppb shifted to 1 ppb. This was done to facilitate visualization between extreme ranges of gold concentrations (.001 to 2190 ppb). Samples greater than 20ppb in gold are marked with red crosses. The results of the detailed Mammoth survey are plotted as small red crosses for samples greater than 20 ppb gold, but are not included in the gradient map.**

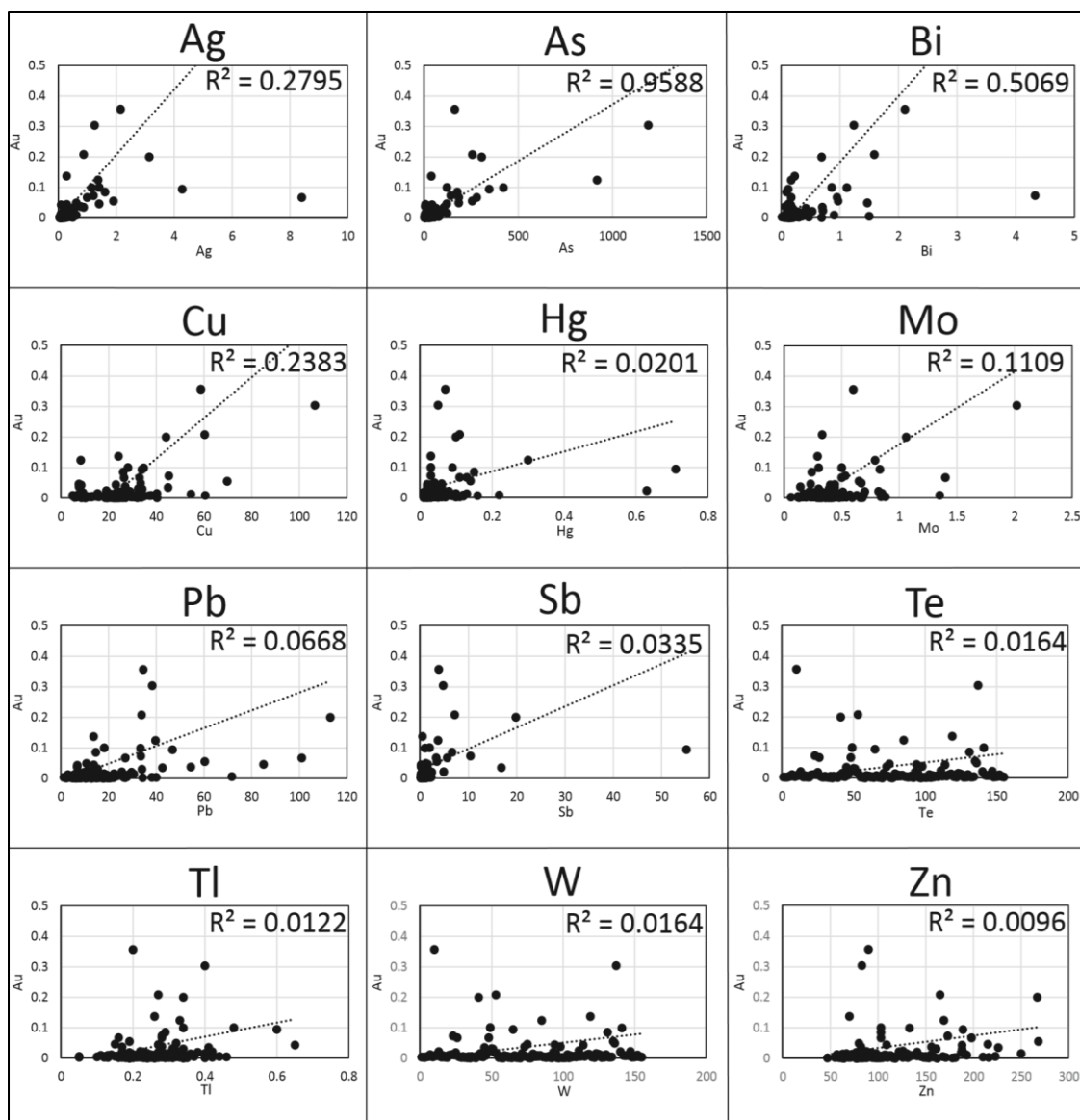


**Figure 5.4.** Au concentration (y-axis) vs. elemental concentration (x-axis) with the  $R^2$  value of dotted linear trend line given. The high  $R^2$  values of arsenic (0.9588) and bismuth (0.5069) are likely indicative that locally gold is hosted in arsenopyrite with Bi substituting into the arsenopyrite lattice in place of arsenic. Lesser correlations with Ag ( $R^2 = 0.2795$ ) and Cu ( $R^2 = 0.2383$ ) are likely due to the presence of pyrrargyrite and owyheeite, and chalcopyrite and tennantite, respectively, as ore minerals.

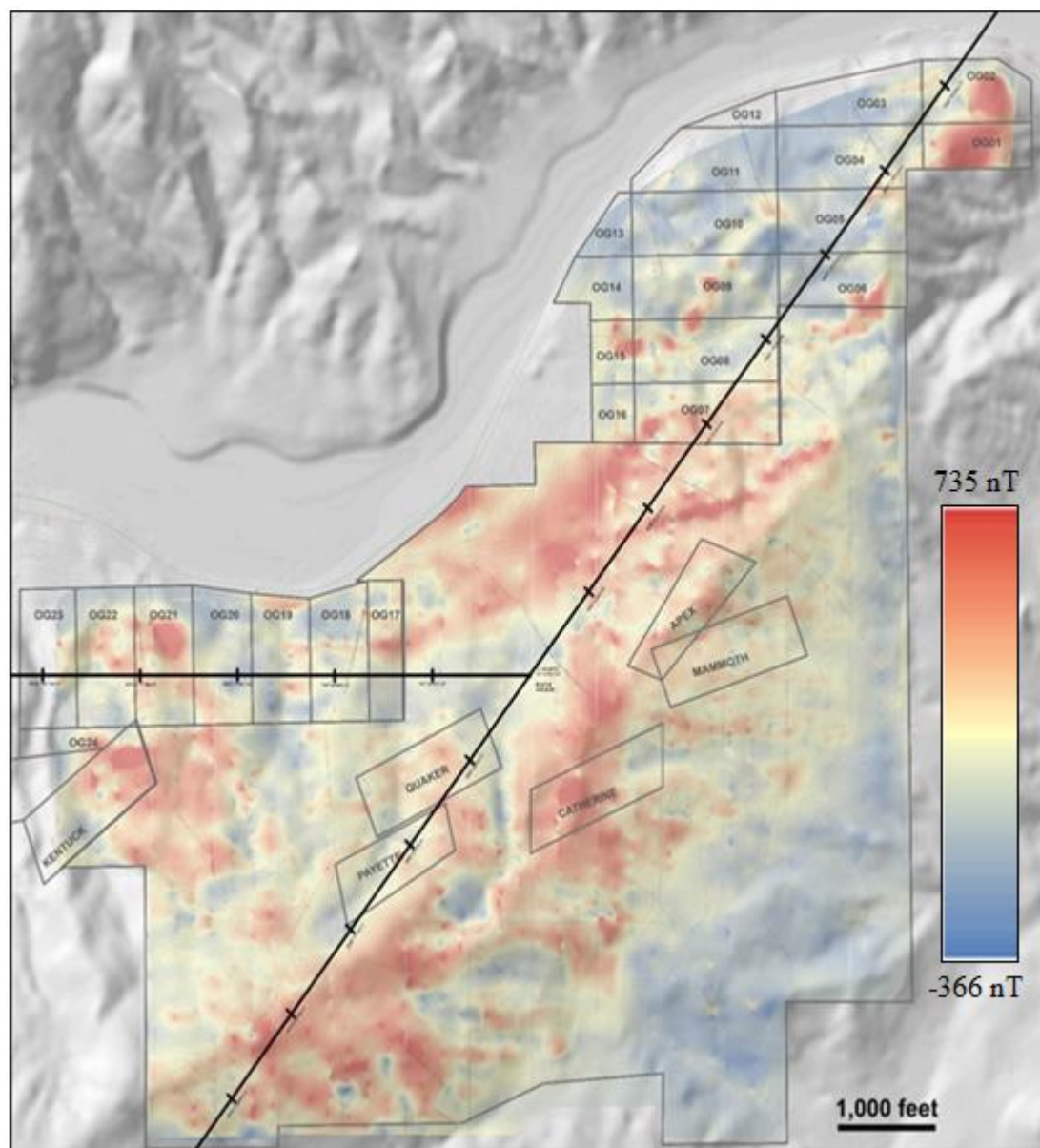


**Figure 6.1.** Magnetic anomaly map reduced to pole data. Scale bar is nanoTesla (nT) deviation from mean.

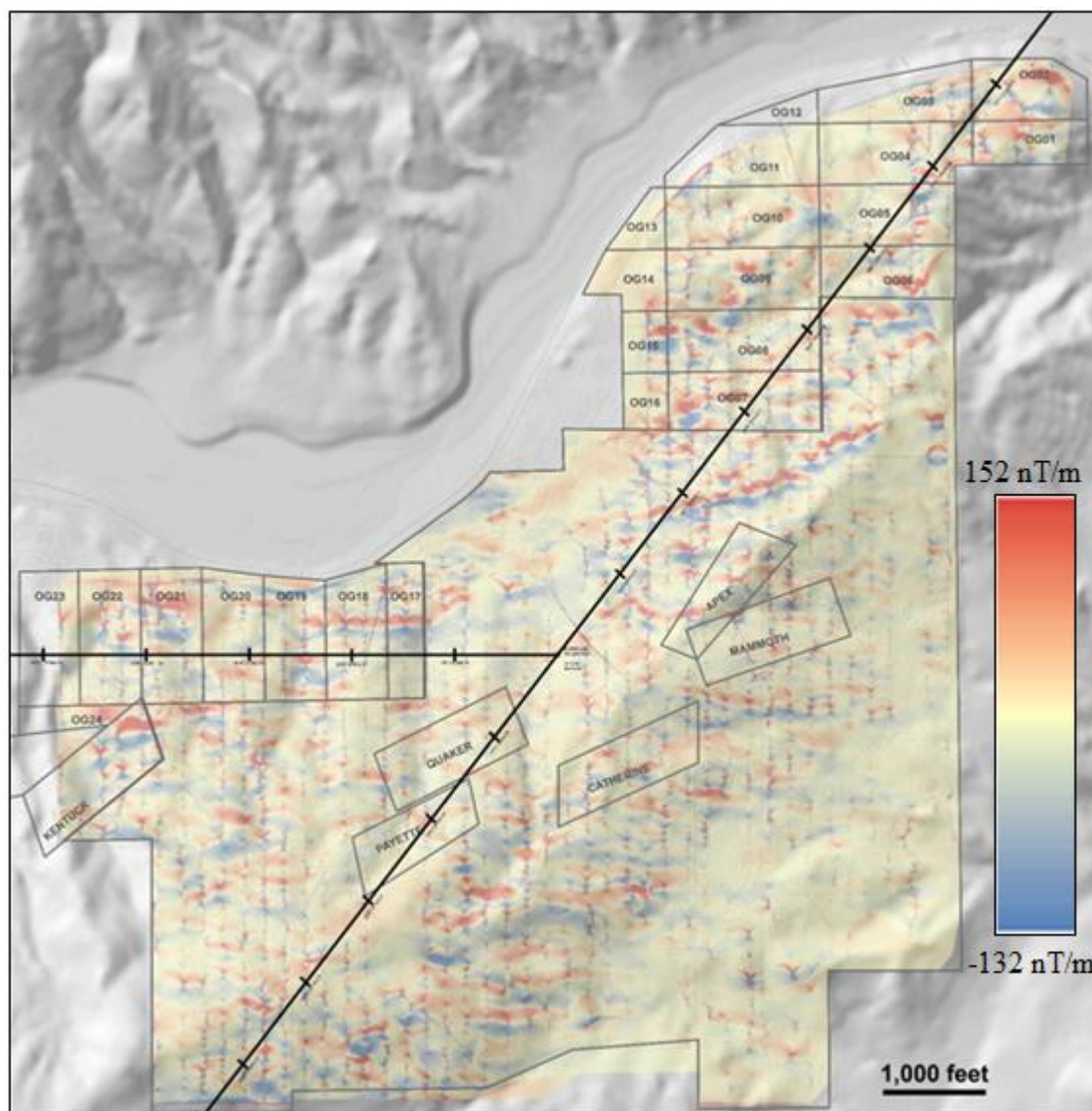


**Figure 6.2.** Magnetic anomaly Y (north-south) gradient data. Scale bar is nanoTeslas per meter (nT/m) deviation from mean.

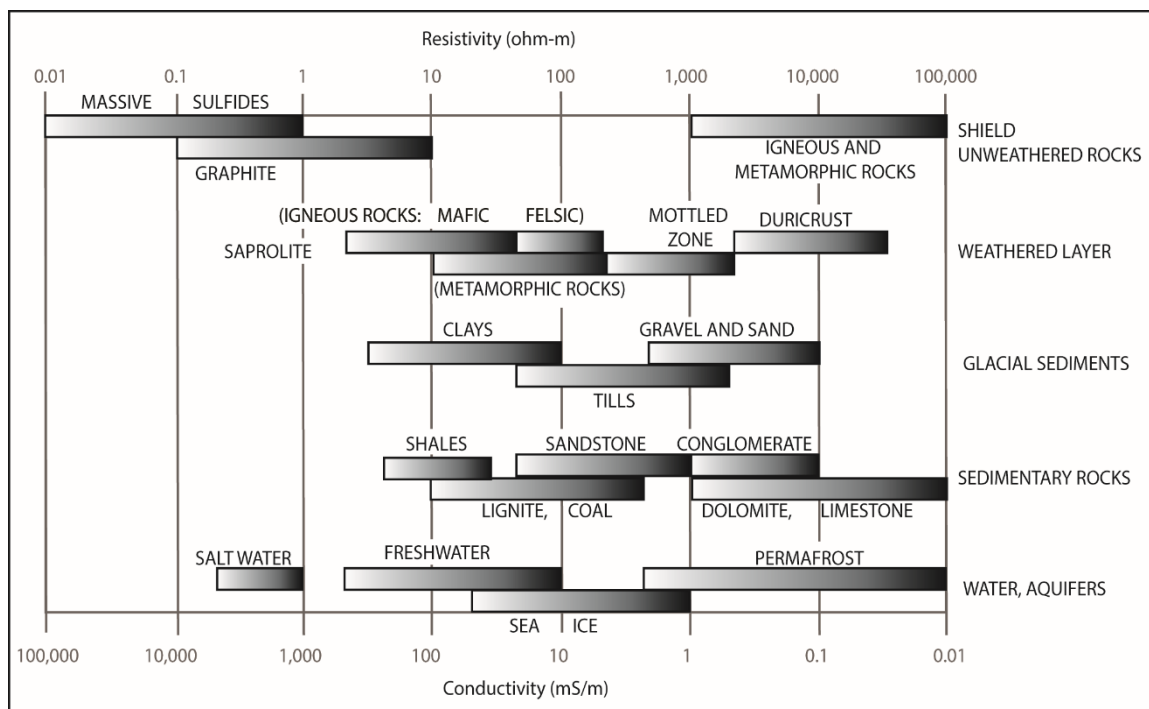


**Figure 7.1. Ranges of electrical resistivity (ohm-m) and electrical conductivity (mS/m) for common earth materials. From Palacky, 1988.**

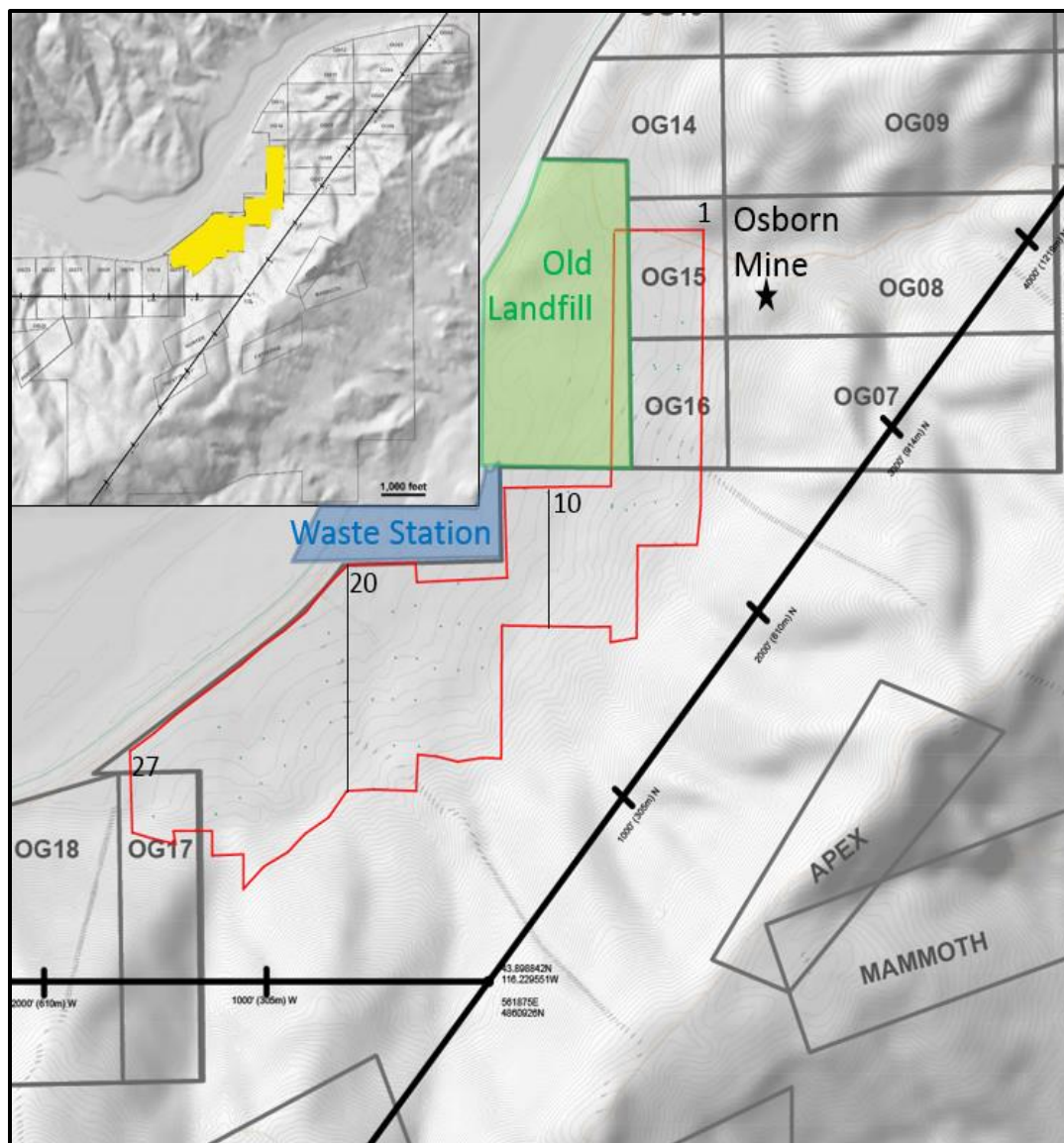


**Figure 7.2.** Location of IP/ER survey of July and August 2014. Numbers in red polygon are lines 1, 10, 20, and 27. Green dots indicate line segment endpoints.

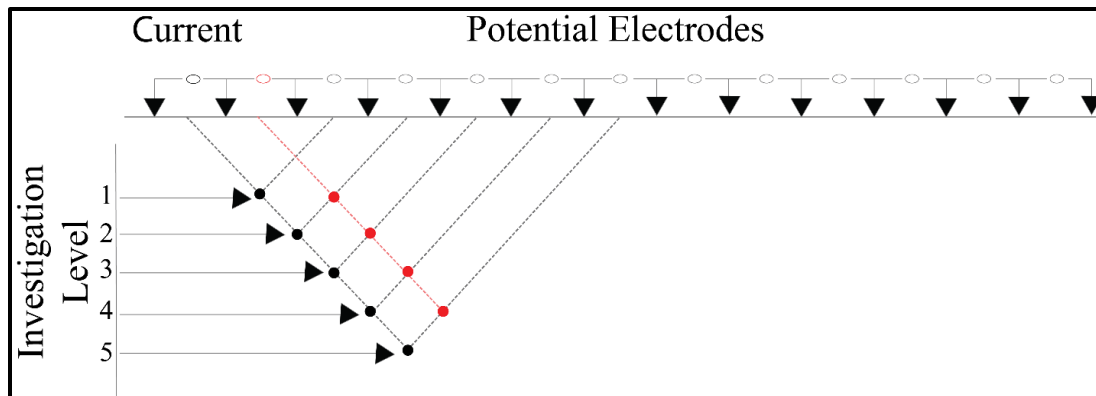


**Figure 7.3.** Schematic diagram of a dipole-dipole array. In step 1 current is injected at potential electrode pair 1 and apparent resistivity or chargeability is measured at electrode pairs from 3 onward, different levels of current flow path intersection, given by dashed lines give different levels of investigation, indicated by black dots. In step 2 current is injected at electrode pair 2, denoted in red, and measurements are made at electrode pairs 4 and onward, denoted by red dots. Repeating this process across the whole array gives the apparent resistivity or chargeability at a number of different points, from which inversion software can model resistivity and chargeability sections.

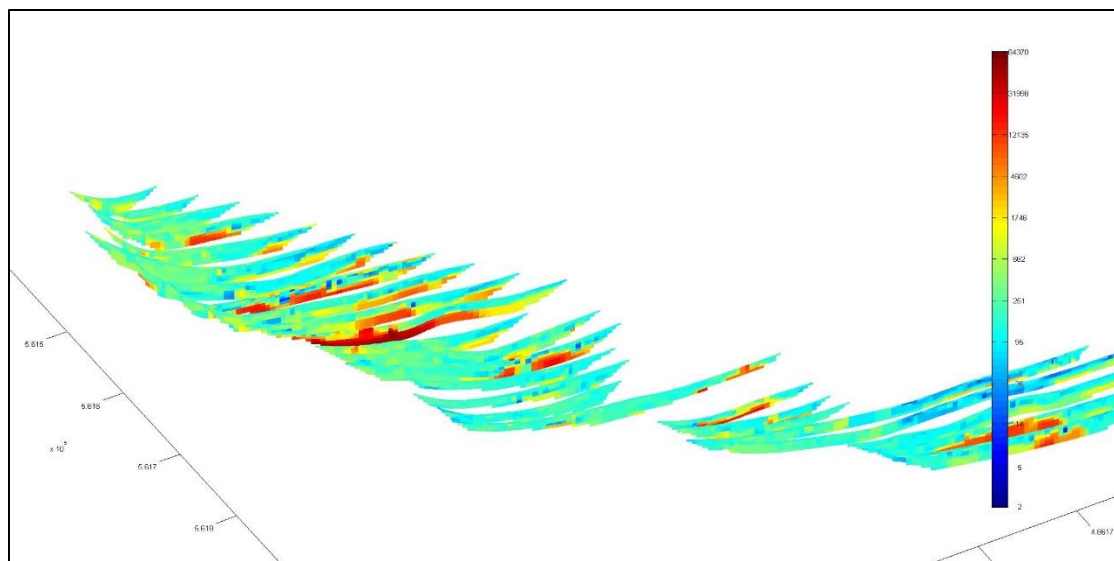


**Figure 7.4.** Results of Electrical Resistivity survey. Lines point north. A roughly NE-SW trend of ER highs is apparent in the series of cross-sections.

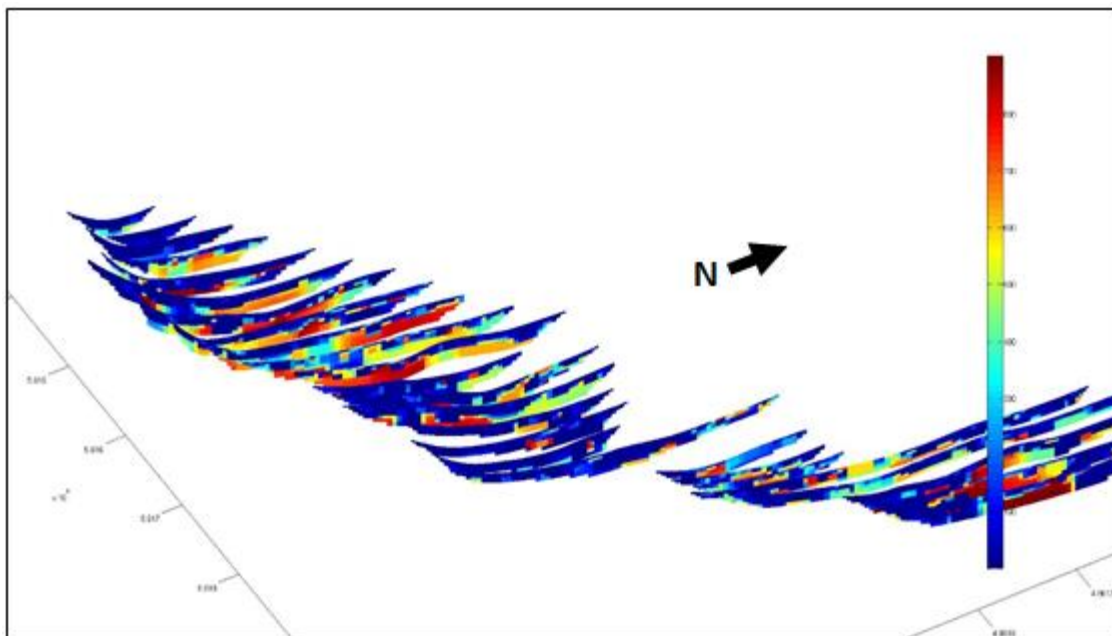


**Figure 7.5.** Results of Induced Polarization survey. Lines point north. A roughly NE-SW trend of IP highs is apparent in the series of cross-sections.

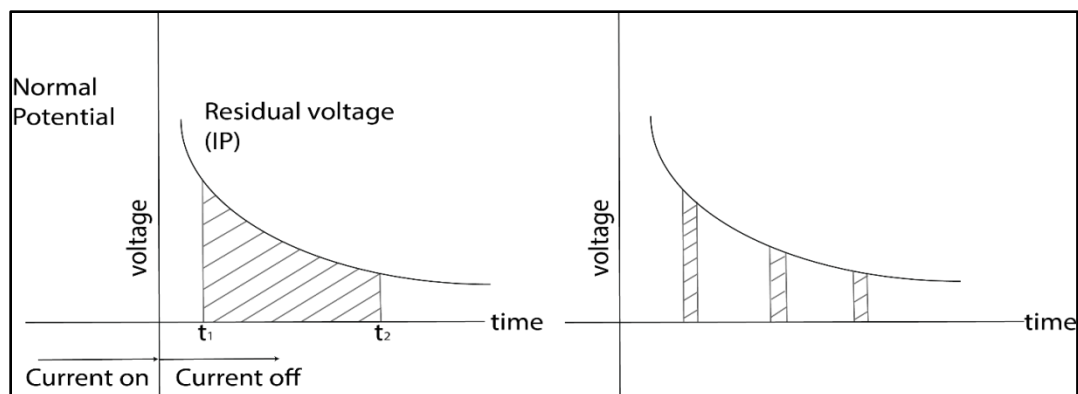


**Figure 7.6. Time integrated measure of IP. On the left is a theoretical decay curve with voltage potential indicated by the hashed area. Because equipment cannot measure the continuous decay of voltage the curve is sampled at multiple points during discharge to reconstruct the decay curve, as shown on the right. Modified from Parasnis (1975).**

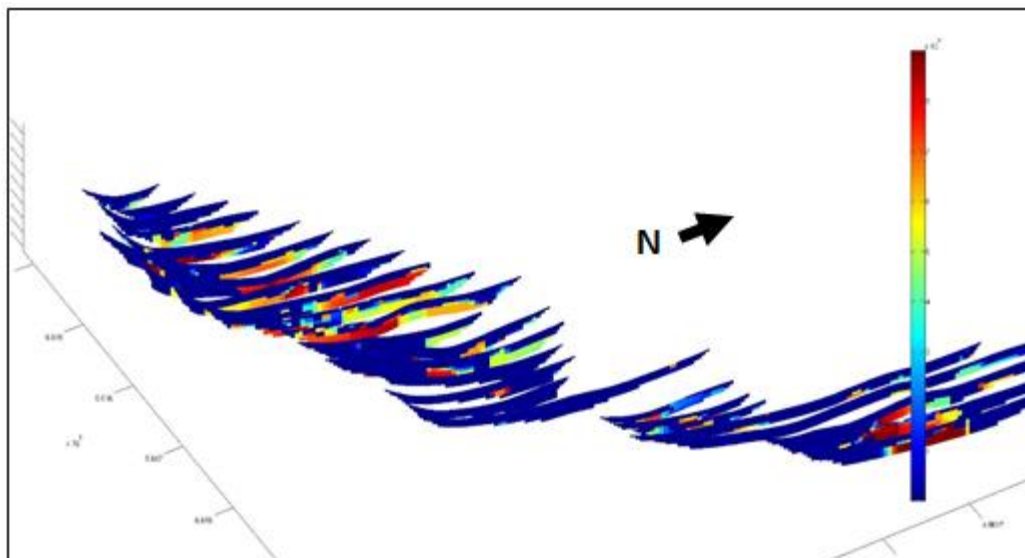


**Figure 7.7.** Results of Metal Factor interpretation method. Lines point north. A roughly NE-SW trend of metal factor highs is apparent in the series of cross-sections.

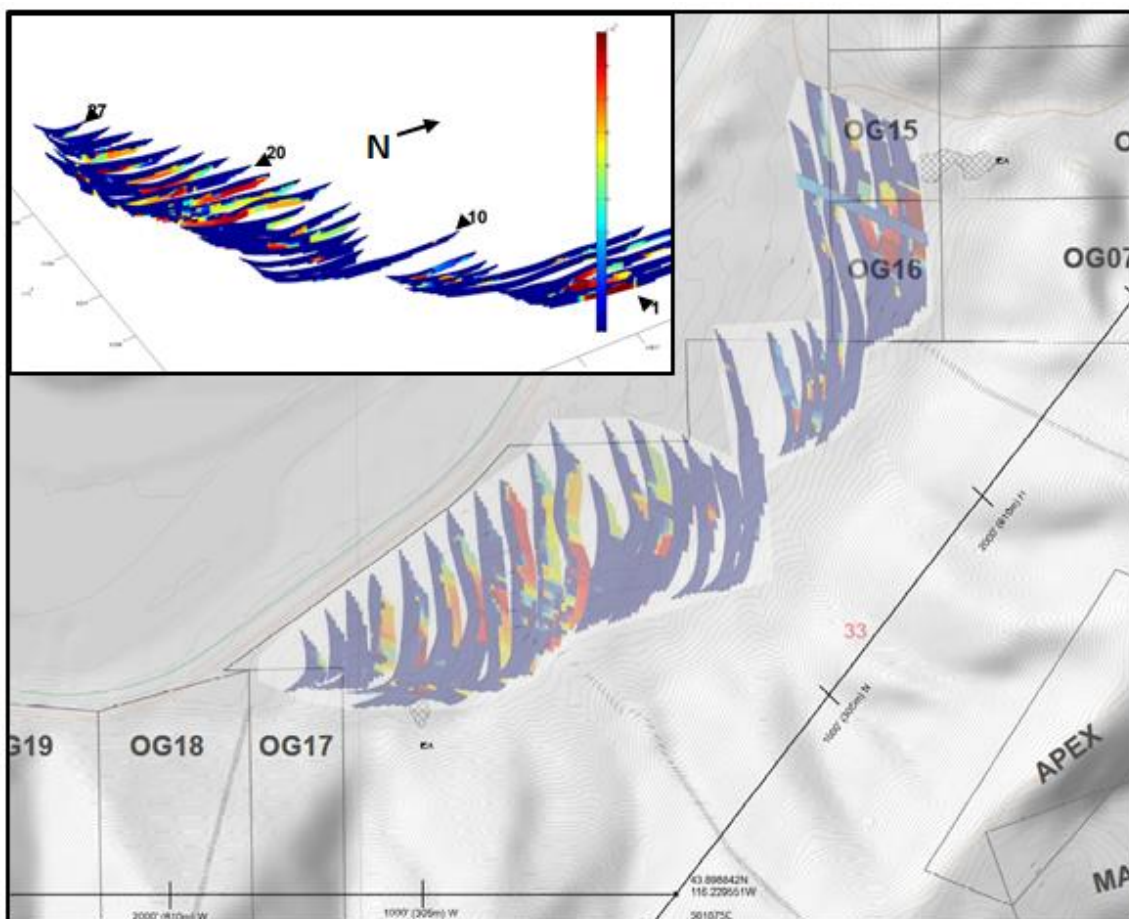


**Figure 7.8. Results of Metal Factor interpretation method located in approximate position on map. Thick red lines are interpreted trends of metal factor highs. Inset: Original figure before map overlay.**

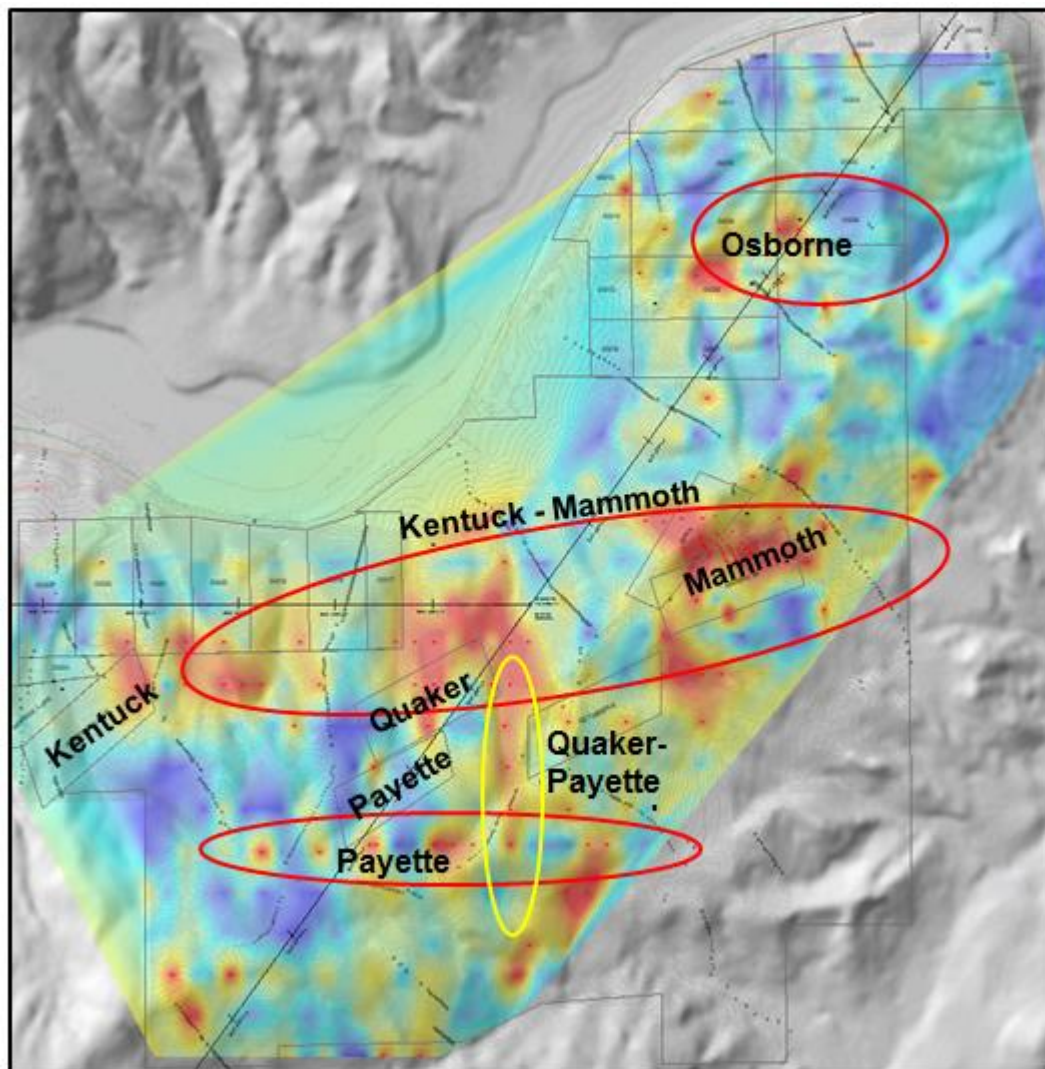


**Figure 8.1. Surface geochemical gold concentration gradient map. There is a distinct east-west trend to anomalies that can't be explained by survey geometry alone. Between east-west trends are anomalous zones that "cross" from one east-west trend to another, where these intersect major east-west trends the areal extent of anomalous zones increases. Three, the Osborn, Kentuck-Mammoth, and Payette, east-west anomalous trends are circled in red, and one, the Quaker-Payette, north-south anomaly is circled in yellow. Values are plotted on log scale with values greater than 100 ppb capped at 100 ppb, and values less than 1 ppb shifted to 1 ppb.**

**This was done to facilitate visualization between extreme ranges of gold concentrations (.001 to 2190 ppb). Samples greater than 20ppb in gold are marked with red crosses. The results of the detailed Mammoth survey are plotted as small red crosses for samples greater than 20 ppb gold, but are not included in the gradient map.**

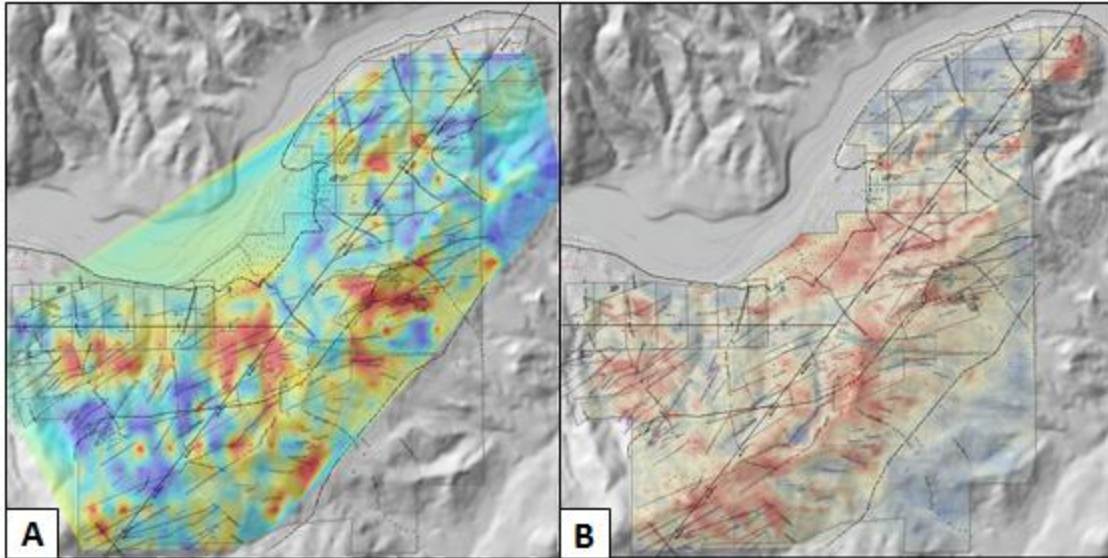


**Figure 8.2.** Surface geochemical soil gold anomaly gradient map (A) and total field magnetic anomaly RTP map (B). The gold anomaly highs (reds on A) align relatively well with magnetic anomaly lows (blues on B). Hydrothermal destruction of primary magnetite and hydrothermal deposition of gold are hypothesized to be the drivers behind the resemblance.

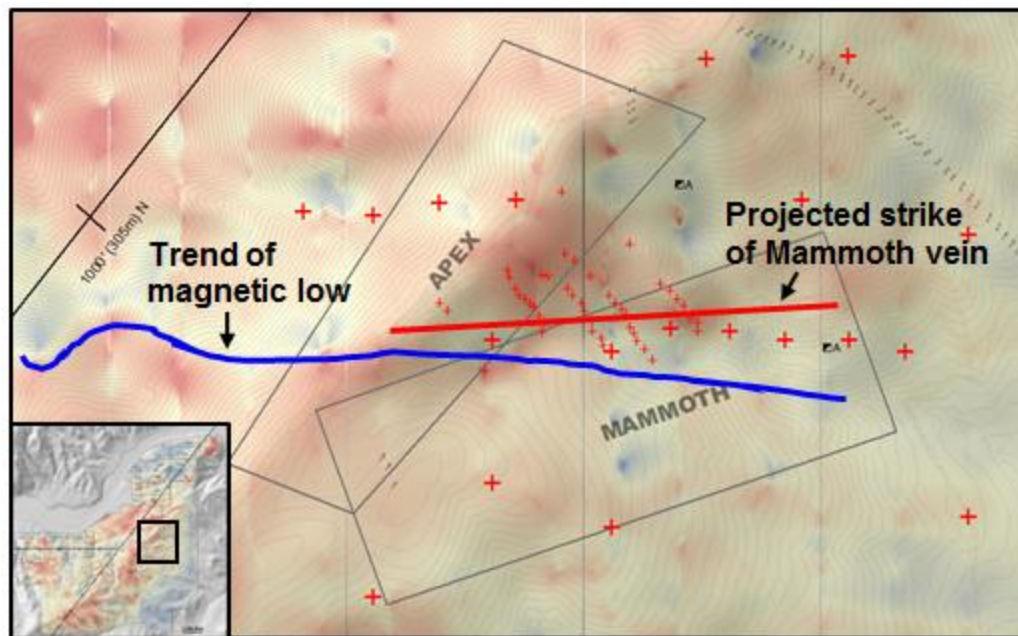


**Figure 8.3.** Total magnetic field anomaly reduced to pole gradient map of the Mammoth and Apex claims with surface gold concentrations  $\geq 20$ ppb plotted as red crosses. Blue line traces the trend of a magnetic low that crosses the Mammoth and Apex claims. Red line is projected strike of the exposed Mammoth vein. Note the correlation between magnetic low trend and strike of Mammoth vein with associated surface samples. Inset: location of Mammoth and Apex claims on the property.

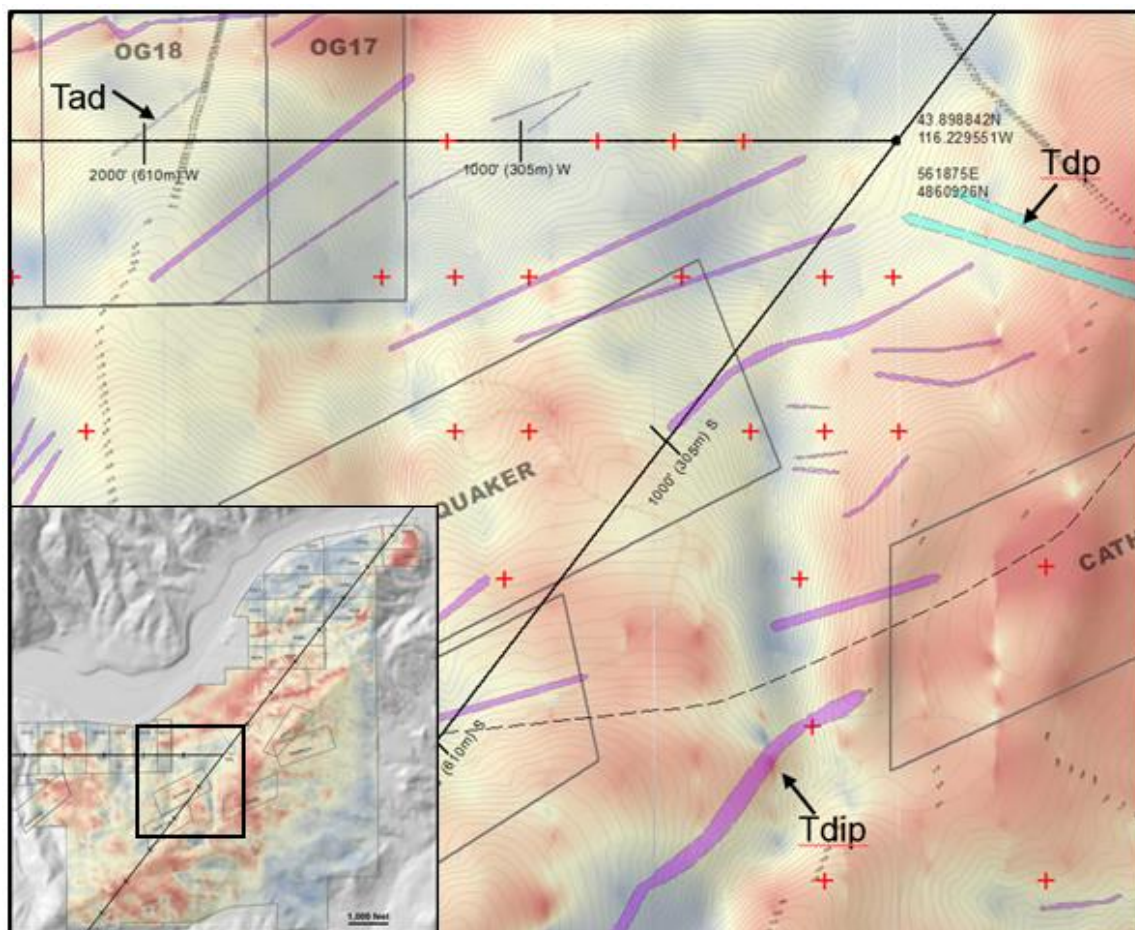


**Figure 8.4.** The Quaker anomaly with RTP magnetic map inset. Red crosses are surface geochemical survey gold concentrations  $\geq 20$ ppb, colored polygons are mapped dikes. In general high gold concentrations overlap with magnetic lows.

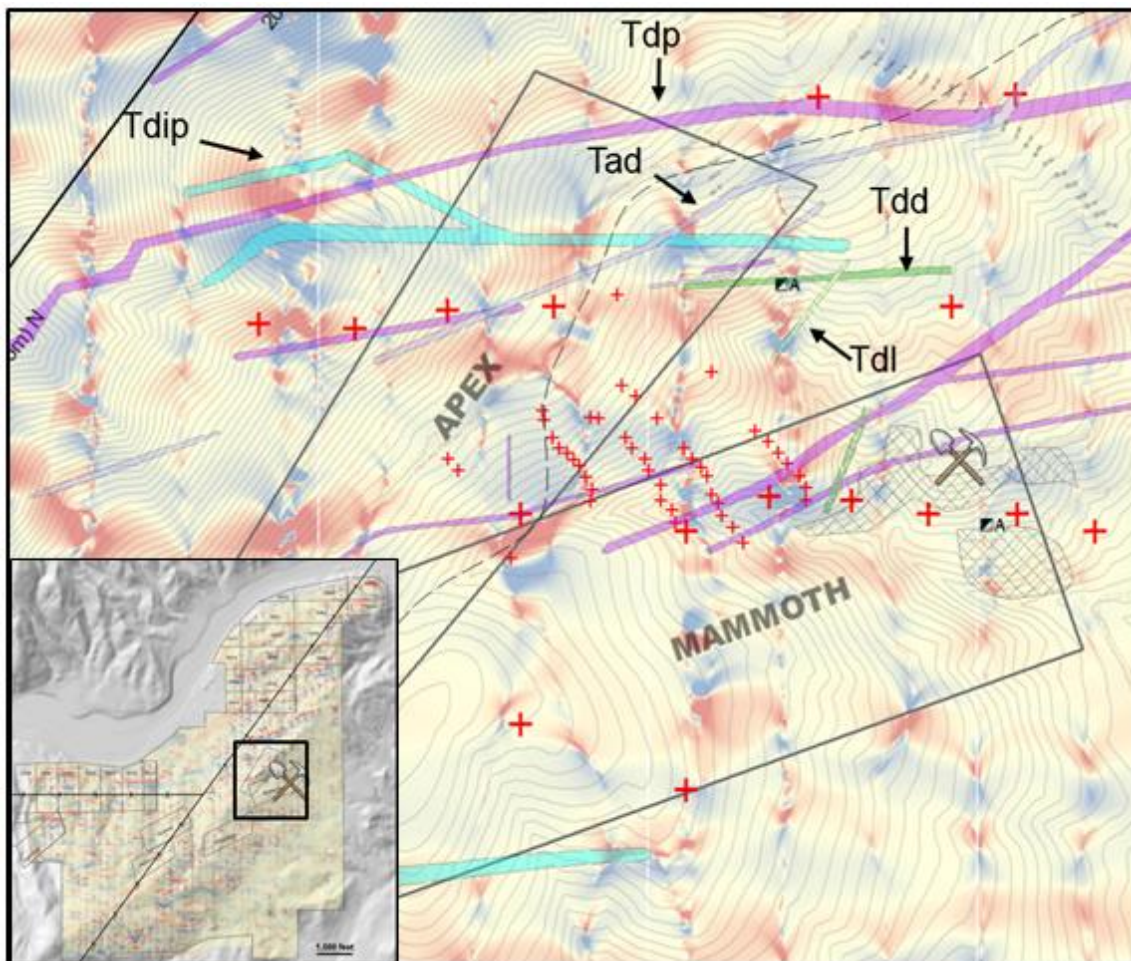


**Figure 8.5.** The Mammoth and Apex claim areas showing results of the summer 2015 (small red crosses) and 2014 (large red crosses) surface geochemical sampling programs along with mapped dikes and edge detection magnetic results. Magnetic lineaments successfully outline the excavated Mammoth vein along its physical and geochemical trace westward up the Mammoth gully. Red crosses are surface geochemical gold concentrations  $\geq 20$ ppb, colored polygons are mapped dikes, crossed red picks symbols are old prospect pits, pick and shovel symbol is location of Mammoth mine excavation, hatched areas are mine or excavation dumps/waste piles. Inset: Whole property magnetic edge detection map with area of large map in the boxed region.

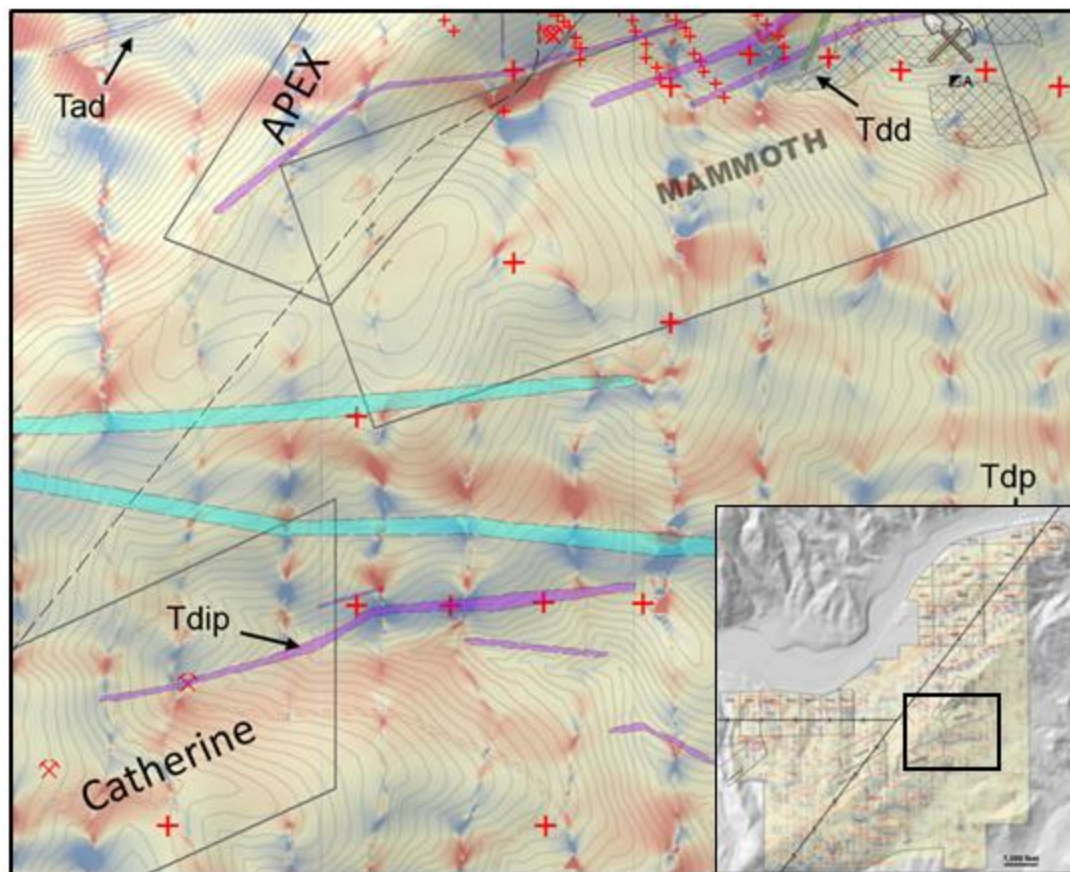


**Figure 8.6. Close-up of area around Catherine claim showing dikes, summer 2014 surface geochemical survey gold concentrations, and edge detection magnetic anomaly results. Note correlation in center of image showing alignment of the three different exploration methods. Red crosses are surface geochemical gold concentrations  $\geq 20$ ppb, colored polygons are mapped dikes, crossed red picks symbols are old prospect pits, pick and shovel symbol is location of Mammoth mine excavation, hatched areas are mine or excavation dumps/waste piles. Inset: Whole property magnetic edge detection map with area of large map in the boxed region.**

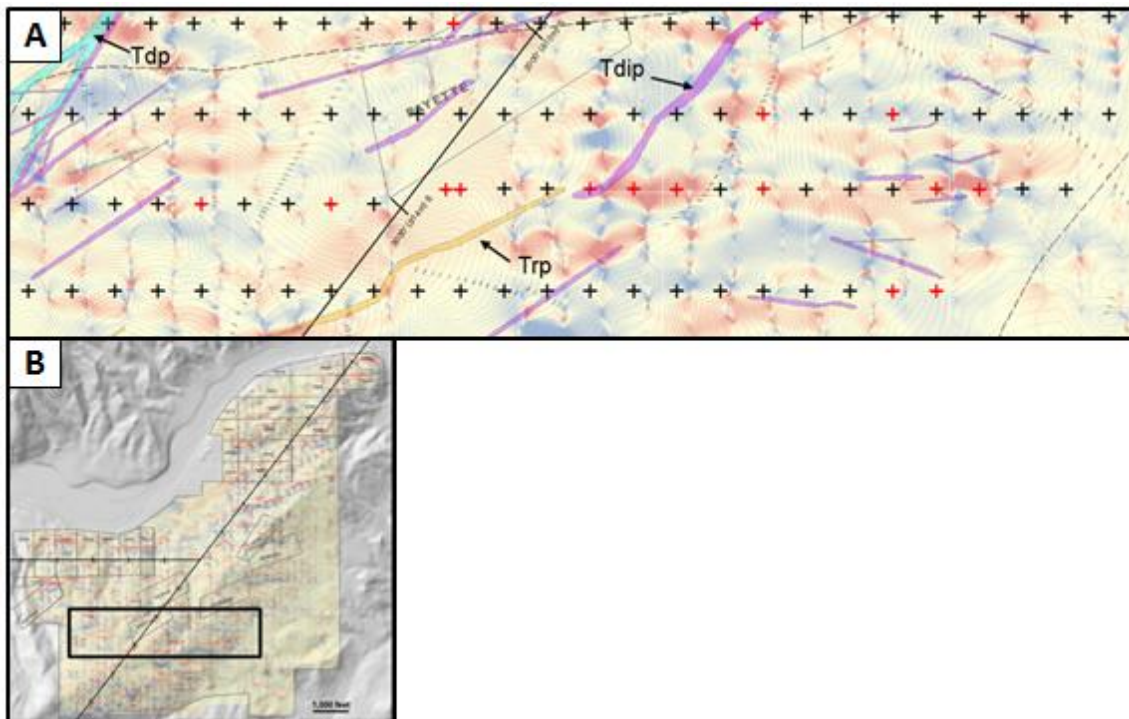


**Figure 8.7. A: East-west trending Payette surface gold concentration anomaly shown with mapped dikes and magnetic edge detection results. Location of anomaly shown in boxed area of B. In the eastern half of the figure the three datasets align well and indicate a good target using the guidelines of figures 27 and 28. In the western half of the figure, near the crest of the ridge, the magnetic and geologic signatures fade out while the gold anomaly signature remains. The dichotomy of the eastern and western halves of the trend may warrant further exploratory work. Red crosses: surface gold  $\geq 20$ ppb. Black crosses: surface gold  $< 20$ ppb. Colored polygons: mapped dikes. Gradient map: magnetic edge detection results.**

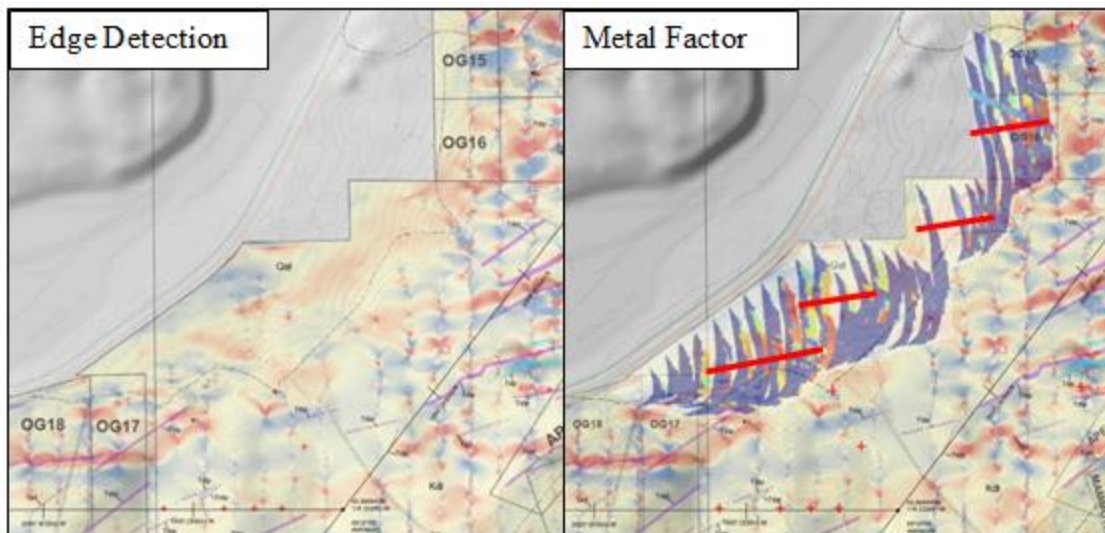


**Figure 8.8.** Edge detection and metal factor comparison. Shown is the area of the IP/ER survey with only the magnetic edge detection results (left) and with metal factor overlaid (right). The red lines on the metal factor overlay indicates the general trends of anomaly highs. This appears to correlate well with the magnetic gradient trend across the area.

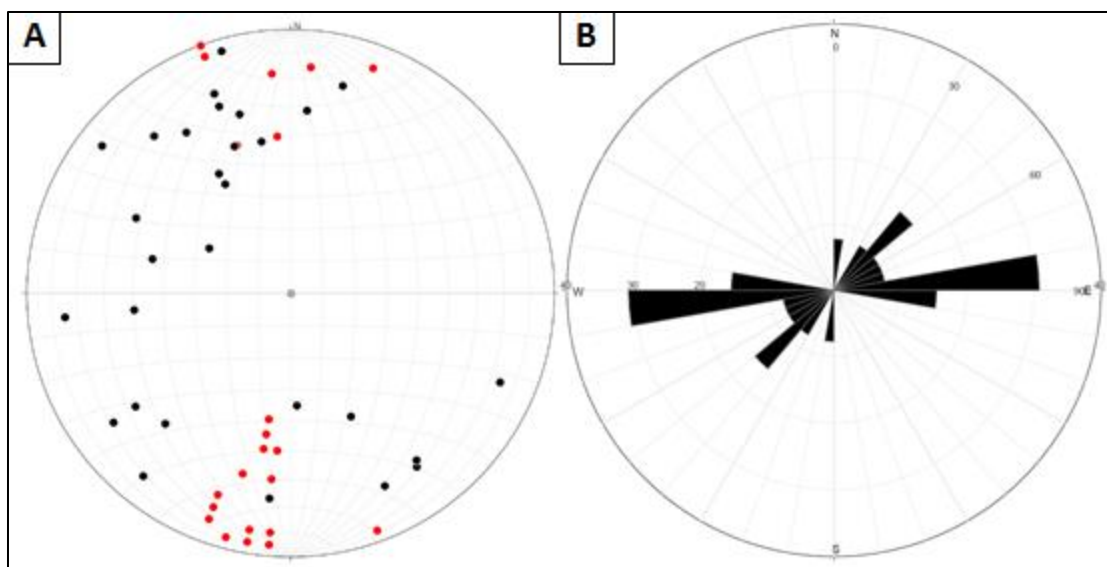


**Figure 8.9. A: Stereonet showing the pole to planes of measured vein strike and dips. The underground data from Anderson (1934) includes workings across the breadth of the Pearl to horseshoe Bend districts and is plotted in red, surface data from this study is plotted in black. Circled in blue are poles that represent east-west vein orientations. B: Rose diagram showing the orientation of veins from this study where dip was unable to be determined.**



**Figure 8.10.** A mineralization node created by the intersection of east-west fracture planes (blue arrows) and north-south fracture planes (red arrows). Picture is looking at the north wall of the recent Mammoth mine excavation.

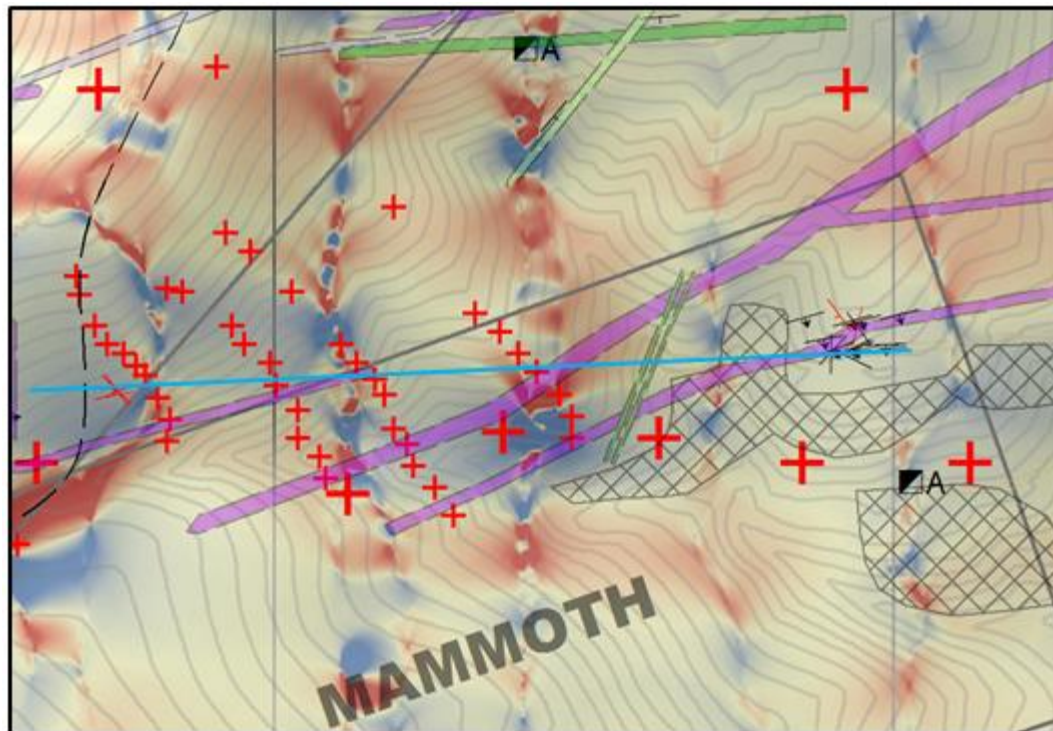


**Figure 8.11. Mammoth mine. The light blue line indicates the trace of the Mammoth vein, strike and dip symbols represent orientation of fractures in the area. The Mammoth vein and fracture trends show the east-west trend of vein systems with NNW fracture intersections. Large red crosses: Orientation surface geochemical survey,  $\geq 20$  ppb. Small red crosses: Mammoth gully surface geochemical survey,  $\geq 20$  ppb. Colored polygons: mapped dikes. Colored gradient map: north-south edge detection. Hashed areas: Mine dumps/excavation waste. Black/white squares with an A: Abandoned mine portals.**

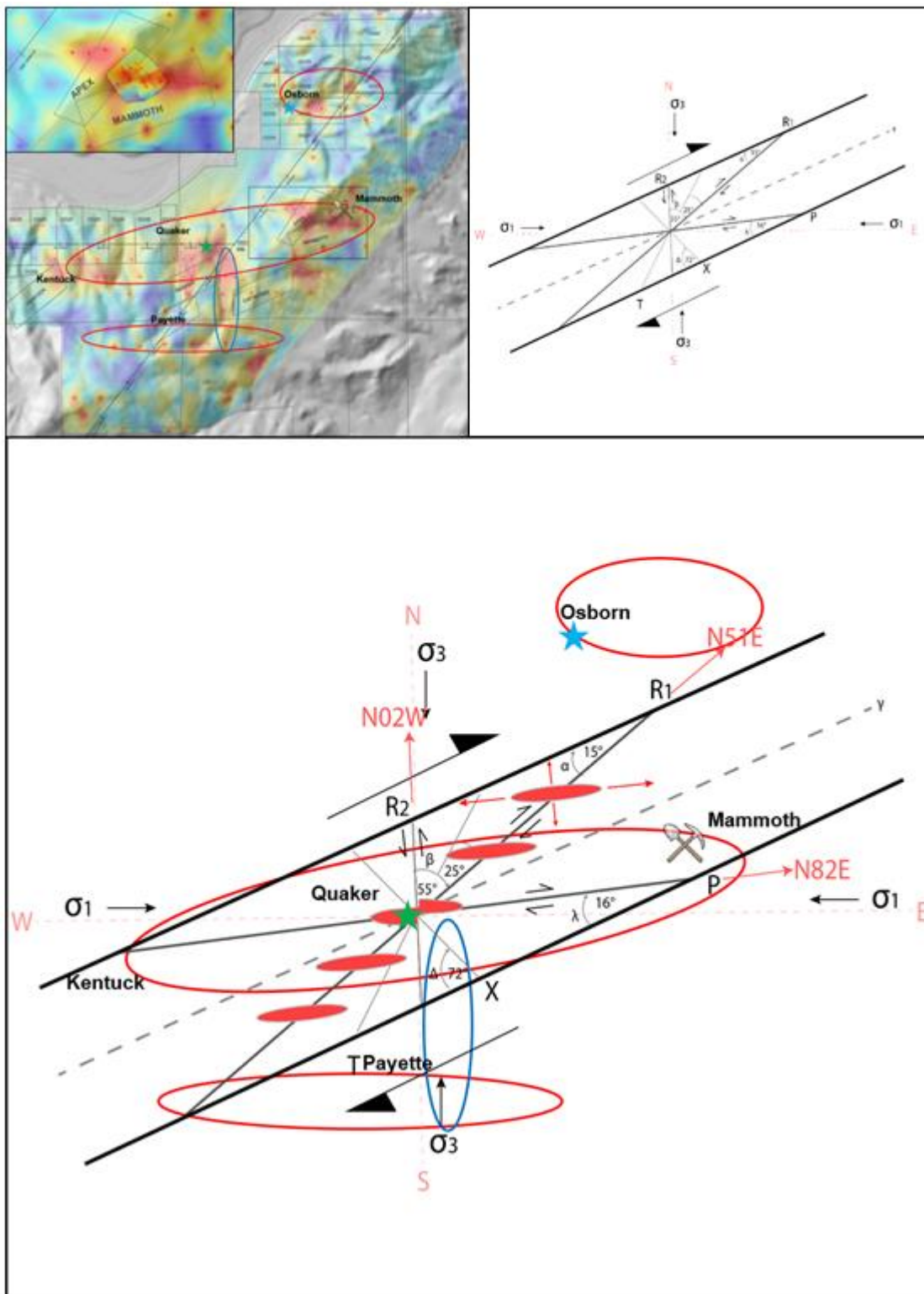
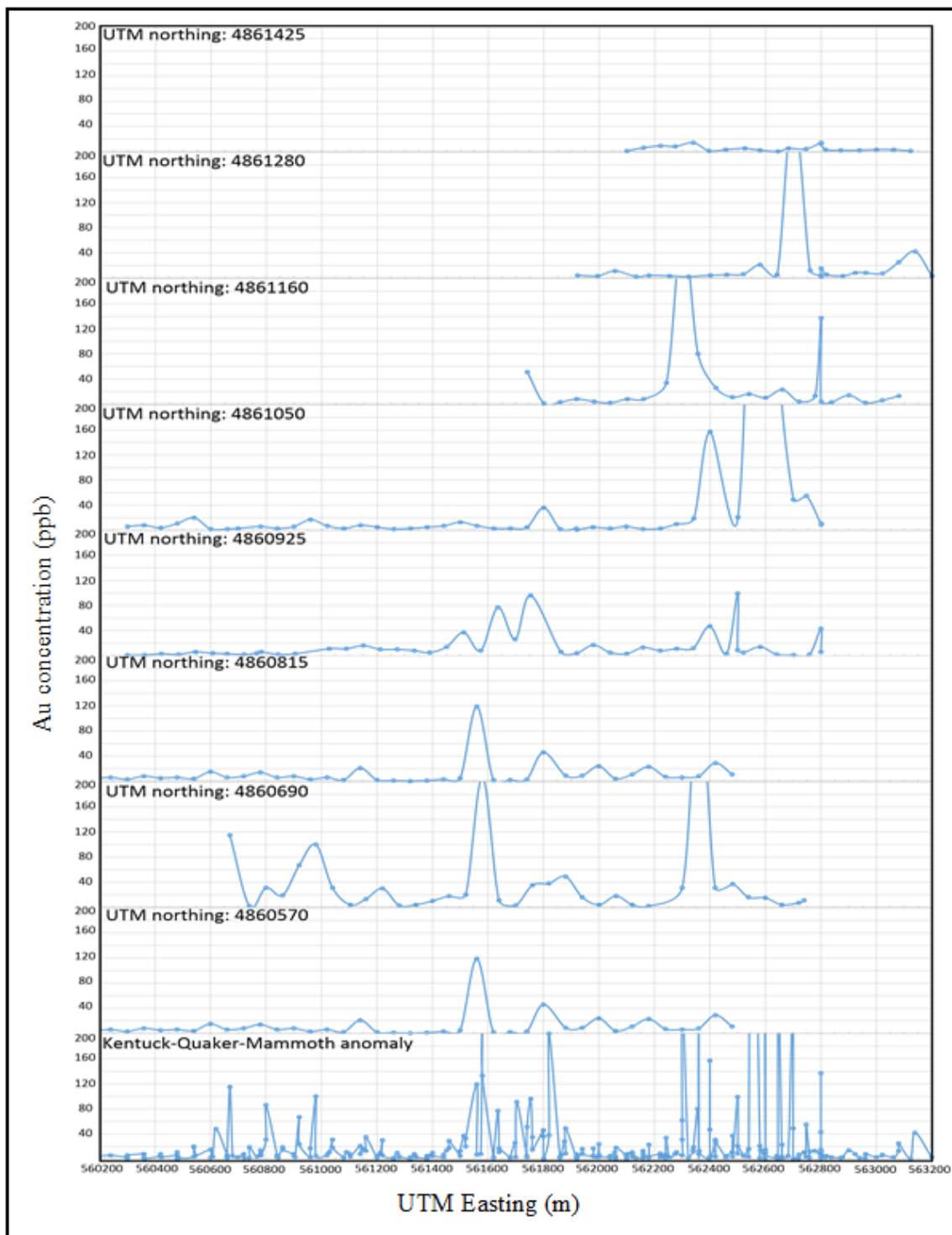
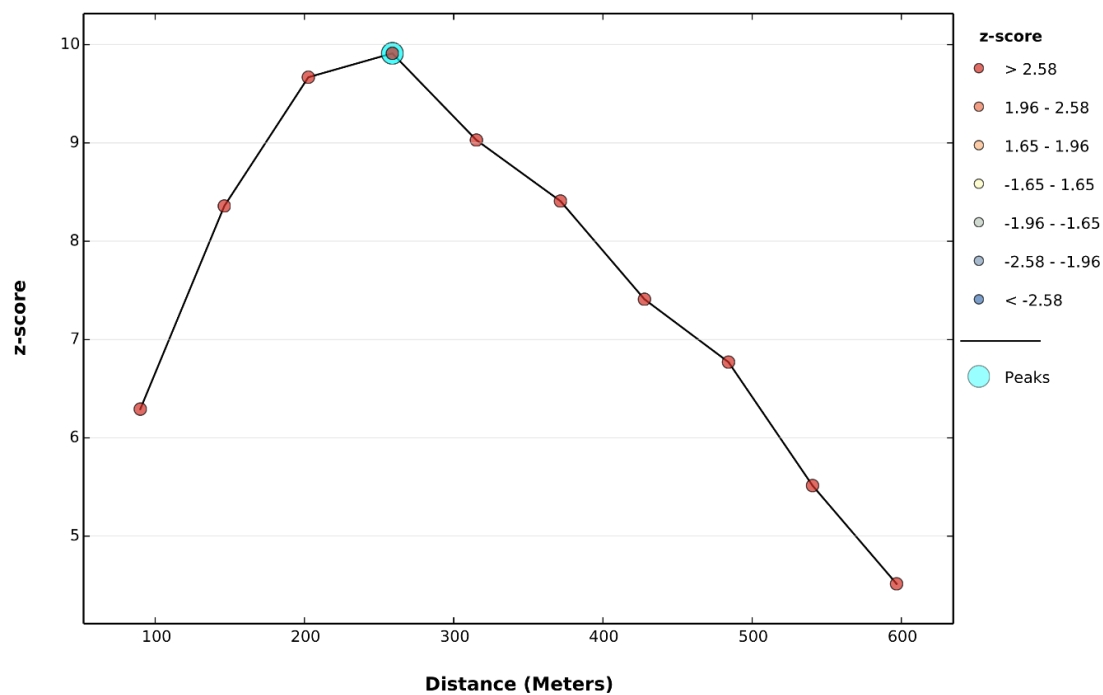


Figure 8.12. The figure shows a right-lateral Riedel shear array with geometry as given by Logan et al. (1979) and its' relationship to surface gold anomalies. A: Surface gold concentration gradient map with three east-west anomalies outlined by red ellipses and one north-south anomaly outlined by a blue ellipse. B: Riedel shear

geometry rotated to the overall trend of the Trans-Challis Fault Zone, N70E, cardinal directions shown in pink. C: Image B overlain onto A and centered on the Quaker anomaly with surface gradient map removed, the locations of the ellipses and Osborn mine (blue star), Quaker anomaly (green star), and Mammoth mine (pick and shovel symbol) are unchanged. The Osborn, Kentuck, Quaker, Mammoth, and Payette labels represent named mining claims in the vicinity. Smaller, solid red ellipses are hypothetical fractures developed in shear array. Principal planes of movement (fractures) are indicated by the thick black lines oriented N70E, secondary movement planes are indicated by thinner black lines labeled P and R<sub>1</sub>, tertiary movement planes are shown by thin grey lines labeled R<sub>2</sub> and X, sense of movement is indicated by the black arrows. Note that the sense of movement on R<sub>2</sub> is antithetical to the rest of the array.



**Figure 8.13.** Au concentration (y-axis) plotted according to UTM easting. The series of plots encompass the north to south width of the Kentuck-Quaker-Mammoth trend of gold anomalies. The bottom graph plots all samples from previous eight graphs without regard to northing.



**Figure 8.14. Incremental spatial autocorrelation analysis of all surface geochemistry samples weighted by gold concentration value, processing done in ArcGIS. The peak z-score of 9.98 occurs as 258m.**

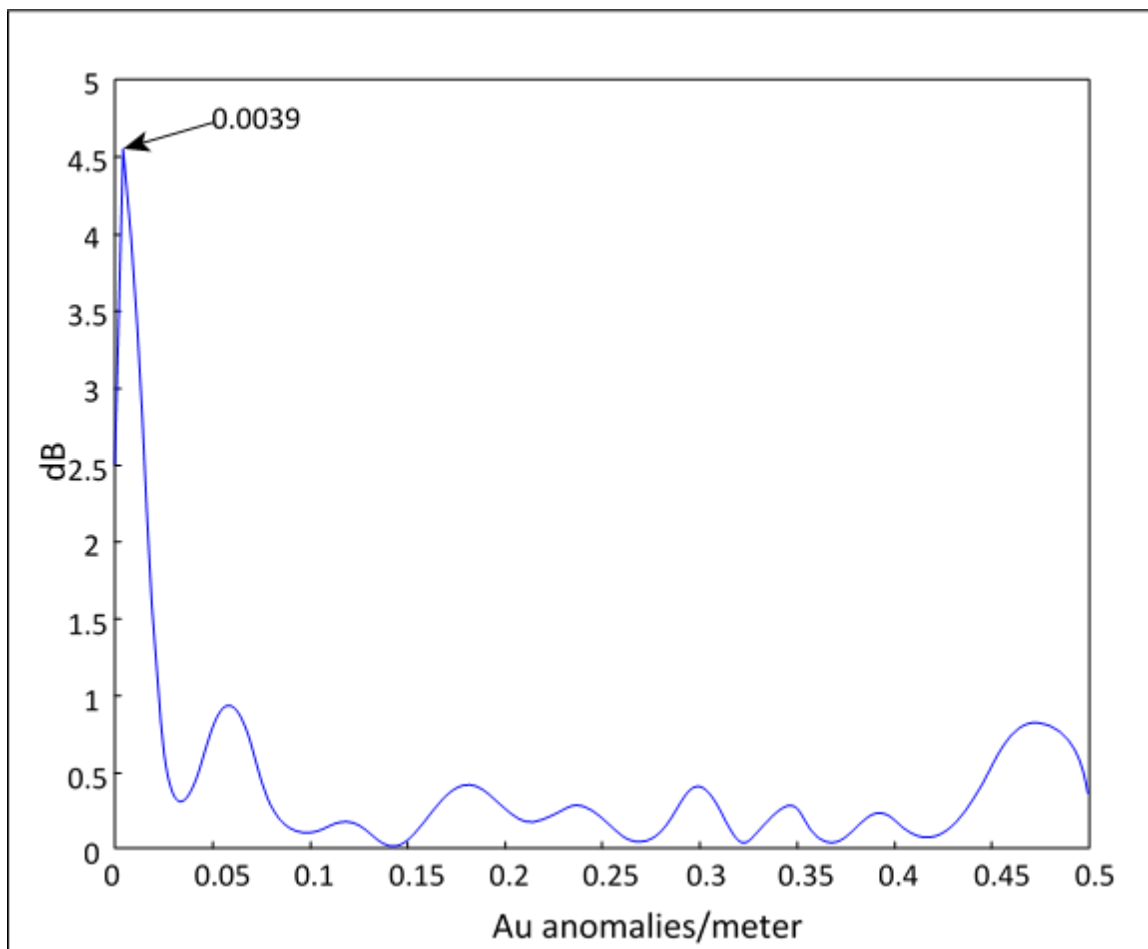


**Figure 8.15. Periodogram of the UTM 4860815 N sampling line. The lowest frequency peak occurs at 0.0039 which corresponds to an anomaly spacing of 256m.**

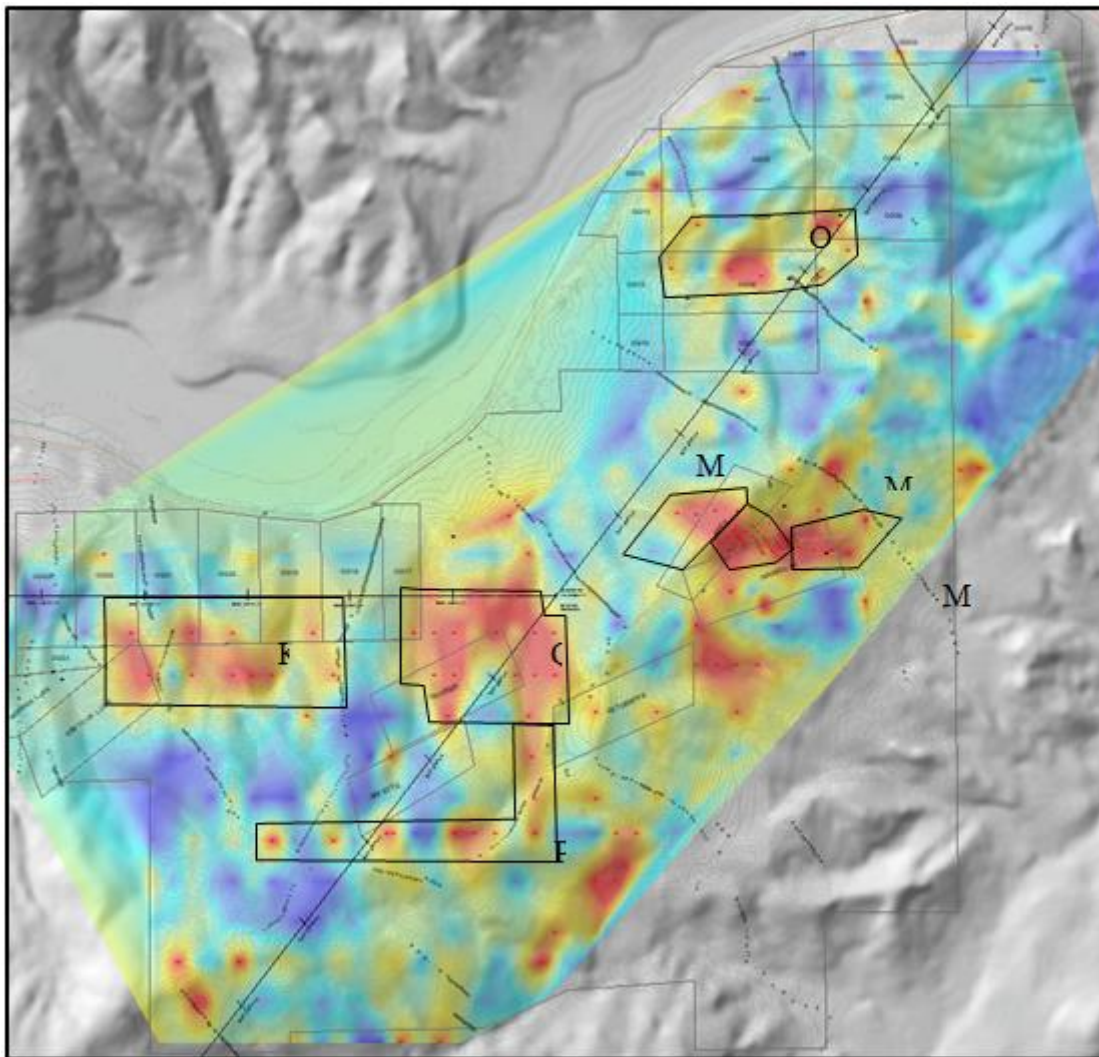


**Figure 9.1. Proposed sampling areas for future high density surface geochemical surveys.**

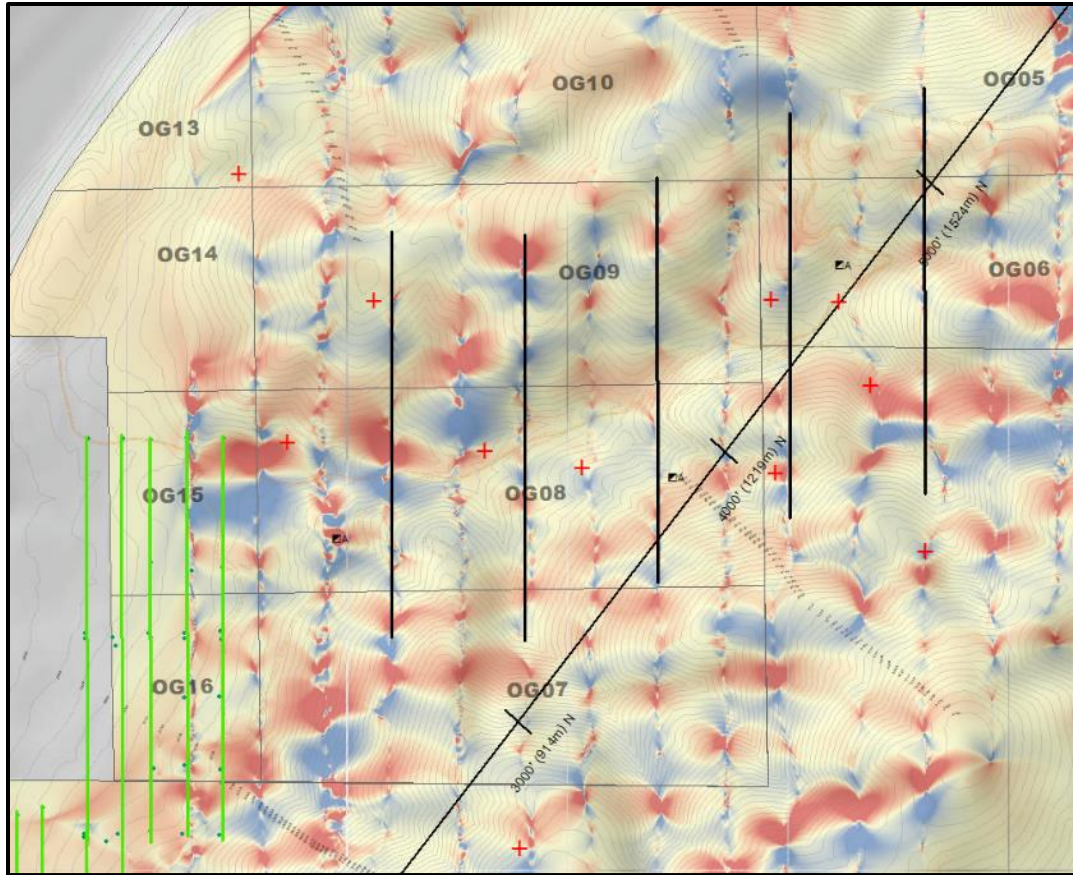


**Figure 9.2.** Area of proposed Osborne IP/ER survey. Five 1200' (360m) north-south lines that cross the Osborne draw, each separated by ~400' (120m) are proposed. Green lines are of previously completed IP/ER survey. Black lines are proposed new lines.

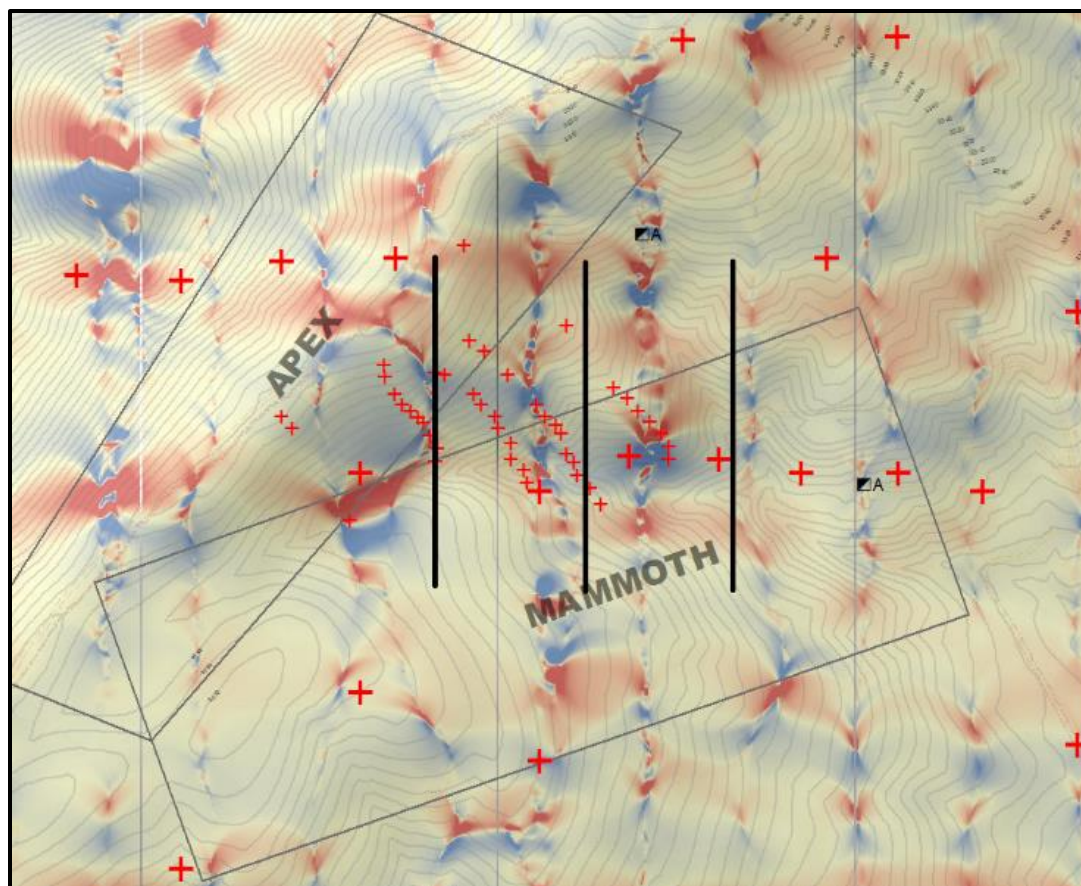


**Figure 9.3.** Area of proposed Mammoth IP/ER survey. Three 600' (180m) north-south lines across the Mammoth gully, each separated by ~200' (60m), are proposed. Black lines are proposed new lines.

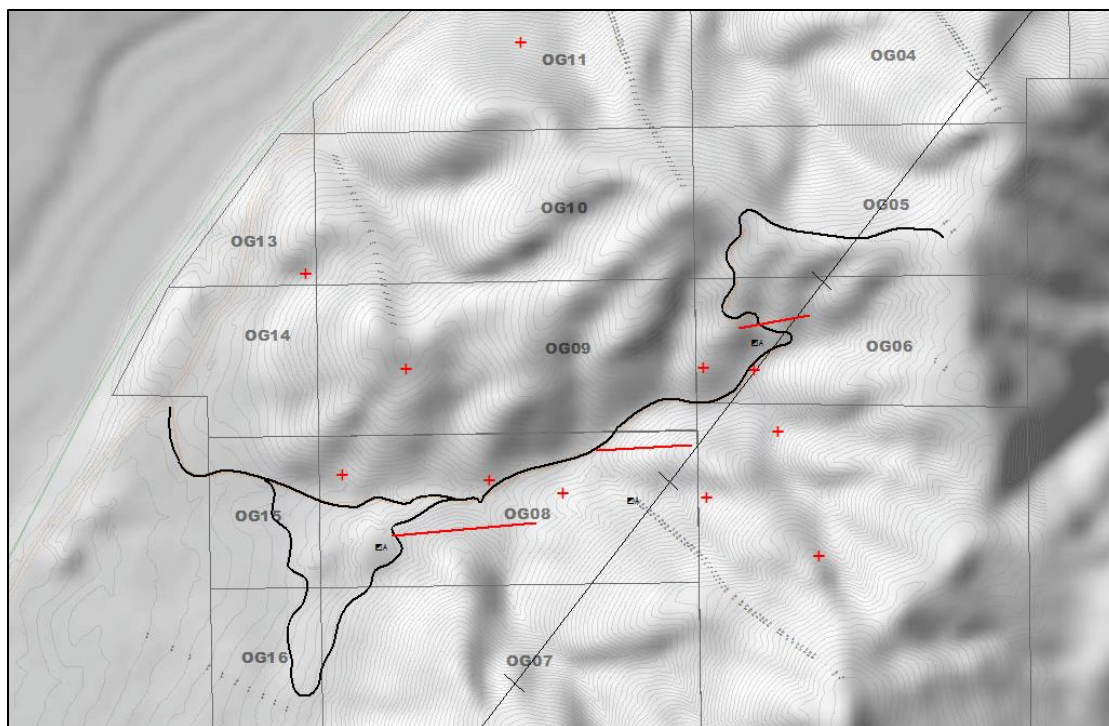


**Figure 9.4. Osborne Jeep trail and vein system. Improving the jeep trail that ascends the Osborne draw would serve the dual purposes of improving access and exposing sections of the Osborne vein. Note northeast trend to en echelon vein sets (red lines).**

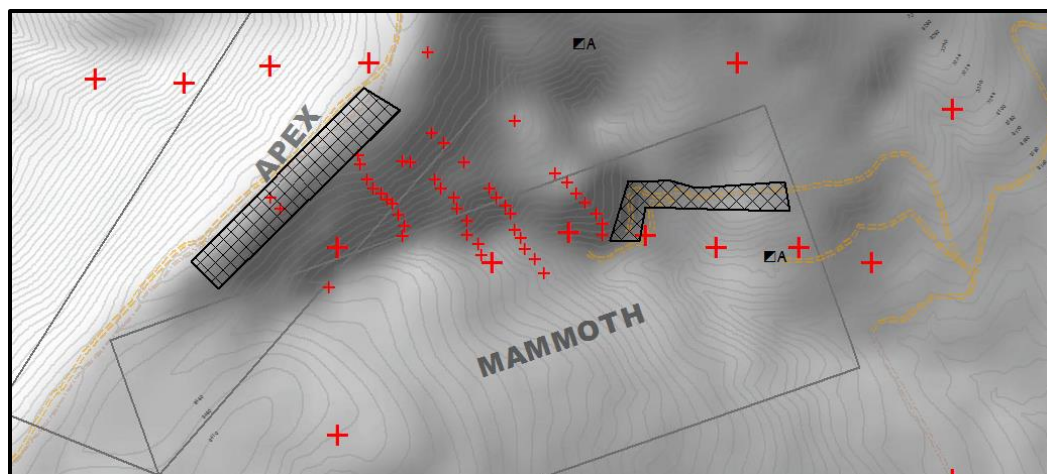


**Figure 9.5.** Areas of proposed Mammoth excavations shown in cross-hatched polygons. Orange lines are preexisting roads or cuts. Red crosses are surface geochemical results of 20ppb or greater.

APPENDIX A  
**Mine Summaries**

Section 6.1 contains brief summaries of every historical mining claim on the property. The list is a compilation of data from the USGS, IGS, and historical reports mentioned above along with claims appearing on the current map of the property, with the exception of the Osborn Group (OG) claims. The OG claims have no historical mention and the areas that they cover have been included under the Hall, Nellie, or Osborn summaries below depending on location. Tables are compiled from data obtained from the IGS. The abbreviation “NOF” in the following tables is defined as Not On File. Table A.1 summarizes the IGS records

**Table A.1. Historical mining claims within Trans-Challis, LLC. Property.  
Compiled from the Idaho Geological Survey.**

<b>Name</b>	<b>IGS #</b>	<b>MILS #</b>	<b>MRDS #</b>	<b>Longitude</b>	<b>Latitude</b>	<b>Township Range Section</b>	<b>UTM North</b>	<b>UTM East</b>
<b>Anticlinal</b>	BO0024	160150174	W0079436	116-16-00W	45-52-37N	6N 2E 7	4858550	560050
<b>Apex Prospect</b>	BO0009	160150163	W007936	116-13-24W	43-54-54N	7N 2E 29	4862500	562350
<b>Atlanta Prospect</b>	BO0013	160150166	W007937	116-13-24W	43-54-54N	7N 2E 28	4862500	562350
<b>Ballentyne</b>	BO0014	160150167	W007834	116-13-09W	43-54-28N	7N 2E 33	4860300	562000
<b>Bobtail</b>	BO0020	160150172	W007941	116-14-42W	43-53-26N	6N 2E 6	4859950	560400
<b>Catherine</b>	NOF	NOF	NOF	NOF	NOF	NOF	NOF	NOF
<b>Clagett Prospect</b>	BO0016	160150168	W007946	116-12-60W	43-54-57N	7N 2E 28	4862600	562900
<b>Hall's Claim</b>	BO0018	160150170	W007934	116-14-30W	43-53-59N	7N 2E 32	4860650	560300
<b>Kentuck Mine</b>	BO0019	160150002	W007916	116-14-21W	43-54-09N	7N 2E 32	4860850	560500
<b>Lambertine</b>	BO0021	160150173	W007942	116-15-35W	45-53-11N	6N 2E 7	4859950	560400
<b>Lost</b>	BO0006	NOF	NOF	116-12-54W	43-54-46N	7N 2E 28	NOF	NOF
<b>Lucky Boy</b>	BO022	160150001	W007918	116-15-39W	43-53-36N	6N 2E 6	4860050	5598000
<b>Mammoth Prospect</b>	BO0008	160150162	W007935	116-13-24W	43-54-54N	7N 2E 28	4862500	562350
<b>Marine</b>	BO0012	160150117	NOF	116-13-59W	43-54-03N	7N 2E 33	NOF	NOF
<b>Mint</b>	BO0023	160150171	W007938	116-14-49W	43-53-19N	6N 2E 5	4859800	559950
<b>Nellie Mine</b>	BO0015	160150003	W007917	116-14-21W	43-54-09N	7N 2E 32	4860950	561150
<b>Osborne Mine</b>	BO0007	160150004	W007919	116-12-57W	43-54-57N	7N 2E 33	4861800	562700
<b>Payette</b>	NOF	NOF	NOF	NOF	NOF	NOF	NOF	NOF
<b>Quaker</b>	NOF	NOF	NOF	NOF	NOF	NOF	NOF	NOF
<b>Sunny Side Prospect</b>	BO0010	160150164	W007835	116-12-42W	43-54-31N	7N 2E 33	4860500	562650
<b>Topeka Prospect</b>	BO0017	160150169	W007837	116-14-12W	43-53-56N	7N 2E 30	4860700	561300
<b>Wonder Prospect*</b>	NOF	NOF	W007933	116-16-55W	43-52-19N	6N 1E 12	4857100	557450

\*Wonder Prospect in the Westview district is not located in property area, all UTM coordinates are in UTM zone 11N. Abbreviations: NOF= Not on file

Name	Mining District	County	Commodity	Owner	Production (oz)	Operation Type	Status	Reference
Anticlinal	WEST VIEW	BOISE	Au Zn	NOF	NR	UNDERG	Unknown	Lindgren, 1898
Apex Prospect	WEST VIEW	BOISE	Au Sb	Private	NR	UNDERG	Unknown	Lindgren, 1898
Atlanta Prospect	WESTVIEW	BOISE	Au Sb	Private	NR	UNDERG	Unknown	Lindgren, 1898
Ballentyne	WESTVIEW	BOISE	Au Sb	BLM	NR	UNDERG	Unknown	Lindgren, 1898
Bobtail	WEST VIEW	BOISE	Au Zn	NOF	NR	UNDERG	Unknown	Lindgren, 1898
Catherine	NOF	BOISE	NOF	NOF	NOF	NOF	NOF	NOF
Clagett Prospect	WEST VIEW	BOISE	Au Sb	BLM	NR	UNDERG	Unknown	Lindgren, 1898
Hall's Claim	WESTVIEW	BOISE	Au Sb	BLM	NR	UNDERG	Past Production	Lindgren, 1898
Kentuck Mine	HORSESHOE BEND	BOISE	Zn Pb Au Ag Cu	BLM	Au: 101-500 Ag: 101-500	UNDERG	Past Production	Anderson, 1934
Lambertine	WEST VIEW	BOISE	Au Zn	NOF	NR	UNDERG	Unknown	Lindgren, 1898
Lost	NOF	BOISE	Au Ag	BLM	Au: 0-50 Ag: 0-50	NOF	NOF	USBM, n.d.; USBM files
Lucky Boy	WEST VIEW	BOISE	Au Pb Hg Ag Zn	NOF	NR	SURF-U	EXP PROS	Anderson, 1934; IBMG P-41
Mammoth Prospect	WEST VIEW	BOISE	Au Sb	Private	NR	UNDERG	Unknown	Lindgren, 1898
Marine	NOF	BOISE	Au Ag	BLM	Au: 0-50 Ag: 0-50	PROSPECT	RAW PROS	USBM, n.d.; USBM files
Mint	WEST VIEW	BOISE	Au Pb Ag Zn	NOF	Au:0-50 Pb:501-1,000(lbs) Ag:51-100	UNDERG	Unknown	Lindgren, 1898
Nellie Mine	HORSESHOE BEND	BOISE	AU	BLM	Au: 51-100 Ag: 0-50	UNDERG	Past Production	Anderson, 1934
Osborne Mine	WESTVIEW	BOISE	Au Ag Zn Pb Cu Sb	BLM	Au: 101-500 Ag: 1001-5000 Cu:501-1001	UNDERG	Past Production	Anderson, 1934
Payette	NOF	BOISE	NOF	NOF	NOF	NOF	NOF	NOF
Quaker	NOF	BOISE	NOF	NOF	NOF	NOF	NOF	NOF
Sunny Side Prospect	WESTVIEW	BOISE	Au Pb	Private	NR	UNDERG	Unknown	Lindgren, 1898
Topeka Prospect	WEST VIEW	BOISE	Au Sb	Private	NR	UNDERG	Unknown	Lindgren, 1898
Wonder Prospect*	WESTVIEW	GEM	Au Zn Pb Cu	NOF	NOF	NOF	NOF	NOF

\*Wonder Prospect in the Westview district is not located in property area. Abbreviations: NOF = Not on file; NR= No Recorded; UNDERG=underground;SURF-U=Surface and underground; EXP PRO=Explored Prospect; RAW PROS=Raw Prospect; BLM=Bureau of Land Management; IBMG=Idaho Bureau of Mining and Geology; USBM=United States Bureau of Mining and Geology

### A.1 Anticlinal

**Table A.2. Anticlinal Claim**

Name	IGS #	MILS #	MRDS #	Mining District	County	Commodity	Owner	Production (oz)	Operation Type
Anticlinal	BO0024	160150174	W0079436	WEST VIEW	BOISE	AU ZN	N.O.F.	No Recorded	UNDERG
Reference	UTM North	UTM East	UTM Zone	Longitude	Latitude	Township	Range	Section	Status
Lindgren, 1898	4858550	560050	11	116-16-00W	45-52-37N	006N	002E	7	Unknown

Lindgren (1898) reported the Anticlinal as a claim east of Rock Creek and under Liberty Cap Hill with no recorded production, it is not in the current property boundary.

### A.2 Apex

**Table A.3. Apex claim**

Name	IGS #	MILS #	MRDS #	Mining District	County	Commodity	Owner	Production (oz)	Operation Type
Apex Prospect	BO0009	160150163	W007936	WEST VIEW	BOISE	AU SB	Private	No Recorded	UNDERG
Reference	UTM North	UTM East	UTM Zone	Longitude	Latitude	Township	Range	Section	Status
Lindgren, 1898	4862500	562350	11	116-13-24W	43-54-54N	007N	002E	29	Unknown

Lindgren (1898) notes that the Apex is along a line of deposits, including the Mammoth, Atlanta, Claggett, Topeka, and Kentuck, that runs and parallel and to the north of a similar line of deposits containing the Ballentyne and Sunny Side. The line is about 1,000 feet above the river, with Hall's claim about 700 feet above the river. He reports the ore as decomposed with free gold on the surface and associated with a gold-free stibnite. Only slight development was reported in 1898.

### A.3 Atlanta

**Table A.4. Atlanta Claim**

Name	IGS #	MILS #	MRDS #	Mining District	County	Commodity	Owner	Production (oz)	Operation Type
Atlanta Prospect	BO0013	160150166	W007937	WESTVIEW	BOISE	AU SB	Private	No Recorded	UNDERG
Reference	UTM North	UTM East	UTM Zone	Longitude	Latitude	Township	Range	Section	Status
Lindgren, 1898	862500	562350	11	116-13-24W	43-54-54N	007N	002E	28	Unknown

Lindgren (1898) notes that the Atlanta is along a line of deposits, including the Mammoth, Apex, Claggett, Topeka, and Kentuck, that runs and parallel and to the north of a similar line of deposits containing the Ballentyne and Sunny Side. The line is about 1,000 feet above the river, with Hall's claim about 700 feet above the river. He reports the ore as decomposed with free gold on the surface and associated with a gold-free stibnite. Only slight development was reported in 1898.

### A.4 Ballentyne

**Table A.5. Ballentyne claim**

Name	IGS #	MILS #	MRDS #	Mining District	County	Commodity	Owner	Production (oz)	Operation Type
Ballentyne	BO0014	160150167	W007834	WESTVIEW	BOISE	AU PB	BLM	No Recorded	UNDERG
Reference	UTM North	UTM East	UTM Zone	Longitude	Latitude	Township	Range	Section	Status
Lindgren, 1898	4860300	562000	11	116-13-09W	43-54-28N	007N	002E	33	Unknown

Lindgren (1898) reports the Ballentyne as being on a line of veins that begin where the northeast trending ridge on the property intersects the Payette River at the eastern extent of the ridge. The vein the Ballentyne is located on is the same that hosts the Sunny Side claim, dips 70°-80°, and is about 2 feet wide. Lindgren (1898) does not give the strike or dip direction of the vein but does describe the vein as “soft and decomposed”, containing free gold and lead carbonate (cerussite), and that a similar vein

is a “short distance” south. The country rock is granite and the vein is associated with a quartz-diorite porphyry dike in the foot wall of the mine.

### A.5 Bobtail

**Table A.6. Bobtail claim**

Name	IGS #	MILS #	MRDS #	Mining District	County	Commodity	Owner	Production (oz)	Operation Type
Bobtail	BO0020	160150172	W007941	WEST VIEW	BOISE	AU ZN	NOF	No Recorded	UNDERG
Reference	UTM North	UTM East	UTM Zone	Longitude	Latitude	Township	Range	Section	Status
Lindgren, 1898	4859950	560400	11	116-14-42W	43-53-26N	006N	002E	5	Unknown

Lindgren (1898) reported the Bobtail as a claim  $\frac{3}{4}$  of a mile east of Rock Creek, with a 200 ft. tunnel intersecting an 8-foot vein of good ore.

### A.6 Catherine

**Table A.7. Catherine claim**

Name	IGS #	MILS #	MRDS #	Mining District	County	Commodity	Owner	Production (oz)	Operation Type
Catherine	N.O.F.	N.O.F.	N.O.F.	N.O.F.	BOISE	N.O.F.	N.O.F.	N.O.F.	N.O.F.
Reference	UTM North	UTM East	UTM Zone	Longitude	Latitude	Township	Range	Section	Status
N.O.F.	N.O.F.	N.O.F.	N.O.F.	N.O.F.	N.O.F.	N.O.F.	N.O.F.	N.O.F.	N.O.F.

The Catherine Claim is named within the current property boundary; no historical mention has been found.

### A.7 Claggett

**Table A.8. Claggett claim.**

Name	IGS #	MILS #	MRDS #	Mining District	County	Commodity	Owner	Production (oz)	Operation Type
Claggett Prospect	BO0016	160150168	W007946	WEST VIEW	BOISE	AU SB	BLM	No Recorded	UNDERG
Reference	UTM North	UTM East	UTM Zone	Longitude	Latitude	Township	Range	Section	Status
Lindgren, 1898	4862600	562900	11	116-12-60W	43-54-57N	007N	002E	28	Unknown

Lindgren (1898) notes that the Claggett is along a line of deposits, including the Mammoth, Apex, Atlanta, Topeka, and Kentuck, that runs and parallel and to the north of

a similar line of deposits containing the Ballentyne and Sunny Side. The line is about 1,000 feet above the river, with Hall's claim about 700 feet above the river. He reports the ore as decomposed with free gold on the surface and associated with a gold-free stibnite. Only slight development was reported in 1898.

### A.8 Hall

**Table A.9. Hall claim**

Name	IGS #	MILS #	MRDS #	Mining District	County	Commodity	Owner	Production (oz)	Operation Type
Hall's Claim	BO0018	160150170	W007934	WEST VIEW	BOISE	AU Sb	BLM	No Recorded	UNDERG
Reference	UTM North	UTM East	UTM Zone	Longitude	Latitude	Township	Range	Section	Status
Lindgren, 1898	4860650	560300	11	116-14-30W	43-53-59N	007N	002E	32	Past Pro

Lindgren (1898) notes that the Hall claim is along a line of deposits, including the Mammoth, Apex, Atlanta, Claggett, Topeka, and Kentuck, that runs and parallel and to the north of a similar line of deposits containing the Ballentyne and Sunny Side. The line is about 1,000 feet above the river, with Hall's claim about 700 feet above the river. He reports the ore as decomposed with free gold on the surface and associated with a gold-free stibnite. Only slight development was reported in 1898.

### A.9 Kentuck

**Table A.10. Kentuck claim**

Name	IGS #	MILS #	MRDS #	Mining District	County	Commodity	Owner	Production (oz)	Operation Type
Kentuck Mine	BO0019	160150002	W007916	HORSESHOE BEND	BOISE	ZN PB AU AG CU	BLM	Au: 101-500 Ag: 101-500	UNDERG
Reference	UTM North	UTM East	UTM Zone	Longitude	Latitude	Township	Range	Section	Status
Anderson, 1934; Leppert and Gillerman, 2005	4860850	560500	11	116-14-21W	43-54-09N	007N	002E	32	Past Pro

Lindgren (1898) notes that the Kentuck is along a line of deposits, including the Mammoth, Apex, Atlanta, Claggett, and Topeka that runs and parallel and to the north of a similar line of deposits containing the Ballentyne and Sunny Side. The line is about

1,000 feet above the river, with Hall's claim about 700 feet above the river. He reports the ore as decomposed with free gold on the surface and associated with a gold-free stibnite. Only slight development was reported in 1898.

Anderson (1934) also reports on the Kentuck claim. The Kentuck is hosted in sheared and altered diorite and proximal to east-northeast and west-northwest trending dacite and granite porphyry dikes. By 1934 the lode had been intersected by a crosscut 900 feet below surface exposure and presumably 100 feet above the river. The load is heavily fractured at the level of the crosscut but intermediate workings had ore bodies reported as 4 to 9 feet thick. Arsenopyrite and pyrite, minor sphalerite and galena, in a quartz-carbonate gangue compose the stringers, seams, and lenses that characterize the ore.

#### A.10 Lambertine

**Table A.11. Lambertine claim**

Name	IGS #	MILS #	MRDS #	Mining District	County	Commodity	Owner	Production (oz)	Operation Type
Lambertine	BO0021	160150173	W007942	WEST VIEW	BOISE	AU ZN	NOF	No Recorded	UNDERG
Reference	UTM North	UTM East	UTM Zone	Longitude	Latitude	Township	Range	Section	Status
Lindgren, 1898	4859950	560400	11	116-15-35W	45-53-11N	006N	002E	5	Unknown

Lindgren (1898) reported the Lambertine as a claim  $\frac{3}{4}$  of a mile east of Rock Creek with little work done on it in 1896.

#### A.11 Lost

**Table A.12. Lost claim**

Name	IGS #	MILS #	MRDS #	Mining District	County	Commodity	Owner	Production (oz)	Operation Type
Lost	BO0006	N.O.F.	N.O.F.	N.O.F.	BOISE	AU AG	BLM	Au: 0-50 Ag: 0-50	N.O.F.
Reference	UTM North	UTM East	UTM Zone	Longitude	Latitude	Township	Range	Section	Status
USBM, n.d.; USBM	N.O.F.	N.O.F.	N.O.F.	116-12-54W	43-54-46N	007N	002E	28	N.O.F.

The Lost claim has no known information beyond that presented in tables A.1 and A.12.

### A.12 Lucky Boy

**Table A.13. Lucky boy claim**

Name	IGS #	MILS #	MRDS #	Mining District	County	Commodity	Owner	Production (oz)	Operation Type
Lucky Boy	BO022	160150001	W007918	WEST VIEW	BOISE	AU PB HG AG ZN	N.O.F.	No Recorded	SURF-U
Reference	UTM North	UTM East	UTM Zone	Longitude	Latitude	Township	Range	Section	Status
Anderson, 1934; IBMG P-41	4860050	5598000	11	116-15-39W	43-53-36N	006N	002E	6	EXP PROS

The Lucky Boy lies just west of the current property boundaries near the top of the eastern ridge that lines the Rock Creek Gully.

### A.13 Mammoth

**Table A.14. Mammoth claim**

Name	IGS #	MILS #	MRDS #	Mining District	County	Commodity	Owner	Production (oz)	Operation Type
Mammoth Prospect	BO0008	160150162	W007935	WEST VIEW	BOISE	AU SB	Private	No Recorded	UNDERG
Reference	UTM North	UTM East	UTM Zone	Longitude	Latitude	Township	Range	Section	Status
Lindgren, 1898	4862500	562350	11	116-13-24W	43-54-54N	007N	002E	28	Unknown

Lindgren (1898) notes that the Mammoth is along a line of deposits, including the Kentuck, Apex, Atlanta, Claggett, and Topeka that runs and parallel and to the north of a similar line of deposits containing the Ballentyne and Sunny Side. The line is about 1,000 feet above the river, with Hall's claim about 700 feet above the river. He reports the ore as decomposed with free gold on the surface and associated with a gold-free stibnite. Only slight development was reported in 1898.

### A.14 Marine

**Table A.15. Marine Claim**

Name	IGS #	MILS #	MRDS #	Mining District	County	Commodity	Owner	Production (oz)	Operation Type
Marine	BO0012	160150117	N.O.F.	N.O.F.	BOISE	AU AG	BLM	Au: 0-50 Ag: 0-50	PROSPE
Reference	UTM North	UTM East	UTM Zone	Longitude	Latitude	Township	Range	Section	Status
USBM, n.d.; USBM	N.O.F.	N.O.F.	N.O.F.	116-13-59W	43-54-03N	007N	002E	33	RAW PROS

The Marine claim has no known information beyond that presented in tables A.1 and A.12.

### A.15 Mint

**Table A.16. Mint claim**

Name	IGS #	MILS #	MRDS #	Mining District	County	Commodity	Owner	Production (oz)	Operation Type
Mint	BO0023	160150171	W007938	WEST VIEW	BOISE	AU PB AG ZN	NOF	AU:0-50 PB:501-1,000(lbs) AG:51-100	UNDERG
Reference	UTM North	UTM East	UTM Zone	Longitude	Latitude	Township	Range	Section	Status
Lindgren, 1898	4859800	559950	11	116-14-49W	43-53-19N	006N	002E	5	Unknown

Lindgren (1898) reported the Mint as a claim  $\frac{3}{4}$  of a mile east of Rock Creek with little work done on it in 1896.

### A.16 Nellie

**Table A.17. Nellie claim**

Name	IGS #	MILS #	MRDS #	Mining District	County	Commodity	Owner	Production (oz)	Operation Type
Nellie Mine	BO0015	160150003	W007917	HORSESHOE BEND	BOISE	AU	BLM	Au: 51-100 Ag: 0-50	UNDERG
Reference	UTM North	UTM East	UTM Zone	Longitude	Latitude	Township	Range	Section	Status
Anderson, 1934	4860950	561150	11	116-14-21W	43-54-09N	007N	002E	32	PAST PRO

Anderson (1934) first described the Nellie, at the time no underground workings were still accessible but he states that reports indicate an ~1,800 ft. crosscut tunnel that projected to about 800 to 900 feet below outcrop. As of 1934 a ten stamp mill on site had

already been dismantled. Diorite is the country rock and the lode is proximal to dacite porphyry dikes. Surface exposures of the load were 8 to 10 feet thick but no surface strike, dip, or length is given. Smaller, 2-10 inch thick, shoots of ore are in the vicinity, some reportedly intersecting the crosscut tunnel. Assays of the ores were from 0.25 to 1.25 oz./ton, with the main load at about .50 oz./ton. Pyrite and arsenopyrite are contained in the ore.

### A.17 Osborne

**Table A.18. Osborne claim**

Name	IGS #	MILS #	MRDS #	Mining District	County	Commodity	Owner	Production (oz)	Operation Type
Osborne Mine	BO0007	160150004	W007919	WESTVIEW	Boise	AU AG ZN PB CU SB	BLM	10-500	UNDERG
Reference	UTM North	UTM East	UTM Zone	Longitude	Latitude	Township	Range	Section	Status
Anderson, 1934	4861800	562700	11	116-12-57W	43-54-57N	007N	002E	33	Past Pro

The Osborne Mine and the OG01-16 group of claims are located about 1.25 miles west of Horseshoe Bend and within ¼ mile of the Payette River to the west. Access is along the Old Emmett Road, a well maintained improved dirt road used to access the county solid waste transfer station, and a short section of unimproved dirt road. Water is available via water rights secured by riverfront property. Power to the site is 3 phase 440. The old mill site is at an elevation of 2750 ft. and old workings extended up the gully to about 3050 ft.

Anderson (1934) reports a maximum shaft depth of 400 feet with drifts on the 200, 300, and 400 foot levels, ~5,000 feet of drifts, and lodes from 2 to 12 feet thick. Hand selected ore was assayed at up to 1.92 oz./ton with an average of 0.40 oz./ton. The majority of work was done before 1910, 2,000 tons of ore were removed from 1910-1919, no mention of pre-1910 production was found. Production was discontinued by

1919 due to poor recovery by the cyaniding and amalgamation methods of the time.

Lodes at the Osborne strike generally 070 and dip steeply north except for one that dips south. Dacite dikes associated, but not in contact, with mineralization in the area strike either northeast or west-northwest and are hosted in the diorite stock. Post ore shearing has created gouge bands up to several inches thick. Sunshine Mining recommended future exploration of the Osborne area in a 1981 memo.

### A.18 Payette

**Table A.19. Payette claim**

Name	IGS #	MILS #	MRDS #	Mining District	County	Commodity	Owner	Production (oz)	Operation Type
Payette	N.O.F.	N.O.F.	N.O.F.	N.O.F.	BOISE	N.O.F.	N.O.F.	N.O.F.	N.O.F.
Reference	UTM North	UTM East	UTM Zone	Longitude	Latitude	Township	Range	Section	Status
N.O.F.	N.O.F.	N.O.F.	N.O.F.	N.O.F.	N.O.F.	N.O.F.	N.O.F.	N.O.F.	N.O.F.

The Payette is a claim named in the current property boundary; no historical mention.

### A.19 Quaker

**Table A.20. Quaker claim**

Name	IGS #	MILS #	MRDS #	Mining District	County	Commodity	Owner	Production (oz)	Operation Type
Quaker	N.O.F.	N.O.F.	N.O.F.	N.O.F.	BOISE	N.O.F.	N.O.F.	N.O.F.	N.O.F.
Reference	UTM North	UTM East	UTM Zone	Longitude	Latitude	Township	Range	Section	Status
N.O.F.	N.O.F.	N.O.F.	N.O.F.	N.O.F.	N.O.F.	N.O.F.	N.O.F.	N.O.F.	N.O.F.

The Quaker is a claim named in the current property boundary; no historical mention.

## A.20 Sunny Side

**Table A.21. Sunny Side claim**

Name	IGS #	MILS #	MRDS #	Mining District	County	Commodity	Owner	Production (oz)	Operation Type
Sunny Side Prospect (Sunlight)	BO0010	160150164	W007835	WEST VIEW	BOISE	AU PB	Private	No Recorded	UNDERG
Reference	UTM North	UTM East	UTM Zone	Longitude	Latitude	Township	Range	Section	Status
Lindgren, 1898	4860500	562650	11	116-12-42W	43-54-31N	007N	002E	33	Unknown

Lindgren (1898) reports the Sunny Side as being on a line of veins that begin where the northeast trending ridge on the property intersects the Payette River at the eastern extent of the ridge. The vein the Sunny Side is located on is the same that hosts the Ballentyne claim, dips 70°-80°, and is about 2 feet wide. Lindgren (1898) does not give the strike or dip direction of the vein but does describe the vein as “soft and decomposed”, containing free gold and lead carbonate (cerussite), and that a similar vein is a “short distance” south. The country rock is granite and the vein is associated with a quartz-diorite porphyry dike in the foot wall of the mine.

## A.21 Topeka

**Table A.22. Topeka claim**

Name	IGS #	MILS #	MRDS #	Mining District	County	Commodity	Owner	Production (oz)	Operation Type
Topeka Prospect	BO0017	160150169	W007837	WEST VIEW	BOISE	AU SB	Private	No Recorded	UNDERG
Reference	UTM North	UTM East	UTM Zone	Longitude	Latitude	Township	Range	Section	Status
Lindgren, 1899	4860700	561300	11	116-14-12W	43-53-56N	007N	002E	30	Unknown

Lindgren (1898) notes that the Topeka is along a line of deposits, including the Mammoth, Apex, Atlanta, Claggett, and Kentuck, that runs and parallel and to the north of a similar line of deposits containing the Ballentyne and Sunny Side. The line is about 1,000 feet above the river, with Hall’s claim about 700 feet above the river. He reports

the ore as decomposed with free gold on the surface and associated with a gold-free stibnite. Only slight development was reported in 1898.

APPENDIX B

**Drill Records**

All drill records are from the Sunshine exploration program of 1980-1982 and do not include any data from the current property area. Table is verbatim from Sunshine Mining. No discussion of the drilling is presented here.

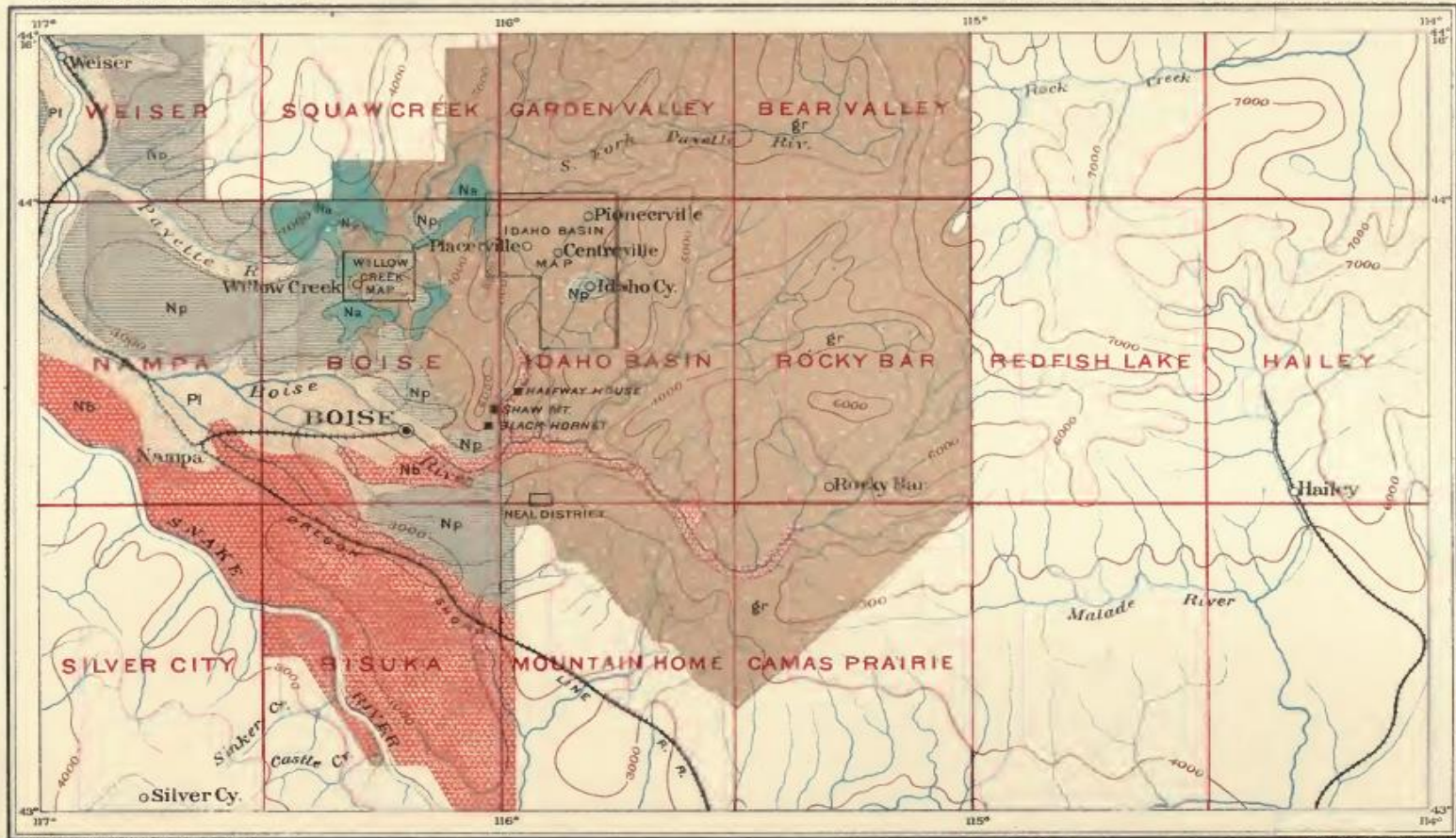
**Table B.1. Summary of the Sunshine Mining drilling program from the 1980 to 1982 exploration of the Pearl Mining District. Note that none of these holes are in the current property area.**

<u>DRILL HOLE DATA</u>			
Hole No.:	<u>DDH-81-5</u>	<u>DDH-81-6</u>	<u>DDH-81-7</u>
Bearing:	S. 28 W.	S. 7 W.	S. 25 W.
Inclination:	-62°	-46°	-45°
Property:	Lincoln	Granite State	Granite State
Feature; location:	Below old workings E. of shaft	El Paso vein; El Paso claim	El Paso vein; El Paso claim
Coordinates: N. E.			
Collar Elev. (approx.)	4058	4572	4617
Size Hole:	HQ/NQ	HQ	HQ/NQ
% Recovery Bedrock: Vein Zone:	86.2 -	89.1 64.3	89.1 42.1
Depth: Overburden: Main target vein: Total (bottom):	22.6 - 640.0	21.6 149.5 400.0	2.0 187.0 423.0
Drilled by:	Udy	Udy	Udy
Logged by:	T. Alvarez D. Hall	D. Hall	D. Hall
Sampled by:	D. Hall	G. Ojala D. Hall	D. Hall

APPENDIX C

**Geologic Maps**





Topography by U.S. Geological Survey.

Geology by W. Lindgren.

GENERAL MAP OF THE LOWER SNAKE RIVER VALLEY, IDAHO

Scale of miles

Contour Interval 1000 feet

LEGEND

PLEISTOCENE

PI SANDS & GRAVEL, River terraces.

NEOGENE

Np PAYETTE FORMATION Sandy Lake beds, Early Neocene

Na BASALT AND RHYOLITE of the age of the Payette Lake beds.

Nb BASALT (Late Neocene) with Lake beds of same age

PRE-NEOCENE

gr GRANITE

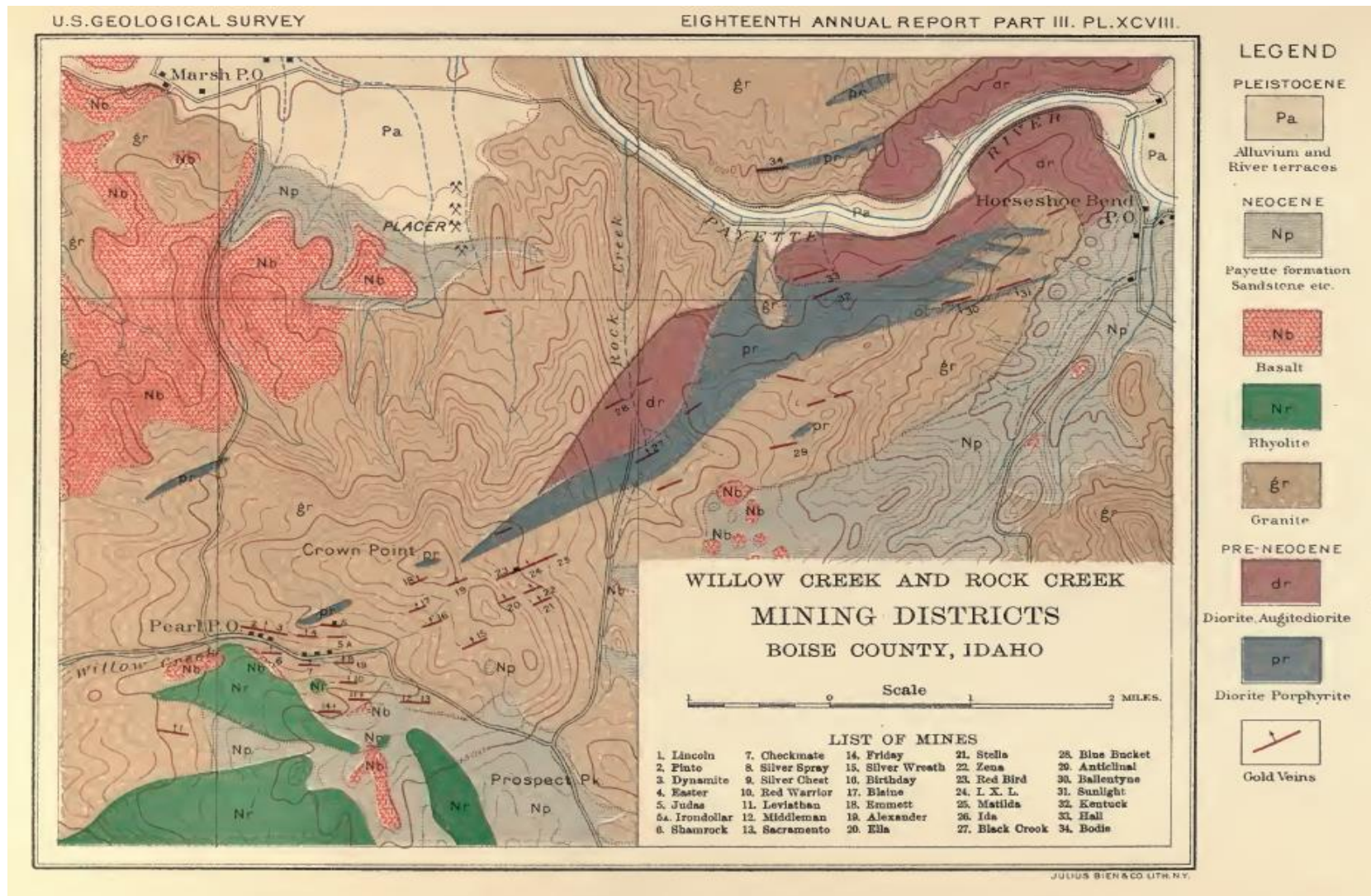


Figure C.2. Geologic map of the Pearl to Horseshoe Bend mining districts from Lindgren (1898).

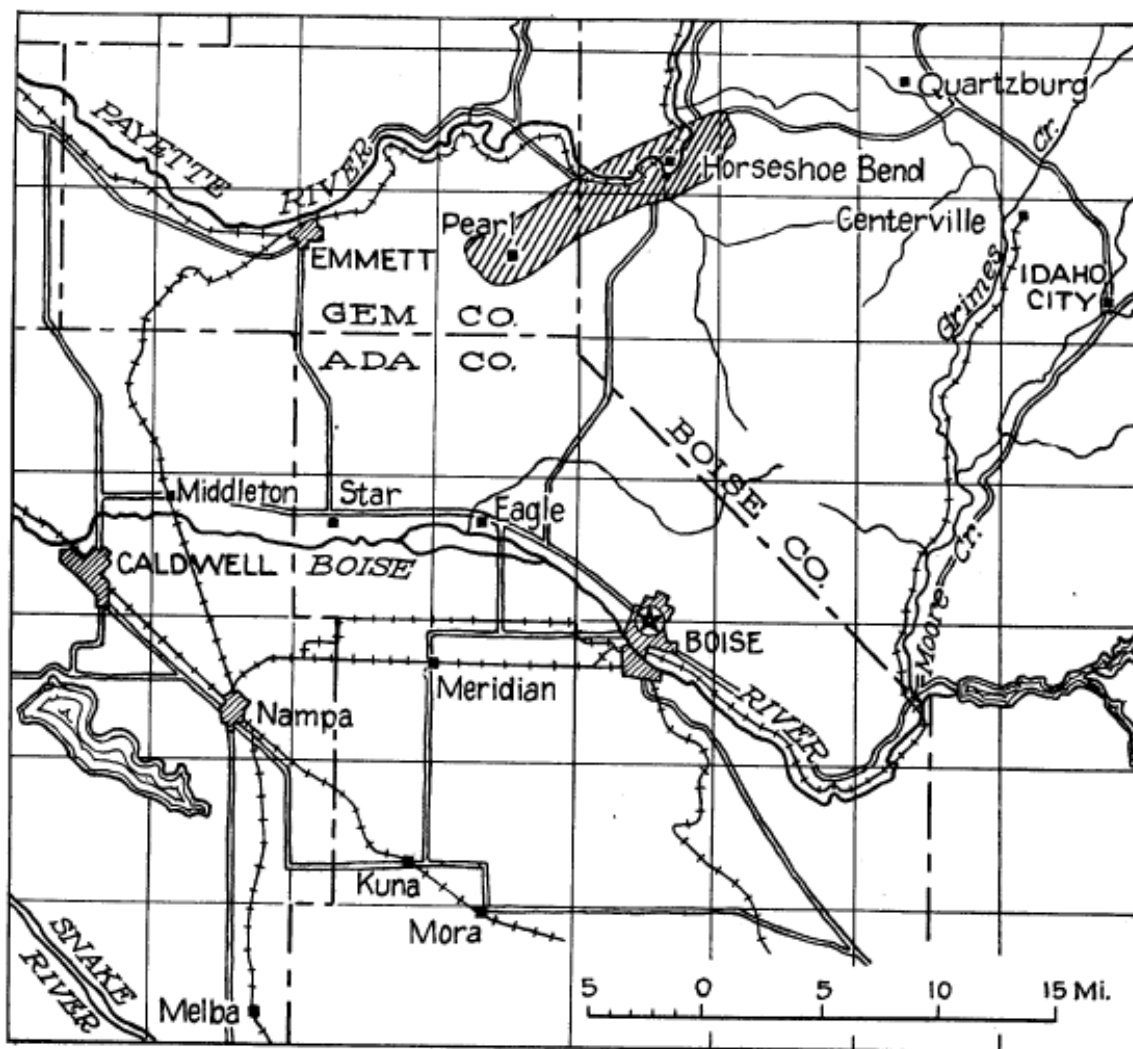


Figure C.3. Map showing location of the Pearl to Horseshoe Bend mining districts from Anderson (1934).

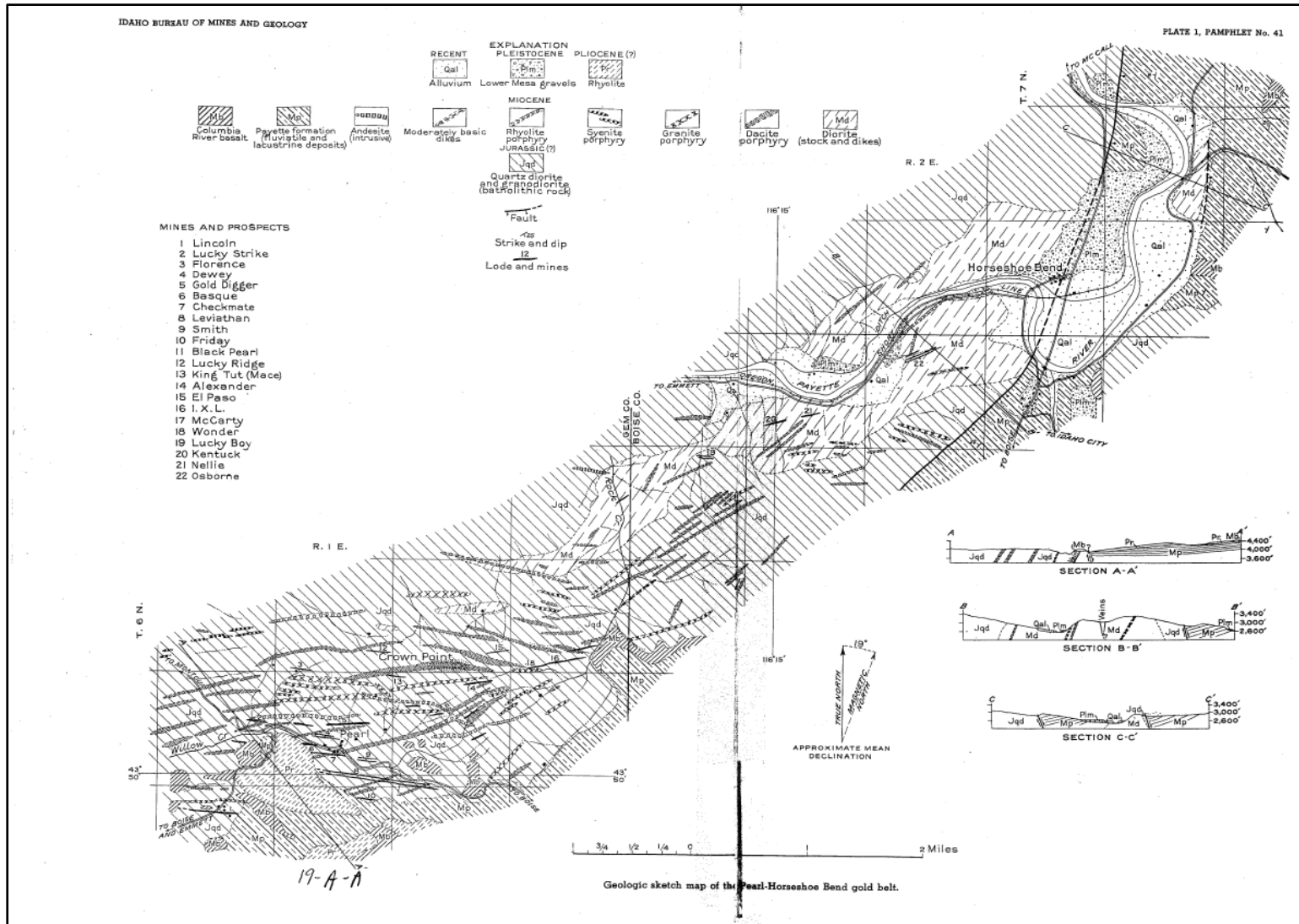


Figure C.4. Geologic map of the Pearl to Horseshoe Bend mining districts from Anderson (1934).

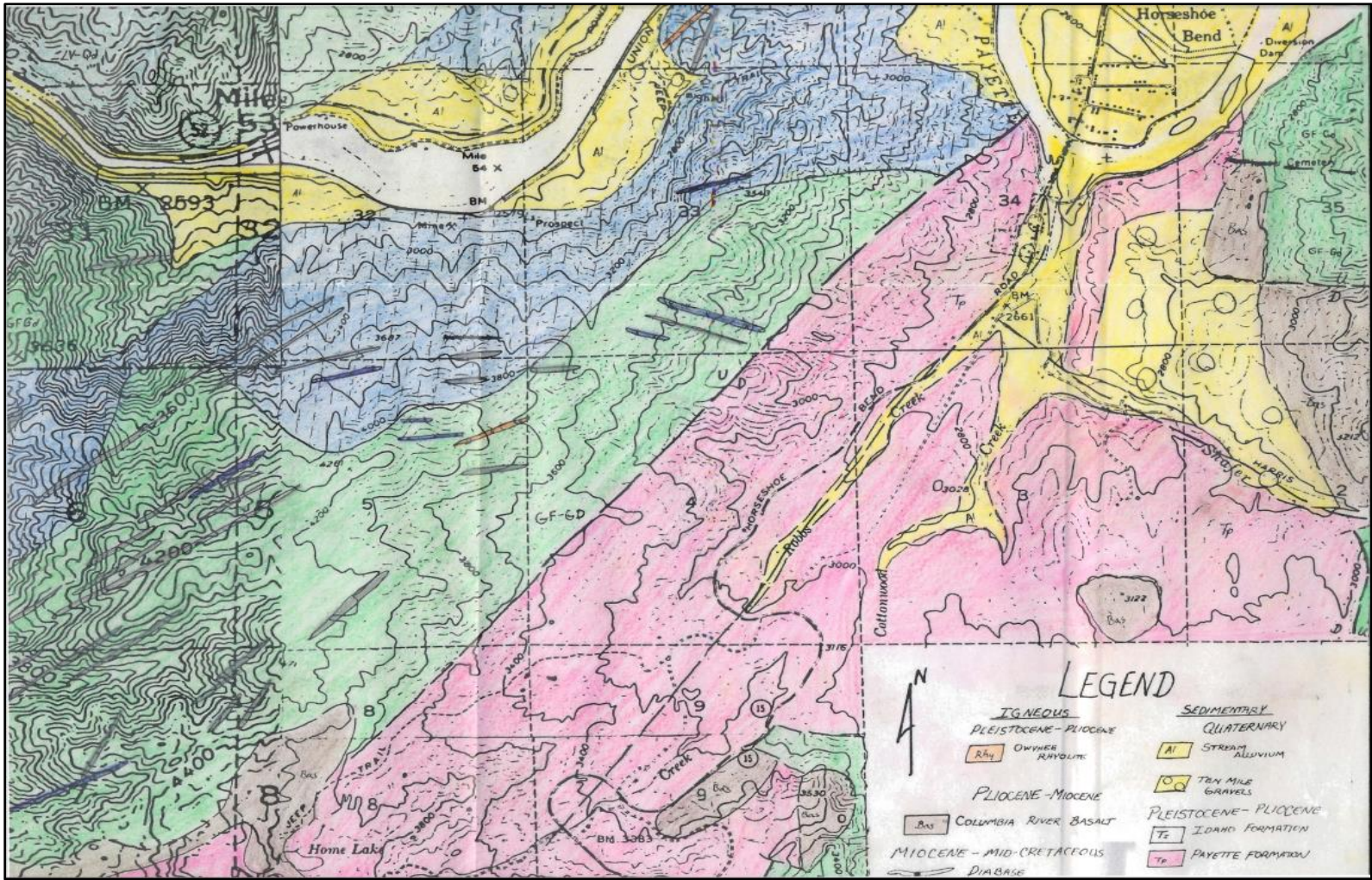


Figure C.5. Geologic map of the property and surrounding area from Alvarez and Ojala (1981)

APPENDIX D

**ALS Geochemistry Lab Methods**

#### Au-ICP21 methods

Sample Decomposition: Fire Assay Fusion (FA-FUSPG1 & FA-FUSPG2).

Analytical Method: Inductively Coupled Plasma – Atomic Emission Spectrometry (ICP-AES).

A prepared sample is fused with a mixture of lead oxide, sodium carbonate, borax, silica and other reagents as required, inquarted with 6 mg of gold-free silver and then cupelled to yield a precious metal bead.

The bead is digested in 0.5 mL dilute nitric acid in the microwave oven. 0.5 mL concentrated hydrochloric acid is then added and the bead is further digested in the microwave at a lower power setting. The digested solution is cooled, diluted to a total volume of 4 mL with de-mineralized water, and analyzed by inductively coupled plasma atomic emission spectrometry against matrix-matched standards.

#### Au-GRA21 methods

Sample Decomposition: Fire Assay Fusion (FA-FUSAG1, FA-FUSAG2, FA-FUSGV1 and FA-FUSGV2). Analytical Method: Gravimetric.

A prepared sample is fused with a mixture of lead oxide, sodium carbonate, borax, silica and other reagents in order to produce a lead button. The lead button containing the precious metals is cupelled to remove the lead. The remaining gold and silver bead is parted in dilute nitric acid, annealed and weighed as gold. Silver, if requested, is then determined by the difference in weights.

#### Au-TL43/44 methods

Sample Decomposition: aqua regia gold digestion.

Analytical Method: Inductively coupled mass spectrometry (ICPMS) or Atomic absorption spectrometry (AAS)

A finely pulverised sample (25 – 50 g) is digested in a mixture of 3 parts hydrochloric acid and 1 part nitric acid (aqua regia). This acid mixture generates nascent chlorine and nitrosyl chloride, which will dissolve free gold and gold compounds such as calaverite, AuTe<sub>2</sub>. The dissolved gold is complexed and extracted with Kerosene/DBS and determined by graphite furnace AAS. Alternatively gold is determined by ICPMS directly from the digestion liquor. This method allows for the simple and economical addition of extra elements by running the digestion liquor through the ICPAES or ICPMS.

Note: Samples high in sulphide or carbon content may lead to low gold recoveries unless they are roasted prior to digestion.

#### Au-AA23/24 methods

Sample Decomposition: Fire Assay Fusion (FA-FUS01 & FA-FUS02)

Analytical Method: Atomic Absorption Spectroscopy (AAS)

A prepared sample is fused with a mixture of lead oxide, sodium carbonate, borax, silica and other reagents as required, inquarted with 6 mg of gold-free silver and then cupelled to yield a precious metal bead. The bead is digested in 0.5 mL dilute nitric acid in the microwave oven, 0.5 mL concentrated hydrochloric acid is then added and the bead is further digested in the microwave at a lower power setting. The digested solution is cooled, diluted to a total volume of 4 mL with de-mineralized water, and analyzed by atomic absorption spectroscopy against matrix-matched standards.

ME-MS41 methods

Sample decomposition: Aqua Regia Digestion (GEO-AR01)

Analytical Method: ICP-MS or ICP-AES

A prepared sample (0.50 g) is digested with aqua regia in a graphite heating block. After cooling, the resulting solution is diluted to with deionized water, mixed and analyzed by inductively coupled plasma-atomic emission spectrometry. Following this analysis, the results are reviewed for high concentrations of bismuth, mercury, molybdenum, and element spectral interferences.

## APPENDIX E

**Magnetic Anomaly Matlab Code**

## Magnetic anomaly

View Data code

```
clear all
close all

load processed_data1.mat
xi1 = XI;
yi1 = YI;
mag1 = ZI2;
x1 = x;
y1 = y;

clear XI YI ZI2 x y

load processed_data2.mat
xi2 = XI;
yi2 = YI;
mag2 = ZI2;
x2 = x;
y2 = y;

clear XI YI ZI2 x y

load processed_data3.mat
xi3 = XI;
yi3 = YI;
mag3 = ZI2;
x3 = x;
y3 = y;

clear XI YI ZI2 x y

load processed_data4.mat
xi4 = XI;
yi4 = YI;
mag4 = ZI2;
x4 = x;
y4 = y;

clear XI YI ZI2 x y

load processed_data6.mat
xi6 = XI;
yi6 = YI;
mag6 = ZI2;
x6 = x;
y6 = y;

clear XI YI ZI2 x y

load processed_data7.mat
xi7 = XI;
```

```
Yi7 = YI;  
mag7 = ZI2;  
x7 = x;  
y7 = y;  
  
clear XI YI ZI2 x y  
  
load processed_data8.mat  
xi8 = XI;  
Yi8 = YI;  
mag8 = ZI2;  
x8 = x;  
y8 = y;  
  
clear XI YI ZI2 x y  
  
load processed_data9.mat  
xi9 = XI;  
Yi9 = YI;  
mag9 = ZI2;  
x9 = x;  
y9 = y;  
  
clear XI YI ZI2 x y  
  
load processed_data10.mat  
xi10 = XI;  
Yi10 = YI;  
mag10 = ZI2;  
x10 = x;  
y10 = y;  
  
clear XI YI ZI2 x y  
  
load processed_data11.mat  
xi11 = XI;  
Yi11 = YI;  
mag11 = ZI2;  
x11 = x;  
y11 = y;  
  
clear XI YI ZI2 x y  
  
load processed_data12.mat  
xi12 = XI;  
Yi12 = YI;  
mag12 = ZI2;  
x12 = x;  
y12 = y;  
  
clear XI YI ZI2 x y  
  
load processed_data13.mat  
xi13 = XI;
```

```
Yi13 = YI;
mag13 = ZI2;
x13 = x;
y13 = y;

clear XI YI ZI2 x y

load processed_data14.mat
xi14 = XI;
Yi14 = YI;
mag14 = ZI2;
x14 = x;
y14 = y;

clear XI YI ZI2 x y

load processed_data15.mat
xi15 = XI;
Yi15 = YI;
mag15 = ZI2;
x15 = x;
y15 = y;

clear XI YI ZI2 x y

load processed_data16.mat
xi16 = XI;
Yi16 = YI;
mag16 = ZI2;
x16 = x;
y16 = y;

clear XI YI ZI2 x y

load processed_data17.mat
xi17 = XI;
Yi17 = YI;
mag17 = ZI2;
x17 = x;
y17 = y;

clear XI YI ZI2 x y

load processed_data18.mat
xi18 = XI;
Yi18 = YI;
mag18 = ZI2;
x18 = x;
y18 = y;

clear XI YI ZI2 x y

load processed_data19.mat
xi19 = XI;
```

```
Yi19 = YI;
mag19 = ZI2;
x19 = x;
y19 = y;

clear XI YI ZI2 x y

load processed_data20.mat
xi20 = XI;
Yi20 = YI;
mag20 = ZI2;
x20 = x;
y20 = y;

clear XI YI ZI2 x y

load processed_data21.mat
xi21 = XI;
Yi21 = YI;
mag21 = ZI2;
x21 = x;
y21 = y;

clear XI YI ZI2 x y

load processed_data22.mat
xi22 = XI;
Yi22 = YI;
mag22 = ZI2;
x22 = x;
y22 = y;

clear XI YI ZI2 x y

load processed_data23.mat
xi23 = XI;
Yi23 = YI;
mag23 = ZI2;
x23 = x;
y23 = y;

clear XI YI ZI2 x y

load processed_data24.mat
xi24 = XI;
Yi24 = YI;
mag24 = ZI2;
x24 = x;
y24 = y;

clear XI YI ZI2 x y

load processed_data25.mat
xi25 = XI;
```

```

Yi25 = YI;
mag25 = ZI2;
x25 = x;
y25 = y;

clear XI YI ZI2 x y

load processed_data26.mat
xi26 = XI;
Yi26 = YI;
mag26 = ZI2;
x26 = x;
y26 = y;

clear XI YI ZI2 x y

xx =
[x1;x2;x3;x4;x6;x7;x8;x9;x10;x11;x12;x13;x14;x15;x16;x17;x18;x19;x20;x21;x22;x23;x24;x25;
x26];
yy =
[y1;y2;y3;y4;y6;y7;y8;y9;y10;y11;y12;y13;y14;y15;y16;y17;y18;y19;y20;y21;y22;y23;y24;y25;
y26];

figure(1)

contourf(xi1,Yi1,mag1)
axis([min(xx) max(xx) min(yy) max(yy)])
hold on
contourf(xi2,Yi2,mag2)
axis([min(xx) max(xx) min(yy) max(yy)])
contourf(xi3,Yi3,mag3)
axis([min(xx) max(xx) min(yy) max(yy)])
contourf(xi4,Yi4,mag4)
axis([min(xx) max(xx) min(yy) max(yy)])
contourf(xi6,Yi6,mag6)
axis([min(xx) max(xx) min(yy) max(yy)])
contourf(xi7,Yi7,mag7)
axis([min(xx) max(xx) min(yy) max(yy)])
contourf(xi8,Yi8,mag8)
axis([min(xx) max(xx) min(yy) max(yy)])
contourf(xi9,Yi9,mag9)
axis([min(xx) max(xx) min(yy) max(yy)])
contourf(xi10,Yi10,mag10)
axis([min(xx) max(xx) min(yy) max(yy)])
contourf(xi11,Yi11,mag11)
axis([min(xx) max(xx) min(yy) max(yy)])
contourf(xi12,Yi12,mag12)
axis([min(xx) max(xx) min(yy) max(yy)])
contourf(xi13,Yi13,mag13)
axis([min(xx) max(xx) min(yy) max(yy)])
contourf(xi14,Yi14,mag14)
axis([min(xx) max(xx) min(yy) max(yy)])
contourf(xi15,Yi15,mag15)
axis([min(xx) max(xx) min(yy) max(yy)])

```

```
contourf(Xi16,Yi16,mag16)
axis([min(xx) max(xx) min(yy) max(yy)])
contourf(Xi17,Yi17,mag17)
axis([min(xx) max(xx) min(yy) max(yy)])
contourf(Xi18,Yi18,mag18)
axis([min(xx) max(xx) min(yy) max(yy)])
contourf(Xi19,Yi19,mag19)
axis([min(xx) max(xx) min(yy) max(yy)])
contourf(Xi20,Yi20,mag20)
axis([min(xx) max(xx) min(yy) max(yy)])
contourf(Xi21,Yi21,mag21)
axis([min(xx) max(xx) min(yy) max(yy)])
contourf(Xi22,Yi22,mag22)
axis([min(xx) max(xx) min(yy) max(yy)])
contourf(Xi23,Yi23,mag23)
axis([min(xx) max(xx) min(yy) max(yy)])
contourf(Xi24,Yi24,mag24)
axis([min(xx) max(xx) min(yy) max(yy)])
contourf(Xi25,Yi25,mag25)
axis([min(xx) max(xx) min(yy) max(yy)])
contourf(Xi26,Yi26,mag26)
axis([min(xx) max(xx) min(yy) max(yy)])

axis image
```

## Code to combine all grids

```
% This code combines all individual magnetic surveys into one master grid
% with all of the data.

clear all
close all

load processed_data1.mat

X = x2;
Y = y2;
mag = z2;

clear XI YI ZI2 x x2 y y2 z2

load processed_data2.mat
X = [x2;X];
Y = [y2;Y];
mag = [z2;mag];

clear XI YI ZI2 x x2 y y2 z2

load processed_data3.mat
X = [x2;X];
Y = [y2;Y];
mag = [z2;mag];

clear XI YI ZI2 x x2 y y2 z2

load processed_data4.mat
X = [x2;X];
Y = [y2;Y];
mag = [z2;mag];

clear XI YI ZI2 x x2 y y2 z2

load processed_data6.mat
X = [x2;X];
Y = [y2;Y];
mag = [z2;mag];

clear XI YI ZI2 x x2 y y2 z2

load processed_data7.mat
X = [x2;X];
Y = [y2;Y];
mag = [z2;mag];

clear XI YI ZI2 x x2 y y2 z2

load processed_data8.mat
X = [x2;X];
```

```
Y = [y2;Y];
mag = [z2;mag];

clear XI YI ZI2 x x2 y y2 z2

load processed_data9.mat
X = [x2;X];
Y = [y2;Y];
mag = [z2;mag];

clear XI YI ZI2 x x2 y y2 z2

load processed_data10.mat
X = [x2;X];
Y = [y2;Y];
mag = [z2;mag];

clear XI YI ZI2 x x2 y y2 z2

load processed_data11.mat
X = [x2;X];
Y = [y2;Y];
mag = [z2;mag];

clear XI YI ZI2 x x2 y y2 z2

load processed_data12.mat
X = [x2;X];
Y = [y2;Y];
mag = [z2;mag];

clear XI YI ZI2 x x2 y y2 z2

load processed_data13.mat
X = [x2;X];
Y = [y2;Y];
mag = [z2;mag];

clear XI YI ZI2 x x2 y y2 z2

load processed_data14.mat
X = [x2;X];
Y = [y2;Y];
mag = [z2;mag];

clear XI YI ZI2 x x2 y y2 z2

load processed_data15.mat
X = [x2;X];
Y = [y2;Y];
mag = [z2;mag];

clear XI YI ZI2 x x2 y y2 z2
```

```
load processed_data16.mat
X = [x2;X];
Y = [y2;Y];
mag = [z2;mag];

clear XI YI ZI2 x x2 y y2 z2

load processed_data17.mat
X = [x2;X];
Y = [y2;Y];
mag = [z2;mag];

clear XI YI ZI2 x x2 y y2 z2

load processed_data18.mat
X = [x2;X];
Y = [y2;Y];
mag = [z2;mag];

clear XI YI ZI2 x x2 y y2 z2

load processed_data19.mat
X = [x2;X];
Y = [y2;Y];
mag = [z2;mag];

clear XI YI ZI2 x x2 y y2 z2

load processed_data20.mat
X = [x2;X];
Y = [y2;Y];
mag = [z2;mag];

clear XI YI ZI2 x x2 y y2 z2

load processed_data21.mat
X = [x2;X];
Y = [y2;Y];
mag = [z2;mag];

clear XI YI ZI2 x x2 y y2 z2

load processed_data22.mat
X = [x2;X];
Y = [y2;Y];
mag = [z2;mag];

clear XI YI ZI2 x x2 y y2 z2

load processed_data23.mat
X = [x2;X];
Y = [y2;Y];
mag = [z2;mag];
```

```

clear XI YI ZI2 x x2 y y2 z2

load processed_data24.mat
X = [x2;X];
Y = [y2;Y];
mag = [z2;mag];

clear XI YI ZI2 x x2 y y2 z2

load processed_data25.mat
X = [x2;X];
Y = [y2;Y];
mag = [z2;mag];

clear XI YI ZI2 x x2 y y2 z2

load processed_data26.mat
X = [x2;X];
Y = [y2;Y];
mag = [z2;mag];

clear XI YI ZI2 x x2 y y2 z2

% Grids the data into one master grid
xi = linspace(min(X),max(X),3000); % 3000 points in X direction
yi = linspace(min(Y),max(Y),3110); % 3110 points in Y direction
[XI,YI] = meshgrid(xi,yi);

F = TriScatteredInterp(X,Y,mag,'natural');

qz = F(XI,YI);

figure()
contourf(XI,YI,qz);
%imagesc(X,Y,flip1r(qz))
hold on
%plot(X,Y,'kx')
axis image
caxis([52600 53200])
colorbar

```

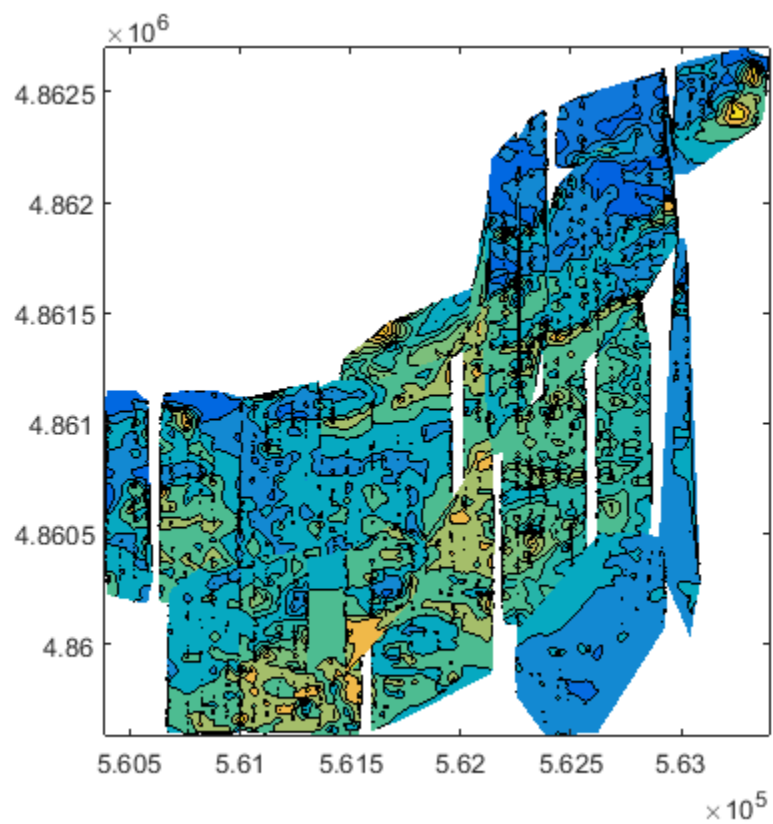


**Figure E.1.** Combined magnetic anomaly grids.

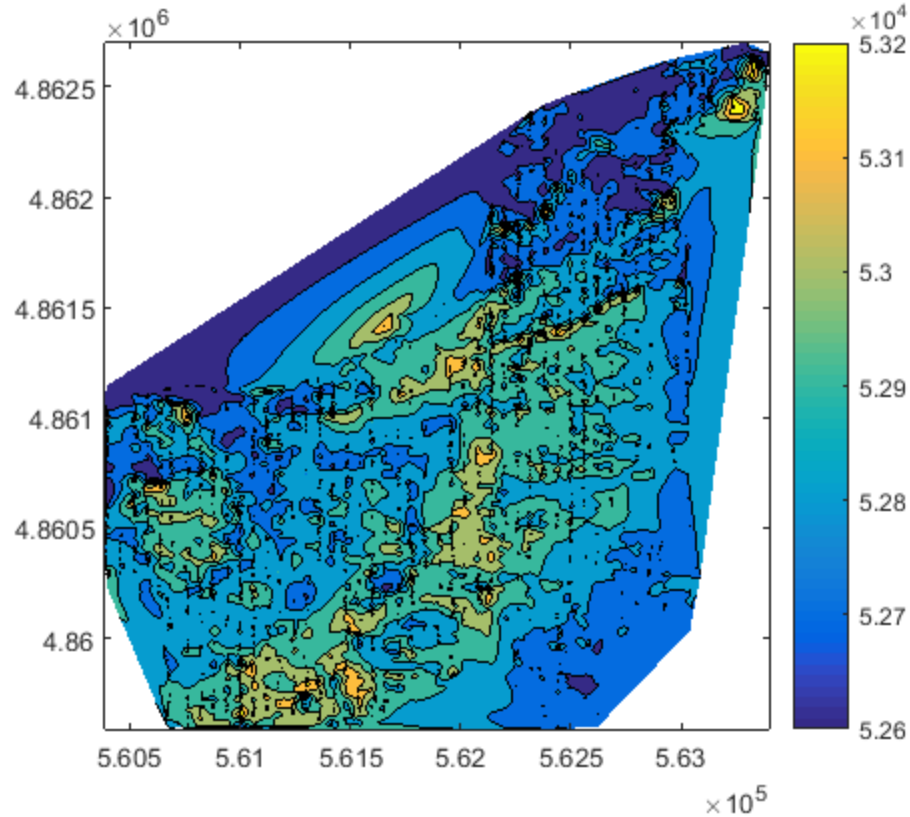


**Figure E.2.** Combined and interpolated magnetic anomaly grids

```
% Saves combined gridded data
save('grids_combined_all.mat','X','Y','mag','xi','yi','qz','XI','YI')

test = inpaint_nans(qz,5);

save('grid_interpolated_edges_all.mat','X','Y','mag','xi','yi','test','XI','YI')
```

*Published with MATLAB® R2015a*

### Interpolation of data

```
clear all
close all

load grid_interpolated_edges_all.mat % load data
qz = test; % assign mag data

data1 = flipud((qz-mean(qz(:)))); % remove the mean of data so just working
with magnetic anomaly
TR = data1'; % transpose data to get x and y dimensions
```

correct

```

I = 70*pi/180; % Magnetic inclination @ Horseshoe Bend, ID
(radians)
D = 13*pi/180; % Magnetic declination @ Horseshoe Bend, ID
(radians)
[nx,ny] = size(TR); % get x and y dimensions
dx = mean(diff(xi)); % calculate x-spacing
dy = mean(diff(yi)); % calculate y-spacing

nmax=max([nx ny]); % calculate largest direction
npts=2^nextpow2(nmax); % # of points to pad grid with for FFTs
cdiff=floor((npts-ny)/2); % # of points to add to grid in y-direction
on each side
rdiff=floor((npts-nx)/2); % # of points to add to grid in x-direction
on each side
data=taper2d(TR,npts,nx,ny,rdiff,cdiff); % create the padded grid to prevent
wraparound effects from FFTs
TR1 = data; % create temporary variable of mag data

nyqx=(1/(2*dx)); % nyquist frequency in x-direction
nyqy=(1/(2*dy)); % nyquist frequency in y-direction

kx=linspace(-nyqx,nyqx,npts); % create vector of x-wavenumbers
ky=linspace(-nyqy,nyqy,npts); % create vector of y-wavenumbers

% create some constants needed for the RTP filter. These correspond to
% ambient field direction and body magnetization direction. This code
% assumes that direction of body magnetization is the same as that of the
% ambient field. This can be easily altered by entering the inclination and
% declination of the body magnetization for the lower case variables
% (l,r,q).
L=cos(I)*cos(D);
l=cos(I)*cos(D);
R=cos(I)*sin(D);
r=cos(I)*sin(D);
Q=-sin(I);
q=-sin(I);

[KX KY]=meshgrid(kx,ky); % create a grid of x and y wavenumbers
KX=KX.*KX; % square x-wavenumber for calculations
KY=KY.*KY; % square y-wavenumber for calculations

% This loop calculates the RTP filter in the Fourier domain. Refer to
% Blakely (1995, Potential Theory in Gravity and Magnetic Applications)
% Equation 12.31 for details.
for m= 1:npts
    for n= 1:npts
        RTP(m,n) =
(KX(m,n)+KY(m,n))/(((i*L*KX(m,n))+i*R*KY(m,n))+Q*((KX(m,n)+KY(m,n)).^0.5)))*((i*l*KX(m
,n))+i*r*KY(m,n))+q*((KX(m,n)+KY(m,n)).^0.5));
    end
end

```

```

RTP=fftshift(RTP); % shift zeros around in filter

filtR_dat1=(ifft2(fft2(TR1).*RTP)); % Fourier transform the data, multiply by the
RTP filter and then inverse fourier transform data back to the space-domain.
out=real(filtR_dat1(1+rdiff:nx+rdiff,1+cdiff:ny+cdiff)); % Accept only the real part of
the data and extract the original data from the padded data.

out = out'; % transpose data back to original orientation

```

---

```

load grids_combined_all.mat % load original data with NaNs instead
of mean
inds = isnan(flipud(qz)); % find NaN's
out(inds) = nan; % replace RTPed data with NaNs where they
originally were
data1(inds) = nan; % replace original data with NaNs where they
originally were

[FX,FY] = gradient(out,dx,dy); % calculate X-gradient (FX) and Y-gradient
(FY) of RTPed data.

```

---

```

%R = georasterref

% plot the RTP'd data
figure()
imagesc(out)
out1 = flipud(out);
colorbar
title('RTP')
axis image
caxis([-200 600])
XI2 = XI(:);
YI2 = YI(:);
out2 = out1(:);
RTP_data_all = [XI2 YI2 out2];
RTP_data_all(any(isnan(RTP_data_all),2),:)=[];
% write data
dlmwrite('RTP_data_all_1.txt',RTP_data_all,'delimiter','\t','precision',8);
%save('RTP_data_all.txt','RTP_data_all','-ascii');

%% plot the RTP'd data
% figure()
% imagesc(out)
% out1 = flipud(out);
% colorbar
% title('RTP')
% axis image
% caxis([-200 600])
% XI2 = XI(:);
% YI2 = YI(:);
% out2 = out1(:);
%% XI2 = linspace(min(XI),max(XI),3000); % 3000 points in X direction
%% YI2 = linspace(min(YI),max(YI),3110); % 3110 points in Y direction
%% [XI,YI] = meshgrid(xi,yi);
% RTP_data_all = [XI2 YI2 out2];

```

```

% RTP_data_all(any(isnan(RTP_data_all),2),:)=[];
%
% % write to file
%     fid1 = fopen('RTP_data_all.txt','a');
%
%     % write header info
%     fprintf(fid1,'%s\r\n','NCOLS 3000');           % number of columns
%     fprintf(fid1,'%s\r\n','NROWS 3110');          % number of rows
%     fprintf(fid1,'%s\r\n','XLLCORNER 560386');    % Top NW corner easting
%     fprintf(fid1,'%s\r\n','YLLCORNER 4862661');  % Top NW corner northing
%     fprintf(fid1,'%s\r\n','CELLSIZE 1');         % size of cells in grid
%     fprintf(fid1,'%s\r\n','NODATA_VALUE -32768'); % size of cells in grid
%
% % write data
%     dlmwrite('RTP_data_all.txt',RTP_data_all,'delimiter',' ','-
append','newline','pc','precision',8);
%
%
%
%
%
%
% geotiffwrite('RTP_data_all',RTP_data_all,'cmap','R')
% set(gca,'Ytick',[4859600, 4860000, 4860400, 4860800, 4861200, 4861600, 4862000,
4862400])
% set(gca,'YtickLabel',[4859600, 4860000, 4860400, 4860800, 4861200, 4861600, 4862000,
4862400])
% set(gca,'Xtick',[560200, 560600, 561000, 561400, 561800, 562200, 562600, 563000,
563400])
% set(gca,'XtickLabel',[560200, 560600, 561000, 561400, 561800, 562200, 562600, 563000,
563400])
% save('RTP_data_all.txt','RTP_data_all','-ascii');

% plot the original data
figure()
imagesc(data1)
data_123 = flipud(data1);
colorbar
title('Original Data')
axis image
caxis([-200 600])
XI2 = XI(:);
YI2 = YI(:);
data12 = data_123(:);
Original_data_all = [XI2 YI2 data12];
Original_data_all(any(isnan(Original_data_all),2),:)=[];
dlmwrite('Original_data_all_1.txt',Original_data_all,'delimiter','\t','precision',8);
%save('Original_data_all.txt','Original_data_all','-ascii');

```

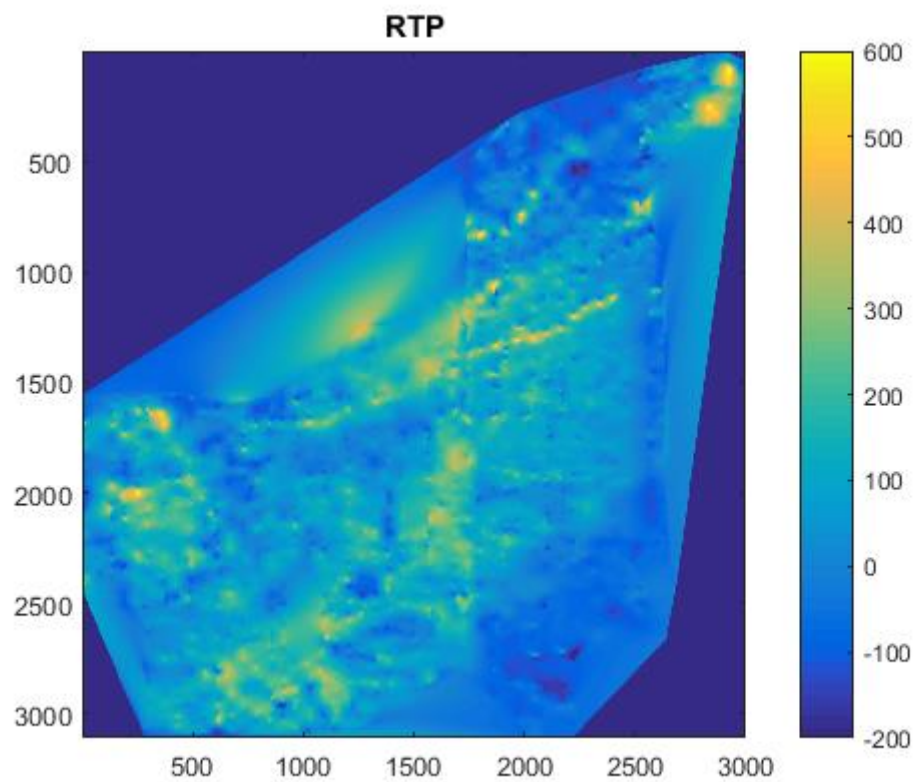


**Figure E.3. Reduced to Pole (RTP) magnetic anomaly grid. Scale is nT.**

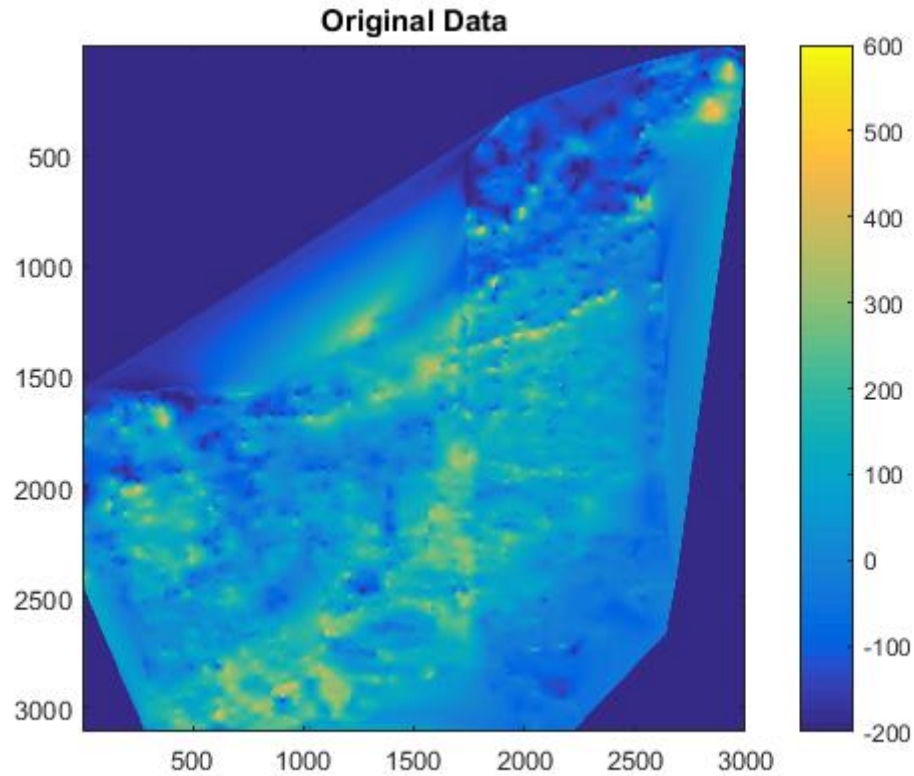


**Figure E.4.** Original data magnetic anomaly grid. Scale is nT.

```

% plot the X-gradient
figure()
imagesc(FX)
FX1 = flipud(FX);
colorbar
title('X-derivative')
axis image
caxis([-10 10])
XI2 = XI(:);
YI2 = YI(:);
FX2 = FX1(:);
X_gradient_all = [XI2 YI2 FX2(:)];
X_gradient_all(any(isnan(X_gradient_all),2),:)=[];
dlmwrite('X_gradient_all.txt',X_gradient_all,'delimiter','\t','precision',8);
%save('X_Gradient_all.txt','X_gradient_all','-ascii');

% plot the Y-gradient
figure()
imagesc(FY)
FY1 = flipud(FY);
colorbar

```

```
title('Y-derivative')
axis image
caxis([-10 10])
XI2 = XI(:);
YI2 = YI(:);
FY2 = FY1(:);
Y_gradient_all = [XI2(:) YI2(:) FY2(:)];
Y_gradient_all(any(isnan(Y_gradient_all),2),:)=[];
dlmwrite('Y_gradient_all.txt',Y_gradient_all,'delimiter','\t','precision',8);
%save('Y_gradient_all.txt','Y_gradient_all','-ascii');
```

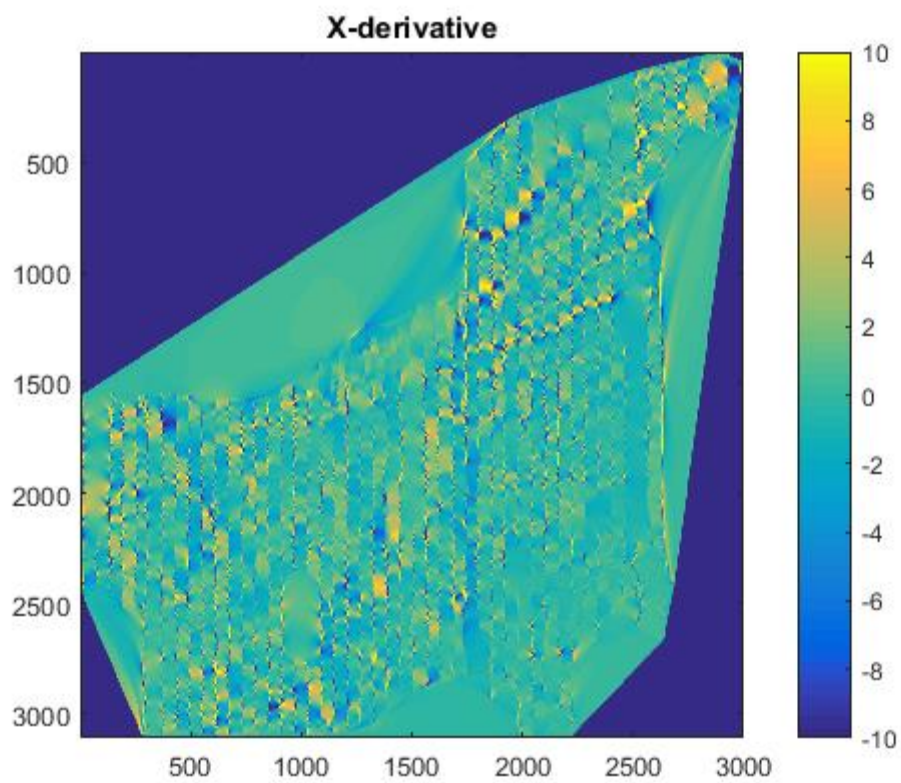


**Figure E.5.** X-derivative (E-W gradient) magnetic anomaly grid. Scale is nT/m.

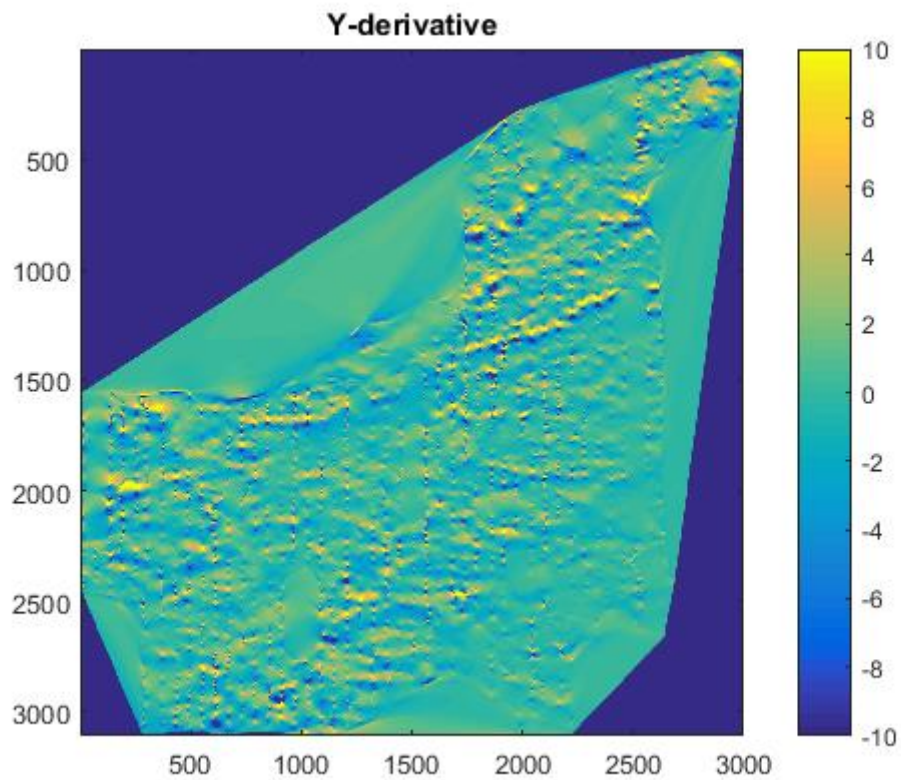


**Figure E.5.** Y-derivative (N-S gradient) magnetic anomaly grid. Scale is nT/m.

## APPENDIX F

**Magnetic Anomaly Maps and Figures**

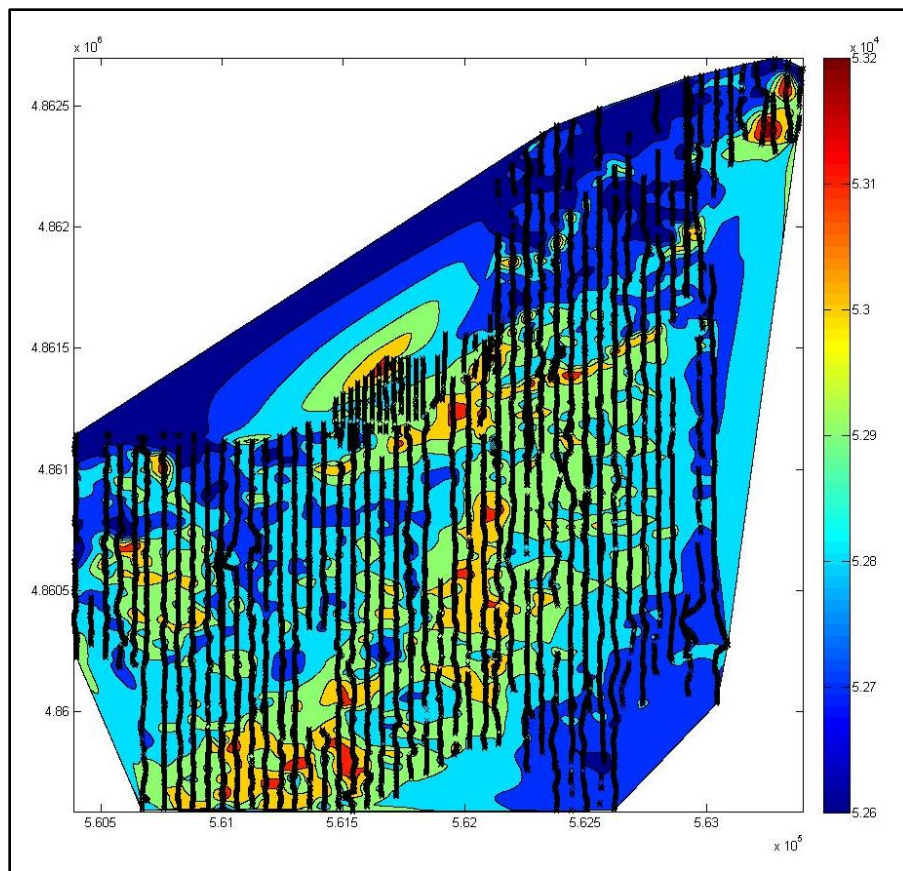


**Figure F.1.** Combined magnetic anomaly map. Black lines show the trace of individual collection lines. Scale bar in nT.

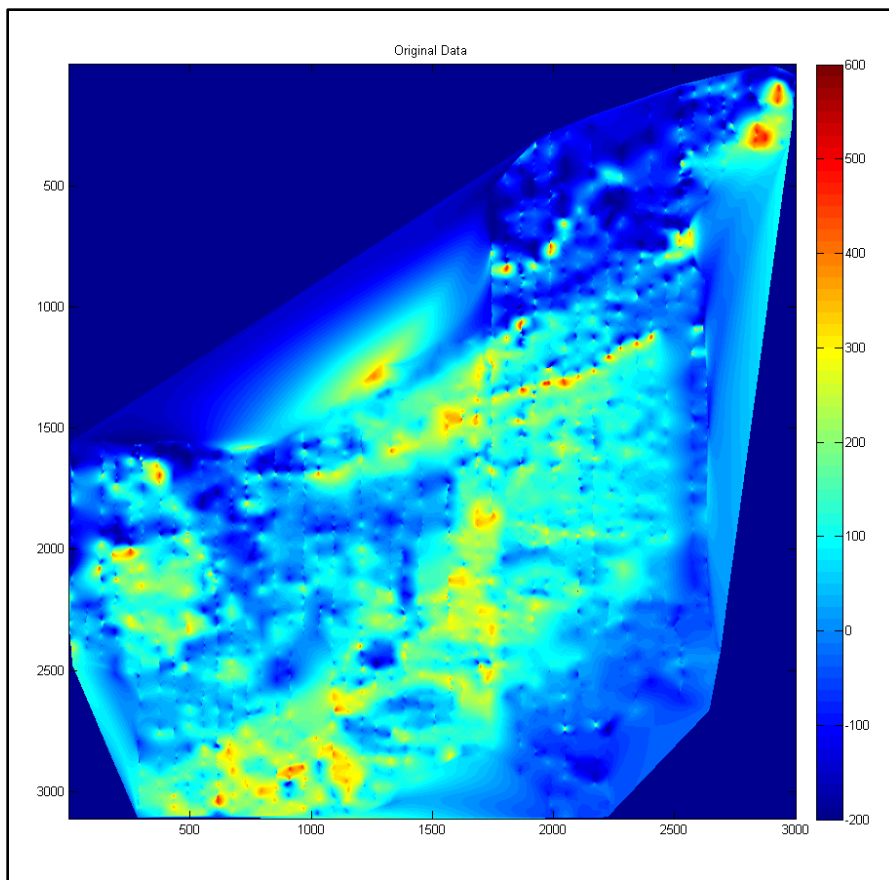


**Figure F.2. Interpolated total field magnetic anomaly map as produced in Matlab. Final map produced in ArcGIS. Scale bar in nT.**

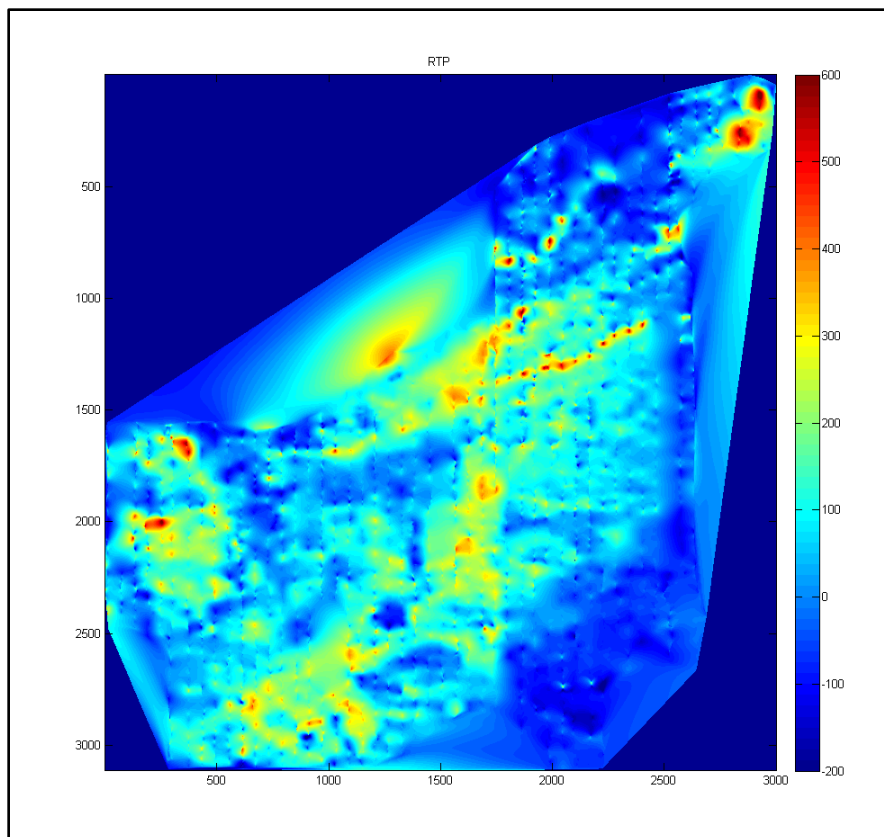


**Figure F.3.** Interpolated reduced to pole magnetic anomaly map as produced in Matlab. Final map produced in ArcGIS. Scale bar in nT.

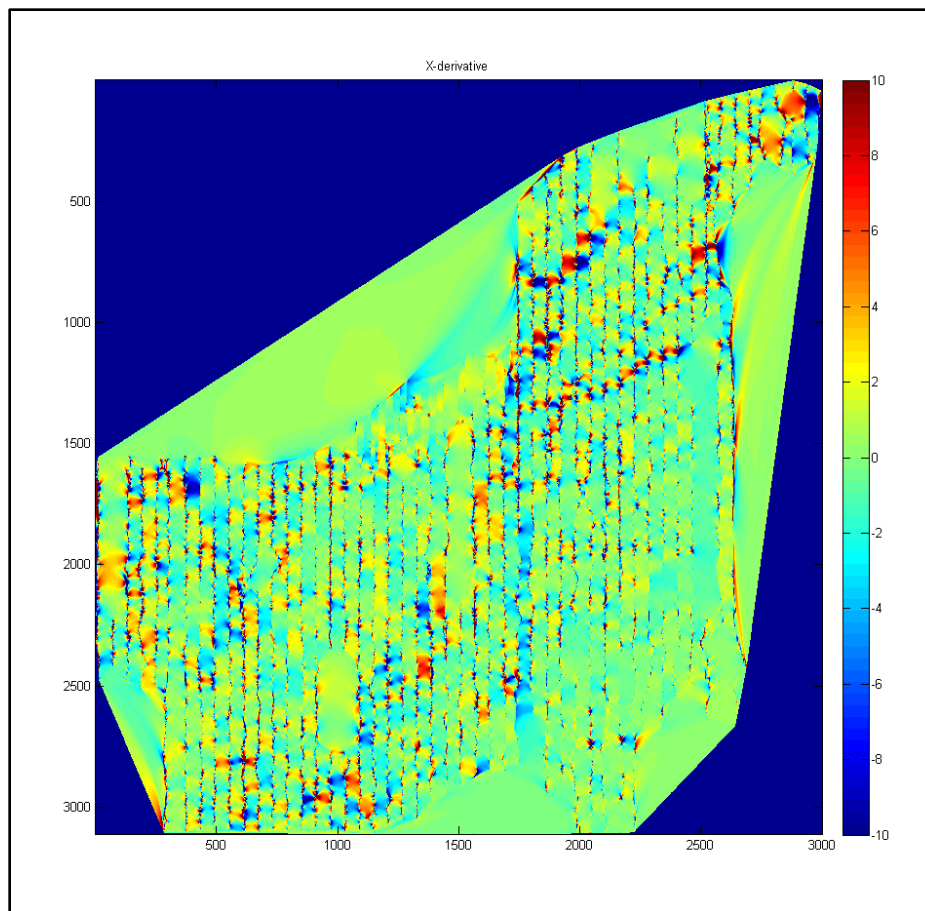


**Figure F.4.** Interpolated x-derivative (east-west magnetic gradient) magnetic anomaly map as produced in Matlab. Final map produced in ArcGIS. Scale bar in nT.

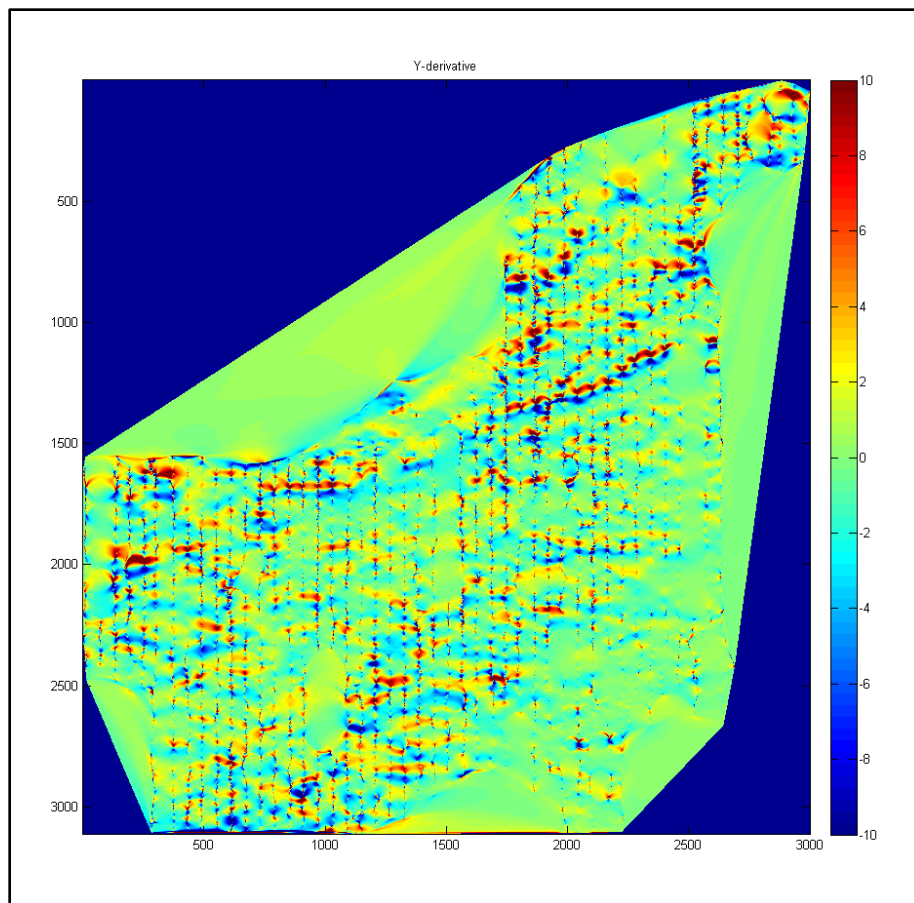


**Figure F.5.** Interpolated y-derivative (north-south magnetic gradient) magnetic anomaly map as produced in Matlab. Final map produced in ArcGIS. Scale bar in nT.

## APPENDIX G

**Electrical Resistivity, Induced Polarization, and Metal Factor Matlab Code**

All code authored by Hank Hetrick

## Calc Error

```

function rmse = calc_error(T,Ms,n)

for j = 1:size(T,1)
    x = T(j,:)' ;
    y = Ms(j,:)' ;

    % create A matrix
    A = ones(size(x));
    for i = 2:n
        A = [A 1./x.^i];
    end

    % invert for optimal coeff's
    c = inv(A'*A)*A'*y;

    % find optimal function
    f = c(1).*ones(size(x));
    for i = 2:n
        f = f + c(i)./x.^i;
    end

    % calculate error
    rmse(j) = norm(f-y,2) ./ norm(y,2);

    %     figure(1); clf
    %     plot(x,y,'.r'); hold on
    %     plot(x,f)

    % flag for monotonic trend in f
    if f(1)>0
        test = all(diff(f)<0);
    else
        test = all(diff(f)>0);
    end

    if test==0
        rmse(j) = norm(y);
    end

    %     rmse(j)
    %     pause
end

```

## Combine Data

```

clear all; % clear variables

% edit this to read txt files
% this block of code ID's all of the .dat files in your current folder
files = ls; % strings of files in matlab folder your in
iter = 1; % for indexing "dat_files" properly (remember . and ..)
for i = 1:size(files,1) % loop through number of files in folder
    dat_find = strfind(files(i,:),'.dat'); % returns location where ".dat" is
    in string
    if size(dat_find) > 0 % if "dat_files" is not empty (aka is a dat file)
        dat_files(iter,:) = files(i,:); % store the file name
        iter = iter+1;
    end
end

% find unique line data
for i = 1:size(dat_files,1)
    lines_str(i,:) = dat_files(i,2:3);
    lines(i) = str2num(dat_files(i,2:3));
end
lines_str = unique(lines_str,'rows');
num_lines = max(lines);

% loop through lines, edit, filter, and write data
for j = 1:size(lines_str,1)
    line = str2num(lines_str(j,:));
    I = find(lines==j);

    if size(I,2)==0
        continue;
    end

    % will be different when we read txt file instead
    % we store each dat file's data into one of the cell's in the variable, d
    for i = 1:length(I) % size(dat_files,1) % loop through dat files in folder
        temp_data = importfile(dat_files(I(i),:)); % make a temporary matrix of
        data from each file
        d{i} = temp_data; % store temp data into cell, d
    end

    % loop through all data and store the electrode locations in variable x
    x = [];
    dat = [];
    for i = 1:size(d,2) % loop through each file's data
        x = [x; d{i}(:,1:9)]; % create "location matrix"
        dat = [dat; d{i}(:,10:end)];
    end

    % determine all of the unique locations out of all of the data combined

```

```

    x_unique = unique(x,'rows'); % determine all unique rows in "location
matrix"

    % filter noisy res data
    % - high dev
    % - negative values

    % filter noisy IP data
    % - high rmse fit
    % - Vp/Vs or Cole-Cole model?

    % All has not just all of the location data, but the rest of the data too
    All = [x dat]; % once you have x_unique, now make you All matrix which you
will paste into your new line file

    % find duplicate locations, scrap all of them except for the first one
    for i=1:length(x_unique) % loop through unique x-coords
        I = find(All(i,1:9) == x_unique(i,:)); % find indexes where all of the
data is equal to a unique location
        if I>1 % if more than one unique point exists
            All(i,I(2:end)) = []; % then scrap all of the duplicates after the
first location
        end
    end

    % edit written file format
    % write to file
    dlmwrite(['L' lines_str(j,:) '_combined.txt'],All,'delimiter',' ') % write
this to a txt file for your new line file!
end

```

## Combine Text data

```

clear all; % clear variables

txt_path = '../preprocessed_text_files';
dat_path = '../preprocessed_dat_files';
gps_path = '../TXT Topo';

gps_files = ls([gps_path '/*.txt']);

% this block of code ID's all of the .txt files in your current folder
files = ls(txt_path); % strings of files in matlab folder your in
iter = 1; % for indexing "dat_files" properly (remember . and ..)
for i = 1:size(files,1) % loop through number of files in folder
    txt_find = strfind(files(i,:),'.txt'); % returns location where ".dat" is
in string
    if size(txt_find) > 0 % if "dat_files" is not empty (aka is a dat file)
        txt_files(iter,:) = files(i,:); % store the file name
        iter = iter+1;
    end
end

```

```

    end
end

% find unique line data
for i = 1:size(txt_files,1)
    lines_str(i,:) = txt_files(i,2:3);
    lines(i) = str2num(txt_files(i,2:3));
end
lines_str = unique(lines_str,'rows');
num_lines = max(lines);

% loop through lines, edit, filter, and write data
for j = 6:6 % 1:size(lines_str,1)
    line = str2num(lines_str(j,:));
    I = find(lines==line);

    if size(I,2)==0
        continue;
    end

    % define the following variable before the for loop
    I_res_filt = [];
    I_IP_filt = [];
    d = cell(length(I),1);
    loc = [];
    loc_temp = [];
    y = [];
    dat = [];
    res = [];
    IP = [];
    DEV = [];
    RMSE = [];
    EL_loc = [];
    utm_E = [];
    utm_N = [];
    ELEV = [];
    y_array = [];
    z_array = [];

    % we store each dat file's data into one of the cell's in the variable, d
    for i = 1:length(I) % size(dat_files,1) % loop through dat files in folder
        D = importdata([txt_path '\' txt_files(I(i),:)],' ',1);
        hdr = D.textdata;
        data = D.data;

        GPS = importdata([gps_path '/' gps_files(I(i),:)],'\t',1);
        hdr_gps = GPS.textdata;

        disp(gps_files(I(i),:))

        % INDEXES
        % location data
        for k = 1:2

```

```

        I_s1(k) = find(strcmpi(hdr,['Spa.' num2str( ((k-1)*4)+1 )])==1);
        I_s2(k) = find(strcmpi(hdr,['Spa.' num2str( ((k-1)*4)+2 )])==1);
        I_r1(k) = find(strcmpi(hdr,['Spa.' num2str( ((k-1)*4)+3 )])==1);
        I_r2(k) = find(strcmpi(hdr,['Spa.' num2str( ((k-1)*4)+4 )])==1);
    end
    I_ns = [I_s2(1) I_s1(1) I_r1(1) I_r2(1)];
    I_coords = [I_s2 I_s1 I_r1 I_r2];

    % res data
    I_rho = find(strcmpi(hdr,'Rho')==1);
    I_dev = find(strcmpi(hdr,'Dev.')==1);
    I_V = find(strcmpi(hdr,'Vp')==1);
    I_Vab = find(strcmpi(hdr,'Vab')==1);
    I_In = find(strcmpi(hdr,'In')==1);
    I_R = find(strcmpi(hdr,'Rab')==1);
    I_SP = find(strcmpi(hdr,'SP')==1);

    % IP data
    I_Ms = [];
    I_TMs = [];
    for k = 1:20
        I_Ms = [I_Ms find(strcmpi(hdr,['M' num2str(k)])==1)];
        I_TMs = [I_TMs find(strcmpi(hdr,['TM' num2str(k)])==1)];
    end
    I_Mdly = find(strcmpi(hdr,'Mdly')==1);
    I_M = find(strcmpi(hdr,'M')==1);

    % VARIABLES
    % electrode locations
    if (line == 1 || line == 2 || line == 3)
        if i<=2
            data(:,I_ns) = data(:,I_ns) + 60.*(i-1); % correct positions
            D.data(:,I_ns) = D.data(:,I_ns) + 60.*(i-1); % correct position
        end
        if i>2
            data(:,I_ns) = data(:,I_ns) + 60.*(i-1) + 60; % correct
positions
            D.data(:,I_ns) = D.data(:,I_ns) + 60.*(i-1) + 60; % correct
position
        end
    elseif (line == 4 || line==5)
        data(:,I_ns) = data(:,I_ns) + 180.*(i-1); % correct positions
        D.data(:,I_ns) = D.data(:,I_ns) + 180.*(i-1); % correct position
    elseif (line == 10)
        if i<=2
            data(:,I_ns) = data(:,I_ns) + 120.*(i-1); % correct positions
            D.data(:,I_ns) = D.data(:,I_ns) + 120.*(i-1); % correct
position
        end
        if i>2
            data(:,I_ns) = data(:,I_ns) + 120.*(i-1) - 60; % correct
positions
        end
    end
end

```

```

        D.data(:,I_ns) = D.data(:,I_ns) + 120.*(i-1) - 60; % correct
position
        end
elseif (line == 14 || line == 15 || line == 23)
        data(:,I_ns) = data(:,I_ns) + 60.*(i-1); % correct positions
        D.data(:,I_ns) = D.data(:,I_ns) + 60.*(i-1); % correct position
else
        data(:,I_ns) = data(:,I_ns) + 120.*(i-1); % correct positions
        D.data(:,I_ns) = D.data(:,I_ns) + 120.*(i-1); % correct positions
end

s1 = data(:,I_s1);
s2 = data(:,I_s2);
r1 = data(:,I_r1);
r2 = data(:,I_r2);
coords = data(:,I_coords);
y_array = [y_array; coords(:,[1 3 5 7])];

el_loc = GPS.data(:,1);
utm_E = [utm_E; GPS.data(:,2)];
utm_N = [utm_N; GPS.data(:,3)];
elev = GPS.data(:,4).*12.*2.54./100;
EL_loc = [EL_loc; el_loc];
ELEV = [ELEV; elev];

% res data
rho = data(:,I_rho);
dev = data(:,I_dev);
Vo = data(:,I_V);
Vab = data(:,I_Vab);
In = data(:,I_In);
R = data(:,I_R);
sp = data(:,I_SP);

% IP data
M = abs(data(:,I_M));
Mdly = data(:,I_Mdly);
Ms = data(:,I_Ms);
TMs = data(:,I_TMs);

% correct time scale for TMs
T = zeros(size(TMs));
T(:,1) = TMs(:,1);
for k = 2:size(TMs,2)
        T(:,k) = TMs(:,k) + T(:,k-1);
end
for k = 1:size(TMs,1)
        T(k,:) = T(k,:) + Mdly(k);
end
T = T./1000;

% compute cole-cole model estimate with error
[x_opt,rmse] = calc_cole_cole(Ms,T,R,In,100);

```

```

rmse = calc_error(T,Ms,4);

% accumulate res and IP data that will be filtered
%Irf = find(dev>5 | rho<=0);
%Imf = find(rmse'>0.10 | rho<=0);
%I_res_filt = [I_res_filt; Irf];
%I_IP_filt = [I_IP_filt; Imf];

% set the d cell variable to hold all of the data
d{i} = D.data;
I_remaining = setxor(1:size(d{i},2),I_coords);

% store the electrode locations in variable x, and rest in dat
loc = [loc; d{i}(:,I_coords)]; % create "location matrix"
dat = [dat; d{i}(:,I_remaining)];
res = [res; rho];
DEV = [DEV; dev];
IP = [IP; M];
RMSE = [RMSE; rmse'];

% these arrays are used to correct the indexes for the res and IP
filters
num_d(i) = size(d{i},1);
num_r(i) = length(Irf);
num_ip(i) = length(Imf);
end

% interpolate elevation in y variable
y_array = unique(y_array(:));
[uniqueE yy jj] = unique(EL_loc,'first');
elev_interp = interp1(y_array(EL_loc(yy)),ELEV(yy)',y_array,'cubic');
for ii = 1:size(loc,1)
    for jj = 1:2:size(loc,2)
        Itemp = find(y_array==loc(ii,jj));
        loc(ii,jj+1) = elev_interp(Itemp);
    end
end

% interpolate utm_E (x's) in y variable
utm_E_interp = interp1(y_array(EL_loc(yy)),utm_E(yy)',y_array,'cubic');
% for ii = 1:size(loc,1)
%     iter = 0;
%     for jj = 1:2:size(loc,2)
%         iter = iter+1;
%         Itemp = find(y_array==loc(ii,jj));
%         loc_temp(ii,iter) = utm_E_interp(Itemp);
%     end
% end

% interpolate utm_N (y's)
utm_N_interp = linspace(min(utm_N),max(utm_N),length(y_array));
% for ii = 1:size(loc,1)
%     for jj = 1:2:size(loc,2)

```

```

%         iter = iter+1;
%         Itemp = find(y_array==loc(ii,jj));
%         loc(ii,jj) = utm_N_interp(Itemp);
%     end
% end

% merge temp utm_E data into loc matrix
%loc = [loc_temp(:,1) loc(:,1:2) loc_temp(:,2) loc(:,3:4) loc_temp(:,3)
loc(:,5:6) loc_temp(:,4) loc(:,7:8)];

%     figure(1); clf
%     subplot(3,1,1)
%     plot(y_array(EL_loc(yy)),ELEV(yy),'r'); hold on
%     plot(y_array,elev_interp)
%
%     subplot(3,1,2)
%     plot(y_array(EL_loc(yy)),utm_E(yy)-mean(utm_E(yy)),'r'); hold on
%     plot(y_array,utm_E_interp-mean(utm_E(yy)))
%
%     subplot(3,1,3)
%     plot(y_array(EL_loc(yy)),utm_N(yy)-mean(utm_N(yy)),'r'); hold on
%     plot(y_array,utm_N_interp-mean(utm_N(yy)))

% fix IP and res indexes
%Istart = 1;
%add = 0;
%for n = 1:size(d,2)
%     Istop = Istart + num_r(n) - 1;
%     I_res_filt(Istart:Istop) = I_res_filt(Istart:Istop) + add;
%     I_IP_filt(Istart:Istop) = I_IP_filt(Istart:Istop) + add;
%     Istart = Istart + num_r(n);
%     add = num_d(n);
%end

% index for elevation data

rAM = sqrt((loc(:,3)-loc(:,5)).^2+(loc(:,4)-loc(:,6)).^2);
rAN = sqrt((loc(:,3)-loc(:,7)).^2+(loc(:,4)-loc(:,8)).^2);
rBM = sqrt((loc(:,1)-loc(:,5)).^2+(loc(:,2)-loc(:,6)).^2);
rBN = sqrt((loc(:,1)-loc(:,7)).^2+(loc(:,2)-loc(:,8)).^2);
k = 1./(1./rAM - 1./rAN - 1./rBM + 1./rBN);
a = abs(loc(:,1)-loc(:,3));
for i = 1:length(k)
    p = [1 3 2 -2.*k(i).*a(i)];
    n(i) = max(roots(p)+10000)-10000;
end
%rho_a = 2.*pi.*Vo.*k./In;

I_res_filt = find(DEV>5 | res<=10 | res>50000 | n'>=7);
I_IP_filt = find(RMSE>0.10 | res<=10 | res>50000 | IP>=400 | n'>=7);

% determine all of the unique locations out of all of the data combined

```

```

loc_unique = unique(loc,'rows'); % determine all unique rows in "location
matrix"

% All has not just all of the location data, but the rest of the data too
All = [loc dat]; % once you have x_unique, now make you All matrix which
you will paste into your new line file

% find duplicate locations, scrap all of them except for the first one
I_duplicates = [];
for i=1:length(loc_unique) % loop through unique x-coords
    Itemp = find(ismember(All(:,1:8),loc_unique(i,:), 'rows')==1);
    if length(Intemp)>1 % if more than one unique point exists
        I_duplicates = [I_duplicates; Itemp(2:end)];
    end
end

% filter the data for each line, both res and IP
I_res_all = [I_res_filt; I_duplicates];
I_IP_all = [I_IP_filt; I_duplicates];

I_res_all = setxor(I_res_all,1:size(All,1));
I_IP_all = setxor(I_IP_all,1:size(All,1));

All_res = [4.*ones(length(I_res_all),1) loc(I_res_all,:) res(I_res_all)];
%All(I_res_all,:);
All_IP = [4.*ones(length(I_IP_all),1) loc(I_IP_all,:) res(I_IP_all)
IP(I_IP_all)]; % All(I_IP_all,:);

% write to file
res_write = [dat_path '\L' lines_str(j,:) '_res_combined.dat'];
IP_write = [dat_path '\L' lines_str(j,:) '_IP_combined.dat'];
fid1 = fopen(res_write,'a');
fid2 = fopen(IP_write,'a');

% write header info
fprintf(fid1,'%30s\r\n',res_write); % file name
fprintf(fid1,'%5s\r\n','5.00'); % a-spacing
fprintf(fid1,'%5s\r\n','11'); % data flag
fprintf(fid1,'%5s\r\n','3'); % ?
fprintf(fid1,'%60s\r\n','Type of measurement (0=app.
resistivity,1=resistance)');
fprintf(fid1,'%5s\r\n','0'); % apparent resistivity
fprintf(fid1,'%5s\r\n',num2str(length(I_res_all))); % number of
measurements
fprintf(fid1,'%5s\r\n','2'); % el location type
fprintf(fid1,'%5s\r\n','0'); % IP flag
%fprintf(fid1,'%5s\r\n','Chargeability'); % IP header
%fprintf(fid1,'%5s\r\n','mV/V'); % IP unit
%fprintf(fid1,'%5s\r\n','0.04,1.0'); % delay, integration time

fprintf(fid2,'%30s\r\n',IP_write); % file name
fprintf(fid2,'%5s\r\n','5.00'); % a-spacing
fprintf(fid2,'%5s\r\n','11'); % data flag

```

```

fprintf(fid2,'%5s\r\n','3'); % ?
fprintf(fid2,'%60s\r\n','Type of measurement (0=app.
resistivity,1=resistance)');
fprintf(fid2,'%5s\r\n','0'); % apparent resistivity
fprintf(fid2,'%5s\r\n',num2str(length(I_IP_all))); % number of measurements
fprintf(fid2,'%5s\r\n','2'); % e1 location type
fprintf(fid2,'%5s\r\n','1'); % IP flag
fprintf(fid2,'%5s\r\n','Chargeability'); % IP header
fprintf(fid2,'%5s\r\n','mV/V'); % IP unit
fprintf(fid2,'%5s\r\n','0.04,1.0'); % delay, integration time

% write data
dlmwrite(res_write,All_res,'delimiter',' ','-
append','newline','pc','precision',8); % write this to a txt file for your new
line file!
dlmwrite(IP_write,All_IP,'delimiter',' ','-
append','newline','pc','precision',8); % write this to a txt file for your new
line file!

% write utm coords
fprintf(fid1,'%5s\r\n','Global Coordinates present');
fprintf(fid1,'%5s\r\n','Number of coordinate points');
fprintf(fid1,'%5s\r\n',num2str(length(y_array)));
fprintf(fid1,'%5s\r\n','Local Easting Northing');
for i = 1:length(y_array)
    fprintf(fid1,'%30s\r\n',[num2str(y_array(i)) ' '
num2str(utm_E_interp(i)) ' ' num2str(utm_N_interp(i))]);
end

    fprintf(fid2,'%5s\r\n','Global Coordinates present');
    fprintf(fid2,'%5s\r\n','Number of coordinate points');
    fprintf(fid2,'%5s\r\n',num2str(length(y_array)));
    fprintf(fid2,'%5s\r\n','Local Easting Northing');
    for i = 1:length(y_array)
        fprintf(fid2,'%30s\r\n',[num2str(y_array(i)) ' '
num2str(utm_E_interp(i)) ' ' num2str(utm_N_interp(i))]);
    end

% zeros
fprintf(fid1,'%4s\r\n','0,0,0,0');
fprintf(fid2,'%4s\r\n','0,0,0,0');

fclose(fid1);
fclose(fid2);
end

```

## Combine text data 3D

```

clear all; % clear variables

txt_path = '../preprocessed_text_files';
dat_path = '../preprocessed_dat_files';
gps_path = '../TXT Topo';

gps_files = ls([gps_path '/*.txt']);

% this block of code ID's all of the .txt files in your current folder
files = ls(txt_path); % strings of files in matlab folder your in
iter = 1; % for indexing "dat_files" properly (remember . and ..)
for i = 1:size(files,1) % loop through number of files in folder
    txt_find = strfind(files(i,:),'.txt'); % returns location where ".dat" is
in string
    if size(txt_find) > 0 % if "dat_files" is not empty (aka is a dat file)
        txt_files(iter,:) = files(i,:); % store the file name
        iter = iter+1;
    end
end

% find unique line data
for i = 1:size(txt_files,1)
    lines_str(i,:) = txt_files(i,2:3);
    lines(i) = str2num(txt_files(i,2:3));
end
lines_str = unique(lines_str,'rows');
num_lines = max(lines);
All_res = [];
All_IP = [];

% loop through lines, edit, filter, and write data
for j = 1:size(lines_str,1)
    line = str2num(lines_str(j,:));
    I = find(lines==line);

    if size(I,2)==0
        continue;
    end

    % define the following variable before the for loop
    I_res_filt = [];
    I_IP_filt = [];
    d = cell(length(I),1);
    loc = [];
    loc_temp = [];
    y = [];
    dat = [];
    res = [];
    IP = [];
    DEV = [];

```

```

RMSE = [];
EL_loc = [];
utm_E = [];
utm_N = [];
ELEV = [];
y_array = [];
z_array = [];

% we store each dat file's data into one of the cell's in the variable, d
for i = 1:length(I) % size(dat_files,1) % loop through dat files in folder
    D = importdata([txt_path '\' txt_files(I(i),:)], ' ',1);
    hdr = D.textdata;
    data = D.data;

    GPS = importdata([gps_path '/' gps_files(I(i),:)], '\t',1);
    hdr_gps = GPS.textdata;

    disp(gps_files(I(i),:))

    % INDEXES
    % location data
    for k = 1:2
        I_s1(k) = find(strcmpi(hdr,['Spa.' num2str( ((k-1)*4)+1 )]) ==1);
        I_s2(k) = find(strcmpi(hdr,['Spa.' num2str( ((k-1)*4)+2 )]) ==1);
        I_r1(k) = find(strcmpi(hdr,['Spa.' num2str( ((k-1)*4)+3 )]) ==1);
        I_r2(k) = find(strcmpi(hdr,['Spa.' num2str( ((k-1)*4)+4 )]) ==1);
    end
    I_ns = [I_s2(1) I_s1(1) I_r1(1) I_r2(1)];
    I_coords = [I_s2 I_s1 I_r1 I_r2];

    % res data
    I_rho = find(strcmpi(hdr,'Rho')==1);
    I_dev = find(strcmpi(hdr,'Dev.')==1);
    I_V = find(strcmpi(hdr,'Vp')==1);
    I_Vab = find(strcmpi(hdr,'Vab')==1);
    I_In = find(strcmpi(hdr,'In')==1);
    I_R = find(strcmpi(hdr,'Rab')==1);
    I_SP = find(strcmpi(hdr,'SP')==1);

    % IP data
    I_Ms = [];
    I_TMs = [];
    for k = 1:20
        I_Ms = [I_Ms find(strcmpi(hdr,['M' num2str(k)]) ==1)];
        I_TMs = [I_TMs find(strcmpi(hdr,['TM' num2str(k)]) ==1)];
    end
    I_Mdly = find(strcmpi(hdr,'Mdly')==1);
    I_M = find(strcmpi(hdr,'M')==1);

    % VARIABLES
    % electrode locations
    if (line == 1 || line == 2 || line == 3)
        if i<=2

```

```

        data(:,I_ns) = data(:,I_ns) + 60.*(i-1); % correct positions
        D.data(:,I_ns) = D.data(:,I_ns) + 60.*(i-1); % correct position
    end
    if i>2
        data(:,I_ns) = data(:,I_ns) + 60.*(i-1) + 60; % correct
positions
        D.data(:,I_ns) = D.data(:,I_ns) + 60.*(i-1) + 60; % correct
position
    end
    elseif (line == 4 || line==5)
        data(:,I_ns) = data(:,I_ns) + 180.*(i-1); % correct positions
        D.data(:,I_ns) = D.data(:,I_ns) + 180.*(i-1); % correct position
    elseif (line == 10)
        if i<=2
            data(:,I_ns) = data(:,I_ns) + 120.*(i-1); % correct positions
            D.data(:,I_ns) = D.data(:,I_ns) + 120.*(i-1); % correct
position
        end
        if i>2
            data(:,I_ns) = data(:,I_ns) + 120.*(i-1) - 60; % correct
positions
            D.data(:,I_ns) = D.data(:,I_ns) + 120.*(i-1) - 60; % correct
position
        end
    elseif (line == 14 || line == 15 || line == 23)
        data(:,I_ns) = data(:,I_ns) + 60.*(i-1); % correct positions
        D.data(:,I_ns) = D.data(:,I_ns) + 60.*(i-1); % correct position
    else
        data(:,I_ns) = data(:,I_ns) + 120.*(i-1); % correct positions
        D.data(:,I_ns) = D.data(:,I_ns) + 120.*(i-1); % correct positions
    end

s1 = data(:,I_s1);
s2 = data(:,I_s2);
r1 = data(:,I_r1);
r2 = data(:,I_r2);
coords = data(:,I_coords);
y_array = [y_array; coords(:,[1 3 5 7])];

el_loc = GPS.data(:,1);
utm_E = [utm_E; GPS.data(:,2)];
utm_N = [utm_N; GPS.data(:,3)];
elev = GPS.data(:,4).*12.*2.54./100;
EL_loc = [EL_loc; el_loc];
ELEV = [ELEV; elev];

% res data
rho = data(:,I_rho);
dev = data(:,I_dev);
Vo = data(:,I_V);
Vab = data(:,I_Vab);
In = data(:,I_In);
R = data(:,I_R);

```

```

sp = data(:,I_SP);

% IP data
M = abs(data(:,I_M));
Mdly = data(:,I_Mdly);
Ms = data(:,I_Ms);
TMs = data(:,I_TMs);

% correct time scale for TMs
T = zeros(size(TMs));
T(:,1) = TMs(:,1);
for k = 2:size(TMs,2)
    T(:,k) = TMs(:,k) + T(:,k-1);
end
for k = 1:size(TMs,1)
    T(k,:) = T(k,:) + Mdly(k);
end
T = T./1000;

% compute cole-cole model estimate with error
rmse = calc_error(T,Ms,4);

% set the d cell variable to hold all of the data
d{i} = D.data;
I_remaining = setxor(1:size(d{i},2),I_coords);

% store the electrode locations in variable x, and rest in dat
loc = [loc; d{i}(:,I_coords)]; % create "location matrix"
dat = [dat; d{i}(:,I_remaining)];
res = [res; rho];
DEV = [DEV; dev];
IP = [IP; M];
RMSE = [RMSE; rmse'];
end

% interpolate elevation in y variable
y_array = unique(y_array(:));
[uniqueE yy jj] = unique(EL_loc,'first');
elev_interp = interp1(y_array(EL_loc(yy)),ELEV(yy)',y_array,'cubic');
for ii = 1:size(loc,1)
    for jj = 1:2:size(loc,2)
        Itemp = find(y_array==loc(ii,jj));
        loc(ii,jj+1) = elev_interp(Itemp);
    end
end

% interpolate utm_E (x's) in y variable
utm_E_interp = interp1(y_array(EL_loc(yy)),utm_E(yy)',y_array,'cubic');
for ii = 1:size(loc,1)
    iter = 0;
    for jj = 1:2:size(loc,2)
        iter = iter+1;
        Itemp = find(y_array==loc(ii,jj));

```

```

        loc_temp(ii,iter) = utm_E_interp(Itemp);
    end
end

% interpolate utm_N (y's)
utm_N_interp = linspace(min(utm_N),max(utm_N),length(y_array));
for ii = 1:size(loc,1)
    for jj = 1:2:size(loc,2)
        iter = iter+1;
        Itemp = find(y_array==loc(ii,jj));
        loc(ii,jj) = utm_N_interp(Itemp);
    end
end

% geometric factor
rAM = sqrt((loc(:,3)-loc(:,5)).^2+(loc(:,4)-loc(:,6)).^2);
rAN = sqrt((loc(:,3)-loc(:,7)).^2+(loc(:,4)-loc(:,8)).^2);
rBM = sqrt((loc(:,1)-loc(:,5)).^2+(loc(:,2)-loc(:,6)).^2);
rBN = sqrt((loc(:,1)-loc(:,7)).^2+(loc(:,2)-loc(:,8)).^2);
k = 1./(1./rAM - 1./rAN - 1./rBM + 1./rBN);
a = abs(loc(:,1)-loc(:,3));
n = zeros(size(k));
for i = 1:length(k)
    p = [1 3 2 -2.*k(i).*a(i)];
    rts = roots(p);
    for ii = 1:length(rts);
        Irts(ii) = isreal(rts(ii));
    end
    n(i) = max(rts(Irts)+10000)-10000;
end
%rho_a = 2.*pi.*Vo.*k./In;

% merge temp utm_E data into loc matrix
loc = [loc_temp(:,1) loc(:,1:2) loc_temp(:,2) loc(:,3:4) loc_temp(:,3)
loc(:,5:6) loc_temp(:,4) loc(:,7:8)];

% filter data
I_res_filt = find(DEV>5 | res<=10 | res>50000 | n>=7);
I_IP_filt = find(RMSE>0.10 | res<=10 | res>50000 | IP>=400 | n>=7);
% determine all of the unique locations out of all of the data combined
loc_unique = unique(loc,'rows'); % determine all unique rows in "location
matrix"

% All has not just all of the location data, but the rest of the data too
All = [loc dat]; % once you have x_unique, now make you All matrix which
you will paste into your new line file

% find duplicate locations, scrap all of them except for the first one
I_duplicates = [];
for i=1:length(loc_unique) % loop through unique x-coords
    Itemp = find(ismember(All(:,1:12),loc_unique(i,:), 'rows')==1);
    if length(Itemp)>1 % if more than one unique point exists
        I_duplicates = [I_duplicates; Itemp(2:end)];
    end
end

```

```

        end
    end

    % filter the data for each line, both res and IP
    I_res_all = [I_res_filt; I_duplicates];
    I_IP_all = [I_IP_filt; I_duplicates];

    I_res_all = setxor(I_res_all,1:size(All,1));
    I_IP_all = setxor(I_IP_all,1:size(All,1));

    All_res = [All_res; 4.*ones(length(I_res_all),1) loc(I_res_all,:)
res(I_res_all)]; %All(I_res_all,:);
    All_IP = [All_IP; 4.*ones(length(I_IP_all),1) loc(I_IP_all,:) res(I_IP_all)
IP(I_IP_all)]; % All(I_IP_all,:);

%     % write to file
%     res_write = [dat_path '\L' lines_str(j,:) '_res_combined.dat'];
%     IP_write = [dat_path '\L' lines_str(j,:) '_IP_combined.dat'];
%     fid1 = fopen(res_write,'a');
%     fid2 = fopen(IP_write,'a');
%
%     % write header info
%     fprintf(fid1,'%30s\r\n',res_write); % file name
%     fprintf(fid1,'%5s\r\n','5.00'); % a-spacing
%     fprintf(fid1,'%5s\r\n','11'); % data flag
%     fprintf(fid1,'%5s\r\n','3'); % ?
%     fprintf(fid1,'%60s\r\n','Type of measurement (0=app.
resistivity,1=resistance)');
%     fprintf(fid1,'%5s\r\n','0'); % apparent resistivity
%     fprintf(fid1,'%5s\r\n',num2str(length(I_res_all))); % number of
measurements
%     fprintf(fid1,'%5s\r\n','2'); % el location type
%     fprintf(fid1,'%5s\r\n','0'); % IP flag
%     %fprintf(fid1,'%5s\r\n','Chargeability'); % IP header
%     %fprintf(fid1,'%5s\r\n','mV/V'); % IP unit
%     %fprintf(fid1,'%5s\r\n','0.04,1.0'); % delay, integration time
%
%     fprintf(fid2,'%30s\r\n',IP_write); % file name
%     fprintf(fid2,'%5s\r\n','5.00'); % a-spacing
%     fprintf(fid2,'%5s\r\n','11'); % data flag
%     fprintf(fid2,'%5s\r\n','3'); % ?
%     fprintf(fid2,'%60s\r\n','Type of measurement (0=app.
resistivity,1=resistance)');
%     fprintf(fid2,'%5s\r\n','0'); % apparent resistivity
%     fprintf(fid2,'%5s\r\n',num2str(length(I_IP_all))); % number of
measurements
%     fprintf(fid2,'%5s\r\n','2'); % el location type
%     fprintf(fid2,'%5s\r\n','1'); % IP flag
%     fprintf(fid2,'%5s\r\n','Chargeability'); % IP header
%     fprintf(fid2,'%5s\r\n','mV/V'); % IP unit
%     fprintf(fid2,'%5s\r\n','0.04,1.0'); % delay, integration time
%
%     % write data

```

```

%      dlmwrite(res_write,All_res,'delimiter',' ','-
append','newline','pc','precision', 8); % write this to a txt file for your new
line file!
%      dlmwrite(IP_write,All_IP,'delimiter',' ','-
append','newline','pc','precision', 8); % write this to a txt file for your new
line file!
%
%      % write utm coords
%      fprintf(fid1,'%5s\r\n','Global Coordinates present');
%      fprintf(fid1,'%5s\r\n','Number of coordinate points');
%      fprintf(fid1,'%5s\r\n',num2str(length(y_array)));
%      fprintf(fid1,'%5s\r\n','Local Easting Northing');
%      for i = 1:length(y_array)
%          fprintf(fid1,'%30s\r\n',[num2str(y_array(i)) ' '
num2str(utm_E_interp(i)) ' ' num2str(utm_N_interp(i))]);
%      end
%
%      fprintf(fid2,'%5s\r\n','Global Coordinates present');
%      fprintf(fid2,'%5s\r\n','Number of coordinate points');
%      fprintf(fid2,'%5s\r\n',num2str(length(y_array)));
%      fprintf(fid2,'%5s\r\n','Local Easting Northing');
%      for i = 1:length(y_array)
%          fprintf(fid2,'%30s\r\n',[num2str(y_array(i)) ' '
num2str(utm_E_interp(i)) ' ' num2str(utm_N_interp(i))]);
%      end
%
%      % zeros
%      fprintf(fid1,'%4s\r\n','0,0,0,0');
%      fprintf(fid2,'%4s\r\n','0,0,0,0');
%
%      fclose(fid1);
%      fclose(fid2);

```

### end interpolate onto grid - res

```

dx = 30; % [m]
dy = 5; % [m]
max_grid = 1000; % [m]

% interp utm E to x-grid
xmin = min(min([All_res(:,2) All_res(:,5) All_res(:,8) All_res(:,11)]));
x = [All_res(:,2) All_res(:,5) All_res(:,8) All_res(:,11)] - xmin;
Xintp = round2(x,dx);

% interp utm N to y-grid
ymin = min(min([All_res(:,3) All_res(:,6) All_res(:,9) All_res(:,12)]));
y = [All_res(:,3) All_res(:,6) All_res(:,9) All_res(:,12)] - ymin;
Yintp = round2(y,dy);

Zintp = [All_res(:,4) All_res(:,7) All_res(:,10) All_res(:,13)];

% creat new loc All_res matrix
Rintp = All_res(:,end);
[r, c] = find(Xintp>max_grid | Yintp>max_grid);

```

```

Xintp(r,:) = [];
Yintp(r,:) = [];
Zintp(r,:) = [];
Rintp(r,:) = [];

I = find(Yintp(:,1)-Yintp(:,2)==0 | Yintp(:,1)-Yintp(:,3)==0 |
Yintp(:,1)-Yintp(:,4)==0 | Yintp(:,2)-Yintp(:,4)==0 | Yintp(:,3)-
Yintp(:,4)==0);
Xintp(I,:) = [];
Yintp(I,:) = [];
Zintp(I,:) = [];
Rintp(I,:) = [];

RES = [4.*ones(size(Xintp(:,1))) Xintp(:,1) Yintp(:,1) Xintp(:,2)
Yintp(:,2) Xintp(:,3) Yintp(:,3) Xintp(:,4) Yintp(:,4) Rintp]

```

**interpolate onto grid - IP**

interp utm E to x-grid

```

xmin = min(min([All_IP(:,2) All_IP(:,5) All_IP(:,8) All_IP(:,11)]));

x = [All_IP(:,2) All_IP(:,5) All_IP(:,8) All_IP(:,11)] - xmin;

Xintp = round2(x,dx);

% interp utm N to y-grid
ymin = min(min([All_IP(:,3) All_IP(:,6) All_IP(:,9) All_IP(:,12)]));
y = [All_IP(:,3) All_IP(:,6) All_IP(:,9) All_IP(:,12)] - ymin;
Yintp = round2(y,dy);

% creat new loc All_res matrix
RIPintp = [All_IP(:,end-1) All_IP(:,end)];
[r, c] = find(Xintp>max_grid | Yintp>max_grid);
Xintp(r,:) = [];
Yintp(r,:) = [];
RIPintp(r,:) = [];

I = find(Yintp(:,1)-Yintp(:,2)==0 | Yintp(:,1)-Yintp(:,3)==0 |
Yintp(:,1)-Yintp(:,4)==0 | Yintp(:,2)-Yintp(:,4)==0 | Yintp(:,3)-
Yintp(:,4)==0);
Xintp(I,:) = [];
Yintp(I,:) = [];
RIPintp(I,:) = [];

IP = [4.*ones(size(Xintp(:,1))) Xintp(:,1) Yintp(:,1) Xintp(:,2)
Yintp(:,2) Xintp(:,3) Yintp(:,3) Xintp(:,4) Yintp(:,4) RIPintp]
res_write = [dat_path '\3D_res_combined.dat'];
fidl = fopen(res_write,'a');

```

**write file**

```

fprintf(fid1,'%30s\r\n',res_write); % file name
fprintf(fid1,'%30s\r\n',num2str(length(0:dx:max(Xintp(:))))); % x grid
fprintf(fid1,'%30s\r\n',num2str(length(0:dy:max(Yintp(:))))); % y grid
fprintf(fid1,'%30s\r\n',num2str(dx)); % x el spacing
fprintf(fid1,'%30s\r\n',num2str(dy)); % y el spacing
fprintf(fid1,'%30s\r\n','11'); % general array type
fprintf(fid1,'%30s\r\n','0'); % sub-array type
fprintf(fid1,'%30s\r\n','Type of data (0=apparent
resistivity,1=resistance)'); % sub-array type
fprintf(fid1,'%30s\r\n','0'); % app res
fprintf(fid1,'%30s\r\n',num2str(size(RES,1))); % number of data points
dlmwrite(res_write,RES,'delimiter',' ','-
append','newline','pc','precision',8); % write this to a txt file for your new
line file!
fprintf(fid1,'%4s\r\n','0,0,0,0');
fclose(fid1);

IP_write = [dat_path '\3D_IP_combined.dat'];
fid2 = fopen(IP_write,'a');
fprintf(fid2,'%30s\r\n',res_write); % file name
fprintf(fid2,'%30s\r\n',num2str(length(0:dx:max(Xintp(:))))); % x grid
fprintf(fid2,'%30s\r\n',num2str(length(0:dy:max(Yintp(:))))); % y grid
fprintf(fid2,'%30s\r\n',num2str(dx)); % x el spacing
fprintf(fid2,'%30s\r\n',num2str(dy)); % y el spacing
fprintf(fid2,'%30s\r\n','11'); % general array type
fprintf(fid2,'%30s\r\n','0'); % sub-array type
fprintf(fid2,'%30s\r\n','Type of data (0=apparent
resistivity,1=resistance)'); % sub-array type
fprintf(fid2,'%30s\r\n','0'); % app res
fprintf(fid2,'%30s\r\n',num2str(size(IP,1))); % number of data points
fprintf(fid2,'%30s\r\n','IP present'); % chargeability header
fprintf(fid2,'%30s\r\n','Chargeability'); % type of IP data
fprintf(fid2,'%30s\r\n','mV/V'); % IP unit
fprintf(fid2,'%30s\r\n','0.1,1.0'); % Delay, int time
dlmwrite(IP_write,IP,'delimiter',' ','-
append','newline','pc','precision',8); % write this to a txt file for your new
line file!
fprintf(fid1,'%4s\r\n','0,0,0,0');
fclose(fid1);

```

## Plot all variables

```

clear all; % clear variables

xyz_path = '../xyz_files';
gps_path = '../combined txt gps files';

gps_files = ls([gps_path '/*.txt']);

% this block of code ID's all of the .xyz files in your current folder
files = ls(xyz_path); % strings of files in matlab folder your in
iter = 1; % for indexing "dat_files" properly (remember . and ..)
for i = 1:size(files,1) % loop through number of files in folder
    xyz_find = strfind(files(i,:),'.xyz'); % returns location where ".dat" is
in string
    IP_find = strfind(files(i,),'IP'); % returns location where ".dat" is in
string
    res_find = strfind(files(i,),'res');
    if (size(xyz_find) > 0 & size(res_find) > 0)% if "dat_files" is not empty
(aka is a dat file)
        xyz_files(iter,:) = files(i,:); % store the file name
        iter = iter+1;
    end
end

% find unique line data
for i = 1:size(xyz_files,1)
    lines_str(i,:) = xyz_files(i,2:3);
    lines(i) = str2num(xyz_files(i,2:3));
end
lines_str = unique(lines_str,'rows');
num_lines = max(lines);

% load data
for i = 1:length(lines)
    fid = fopen([xyz_path '/' xyz_files(i,)],'r');
    test = fgets(fid);
    line = ' ';
    j = 1;
    temp_data = [];
    while strcmp(line(1), '/')==0
        line = fgets(fid);
        if strcmp(line(1), '/')==0
            temp_data(j,:) = str2num(line);
        end
        j = j+1;
    end
end

```

```

    d{i} = temp_data;
    min_res(i) = min(temp_data(:,3));
    max_res(i) = max(temp_data(:,3));
    fclose(fid);
end
rmax = max(max_res);
rmin = min(min_res);
log_ticks = round(logspace(log(rmin)./log(10),log(rmax)./log(10),12));
tickstr = num2str(log_ticks');

% convert locations to coords/elev
for i = 1:length(d)
    data = [];
    line = str2num(lines_str(i,:));

    % load gps data
    GPS = importdata([gps_path '/' gps_files(i,:)], '\t', 1);
    loc = (GPS.data(:,1)-1)*5;
    utm_E = GPS.data(:,2);
    utm_N = GPS.data(:,3);
    elev = GPS.data(:,4);

    % load y,z,rho data
    y = d{i}(:,1);
    z = d{i}(:,2);
    rho = d{i}(:,3);

    % create gridded rho data
    yi = unique(y);
    zi = unique(z); %min(z):h:max(z);
    Rc = griddata(y,z,rho,yi,zi. ');

    % grid y,z data
    Yi = ones(length(zi),1)*yi';
    Zi = zi*ones(1,length(yi));

    % vectorize gridded coords
    yi = Yi(:);
    zi = Zi(:);
    xi = interp1(loc,utm_E,yi,'cubic');

    % find all nan's and shape back into matrices
    xc = nan(size(yi));
    yc = nan(size(yi));
    zc = nan(size(yi));
    for k = 1:length(y)
        I = find(yi==y(k) & zi==z(k));
        xc(I) = xi(I);
        yc(I) = yi(I);
        zc(I) = zi(I);
    end
    Xc = reshape(xc,size(Yi));
    Yc = reshape(yc,size(Yi));

```

```

Zc = reshape(zc,size(Yi));

% correct Zc
elev_cor = interp1(loc,elev,Yc(1,:), 'cubic');
for j = 1:size(Zc,2)
    Zc(:,j) = elev_cor(j) - Zc(:,j);
end

% correct Yc
Yc = interp1(loc,utm_N,Yc, 'cubic');

% store data
d1{i} = Xc;
d2{i} = Yc;
d3{i} = Zc;
d4{i} = Rc;
end

% plot data
figure(1); hold on
ax1 = subplot(1,2,1); hold on
for i = 1:length(d1)
    Xc = d1{i};
    Yc = d2{i};
    Zc = d3{i};
    Rc = d4{i};

    surface(Xc,Yc,Zc,log10(Rc))
    shading interp
    axis image
    cbar = colorbar;
    caxis([log10(rmin) log10(rmax)])
    set(cbar, 'YTick',log10(log_ticks));
    set(cbar, 'YTickLabel',{tickstr});
    view(60,45);
end
xlabel('UTM E [m]')
ylabel('UTM N [m]')
zlabel('Elevation [m]')

% this block of code ID's all of the .xyz files in your current folder
files = ls(xyz_path); % strings of files in matlab folder your in
iter = 1; % for indexing "dat_files" properly (remember . and ..)
for i = 1:size(files,1) % loop through number of files in folder
    xyz_find = strfind(files(i,:),'.xyz'); % returns location where ".dat" is
in string
    IP_find = strfind(files(i,:), 'IP'); % returns location where ".dat" is in
string
    res_find = strfind(files(i,:), 'res');
    if (size(xyz_find) > 0 & size(IP_find) > 0)% if "dat_files" is not empty
(aka is a dat file)
        xyz_files(iter,:) = files(i,:); % store the file name
    end
end

```

```

        iter = iter+1;
    end
end

% find unique line data
for i = 1:size(xyz_files,1)
    lines_str(i,:) = xyz_files(i,2:3);
    lines(i) = str2num(xyz_files(i,2:3));
end
lines_str = unique(lines_str,'rows');
num_lines = max(lines);

% load data
for i = 1:length(lines)
    fid = fopen([xyz_path '/' xyz_files(i,:)], 'r');
    test = fgets(fid);
    test = fgets(fid); % ----- IP ONLY !!!-----
    line = ' ';
    j = 1;
    temp_data = [];
    while strcmp(line(1), '/') == 0
        line = fgets(fid);
        if strcmp(line(1), '/') == 0
            temp_data(j,:) = str2num(line);
        end
        j = j+1;
    end

    d{i} = temp_data;
    min_res(i) = min(temp_data(:,3));
    max_res(i) = max(temp_data(:,3));

    min_ip(i) = min(temp_data(:,5)); % ----- IP ONLY !!!-----
    max_ip(i) = max(temp_data(:,5)); % ----- IP ONLY !!!-----
    fclose(fid);
end

rmax = max(max_res);
rmin = min(min_res);
imax = max(max_ip); % ----- IP ONLY !!!-----
imin = min(min_ip); % ----- IP ONLY !!!-----

log_ticks = round(logspace(log(rmin)/log(10), log(rmax)/log(10), 12));
log_ticks = round(logspace(log(imin)/log(10), log(imax)/log(10), 12)); % -----
IP ONLY !!!-----
tickstr = num2str(log_ticks');

% convert locations to coords/elev
for i = 1:length(d)
    data = [];

```

```

line = str2num(lines_str(i,:));

% load gps data
GPS = importdata([gps_path '/' gps_files(i,:)], '\t', 1);
loc = (GPS.data(:,1)-1)*5;
utm_E = GPS.data(:,2);
utm_N = GPS.data(:,3);
elev = GPS.data(:,4);

% load y,z,rho data
y = d{i}(:,1);
z = d{i}(:,2);
rho = d{i}(:,3);
ip = d{i}(:,5); % ----- IP ONLY !!!-----

% create gridded rho data
yi = unique(y);
zi = unique(z); %min(z):h:max(z);
Rc = griddata(y,z,rho,yi,zi.);
IPC = griddata(y,z,ip,yi,zi.); % ----- IP ONLY !!!-----

% grid y,z data
Yi = ones(length(zi),1)*yi';
Zi = zi*ones(1,length(yi));

% vectorize gridded coords
yi = Yi(:);
zi = Zi(:);
xi = interp1(loc,utm_E,yi,'cubic');

% find all nan's and shape back into matrices
xc = nan(size(yi));
yc = nan(size(yi));
zc = nan(size(yi));
for k = 1:length(y)
    I = find(yi==y(k) & zi==z(k));
    xc(I) = xi(I);
    yc(I) = yi(I);
    zc(I) = zi(I);
end
Xc = reshape(xc,size(Yi));
Yc = reshape(yc,size(Yi));
Zc = reshape(zc,size(Yi));

% correct Zc
elev_cor = interp1(loc,elev,Yc(1,:), 'cubic');
for j = 1:size(Zc,2)
    Zc(:,j) = elev_cor(j) - Zc(:,j);
end

% correct Yc
Yc = interp1(loc,utm_N,Yc,'cubic');

```

```

    % store data
    d1{i} = Xc;
    d2{i} = Yc;
    d3{i} = Zc;
    d4{i} = Rc;
    d5{i} = IPC; % ----- IP ONLY !!!-----
end

% plot data
% figure(1); hold on
ax2 = subplot(1,2,2); hold on
for i = 1:length(d1)
    Xc = d1{i};
    Yc = d2{i};
    Zc = d3{i};
    Rc = d4{i};
    IPC = d5{i}; % ----- IP ONLY !!!-----

    %surface(Xc,Yc,Zc,log10(Rc))
    surface(Xc,Yc,Zc,IPC) % ----- IP ONLY !!!-----
    shading flat
    axis image
    cbar = colorbar;
    %caxis([log10(rmin) log10(rmax)])
    % caxis([log10(imin) log10(imax)]) % ----- IP ONLY !!!-----
    % set(cbar,'YTick',log10(log_ticks));
    % set(cbar,'YTickLabel',{tickstr});
    view(60,45);
end
xlabel('UTM E [m]')
ylabel('UTM N [m]')
zlabel('Elevation [m]')

linkaxes([ax1 ax2],'xy')
Published with MATLAB® R2015a

```

## Plot all IP data

```

clear all; % clear variables

xyz_path = '../xyz_files';
gps_path = '../combined txt gps files';

gps_files = ls([gps_path '/*.txt']);

% this block of code ID's all of the .xyz files in your current folder
files = ls(xyz_path); % strings of files in matlab folder your in
iter = 1; % for indexing "dat_files" properly (remember . and ..)
for i = 1:size(files,1) % loop through number of files in folder
    xyz_find = strfind(files(i,:),'.xyz'); % returns location where ".dat" is
in string
    IP_find = strfind(files(i,),'IP'); % returns location where ".dat" is in
string
    res_find = strfind(files(i,),'res');
    if (size(xyz_find) > 0 & size(IP_find) > 0)% if "dat_files" is not empty
(aka is a dat file)
        xyz_files(iter,:) = files(i,:); % store the file name
        iter = iter+1;
    end
end

% find unique line data
for i = 1:size(xyz_files,1)
    lines_str(i,:) = xyz_files(i,2:3);
    lines(i) = str2num(xyz_files(i,2:3));
end
lines_str = unique(lines_str,'rows');
num_lines = max(lines);

% load data
for i = 1:length(lines)
    fid = fopen([xyz_path '/' xyz_files(i,)],'r');
    test = fgets(fid);
    test = fgets(fid); % ----- IP ONLY !!!-----
    line = ' ';
    j = 1;
    temp_data = [];
    while strcmp(line(1),'/')==0
        line = fgets(fid);
        if strcmp(line(1),'/')==0
            temp_data(j,:) = str2num(line);
        end
        j = j+1;
    end
end

```

```

d{i} = temp_data;
min_res(i) = min(temp_data(:,3));
max_res(i) = max(temp_data(:,3));

min_ip(i) = min(temp_data(:,5)); % ----- IP ONLY !!!-----
max_ip(i) = max(temp_data(:,5)); % ----- IP ONLY !!!-----
fclose(fid);
end
rmax = max(max_res);
rmin = min(min_res);
imax = max(max_ip); % ----- IP ONLY !!!-----
imin = min(min_ip); % ----- IP ONLY !!!-----

log_ticks = round(logspace(log(rmin)./log(10),log(rmax)./log(10),12));
log_ticks = round(logspace(log(imin)./log(10),log(imax)./log(10),12)); % -----
IP ONLY !!!-----
tickstr = num2str(log_ticks');

% convert locations to coords/elev
for i = 1:length(d)
    data = [];
    line = str2num(lines_str(i,:));

    % load gps data
    GPS = importdata([gps_path '/' gps_files(i,:)], '\t', 1);
    loc = (GPS.data(:,1)-1)*5;
    utm_E = GPS.data(:,2);
    utm_N = GPS.data(:,3);
    elev = GPS.data(:,4);

    % load y,z,rho data
    y = d{i}(:,1);
    z = d{i}(:,2);
    rho = d{i}(:,3);
    ip = d{i}(:,5); % ----- IP ONLY !!!-----

    % create gridded rho data
    yi = unique(y);
    zi = unique(z); %min(z):h:max(z);
    Rc = griddata(y,z,rho,yi,zi. ');
    IPc = griddata(y,z,ip,yi,zi. '); % ----- IP ONLY !!!-----

    % grid y,z data
    Yi = ones(length(zi),1)*yi';
    Zi = zi*ones(1,length(yi));

    % vectorize gridded coords
    yi = Yi(:);
    zi = Zi(:);
    xi = interp1(loc,utm_E,yi,'cubic');

    % find all nan's and shape back into matrices

```

```

xc = nan(size(yi));
yc = nan(size(yi));
zc = nan(size(yi));
for k = 1:length(y)
    I = find(yi==y(k) & zi==z(k));
    xc(I) = xi(I);
    yc(I) = yi(I);
    zc(I) = zi(I);
end
Xc = reshape(xc,size(Yi));
Yc = reshape(yc,size(Yi));
Zc = reshape(zc,size(Yi));

% correct Zc
elev_cor = interp1(loc,elev,Yc(1,:), 'cubic');
for j = 1:size(Zc,2)
    Zc(:,j) = elev_cor(j) - Zc(:,j);
end

% correct Yc
Yc = interp1(loc,utm_N,Yc, 'cubic');

% store data
d1{i} = Xc;
d2{i} = Yc;
d3{i} = Zc;
d4{i} = Rc;
d5{i} = IPC; % ----- IP ONLY !!!-----
end

% plot data
figure(2); clf; hold on
for i = 1:length(d1)
    Xc = d1{i};
    Yc = d2{i};
    Zc = d3{i};
    Rc = d4{i};
    IPC = d5{i}; % ----- IP ONLY !!!-----

    %surface(Xc,Yc,Zc,log10(Rc))
    surface(Xc,Yc,Zc,IPC) % ----- IP ONLY !!!-----
    shading flat
    axis image
    cbar = colorbar;
    %caxis([log10(rmin) log10(rmax)])
    % caxis([log10(imin) log10(imax)]) % ----- IP ONLY !!!-----
    % set(cbar,'YTick',log10(log_ticks));
    % set(cbar,'YTickLabel',{tickstr});
    view(60,45);
end
xlabel('UTM E [m]')
ylabel('UTM N [m]')

```

```
zlabel('Elevation [m]')
```

Published with MATLAB® R2015a

## Plot metal Factor Data

```
clear all; % clear variables

xyz_path = '../xyz_files';
gps_path = '../combined txt gps files';

gps_files = ls([gps_path '/*.txt']);

% this block of code ID's all of the .xyz files in your current folder
files = ls(xyz_path); % strings of files in matlab folder your in
iter = 1; % for indexing "dat_files" properly (remember . and ..)
for i = 1:size(files,1) % loop through number of files in folder
    xyz_find = strfind(files(i,:),'.xyz'); % returns location where ".dat" is
in string
    IP_find = strfind(files(i,),'IP'); % returns location where ".dat" is in
string
    res_find = strfind(files(i,),'res');
    if (size(xyz_find) > 0 & size(res_find) > 0)% if "dat_files" is not empty
(aka is a dat file)
        xyz_files(iter,:) = files(i,:); % store the file name
        iter = iter+1;
    end
end

% find unique line data
for i = 1:size(xyz_files,1)
    lines_str(i,:) = xyz_files(i,2:3);
    lines(i) = str2num(xyz_files(i,2:3));
end
lines_str = unique(lines_str,'rows');
num_lines = max(lines);

% load data
for i = 1:length(lines)
    fid = fopen([xyz_path '/' xyz_files(i,)],'r');
    test = fgets(fid);
    line = ' ';
    j = 1;
    temp_data = [];
```

```

while strcmp(line(1),'/')==0
    line = fgets(fid);
    if strcmp(line(1),'/')==0
        temp_data(j,:) = str2num(line);
    end
    j = j+1;
end

d{i} = temp_data;
min_res(i) = min(temp_data(:,3));
max_res(i) = max(temp_data(:,3));
fclose(fid);
end

rmax = max(max_res);
rmin = min(min_res);
log_ticks = round(logspace(log(rmin)./log(10),log(rmax)./log(10),12));
tickstr = num2str(log_ticks');

% convert locations to coords/elev
for i = 1:length(d)
    data = [];
    line = str2num(lines_str(i,:));

    % load gps data
    GPS = importdata([gps_path '/' gps_files(i,:)],'\t',1);
    loc = (GPS.data(:,1)-1)*5;
    utm_E = GPS.data(:,2);
    utm_N = GPS.data(:,3);
    elev = GPS.data(:,4);

    % load y,z,rho data
    y = d{i}(:,1);
    z = d{i}(:,2);
    rho = d{i}(:,3);

    % create gridded rho data
    yi = unique(y);
    zi = unique(z); %min(z):h:max(z);
    Rc = griddata(y,z,rho,yi,zi. ');

    % grid y,z data
    Yi = ones(length(zi),1)*yi';
    Zi = zi*ones(1,length(yi));

    % vectorize gridded coords
    yi = Yi(:);
    zi = Zi(:);
    xi = interp1(loc,utm_E,yi,'cubic');

    % find all nan's and shape back into matrices
    xc = nan(size(yi));
    yc = nan(size(yi));
    zc = nan(size(yi));

```

```

for k = 1:length(y)
    I = find(yi==y(k) & zi==z(k));
    xc(I) = xi(I);
    yc(I) = yi(I);
    zc(I) = zi(I);
end
Xc = reshape(xc,size(Yi));
Yc = reshape(yc,size(Yi));
Zc = reshape(zc,size(Yi));

% correct Zc
elev_cor = interp1(loc,elev,Yc(1,:), 'cubic');
for j = 1:size(Zc,2)
    Zc(:,j) = elev_cor(j) - Zc(:,j);
end

% correct Yc
Yc = interp1(loc,utm_N,Yc, 'cubic');

% store data
d1{i} = Xc;
d2{i} = Yc;
d3{i} = Zc;
d4{i} = Rc;
end

% this block of code ID's all of the .xyz files in your current folder
files = ls(xyz_path); % strings of files in matlab folder your in
iter = 1; % for indexing "dat_files" properly (remember . and ..)
for i = 1:size(files,1) % loop through number of files in folder
    xyz_find = strfind(files(i,:),'.xyz'); % returns location where ".dat" is
in string
    IP_find = strfind(files(i,:), 'IP'); % returns location where ".dat" is in
string
    res_find = strfind(files(i,:), 'res');
    if (size(xyz_find) > 0 & size(IP_find) > 0) % if "dat_files" is not empty
(aka is a dat file)
        xyz_files(iter,:) = files(i,:); % store the file name
        iter = iter+1;
    end
end

% find unique line data
for i = 1:size(xyz_files,1)
    lines_str(i,:) = xyz_files(i,2:3);
    lines(i) = str2num(xyz_files(i,2:3));
end
lines_str = unique(lines_str, 'rows');
num_lines = max(lines);

% load data
for i = 1:length(lines)
    fid = fopen([xyz_path '/' xyz_files(i,:)], 'r');

```

```

test = fgets(fid);
test = fgets(fid); % ----- IP ONLY !!!-----
line = ' ';
j = 1;
temp_data = [];
while strcmp(line(1), '/')==0
    line = fgets(fid);
    if strcmp(line(1), '/')==0
        temp_data(j,:) = str2num(line);
    end
    j = j+1;
end

d{i} = temp_data;
min_res(i) = min(temp_data(:,3));
max_res(i) = max(temp_data(:,3));

min_ip(i) = min(temp_data(:,5)); % ----- IP ONLY !!!-----
max_ip(i) = max(temp_data(:,5)); % ----- IP ONLY !!!-----
fclose(fid);
end

rmax = max(max_res);
rmin = min(min_res);
imax = max(max_ip); % ----- IP ONLY !!!-----
imin = min(min_ip); % ----- IP ONLY !!!-----

log_ticks = round(logspace(log(rmin)./log(10),log(rmax)./log(10),12));
log_ticks = round(logspace(log(imin)./log(10),log(imax)./log(10),12)); % -----
IP ONLY !!!-----
tickstr = num2str(log_ticks');

% convert locations to coords/elev
for i = 1:length(d)
    data = [];
    line = str2num(lines_str(i,:));

    % load gps data
    GPS = importdata([gps_path '/' gps_files(i,:)], '\t', 1);
    loc = (GPS.data(:,1)-1)*5;
    utm_E = GPS.data(:,2);
    utm_N = GPS.data(:,3);
    elev = GPS.data(:,4);

    % load y,z,rho data
    y = d{i}(:,1);
    z = d{i}(:,2);
    rho = d{i}(:,3);
    ip = d{i}(:,5); % ----- IP ONLY !!!-----

```

```

% create gridded rho data
yi = unique(y);
zi = unique(z); %min(z):h:max(z);
Rc = griddata(y,z,rho,yi,zi. ');
IPc = griddata(y,z,ip,yi,zi. '); % ----- IP ONLY !!!-----

% grid y,z data
Yi = ones(length(zi),1)*yi';
Zi = zi*ones(1,length(yi));

% vectorize gridded coords
yi = Yi(:);
zi = Zi(:);
xi = interp1(loc,utm_E,yi,'cubic');

% find all nan's and shape back into matrices
xc = nan(size(yi));
yc = nan(size(yi));
zc = nan(size(yi));
for k = 1:length(y)
    I = find(yi==y(k) & zi==z(k));
    xc(I) = xi(I);
    yc(I) = yi(I);
    zc(I) = zi(I);
end
Xc = reshape(xc,size(Yi));
Yc = reshape(yc,size(Yi));
Zc = reshape(zc,size(Yi));

% correct Zc
elev_cor = interp1(loc,elev,Yc(1,:), 'cubic');
for j = 1:size(Zc,2)
    Zc(:,j) = elev_cor(j) - Zc(:,j);
end

% correct Yc
Yc = interp1(loc,utm_N,Yc,'cubic');

% store data
d1{i} = Xc;
d2{i} = Yc;
d3{i} = Zc;
d4{i} = Rc;
d5{i} = IPc; % ----- IP ONLY !!!-----
end

% plot data
figure(3); clf; hold on
for i = 1:length(d1)
    Xc = d1{i};
    Yc = d2{i};
    Zc = d3{i};
    Rc = d4{i};

```

```

IPc = d5{i}; % ----- IP ONLY !!!-----

%surface(Xc,Yc,Zc,log10(Rc))
Imf = find(IPc>=5 & Rc>= 500);
MFC = IPc;
MFC(Imf) = MFC(Imf).*100;
surface(Xc,Yc,Zc,MFC) % ----- IP ONLY !!!-----
shading flat
axis image
cbar = colorbar;
%caxis([log10(rmin) log10(rmax)])
% caxis([log10(imin) log10(imax)]) % ----- IP ONLY !!!-----
% set(cbar,'YTick',log10(log_ticks));
% set(cbar,'YTickLabel',{tickstr});
view(60,45);
end
xlabel('UTM E [m]')
ylabel('UTM N [m]')
zlabel('Elevation [m]')

```

*Published with MATLAB® R2015a*

## Plot Resistivity Data

```

clear all; % clear variables

xyz_path = '../xyz_files';
gps_path = '../combined txt gps files';

gps_files = ls([gps_path '/*.txt']);

% this block of code ID's all of the .xyz files in your current folder
files = ls(xyz_path); % strings of files in matlab folder your in
iter = 1; % for indexing "dat_files" properly (remember . and ..)
for i = 1:size(files,1) % loop through number of files in folder
    xyz_find = strfind(files(i,:),'.xyz'); % returns location where ".dat" is
in string
    IP_find = strfind(files(i,),'IP'); % returns location where ".dat" is in
string
    res_find = strfind(files(i,),'res');
    if (size(xyz_find) > 0 & size(res_find) > 0)% if "dat_files" is not empty
(aka is a dat file)
        xyz_files(iter,:) = files(i,:); % store the file name
        iter = iter+1;
    end
end

% find unique line data
for i = 1:size(xyz_files,1)

```

```

        lines_str(i,:) = xyz_files(i,2:3);
        lines(i) = str2num(xyz_files(i,2:3));
    end
    lines_str = unique(lines_str,'rows');
    num_lines = max(lines);

    % load data
    for i = 1:length(lines)
        fid = fopen([xyz_path '/' xyz_files(i,:)], 'r');
        test = fgets(fid);
        line = ' ';
        j = 1;
        temp_data = [];
        while strcmp(line(1), '/') == 0
            line = fgets(fid);
            if strcmp(line(1), '/') == 0
                temp_data(j,:) = str2num(line);
            end
            j = j+1;
        end

        d{i} = temp_data;
        min_res(i) = min(temp_data(:,3));
        max_res(i) = max(temp_data(:,3));
        fclose(fid);
    end

    rmax = max(max_res);
    rmin = min(min_res);
    log_ticks = round(logspace(log(rmin) ./ log(10), log(rmax) ./ log(10), 12));
    tickstr = num2str(log_ticks);

    % convert locations to coords/elev
    for i = 1:length(d)
        data = [];
        line = str2num(lines_str(i,:));

        % load gps data
        GPS = importdata([gps_path '/' gps_files(i,:)], '\t', 1);
        loc = (GPS.data(:,1)-1)*5;
        utm_E = GPS.data(:,2);
        utm_N = GPS.data(:,3);
        elev = GPS.data(:,4);

        % load y,z,rho data
        y = d{i}(:,1);
        z = d{i}(:,2);
        rho = d{i}(:,3);

        % create gridded rho data

```

```

yi = unique(y);
zi = unique(z); %min(z):h:max(z);
Rc = griddata(y,z,rho,yi,zi. ');

% grid y,z data
Yi = ones(length(zi),1)*yi';
Zi = zi*ones(1,length(yi));

% vectorize gridded coords
yi = Yi(:);
zi = Zi(:);
xi = interp1(loc,utm_E,yi,'cubic');

% find all nan's and shape back into matrices
xc = nan(size(yi));
yc = nan(size(yi));
zc = nan(size(yi));
for k = 1:length(y)
    I = find(yi==y(k) & zi==z(k));
    xc(I) = xi(I);
    yc(I) = yi(I);
    zc(I) = zi(I);
end
Xc = reshape(xc,size(Yi));
Yc = reshape(yc,size(Yi));
Zc = reshape(zc,size(Yi));

% correct Zc
elev_cor = interp1(loc,elev,Yc(1,:), 'cubic');
for j = 1:size(Zc,2)
    Zc(:,j) = elev_cor(j) - Zc(:,j);
end

% correct Yc
Yc = interp1(loc,utm_N,Yc,'cubic');

% store data
d1{i} = Xc;
d2{i} = Yc;
d3{i} = Zc;
d4{i} = Rc;
end

% plot data
figure(1); clf; hold on
for i = 1:length(d1)
    Xc = d1{i};
    Yc = d2{i};
    Zc = d3{i};
    Rc = d4{i};

    surface(Xc,Yc,Zc,log10(Rc))
    shading interp

```

```
axis image
cbar = colorbar;
caxis([log10(rmin) log10(rmax)])
set(cbar,'YTick',log10(log_ticks));
set(cbar,'YTickLabel',{tickstr});
view(60,45);
end
xlabel('UTM E [m]')
ylabel('UTM N [m]')
zlabel('Elevation [m]')
```

*Published with MATLAB® R2015a*

## APPENDIX H

**Independent Analysis of Surface Geochemistry Results**

From Tom Gesick, personal communication, 2016.

*Enclosed please find three copies of the Horseshoe Bend gold-in-soils map we put together. It includes all of the samples in your 2014 database, but does not include the 2015 detailed sampling in the Mammoth area. The map is on the old 1:4000 scale (1"= 333') topographic base that we used for our field base map in 2014.*

*As you have already determined, the Apex-Mammoth-Catherine system appears to be the strongest target. I think the strength of the target may in part be due to exposure and dispersal of values through extensive disturbance, possibly including some flyrock from blasting. I suspect the gold in soil anomalies in the NW corner of section 4, T6N, R2E are on the southwest extension of this system.*

*The Kentuck and Quaker area anomalies are both substantial, "orebody-sized" anomalies, with areas exceeding 20 parts per billion gold in soils occupying most of 20 and 40 acres respectively. In my Nevada experience, residual 20 ppb gold in soil anomalies of size are usually indicative of strongly anomalous to well-mineralized bedrock below. In a number of instances, a residual soil anomaly 20 ppb Au contour more or less outlines the suboutcrop footprint of shallow economic mineralization. Residual 50 ppb Au and above anomalies in soils are typically indicative of bedrock mineralization of potential economic interest.*

*I hypothesize that anomalies in the Kentuck area, at the toe of the range north of the Quaker, and around the Osborne are parts of a mostly-covered NE-trending fissure vein system that passes approximately under the weed station.*

*In my opinion, the Quaker, including the area north of it, merits a few holes. One could get some good, first-pass information and probably some grade hits with two or*

*three angle holes, including one relatively long one, from a pad on the road southwest of the southeast corner of the Quaker. One relatively long angle hole directed northwest from west of the north side center of the Catherine would also have potential. These would be directed at anomalies that appear to outline ladder structures oblique to the main trend, but the holes should also intersect and sample any "trend" or fissure vein structures south of or in the vicinity of the postulated NS structures.*

*If a drill station could be permitted at about 3240' elevation in the east center of the Quaker, a lot of information could be acquired drilling from it. This first pass drilling could be RC. In essence you will be doing follow up prospecting with a drill, looking for presence of potentially economic mineralization in the 3rd dimension.*

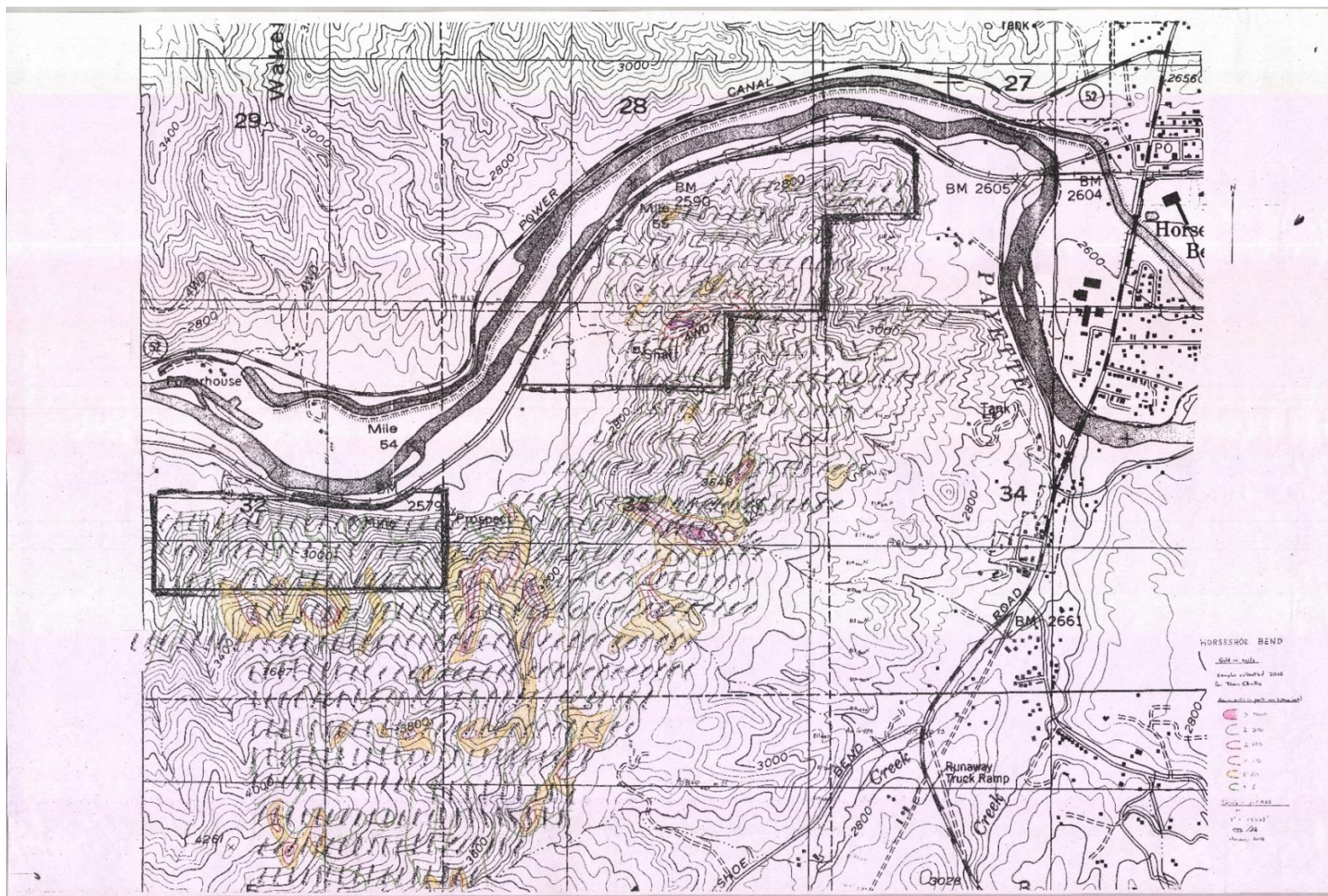


Figure H.1. Surface geochemistry gold concentration map produced by independent consulting geologist Tom Gesick, 2016.